UNIVERSITY OF ZAGREB

FACULTY OF MECHANICAL ENGINEERING AND

NAVAL ARCHITECTURE

Tomislav Lesičar

Multiscale Modeling of Heterogeneous Materials Using Second-Order Homogenization

DOCTORAL THESIS

Supervisor:

Prof. dr. sc. Zdenko Tonković

ZAGREB, 2015.

UNIVERSITY OF ZAGREB

FACULTY OF MECHANICAL ENGINEERING AND

NAVAL ARCHITECTURE

Tomislav Lesičar

Multiscale Modeling of Heterogeneous Materials Using Second-Order Homogenization

DOCTORAL THESIS

Supervisor:

Prof. dr. sc. Zdenko Tonković

ZAGREB, 2015.

SVEUČILIŠTE U ZAGREBU

FAKULTET STROJARSTVA I BRODOGRADNJE

Tomislav Lesičar

Višerazinsko modeliranje heterogenih materijala primjenom homogenizacije drugog reda

DOKTORSKI RAD

Voditelj rada:

Prof. dr. sc. Zdenko Tonković

ZAGREB, 2015.

BIBLIOGRAPHY DATA

UDC:	519.6 : 539.214 519.6 : 539.3 519.6 : 624.044
Keywords:	heterogeneous material, multiscale, C^1 homogenization, C^1 finite element, RVE, gradient boundary conditions
Scientific area:	Technical sciences
Scientific field:	Mechanical engineering
Institution:	Faculty of Mechanical Engineering and Naval Architecture (FAMENA), University of Zagreb
Supervisor:	Dr. sc. Zdenko Tonković, Professor
Number of pages:	183
Number of pictures:	83
Number of tables:	6
Number of references:	157
Date of oral examination:	14. December 2015.
Jury members:	Dr. sc. Zdenko Tonković, Professor Dr. sc. Jurica Sorić, Professor Dr. sc. Alojz Ivanković, Professor
Archive:	FAMENA, University of Zagreb

Acknowledgments

I wish to express my greatest gratitude to my supervisor Professor Zdenko Tonković for his generous and constant support throughout research resulting in this thesis. I am also thankful to Professor Jurica Sorić, who gave me valuable advice during research phase. Also, his stylish tips during writing of this thesis, as all the previous papers had great influence on my writing.

Many thanks to jury member Professor Alojz Ivanković (University College Dublin) for finding time to review this thesis, and for all valuable tips and suggestions required for successfull arrangement of this thesis.

Also I would like to thank to Assistant Professor Tomislav Jarak and Associate Professor Igor Karšaj for many valuable discussions, which were very helpful for solving many doubts and obstacles I had to resolve.

Special thanks to Assistant Professor Ivica Skozrit. His tremendous support along with vibrant debates during past few years starting from my college days, not only in science, but in every aspect of life was influential in many extents.

My special gratitude goes to all my dear colleagues from Laboratory of Numerical Mechanics, especially to Boris Jalušić, mag. ing. mech., whose kind support helped me in many ways. Also, I express my gratitude to all my colleagues from FAMENA, for their friendship and valuable advice.

I wish to express my deepest thanks my family, my parents Ivan and Mirjana, my brother Jasmin, my grandparents Božidar i Marija, who I grew up with. Thank you for all your effort, patience and faith in me.

Finally, I dedicate this thesis to my wife and son, Jelena and Mihael, people who fulfil my life in uncountable ways.

Tomislav Lesičar

Zagreb, December 2015.

Abstract

New demands on reliability and safety, together with the applications of new materials and new production technologies, can only be realized by advanced structural analysis methods involving realistic description of material behavior with microstructural effects. Classical continuum mechanics assumes material homogeneity, therefore, for comprehensive assessment of structural integrity and reliability, an analysis at the microlevel is unavoidable. In this framework, whole new branch of numerical methods arise, concerned with multiscale modelling of material behaviour using homogenization procedures.

Basically, this computational approach is based on the solution of two boundary value problems, one at each length scale. The results obtained by the simulation of a statistically representative sample of material, named Representative Volume Element (RVE), are used as input data at the macrolevel. Based on the micro-macro variable dependence, first- and second-order homogenization procedures are available. The multiscale analysis using the first-order computational homogenization scheme allows explicit modeling of the microstructure, but retains the essential assumptions of continuum mechanics. It is based on the principles of a local continuum and microstructural size is irrelevant. Recently developed second-order homogenization framework represents extension of the first-order homogenization from the mathematical aspect. The formulation relies on a nonlocal continuum theory with microstructural size as an influential parameter. Accordingly, in the finite element setting, C^1 continuity is required at the macrolevel. An important problem in the second-order homogenization framework is the scale transition methodology due to C^1 - C^0 transition at the microlevel. Higher-order gradients at the macroscale cannot be defined on the RVE as volume averages. Also, transfer of the full second-order gradient tensor from macro- to the microlevel is not possible without additional integral relation. On the other hand, higher-order stress at the coarse scale cannot be explicitly averaged, since no higher-order boundary value problem is defined at the microlevel.

In this research, a new multiscale algorithm using second-order computational homogenization is developed, where previously mentioned issues are circumvented by

introduction of higher-order continuum at the microlevel. At first, classical C^1 - C^0 algorithm has been established, firstly for small strains, afterwards for a large strain case. In this framework, a distinct approach has been used at the macrolevel, which is in this research discretized by the fully displacement based C^1 finite elements, contrary to the usually employed C^0 finite elements based on the mixed formulation. Finite element formulation has been re-established for application in multiscale framework. Also, series of patch tests have been conducted for verification of the element. The element, as complete multiscale setting has been implemented into commercial finite element software ABAQUS through user subroutines written in FORTRAN programming language and PYTHON scripts. Implementation aspects regarding microfluctuation integral which arises due to continuity degradation have been examined. Several numerical integration techniques have been tested with emphasis on physically realistic RVE behaviour. In the small strain case material nonlinearity has been considered, which is extended to the geometrical nonlinearity.

Having defined multiscale algorithm and second-order computational homogenization scheme, a new multiscale approach has been developed, preserving C^1 continuity at the microlevel. Linear elastic material behavior and small strains have been adopted, where microlevel is described by the Aifantis strain gradient elasticity theory. In this case, both levels are discretized by the same C^1 finite element. At the macrolevel generalized Aifantis continuum theory is established accounting for heterogeneities, since all the relevant information come from the RVE. Scale transition methodology has been derived, where every macrolevel variable is derived as true volume average of its conjugate on microscale. Displacement gradients at the coarse scale are imposed on the RVE boundaries through gradient- displacement and generalized periodic boundary conditions. By the virtue of higher-order continuum adopted at the microlevel, displacements as displacement derivatives are prescribed or related by periodicity equations. Besides, in Aifantis theory microstructural parameter l^2 appears, as a measure of nonlocality. So, in the new C^1 multiscale setting next to RVE size, another intrinsic nonlocality parameter is available. In the end, efficiency of the derived algorithms has been demonstrated by number of illustrative examples.

Keywords: heterogeneous material, multiscale, C^1 homogenization, C^1 finite element, RVE, gradient boundary conditions

Contents

Prošireni sažetak

Uvod

Primjena novih materijala i tehnologija proizvodnje uz stroge zahtjeve na pouzdanost i sigurnost nameće razvoj naprednih metoda analize konstrukcija i opisivanja ponašanja materijala. Pritom, kao i kod većine drugih problema, numeričke simulacije sve više nadopunjuju mnogo skuplji eksperiment. Osim toga, eksperimentalna analiza u konstrukciji za vrijeme njene eksploatacije u većini slučajeva nije moguća ili je vrlo teško izvediva, uz visoki rizik i cijenu. Stoga je numeričko modeliranje mehaničkog ponašanja heterogenih materijala posljednjih godina sve više predmet znanstvenih istraživanja, budući da su gotovo svi materijali zbog svoje prirodne građe na mikrorazini heterogeni. Za numeričko modeliranje ponašanja materijala do sada se uglavnom koristila fenomenološka mehanika kontinuuma u kombinaciji s metodom konačnih elemenata. No, klasična mehanika kontinuuma ne razmatra strukturne pojave u materijalu na mikrorazini te se javlja ovisnost rezultata o usmjerenosti i gustoći mreže konačnih elemenata. Problem nije isključivo numerički, već leži i u matematičkom modelu. Ubrzanim rastom računalnih resursa, a time i primjene metode konačnih elemenata, u posljednjih nekoliko desetljeća došlo je do razvoja metoda modeliranja na više razina (multiscale metode), koje omogućuju procjenu ponašanja materijala na makrorazini iz poznatih svojstava konstituenata i geometrije mikrostrukture.

Prenošenje rješenja s jedne razine na drugu jedan je od ključnih koraka višerazinske analize. Nakon rješavanja problema rubnih vrijednosti na nekoj od razina koja predstavlja strukturu materijala, dobiveni rezultati se homogeniziraju (uprosječuju po volumenu). Homogenizirani rezultati se prenose na neku od viših razina gdje se koriste kao ulazni podaci u daljnjoj analizi. Očigledno, za provedbu analize potrebna su minimalno dva modela. Jedan model predstavlja makrorazinu, dok drugi, model reprezentativnog volumenskog elementa (RVE-a), predstavlja mikrorazinu, odnosno mikrostrukturu materijala. Drugim riječima, RVE predstavlja najmanji dio mikrostrukture materijala koji sadrži sve osnovne informacije potrebne za opisivanje ponašanja materijala. Na taj način, RVE mora biti statistički reprezentativan uzorak mikrostrukture. Za provedbu analize na mikrorazini na rubove RVE-a

dodjeljuje se tenzor deformacije s makrorazine, koji se transformira u pomake primjenom odgovarajućih rubnih uvjeta. Konstitutivna relacija na makrorazini je *a priori* nepoznata te se dobiva iz analize RVE-a. Pritom se tenzor naprezanja i konstitutivna matrica dobivaju postupkom homogenizacije, odnosno uprosječavanjem po volumenu RVE-a. Za rješavanje problema rubnih vrijednosti na mikrorazini najčešće se primjenjuje metoda konačnih elemenata, no moguća je i primjena ostalih metoda kao što su npr. bezmrežne metode, metoda rubnih elemenata, Fourierova transformacija i sl.

Pošto računalna homogenizacija ne zahtijeva *a priori* pretpostavke o konstitutivnoj relaciji na makrorazini, ona omogućuje modeliranje kompleksnih geometrija i detalja mikrostrukture, kao i različitih nelinearnih materijalnih modela te velikih deformacija. Osim računalne homogenizacije postoje i druge metode, razvijene uglavnom prije računalne homogenizacije, no one su većinom ograničene na jednostavnije geometrijske modele mikrostrukture, linearne i jednostavnije nelinearne materijalne modele te male deformacije. Rezultati dobiveni homogenizacijom (tenzor naprezanja i konstitutivna matrica) uvelike ovise o rubnim uvjetima primijenjenima na RVE-u. U literaturi se najčešće koriste rubni uvjeti pomaka, rubni uvjeti periodičnosti i rubni uvjeti površinskog opterećenja. Istraživanja su pokazala da rezultati homogenizacije dobiveni korištenjem rubnih uvjeta pomaka pokazuju prekruto ponašanje RVE-a, dok rezultati dobiveni primjenom rubnih uvjeta površinskog opterećenja daju prepodatljivo ponašanje RVE-a. Primjena rubnih uvjeta periodičnosti daje najbolje rezultate i najbržu konvergenciju homogeniziranih vrijednosti pri povećanju dimenzije RVE-a. Na temelju ovisnosti varijabli na makrorazini o varijablama na mikrorazini razlikuju se višerazinske metode s primjenom računalne homogenizacije prvog i drugog reda. Računalna homogenizacija prvog reda omogućava eksplicitno modeliranje mikrostrukture, ali zadržava pretpostavke mehanike kontinuuma i stoga daje zadovoljavajuće rezultate samo za jednostavnije slučajeve opterećenja (vlak, tlak, smik) te ne može dobro opisati probleme u kojima se javljaju veliki gradijenti deformiranja i lokalizacija naprezanja. Zbog navedenih nedostataka homogenizacija prvog reda je u literaturi proširena na homogenizaciju drugog reda. Ova formulacija homogenizacije može opisati i kompleksnije načine deformiranja, npr. savijanje, ali zahtijeva kompleksniju formulaciju konačnog elementa na makrorazini, što uključuje zadovoljavanje C^1 kontinuiteta, odnosno uz zahtjev za kontinuitetom pomaka javlja i zahtjev za kontinuitetom deformacija. Na mikrorazini je u tom slučaju i dalje zadržan C^0 kontinuitet zbog jednostavnije formulacije problema rubnih vrijednosti. Za postizanje C^1 kontinuiteta na makrorazini također se javlja potreba za primjenom konačnih elemenata višeg

reda. Takvi konačni elementi temelje se na formulaciji kontinuuma višeg reda te stoga podržavaju dodatne stupnjeve slobode. Ovdje se uz pomake kao stupnjevi slobode javljaju prve i druge derivacije pomaka.

Iako višerazinska analiza uz homogenizaciju drugog reda ima brojne prednosti, primjena različitih pristupa mehanike kontinuuma na makro- i mikrorazini uzrokuje brojne poteškoće u matematičkom modelu višerazinskog opisivanja ponašanja materijala. Pošto je RVE opisan klasičnim kontinuumom, varijable višeg reda koje se prenose s makrorazine i na makrorazinu ne mogu biti adekvatno definirane. Problem se rješava različitim pristupima, a svi se svode na dodavanje integralnih relacija koje omogućuju primjenu homogenizacije drugog reda. Osim toga, u aktualnim istraživanjima za diskretizaciju makrorazine primjenjuju se konačni elementi s mješovitom formulacijom, čija je svrha ostvariti zadovoljavanje C^1 kontinuiteta uz čim manju numeričku kompleksnost. Nažalost, unatoč "pojednostavljenom" pristupu takvi konačni elementi pokazali su se poprilično kompleksnima po formulaciji i zahtjevnima glede numeričkih karakteristika.

Ciljevi i hipoteze istraživanja

Cilj ovog istraživanja je rješavanje otvorenih pitanja višerazinskog modeliranja heterogenih materijala primjenom računalne homogenizacije drugog reda. Unutar istraživanja cilj je izvesti novi višerazinski algoritam u kojem je i mikrorazina opisana kontinuumom višeg reda. Pretpostavka je da će na taj način, kao prvo, matematički model samog algoritma biti konzistentniji. Naravno, konzistentniji algoritam će pritom doprinijeti i fizikalno realnijem opisivanju ponašanja RVE-a, odnosno mikrostrukture. Pri tome se misli na proširenu definiciju gradijentnih rubnih uvjeta, koji će uz pomake definirati i gradijente pomaka po rubovima RVE-a. Uvođenjem kontinuuma višeg reda na mikrorazini trebao bi se riješiti problem prijenosa varijabli između dviju razina, jer u ovom slučaju sve varijable makrorazine postoje i na RVE-u. Drugim riječima, svaka varijabla makrorazine može se prikazati kao volumenski prosjek konjugirane varijable na mikrorazini, što je jedan od osnovnih preduvjeta primjene računalne homogenizacije. Za diskretizaciju obje razine cilj je primijeniti C^1 konačni element s potpunim C^1 kontinuitetom, pošto se u aktualnim istraživanjima pokazalo da mješovita formulacija unatoč težnji za pojednostavljenim pristupom u ostvarivanju C^1 kontinuiteta zadržava kompleksnost u samoj formulaciji te pati od numeričkih nestabilnosti.

Uz to, u postojećim algoritmima nelokalni mehanizmi na makrorazini opisuju se promjenom veličine RVE-a. Budući da je kontinuum višeg reda sam po sebi nelokalnog karaktera, opisivanje mehanizama nelokalnosti trebalo bi biti naprednije u odnosu na postojeće algoritme. Odnosno, u novoizvedenom algoritmu postojat će dva parametra nelokalnosti: veličina RVE-a i nelokalni parametar određen teorijom kontinuuma višeg reda.

Razvoj metoda homogenizacije

Razvoj i primjena višerazinskih metoda doživjeli su nagli procvat u zadnjih nekoliko desetaka godina s povećanjem računalnih resursa, čime je otvoren novi spektar primjene metode konačnih elemenata i ostalih numeričkih metoda analize deformabilnih tijela. Međutim, sama ideja analize utjecaja mikrostrukture na mehaničko ponašanje heterogenog materijala potječe još iz 19. stoljeća. Tu važan utjecaj ima princip miješanja (*rule of mixtures*), zatim Voigtov i Taylorov pristup, prema kojem svi mikrokonstituenti poprimaju konstantnu deformaciju, identičnu makroskopskoj. Nasuprot tome, Sachs i Reuss su predložili pristup u kojem se pretpostavlja da svi mikrokonstituenti poprimaju jednaka naprezanja, identična makroskopskim. Iako zastarjeli, ova dva pristupa i danas imaju značajnu ulogu za „grubu“ procjenu mehaničkih svojstava heterogenih materijala. Naime, Voigtova i Taylorova pretpostavka daje prekruto ponašanje, dok Sachsova i Reussova pretpostavka pokazuje prepodatljivo ponašanje materijala. U ranim fazama razvoja, metode homogenizacije su se temeljile na traženju rješenja u zatvorenoj formi za ponašanje heterogenih materijala. Zbog egzaktnosti rješenja, takve metode su opisivale samo linearno elastično ponašanje materijala, jednostavne geometrijske modele mikrostrukture te su većinom bile ograničene na male deformacije. Neke od metoda temeljenih na tome principu su Voigt-Reuss-Hillova ograničenja, Hashin-Strikmanov varijacijski princip, samokonzistentna metoda, i sl. Važnu ulogu u razvoju homogenizacije imale su i metode matematičke i asimptotske homogenizacije. Za postizanje boljih rješenja razvijene su metode homogenizacije temeljene na kontinuumu višeg reda, kao što je Coserrat-ov kontinuum.

Primjena kompozitnih materijala, a time i kompleksnijih mikrostruktura sa sobom su donijeli razvoj metode jediničnih ćelija (*unit cell*), čiji su rani začeci ostvareni u 60-im godinama dvadesetog stoljeća. Dodatni zamah u razvoju i primjeni metode jediničnih ćelija omogućio je i sve brži rast računalnih resursa i upotrebe numeričkih metoda analize, što je

omogućilo široki spektar primjene ove metode. Prednost jediničnih ćelija u odnosu na analitičke metode je u tome što uz efektivna svojstva materijala pružaju uvid u raspodjelu naprezanja i deformacija, odnosno pomaka na mikrostrukturi. Nažalost, većina metoda se temelji na *a priori* pretpostavkama o konstitutivnoj relaciji, što opet ovu metodu čini neprikladnom za opisivanje nelinearnih konstitutivnih relacija, odnosno, velikih deformacija. Osim toga, metoda jediničnih ćelija je pogodna za materijale s pravilnom mikrostrukturom kod kojih se može pretpostaviti pravilan raspored heterogenosti. Međutim, prostorna nejednolikost mikrostrukture ima značajan utjecaj na svojstva materijala, osobito za vrijeme plastičnog deformiranja, kao i u procesu akumuliranja oštećenja. Daljnjim razvojem višerazinskih metoda prvotni nedostaci i ograničenja metoda jediničnih ćelija su većinom otklonjeni, tako da je jedinična ćelija kao reprezentativni model mikrostrukture i u aktualnim istraživanjima još uvijek atraktivna.

U zadnjih 30-ak godina pojavili su se prvi radovi temeljeni na računalnoj homogenizaciji prvog reda, što je u kasnijim godinama potaknulo primjenu i razvitak ove metode u brojnim istraživanjima. Homogenizacija prvog reda nadilazi ograničenja prethodno spomenutih metoda homogenizacije. Kao što je već prije spomenuto, pristup računalne homogenizacije ne zahtijeva nikakvu pretpostavku o konstitutivnoj relaciji na makrorazini te stoga nije ograničena na određene materijalne modele, niti na male deformacije, a omogućuje i opisivanje prostorne nejednolikosti mikrostrukture. Matematički model računalne homogenizacije temelji se na osrednjavanju tenzora deformacije na makrorazini ili gradijenta deformiranja (teorija velikih deformacija) na makrorazini i virtualnog rada (Hill-Mandelov uvjet) po volumenu RVE-a. Polje pomaka na mikrorazini sastoji se od dva dijela: jedan dio ovisi o deformaciji definiranoj na makrorazini, dok je drugi neovisan o makrorazini i predstavlja mikrofluktuacije, odnosno doprinos mikrorazine (mikrostrukture) polju pomaka. Da bi se zadovoljila jednakost volumenskog prosjeka mikrodeformacije i makrodeformacije, mikrofluktuacije u prosječnom smislu ne smiju imati utjecaj na ponašanje strukture na makrorazini. Očigledno, takav uvjet u matematičkom smislu se osigurava integralnom relacijom na polje mikrofluktuacija. Jednakost volumenskog prosjeka mikrodeformacija i makrodeformacija je osnova za definiranje rubnih uvjeta koji se koriste na RVE-u, uz dodatno zadovoljavanje integralnog uvjeta mikrofluktuacija. Kao što je već prije spomenuto, rubni uvjeti periodičnosti daju najbolje rezultate homogenizacije. S druge strane, Hill-Mandelov uvjet omogućava prijenos tenzora naprezanja i konstitutivne matrice s mikro- na makrorazinu

na temelju uprosječavanja rada, odnosno energije deformiranja. Dobiveni rezultati pri tome također ovise o primijenjenim rubnim uvjetima.

Za adekvatnu primjenu računalne homogenizacije potrebno je zadovoljiti princip separacije razina prema kojem „*karakteristične duljine na mikrorazini su mnogo manje od prostornih duljina varijacije opterećenja na makrorazini*“. Primijeni li se dano pravilo na homogenizaciju prvog reda, zaključujemo da se s makrorazine prenosi tenzor deformacije kao konstantna veličina. Drugim riječima, homogenizacija prvog reda pretpostavlja konstantnu raspodjelu deformacije s makrorazine po čitavom rubu RVE-a. Nažalost, zadovoljavanje principa separacije razina ujedno i ograničava primjenu homogenizacije prvog reda. Kao što je već spomenuto, homogenizacijom prvog reda mogu se opisivati samo jednostavniji slučajevi opterećenja, bez značajnije pojave gradijenata. Osim toga, ova metoda u matematičkom smislu ulazi u okvire lokalne teorije standardne mehanike kontinuuma, što znači da apsolutna veličina mikrokonstituenata nema utjecaja na dobivene rezultate (*size effect*). Unatoč ograničenjima, računalna homogenizacija prvog reda je učestalo korišten alat u brojnim istraživanjima, poput modeliranja postupka ispitivanja mehaničkog ponašanja heterogenih materijala, mehanike oštećenja i loma, tankostijenih konstrukcija, kontaktnih i multidisciplinarnih problema.

Računalna homogenizacija drugog reda

Za prevladavanje ograničenja homogenizacije prvog reda u zadnjih nekoliko godina razvijena je računalna homogenizacija drugog reda. S matematičkog aspekta, homogenizacija drugog reda se temelji na istim principima osrednjavanja kao i homogenizacija prvog reda, uz dodatno proširenje formulacije. Odnosno, s makrorazine se uz tenzor deformacije sada prenosi i gradijent deformacije, dok se prilikom homogenizacije računaju Cauchyev tenzor naprezanja, ali i sekundarna naprezanja (*double stresses*). Računalna homogenizacija drugog reda pretpostavlja linearnu raspodjelu deformacije prenesene s makrorazine po rubu RVE-a, stoga ona omogućuje opisivanje složenijih modova deformiranja, kao i probleme lokalizacije u kojima se ne pojavljuju veliki gradijenti naprezanja i deformacija, u okvirima zadovoljavanja principa separacije razina. Za primjenu računalne homogenizacije drugog reda, na makrorazini se javlja potreba za primjenom nelokalne teorije (zadovoljen C^1 kontinuitet). Primjenom nelokalne teorije veličina RVE-a postaje utjecajni faktor na rezultate

homogenizacije, što ujedno i postavlja ograničenja na odabir i veličinu RVE-a. Što se tiče rubnih uvjeta, i u računalnoj homogenizaciji drugog reda rubni uvjeti periodičnosti daju najbolje rezultate, uz proširenu formulaciju varijablama kontinuuma višeg reda. Za slučaj kada su varijable višeg reda (druge derivacije pomaka) jednake nuli, rubni uvjeti periodičnosti za homogenizaciju drugog reda daju periodične deformirane oblike RVE-a, analogno homogenizaciji prvog reda. No, u općem slučaju gradijent tenzora deformacije je različit od nule, što znači da će se za kompleksnije oblike deformiranja javljati deformirani oblici RVE-a koji nisu geometrijski periodični. Upravo je iz tog razloga kod homogenizacije drugog reda ispravnije govoriti o poopćenim rubnim uvjetima periodičnosti.

U dosadašnjim istraživanjima, na mikrorazini je i dalje zadržan C^0 kontinuitet, što omogućuje primjenu klasičnih konačnih elemenata i materijalnih modela. No matematički model računalne homogenizacije drugog reda još uvijek predstavlja temu brojnih aktualnih istraživanja. Prilikom prijenosa varijabli s makro- na mikrorazinu, zbog prijelaza s C^1 na C^0 kontinuitet, javljaju se dodatna kinematička ograničenja polja mikrofluktuacije. Konkretno, zbog zadržavanja klasičnog kontinuuma na RVE-u, varijable višeg reda koje su potrebne na makrorazini ne mogu se adekvatno prenositi. Pošto na mikrorazini ne postoje gradijenti višeg reda, primjenom poopćenih uvjeta periodičnosti nije moguće prenijeti puni tenzor sekundarnih gradijenata s makrorazine. Da bi primjena rubnih uvjeta periodičnosti u homogenizaciji drugog reda bila moguća, gradijenti višeg reda definiraju se pomoću alternativne integralne relacije, što na kraju rezultira dodatnim integralnim uvjetom polja mikrofluktuacija. Također, prijenos sekundarnih naprezanja na makrorazinu je moguć samo korištenjem posebne integralne formulacije u kojoj su sekundarna naprezanja na mikrorazini u prosječnom smislu definirana kao moment primarnih naprezanja.

Nadalje, kako bi se opisala heterogenost materijala na makrorazini, konstitutivna relacija makromodela poprima poopćeni oblik. Odnosno, u homogenizaciji drugog reda to znači da svako naprezanje ovisi o primarnoj, ali i o sekundarnoj deformaciji, što dovodi do ukupno četiri konstitutivne matrice potrebne za integraciju matrice krutosti elementa. Konstitutivne materijalne matrice se dobivaju homogenizacijom iz postupka statičke kondenzacije. U postupku statičke kondenzacije globalna krutost RVE-a određuje se samo pomoću vanjskih čvorova.

U danom istraživanju također je razrađen algoritam višerazinskog modeliranja uz C^1-C^0 homogenizaciju drugog reda, za male i velike deformacije. Pri tome, makrorazina je diskretizirana trokutnim konačnim elementom s potpunim C^1 kontinuitetom. Formulacija

konačnog elementa prethodno je izvedena i prilagođena primjeni u višerazinskoj analizi. Iako naprednija, višerazinska analiza primjenom računalne homogenizacije drugog reda još ima brojna neriješena pitanja. Iz aktualnih istraživanja jasna je potreba za konzistentnim rješenjem problema degradacije kontinuiteta na mikrorazini.

C^1 računalna homogenizacija drugog reda

U prikazanom istraživanju izveden je novi algoritam računalne homogenizacije drugog reda. U novom algoritmu mikrorazina zadržava C^1 kontinuitet, odnosno i makro- i mikrorazina su opisane istom teorijom kontinuuma. Diskretizacija obje razine provedena je istim C^1 konačnim elementom spomenutim u prethodnom odjeljku. Za opisivanje materijala na mikrorazini odabrana je Aifantisova teorija gradijentne elastičnosti, koja vrijedi za male deformacije. Aifantisova teorija izvedena je kao posebni slučaj druge forme Mindlinove teorije kontinuuma, u kojoj su gradijenti višeg reda izraženi kao gradijenti tenzora deformacije. U svojoj posebnoj formulaciji Aifantis sve gradijentne koeficijente koji u konstitutivnoj relaciji povezuju varijable višeg reda zamjenjuje jednim koeficijentom, l^2. To uvelike pojednostavljuje definiranje materijalnih modela višeg kontinuuma. Konkretno, prema Aifantisovoj teoriji sekundarna naprezanja također ovise o klasičnoj materijalnoj matrici koja povezuje naprezanja i deformacije te mikrostrukturnom parametru. S obzirom da za 2D slučaj postoje gradijenti u smjerovima dviju osi, sekundarne deformacije i naprezanja definirani su pomoću dva različita tenzora. Analogno mikrorazini, makrorazina je opisana poopćenim Aifantisovim materijalnim modelom, što ukupno zahtijeva devet materijalnih matrica, odnosno devet submatrica krutosti elementa na makrorazini. Za razliku od makrorazine, element primijenjen za diskretizaciju RVE-a koristi tri materijalne matrice.

Osim toga, za prijenos varijabli između razina izveden je i novi matematički model homogenizacije. Za prijenos varijabli s makrorazine izvedeni su novi gradijentni rubni uvjeti pomaka i poopćene periodičnosti. U usporedbi s rubnim uvjetima primijenjenima u klasičnoj homogenizaciji drugog reda, u ovom slučaju se osim pomaka definiraju i gradijenti pomaka po rubovima RVE-a. S obzirom na očuvanje C^1 kontinuiteta na RVE-u, potpuni tenzor sekundarnih deformacija moguće je prenijeti na mikrorazinu bez dodatnih integralnih relacija nametnutih na polje mikrofluktuacija. Konzistentnost modela manifestira se i u

homogenizaciji naprezanja. Zahvaljujući teoriji višeg reda, homogenizirana sekundarna naprezanja ne zahtijevaju alternativne formulacije korištenjem primarnih naprezanja.

Nadalje, primjenom teorije višeg reda na mikrorazini uvodi se i nelokalnost $\left(l^2\right)$. Ako uzmemo u obzir da je sama homogenizacija drugog reda po sebi nelokalnog karaktera, gdje je veličina RVE-a, odnosno mikrostrukture parametar nelokalnosti, u slučaju C^1 homogenizacije uvodimo dodatni unutarnji nelokalni parametar. Na taj način, utjecaj okoline na ponašanje točke definiran je preko veličine RVE-a, ali uz to postoji i unutarnji materijalni parametar l^2. Time je omogućena veća fleksibilnost u pogledu utjecaja gradijenata na ponašanje materijala u odnosu na klasičnu homogenizaciju drugog reda.

Zaključak i doprinos rada

Poznato je da klasična mehanika kontinuuma ne razmatra mikrostrukturne pojave u materijalu. U današnje vrijeme, kada utjecaj mikrostrukture na mehanička svojstva i ponašanje materijala postaje predmet sve većeg broja istraživanja, numeričke simulacije sve više nadopunjuju teško izvediva i vrlo često skupa eksperimentalna ispitivanja. Stoga je u skorije vrijeme predložen velik broj naprednih numeričkih metoda višerazinske analize uz primjenu homogenizacije koje razmatraju utjecaj mikrostrukture na ponašanje materijala. U ovom radu je izveden numerički algoritam koji uzima u obzir utjecaj mikrostrukture primjenom homogenizacije drugog reda, a da pritom nadilazi ograničenja i nedostatke aktualnih istraživanja.

Na početku rada dan je osvrt na razvoj metoda homogenizacije te su istaknute njihove prednosti i nedostaci. Od prikazanih metoda ističe se računalna homogenizacija drugog reda, koja je najnaprednija u odnosu na ostale. No za primjenu homogenizacije drugog reda potrebna je diskretizacija makrorazine konačnim elementima s C^1 kontinuitetom. Stoga je u radu odabran trokutni element temeljen na metodi pomaka s potpunim C^1 kontinuitetom, za razliku od aktualnih istraživanja, koja koriste konačne elemente temeljene na mješovitoj formulaciji. Formulacija samog elementa je prilagođena uporabi u višerazinskoj analizi. Pritom su izvedene i osnovne relacije kontinuuma višeg reda. Nakon toga je razrađena višerazinska analiza uz primjenu homogenizacije drugog reda za male deformacije i elastoplastično ponašanje materijala. Izvedeni algoritam implementiran je u komercijalni softverski paket ABAQUS putem korisničkih rutina. Potom je provedena verifikacija

trokutnog elementa, kao i samog algoritma na uobičajenim primjerima iz literature. Zaključeno je da element zadovoljava sve testove numeričke točnosti i stabilnosti. Performanse elementa u usporedbi s ostalim konačnim elementima temeljenima na mješovitoj formulaciji su također zadovoljavajuće. Pokazano je i da primjena komercijalnog softvera u višerazinskoj analizi pruža brojne prednosti u pogledu velikog izbora numeričkih alata koji su dostupni u samom paketu, kao i programiranja korisničkih rutina te brzine računanja.

Postojeći algoritam proširen je na teoriju velikih deformacija. Prije samog proširenja iznova su izvedeni teorijski izrazi nužni za preformulaciju konačnog elementa, kao i matematičkog modela homogenizacije. Nakon teorijskog izvoda, element je verificiran na standardnim numeričkim primjerima. Rezultati višerazinske analize primjenom teorije velikih deformacija uspoređeni su rješenjima dobivenim teorijom malih deformacija. Na temelju dobivenih rezultata potvrđeni su prvobitni rezultati dobiveni primjenom malih deformacija te je zaključeno da primjena geometrijske nelinearnosti omogućuje točniji uvid u fizikalno ponašanje materijala.

Na kraju je izvedena nova metoda višerazinske analize heterogenih materijala primjenom homogenizacije drugog reda u kojoj je RVE opisan kontinuumom višeg reda. U ovom slučaju, odabrana je Aifantisova teorija gradijentne elastičnosti, koja je definirana za male deformacije. Izvedeni su teorijski izrazi Aifantisove teorije te su implementirani u konačni element. Za novoizvedeni algoritam isti konačni element koristi se za diskretizaciju makro- i mikrorazine. Također je detaljno razrađena konzistentna metodologija prijenosa varijabli između razina, kao i novi gradijentni rubni uvjeti. Točnost i učinkovitost novoizvedenog algoritma homogenizacije provjerena je na jednostavnim primjerima iz literature. Nakon toga rezultati dobiveni novom metodologijom uspoređeni su s postojećim algoritmima na uobičajenim primjerima. Za razliku od postojećih metoda, novoizvedeni algoritam omogućuje realnije modeliranje ponašanja heterogenih materijala te zahvaljujući svojoj proširenoj formulaciji može poslužiti kao osnova za razvoj naprednih višerazinskih metoda modeliranja oštećenja u materijalu. Osim toga, nova metoda omogućuje definiranje mikrostrukture materijala s optimalnim mehaničkim svojstvima što će smanjiti troškove projektiranja mehaničkih konstrukcija i povećati njihovu sigurnost.

Generalno gledajući, doprinosi ovog rada dani su u području višerazinskog modeliranja heterogenih materijala i metode računalne homogenizacije drugog reda. Najvažniji doprinosi rada su:

1) Izvod C^1 trokutnog konačnog elementa

- Izvedeni konačni element je prilagođen upotrebi u višerazinskoj analizi. Odnosno, integracija matrice krutosti elementa provedena je metodom numeričke integracije. Odabrana je Gaussova metoda s trinaest točaka integracije, što za zadanu formulaciju elementa predstavlja reduciranu shemu integracije.
- U element je implementirana pojednostavljena prva forma Mindlinovog kontinuuma te Aifantisova teorija gradijentne elastičnosti. Provedena je verifikacija elementa.

2) Razrada višerazinske analize uz primjenu računalne homogenizacije drugog reda

- Algoritam je izveden za male i velike deformacije uz elastoplastično ponašanje materijala. Razrađena je primjena rubnih uvjeta pomaka i poopćenih rubnih uvjeta periodičnosti.
- Razrađeni algoritam je implementiran u komercijalni softverski paket ABAQUS. Ispitan je utjecaj odabira metode numeričke integracije za zadovoljavanje integralnog uvjeta mikrofluktuacija. Na uobičajenim primjerima testirana je efikasnost algoritma.

3) Izvod metode višerazinske analize uz zadržavanje C^1 kontinuiteta na mikrorazini

- Izvedena je metoda prijenosa varijabli između razina. Predložena metoda pokazala se konzistentnijom od aktualnih istraživanja. Svaku varijablu makrorazine moguće je definirati kao potpuni volumenski prosjek varijable na mikrorazini.
- Izvedeni su gradijentni rubni uvjeti pomaka i gradijentni poopćeni rubni uvjeti periodičnosti. Uz konzistentniju metodologiju prijenosa varijabli između razina, novoizvedeni rubni uvjeti omogućuju prijenos punog tenzora sekundarnih deformacija na mikrorazinu bez integralnog uvjeta mikrofluktuacija.
- Efekti utjecaja okoline na ponašanje točke opisani su pomoću dva nelokalna parametra. Prvi parametar je veličina RVE-a, dok je drugi parametar mikrostrukturni parametar definiran Aifantisovom teorijom koji

se javlja kao unutarnja materijalna veličina. Izvedena je korelacija između prethodno navedena dva parametra.

Ključne riječi: heterogeni materijal, višerazinska analiza, C^1 konačni element, C^1 homogenizacija, RVE, gradijentni rubni uvjeti.

Nomenclature

Latin symbols

A	-	surface of the body
$a_1 \dots a_5$	-	gradient coefficients
$a_1 \dots a_{21}$	-	displacement polynomial coefficients
$\underline{\underline{\mathrm{B}}}_{\varepsilon}, \underline{\underline{\mathrm{B}}}_{\eta}, \underline{\underline{\mathrm{B}}}_{\eta_1}, \underline{\underline{\mathrm{B}}}_{\eta_2}, \underline{\underline{\mathrm{B}}}_{F}, \underline{\underline{\mathrm{B}}}_{G}$	-	derivatives of the shape functions
${}^4\underline{\underline{\mathbf{C}}}_{\sigma\varepsilon}, \underline{\underline{\mathrm{C}}}_{\sigma\varepsilon}$	-	material matrix relating stress to strain
${}^4\underline{\underline{\mathbf{C}}}_{PF}, \underline{\underline{\mathrm{C}}}_{PF}$	-	material matrix relating first Piola-Kirchhoff stress to deformation gradient
${}^5\underline{\underline{\mathbf{C}}}_{\sigma\eta}, \underline{\underline{\mathrm{C}}}_{\sigma\eta}$	-	material matrix relating stress to second-order strain
${}^5\underline{\underline{\mathbf{C}}}_{PG}, \underline{\underline{\mathrm{C}}}_{PG}$	-	material matrix relating first Piola-Kirchhoff stress to second-order gradient
${}^5\underline{\underline{\mathbf{C}}}_{\mu\varepsilon}, \underline{\underline{\mathrm{C}}}_{\mu\varepsilon}$	-	material matrix relating double stress to strain
${}^5\underline{\underline{\mathbf{C}}}_{QF}, \underline{\underline{\mathrm{C}}}_{QF}$	-	material matrix relating double stress to deformation gradient
${}^6\underline{\underline{\mathbf{C}}}_{\mu\eta}, \underline{\underline{\mathrm{C}}}_{\mu\eta}$	-	material matrix relating double stress to second-order strain
${}^6\underline{\underline{\mathbf{C}}}_{QG}, \underline{\underline{\mathrm{C}}}_{QG}$	-	material matrix relating double stress to second-order gradient
${}^5\underline{\underline{\mathbf{C}}}_{\sigma\varepsilon}, {}^6\underline{\underline{\mathbf{C}}}_{\sigma\varepsilon_{x1}}, {}^6\underline{\underline{\mathbf{C}}}_{\sigma\varepsilon_{x2}}$	-	generalized Aifantis material matrices
${}^5\underline{\underline{\mathbf{C}}}_{\mu_{x1}\varepsilon}, {}^6\underline{\underline{\mathbf{C}}}_{\mu_{x1}\varepsilon_{x1}}, {}^6\underline{\underline{\mathbf{C}}}_{\mu_{x1}\varepsilon_{x2}}$	-	generalized Aifantis material matrices
${}^5\underline{\underline{\mathbf{C}}}_{\mu_{x2}\varepsilon}, {}^6\underline{\underline{\mathbf{C}}}_{\mu_{x2}\varepsilon_{x1}}, {}^6\underline{\underline{\mathbf{C}}}_{\mu_{x2}\varepsilon_{x2}}$	-	generalized Aifantis material matrices
$\underline{\underline{\mathrm{D}}}$	-	coordinate matrix

E	-	Young's modulus
$\underline{\mathbf{F}}, \underline{\mathrm{F}}$	-	deformation gradient
$\Delta\underline{\mathbf{F}}$	-	iterative correction of deformation gradient
$\underline{\mathrm{F}}_{\mathrm{e}}, \underline{\mathrm{F}}_{\mathrm{i}}$	-	external and internal nodal force vectors
${}^{3}\underline{\mathbf{G}}$	-	second-order gradient
$\Delta{}^{3}\underline{\mathbf{G}}$	-	iterative correction of second-order gradient
$\underline{\underline{\mathrm{H}}}, \underline{\underline{\mathrm{H}}}_1, \underline{\underline{\mathrm{H}}}_2$	-	coordinate matrices
$\underline{\mathbf{I}}$	-	second-order unit tensor
${}^{4}\underline{\mathbf{I}}$	-	fourth order unit tensor
J	-	deformation gradient determinant
$\underline{\underline{\mathrm{J}}}$	-	Jacobian matrix
$\underline{\underline{\mathrm{K}}}$	-	stiffness matrix
$\tilde{\underline{\underline{\mathrm{K}}}}_{\mathrm{bb}}$	-	condensed RVE stiffness matrix
$\underline{\underline{\mathrm{K}}}_{\sigma\varepsilon}, \underline{\underline{\mathrm{K}}}_{\sigma\eta}, \underline{\underline{\mathrm{K}}}_{\mu\varepsilon}, \underline{\underline{\mathrm{K}}}_{\mu\eta}$	-	stiffness submatrices
$\underline{\underline{\mathrm{K}}}_{l}, \underline{\underline{\mathrm{K}}}_{x_1}, \underline{\underline{\mathrm{K}}}_{x_2}$	-	Aifantis stiffness submatrices
$\underline{\underline{\mathrm{K}}}_{uu}, \underline{\underline{\mathrm{K}}}_{u\theta}, \underline{\underline{\mathrm{K}}}_{\theta u}, \underline{\underline{\mathrm{K}}}_{\theta\theta}$	-	coupled thermal-stress stiffness submatrices
L	-	RVE size
L_{C^0}	-	RVE size in C^1-C^0 homogenization
L_{C^1}	-	RVE size in C^1 homogenization
L_1, L_2, L_3	-	area coordinates
l	-	microstructural parameter
$\underline{\underline{\mathrm{N}}}$	-	shape function matrix
$\mathbf{N}, \mathbf{n}$	-	unit outward normal vector
$\underline{\mathbf{P}}$	-	first Piola-Kirchhoff stress tensor
$\underline{\mathrm{P}}$	-	first Piola-Kirchhoff stress vector
$\Delta\underline{\mathbf{P}}$	-	iterative correction of first Piola-Kirchhoff stress
${}^{3}\underline{\mathbf{Q}}$	-	double stress tensor
$\underline{\mathrm{Q}}$	-	double stress vector

$\Delta\underline{\mathbf{Q}}$	-	iterative correction of double stress
$\underline{R}_u, \underline{R}_\theta$	-	mechanical and thermal residual vector
$\mathbf{r}$	-	microfluctuation field
s	-	boundary line
$\underline{\mathbf{T}}$	-	double traction tensor
$\underline{T}$	-	double traction vector
t	-	time
$\mathbf{t}$, $\underline{t}$	-	surface traction vector
$\mathbf{u}, \underline{u}$	-	displacement vector
$\delta\underline{u}$	-	displacement variation
$\underline{u}^i, \underline{u}^{i-1}$	-	displacement at time moments
$\Delta\underline{u}$	-	iterative correction of displacement vector
$\Delta\underline{\theta}$	-	iterative correction of temperature vector
V	-	volume of the body
$\underline{v}$	-	vector of nodal degress of freedom
$\delta\underline{v}$	-	variation of nodal degress of freedom
$\Delta\underline{v}$	-	iterative correction of nodal degress of freedom
$\underline{\mathbf{X}}$	-	position vector in reference configuration
$\underline{\mathbf{x}}$	-	position vector in current configuration
W	-	strain energy density function, work

Greek symbols

$\underline{\boldsymbol{\varepsilon}}$	-	strain tensor
$\underline{\boldsymbol{\varepsilon}}^{\mathrm{L}}$	-	logarithmic strain tensor
$\Delta\underline{\boldsymbol{\varepsilon}}$	-	iterative correction of strain tensor
$\Delta\underline{\boldsymbol{\varepsilon}}_{x_1}, \Delta\underline{\boldsymbol{\varepsilon}}_{x_2}$	-	iterative correction of strain gradient vector
$\underline{\varepsilon}$	-	strain vector
$\underline{\varepsilon}_{x_1}, \underline{\varepsilon}_{x_2}$	-	strain gradient vector

$\delta\underline{\varepsilon}$	-	strain variation
ϕ	-	shape functions describing element geometry
Γ	-	RVE boundary
${}^{3}\underline{\boldsymbol{\eta}}$	-	strain gradient
$\Delta\,{}^{3}\underline{\boldsymbol{\eta}}$	-	iterative correction of second-order strain
$\underline{\eta}$	-	second-order strain vector
$\delta\underline{\eta}$	-	second-order strain variation
λ	-	Lamé constant
${}^{3}\underline{\boldsymbol{\mu}}, {}^{3}\underline{\boldsymbol{\mu}}_{x_1}, {}^{3}\underline{\boldsymbol{\mu}}_{x_2}$	-	double stress tensor
$\underline{\mu}, \underline{\mu}_{x_1}, \underline{\mu}_{x_2}$	-	double stress vector
${}^{3}\underline{\boldsymbol{\mu}}^{i}, {}^{3}\underline{\boldsymbol{\mu}}^{i-1}, {}^{3}\underline{\boldsymbol{\mu}}_{x_1}^{i-1}, {}^{3}\underline{\boldsymbol{\mu}}_{x_2}^{i-1}$	-	double stress tensor at time moment
$\Delta\,{}^{3}\underline{\boldsymbol{\mu}}, \Delta\,{}^{3}\underline{\boldsymbol{\mu}}_{x_1}, \Delta\,{}^{3}\underline{\boldsymbol{\mu}}_{x_2}$	-	iterative correction of double stress tensor
μ	-	Lamé constant
ν	-	Poisson's ratio
$\underline{\boldsymbol{\sigma}}$	-	Cauchy stress tensor
$\underline{\sigma}$	-	Cauchy stress vector
$\underline{\boldsymbol{\sigma}}^{i}, \underline{\boldsymbol{\sigma}}^{i-1}$	-	Cauchy stress tensor at time moments
$\Delta\underline{\boldsymbol{\sigma}}$	-	iterative correction of Cauchy stress tensor
$\underline{\tilde{\boldsymbol{\sigma}}}$	-	effective stress tensor
$\boldsymbol{\tau}$	-	double surface traction vector
ψ	-	nonlinear deformation mapping function

The notation used in the current work is such that scalar quantities are indicated with italics. Tensors of order one are indicated with a bold face font only, while tensors of order greater than one are denoted by a bold face font and under bar. In matrix notation, quantities are denoted by a regular font. Row or a column vectors are indicated by a single under bar, while matrices are denoted by double under bar.

List of Figures

List of Tables

1 Introduction

1.1 Background and motivation

New materials and production technologies bring increased demands on reliability and safety of the structures. Considering engineering in the global sense, there is a tendency to replace highly expensive and often hardly feasible experiments by numerical simulations. These higher requirements cannot be achieved by classical numerical procedures and algorithms, based on a local approach of the classical continuum mechanics. The main disadvantage of the classical local approach is inability to span microstructural mechanisms essential for understanding general behavior of the macrostructure. Besides mathematical limitations, practical numerical problems also involve mesh dependency of the results. Therefore, development of the improved numerical methods for description of the material behavior, including material heterogeneity becomes increasingly important. To overcome aforementioned shortcomings of the classical approach, a new class of multiscale methods has been developed, employing homogenization techniques at the microstructural level. In this way, macrostructural response is directly dependent on the microstructure geometry and material properties of the microconstituents. Rapid increase of the computational power in the last few decades provides additional boost in this field. Generally speaking, multiscale methods can be classified as concurrent, sequential, homogenization, parallel and hybrid. These methods imply dependency between different scales, where solution at one scale is transformed to the other scale in an appropriate way. Hierarchically, we distinguish bottom-up and top-down approaches. In bottom-up approach the solution is driven by the smallest scale. On the other hand, in top-down approach lower scales are added until desired effects are captured. A more detailed overview of development and application of the multiscale methods is presented in [1-4].

Transfer of the solution variables between different scales represents a crucial step in a multiscale procedure. After solving the boundary value problem at the lower scale representing material structure, the obtained results are homogenized. These homogenized results are used at the upper level as an input data. It is obvious, at least two boundary value problems are solved in a micro-macro procedure. One boundary value problem represents the

macrolevel, while the other, named Representative Volume Element (RVE), represents microstructure. In this manner RVE should be a statistically representative part of the microstructure, where RVE size must be large enough to encompass all the relevant material characteristics, as well as microstructural mechanisms which occur at the microscale. Boundary value problem at the microlevel is formulated by displacement gradients from the macrolevel. Through application of the appropriate boundary conditions, displacement gradients from the macrolevel are transformed into nodal displacements on the RVE boundaries. Constitutive relation at the macroscale is *a priori* unknown and it is dependent on the RVE homogenization results. For solution of the RVE boundary value problem finite element method (FEM) is mostly applied [5-10], but other methods are also available, such as meshless methods [11, 12], the boundary element method [13], fast Fourier transforms (FFT) [14], etc.

The computational homogenization method does not require an explicit *a priori* constitutive relation at the macrolevel [8, 10, 15-19]. This is its main advantage because it allows modeling of a complex microstructure geometry, arbitrary non-linear and time dependent material behavior, as well as large deformations and rotations. Besides the computational homogenization, other homogenization methods are available, mostly developed before the computational homogenization, but in the most cases they are limited to a simple microstructure geometries and small strain constitutive models. Such methods are, for example, mathematical method of homogenization, Mori-Tanaka method, double inclusion model, numerical homogenization, etc., as can be found in [20, 21]. The results obtained by the homogenization such as a constitutive matrix and stress tensor depend on the boundary conditions (b. c.) applied for the determination of the RVE boundary nodal displacements. Three most commonly used types of boundary conditions, which are consistent with averaging theorems, are prescribed displacements, prescribed tractions and periodicity conditions. Homogenization results obtained by prescribed displacement boundary conditions show too stiff RVE behavior, while the RVE under traction boundary conditions exhibits too compliant behavior. Periodic boundary conditions may provide the best homogenization results and the fastest convergence properties by increasing RVE size. As shown in [6, 7, 9], the results obtained by the periodic boundary conditions lie between the values obtained by the prescribed displacements (upper bound), and the prescribed tractions (lower bound). In most applications, periodic b. c. require regular RVE discretization in a way that each node on the independent edge must have a couple node on the dependent edge. However, periodic b. c. can also be applied to irregularly discretized RVE models using

polynomial interpolation method [22], which contributes to the easier discretization of irregular microstructure models.

Based on the micro-macro variable dependence, the first-order and the second-order homogenization procedures are available. The multiscale analysis using the first-order computational homogenization scheme allows explicit modeling of the microstructure, but retains essential assumptions of the continuum mechanics, and thus gives satisfactory results only for a simple loading cases (tension, pressure, simple shear). It includes only the first gradient of the macroscopic displacement field and it is based on the principles of a local continuum. Therefore, the size effects, which represent influence of the surrounding material on the behaviour of the material point cannot be captured. Due to the mentioned shortcomings, the first-order computational homogenization scheme has been extended to the second-order computational homogenization framework, where the second-order stress and strain are included. The formulation is based on a non-local continuum theory which takes into account the influence of an environment on the behavior of a material point [23-26]. Furthermore, multiscale analysis using the second-order homogenization approach may describe more complex deformation modes, e. g., bending mode. It requires more complex formulation at the macrolevel (C^1 continuity), which implicates the requirement that both displacements and deformations must be continuous functions. The microlevel in this case can preserve C^0 continuity to keep RVE boundary value problem simple as possible, shown in [10, 18, 27-30]. As it is well-known, to satisfy C^1 continuity condition, the macrolevel model should be discretized by a higher-order finite elements supporting additional degrees of freedom (first and second displacement derivatives). The displacement based C^1 continuity finite element formulations, described in more detail in [31-35], suffer from several drawbacks. They have a complex formulation which complicates their numerical implementation. In addition, some formulations suffer from geometric restraints which may lead to incorrect results for second-order continuum problems. Therefore, for solving second-order continuum problems, the C^0 finite elements based on a mixed formulation have been developed in the last few years. In this case, the continuity requirements are fulfilled only in a weak sense [31, 32, 36-39]. In the mixed formulation, displacements and displacement derivatives are considered as independent variables. Their kinematic relation is enforced by Lagrange multipliers [31, 37, 39], or by penalty method [32, 36]. An approach applied to the solution of a strain gradient-dependent continuum problems is the formulation using discontinuous Galerkin method [40, 41]. This procedure uses C^0 continuous displacement functions, and the continuity of the higher order derivatives at the inter-element boundaries is

enforced by means of a discontinuous Galerkin formulation. Certain authors have developed other numerical methods for the implementation of a gradient elasticity such as meshless methods [42-44] and boundary element method [45, 46].

Despite numerous advantages of the second-order micro-to-macro framework, use of dissimilar continuum mechanics approaches at different scales disrupts mathematical consistency of the micro-macro scale transition methodology. Due to classical local approach established at the microlevel, higher-order variables occurring at the macroscale cannot be adequately derived in an averaged sense. There are several approaches dealing with this issue, proposing additional integral relations. Besides, in actual developments discretization of the model at the macroscale has been mostly performed by the mixed finite element formulations, to establish C^1 continuity with improved numerical efficiency. However, the elements derived have quite complex formulation with demanding computational requirements.

1.2 Historical overview of multiscale modeling concepts

Increased development and application of the multiscale methods has started a few decades ago, along with enhanced computational resources. However, early steps towards multiscale concept of modeling heterogeneous microstructure and its influence on mechanical behaviour of material originate from 19th century. In 1887, Voigt introduced rule of mixtures dealing with heterogeneous materials. Early published works were based on a simple assumptions of heterogeneous microstructure, such as Taylor model [47], assuming constant strains on all constituents, identical to the macroscopic one. On the other hand, according to Sachs model (1928) and Reuss (1929), all constituents take constant stress, identical to the macroscopic one. Although incorrect, these two approaches can serve for a „coarse“ estimate of effective properties of elastic heterogeneous materials. Voigt and Taylor model provide too stiff behaviour, while Sachs and Reuss model provide too compliant material response. In the beginning, homogenization techniques were developed within a closed-form solution framework. Due to solution exactness, only linear elastic behaviour has been considered, assuming simple microstructure geometries and small strains. Several proposed methods within this field are Voigt-Reuss-Hill bounds, Hashin-Strikman variational principle, and self-consistent method. More details can be found in [48]. Effective elastic material properties can also be assessed by methods of mathematical or asymptotic homogenization [49]. For better assessment nonlocal higher-order continuum theories have been considered, such as Cosserat

continuum [50] or gradient theories [51, 52]. Comprehensive historical overview is described in [53].

Development of composite materials brought a new class of so-called unit cell methods. Early contribution in this field has been done by Eshelby [54], solving stress distribution in an infinite material with ellipsoidal inclusion. Unit cell methods became attractive in a recent decades with extended application of numerical methods [55-59]. Compared to the analytical homogenization scheme, unit cell methods offer effective properties of the material including insight into stress and strain distribution. Unfortunately, majority of the unit cell methods are based on *a priori* assumed macroscopic constitutive relations. Obviously, in the case of material and geometrical nonlinearities closed-form assumption on a macroscopic behavior becomes cumbersome. Besides, unit cell model imposes regular arrangement of heterogeneities in the microstructure, which clearly narrows its applicability considering significant quantity of materials with an irregular microstructure. It is demonstrated that microstructural irregularity has a significant influence on the effective properties, especially in case of nonlinear behavior, or damage accumulation [56, 60]. Despite limitations, unit cell as a representative model of the microstructure is attractive even in actual developments [61-65]. For more details, see [1, 66].

First papers dealing with first-order computational homogenization appeared 30 years ago (Suquet 1985, Renard 1987.). Afterwards, computational homogenization methodology develops in a many extents [5-7, 67-74]. First-order computational homogenization concept exceeds all the limitations of the aforementioned homogenization schemes. As declared, no *a priori* assumptions on material behavior are needed. This brings possibility of modeling geometrical and material nonlinearities, as well as description of a microstructural irregularity. Mathematical scheme of computational homogenization framework is derived on the basis of averaging strain tensor (small strain theory) or deformation gradient (large strain theory) calculated at the coarse scale and virtual work (Hill-Mandel energy condition) over the RVE volume. Displacement field at the microscale consist of two parts: macroscale-dependent part depending on displacement gradients derived at the macrolevel and macroscale-independent part representing microfluctuations, i. e. contribution of the microstructure to the RVE displacement field. In order to establish volume average of the variables at the microlevel, microfluctuation field must vanish in an averaged sense, since microfluctuations cannot influence variables at the coarse scale [10, 28]. Dealing with microfluctuations basically distinguishes boundary conditions used on the RVE. As already mentioned, periodic b. c. provide the best homogenized results. On the other hand, Hill-

Mandel energy condition defines micro-to-macro scale transition of the stress tensor and constitutive matrices. The basic hypothesis of computational homogenization relies on scale separation principle enforcing that "*the microscopic length scale is assumed to be much smaller than the characteristic length over which the macroscopic loading varies in space*" [3]. In mathematical sense, first-order homogenization prescribes constant strain tensor on the RVE boundaries. Having this in mind, it is clear that in order to satisfy scale transition principle, first-order homogenization can appropriately describe only simple loading cases, such as simple tension, pressure or shear. Complex loading conditions, as well as problems including strain gradients or stress concentrations cannot be dealt with. Furthermore, first-order homogenization framework fits entirely into classical local continuum mechanics principles. In other words, absolute size of the microconstituents does not affect homogenized results (*size effect*). Nevertheless, first-order homogenization scheme represents widely used and useful numerical tool in many applications such as modeling of heterogeneous materials, fracture mechanics, thin sheets, contact and interdisciplinary problems.

1.2.1 Second-order computational homogenization concept

To overcome limitations mentioned above, extension to first-order framework named second-order computational homogenization has been derived a few years ago [18, 19, 29, 30, 75, 76]. From mathematical point of view, first and second derivatives of the displacement field at the macroscale are included into macro-to-micro scale transition. In a homogenization procedure conducted on RVE, stress and double stress tensor are computed. Second-order homogenization approach prescribes linear distribution of the displacement gradients derived at the coarse scale on the RVE boundaries. This allows modeling of more complex deformation modes, for example bending, as well as strain localization problems satisfying scale separation principle. Application of second-order homogenization implies establishment of a nonlocal theory at the macrolevel, obeying C^1 continuity. By use of a higher-order continuum theory at the macrolevel, RVE size becomes influential parameter in the homogenization procedure, which also puts some limitations on its size [77, 78]. Regarding boundary conditions on RVE, periodicity b. c. again provide the best results, including appropriate extension to higher-order variables. In the case when double strain variables are zero, periodic b. c. in a second-order homogenization provide periodic deformation response of the RVE, analogously to a first-order scheme. Generally speaking, non-zero double strain variables cause geometrically non-periodic deformation responses. Therefore, in the second-

order homogenization it is more correct to discuss about generalized periodic b. c., as declared in [8, 10].

In recent developments RVE boundary value problem is kept classical, as already mentioned before. Different theories used at various length scales cause inconsistencies in a scale transition methodology. Firstly, second-order gradient at the microlevel cannot be related to the macrolevel as a volume average. Secondly, in the Hill-Mandel energy condition, a modified definition of the second-order stress should be derived. Besides, the strain localization and material softening cannot be modeled at the microlevel without loss of ellipticity of governing field equations. Furthermore, to establish a relation between the variables of macro- and microlevel due to C^1 - C^0 transition, there is a need for an alternative relation between the strain gradient at the macroscale and the strain at the microscale, which results in an additional integral condition on the microfluctuation field [18, 27, 29]. There are several approaches to bridge a scale transition with account to the microfluctuation field. In [8], to establish a relation between the macroscopic gradient of the deformation gradient and the microscopic deformation gradient, an auxiliary integral relation has been considered. In this integral, the microscopic gradient of the deformation gradient has a definition of a first moment of the deformation gradient, causing inconsistency. Also, corner nodes fluctuations are fixed to zero, resulting in artificial stress concentrations. A more consistent approach is used in [10], where zero projection of the microfluctuations is enforced through orthogonality. On the other hand, the orthogonality is enforced by a vanishing surface integral of the micro-macro variable scalar product. Even though such formulation has notable advantages, again, relaxed constraints on the fluctuation field are required to avoid stress concentrations at the corners. Besides, the resulting orthogonality integral conditions suffer from demanding numerical implementation. In [79], an unified approach, based on the formulations available in the literature, is proposed for the enforcement of the boundary conditions using multiple constraint projection matrices. To preserve the classical microstructural boundary value problem, an assumption on the second moment of deformed RVE area has been taken, resulting in similar integral constraint as in [8], only for a small strain case. Substantially distinct approach has been used in [17], similar to the asymptotic homogenization method. The micro displacement field is composed of two components, the local macroscopic displacements and the microfluctuations. The unknown fluctuation field is composed of two unknown functions, related to the first-order strain (standard homogenization) and the second-order strain (second-order homogenization), respectively. The homogenization procedure is conducted in a two steps. The first step corresponds to the standard homogenization, whose

results are applied in the second-order homogenization, which is considered as the second step. However, due to the mathematically rigorous and computationally expensive procedure, this tool is only appropriate for a periodic microstructures (unit cell). Another approach is presented in [80], as an extension of the classical homogenization methods. Here, a composite material is replaced by an effective micromorphic continuum model at the macroscale, accounting for Cosserat rotational effects and stretching mechanisms. Such formulation is convenient in the case when scale separation principle is about to fail. The method relies on unambiguous determination of the fluctuation field in applying quadratic and cubic Dirichlet boundary conditions. Unfortunately, this approach also suffers from limitations, and it may fail in a special loading conditions. Only quadratic displacement based boundary conditions have been resolved. Higher order displacement polynomials, as stress-based boundary conditions are still not resolved.

Even though significant research has been undertaken, scale transition methodology in the second-order homogenization framework still remains not fully understood. There are several methods offering solutions, but neither of them can provide straight formulation with an efficient numerical implementation. Open discussions indicate, that for efficient micro-macro algorithm comprising second-order homogenization scheme, higher-order continuum should be introduced at the microlevel. But, higher-order continuity at the microlevel also draws RVE discretization by higher-order finite elements, requiring experimental material data relating second-order variables. It is clear that second-order computational homogenization technique is still not resolved.

1.3 Hypothesis and objectives of research

The main objective of the research is to develop a new multiscale procedure for modeling deformation responses of heterogeneous materials, employing second-order computational homogenization. In contrast to the existing approaches, the material microstructure described by the representative volume element will be modeled as a higher-order continuum. It is assumed that mathematical model of a new developed micro-macro algorithm should be more consistent compared to recent achievements. By introducing higher-order continuum at the microstructural length scale, actual difficulties in the classical C^1 - C^0 second-order approach should be resolved. In a new scheme all variables employed at the macrolevel can be expressed as a volume average of their conjugate variables at the lower scale. In addition, new approach should provide a more realistic representation of the material behavior, particularly

when strain localization or possibly material softening are modeled. The new and extended formulation of boundary conditions will be derived, prescribing not only displacements, but also displacement derivatives on RVE boundaries. Newly developed gradient boundary conditions should describe more realistic deformed shapes of the RVE. Both length scales will be discretized by a displacement based C^1 finite element, since mixed finite element formulations have not achieved significant improvement of numerical efficiency. As known, size effect established in C^1 - C^0 second-order homogenization is described only by RVE size. Introducing nonlocal continuum theory at the microlevel, intrinsic scale parameter is invoked. In this way, accuracy of nonlocality description will not be dependent only on a representative volume size, but also on the microstructural parameter available in higher-order continuum.

1.4 Scope and outline of the thesis

A new multiscale procedure for modeling of heterogeneous materials will be proposed where the material microstructure is described by a higher-order continuum bringing increased numerical and modeling accuracy. Along with multiscale scheme a new micro-macro transition procedure will be developed, where every variable at the macroscale can be defined as a true volume average of the conjugate variable from the lower length scale. A new C^1 continuity finite element based on the Aifantis theory will be formulated for application in a multiscale setting. A new gradient boundary conditions used at the microlevel will be derived, allowing prescription of the complete second-order strain tensor on RVE boundaries. Nonlocal behavior of heterogeneous material will be described by two nonlocal parameters. This should give possibility for further development of a gradient enhanced damage modeling at the microstructural level, as well as development of materials with optimal mechanical properties.

The thesis is organized in 6 chapters. After introductory lines described above, Chapter 2 is concerned with a higher-order continuum theory. Basic relations of a gradient theory used for modeling of the macrostructure are explained. Small and large strains are adopted. Aifantis constitutive behaviour, as a special case of Mindlin's Form II is derived. In Chapter 3, gradient theory relations are implemented into FEM by means of a three node C^1 triangular finite element. Three element formulations based on small strain, large strain and Aifantis theory are discussed. The new element formulations are verified on a simple examples, testing element behaviour and performance. Afterwards, two-scale methodology has been discussed in Chapter 4 for small strain, as well as large strain assumption. Boundary

conditions at the microlevel are derived. Stress homogenization, as well as calculation of a consistent constitutive matrices are declared. In C^1-C^0 homogenization scheme integral relation on the microflucation field rises. For efficient implementation of the microfluctuation integral, various numerical integration techniques are tested. Numerical implementation of the multiscale scheme has been discussed. The algorithms derived are tested on a usual benchmark examples. Comparison of small strain and large strain results has been made. In Chapter 5 a new approach in second-order two-scale scheme is presented, where both length scales are described by a higher-order continuum obeying C^1 continuity. A fully consistent scale-transition methodology is derived, along with a new developed gradient boundary conditions used on the RVE. A special attention has been directed to a nonlocal microstructural parameter occurring at the microscale and its correlation to the RVE size. Again, a few simple examples are considered for verification of the new multiscale model. The results obtained have been compared to the classical C^1-C^0 homogenization scheme. Finally, Chapter 6 gives concluding remarks along with recommendations and possible future research directions.

1.5 Notations

The research presented within this thesis involves continuum mechanics theory as advanced numerical methods. Hence, tensor and indicial notation are adopted in this manuscript. In index notation, the components of tensors are indicated in a subscript font with Latin subscripts. Tensors and tensor operations are defined in a Cartesian coordinate system, with orthonormal basis $\mathbf{e}_i$, where i can take values 1, 2 and 3. Einstein summation convention is used for brevity in vector and tensor operations.

Quantities are defined as:

x	-	scalar,
$\mathbf{x} = x_i \mathbf{e}_i$	-	vector,
$\underline{\underline{\mathbf{X}}} = X_{ij} \mathbf{e}_i \otimes \mathbf{e}_j$	-	second-order tensor,
${}^3\underline{\underline{\mathbf{X}}} = X_{ijk} \mathbf{e}_i \otimes \mathbf{e}_j \otimes \mathbf{e}_k$	-	third-order tensor,
${}^n\underline{\underline{\mathbf{X}}} = X_{ijk\ldots n} \mathbf{e}_i \otimes \mathbf{e}_j \otimes \mathbf{e}_k \ldots \otimes \mathbf{e}_n$	-	nth-order tensor.

Tensor products read:

$\underline{\underline{\mathbf{X}}} \cdot \underline{\underline{\mathbf{Y}}} = X_{ij} Y_{jk} \mathbf{e}_i \otimes \mathbf{e}_k$	-	inner product,
$\underline{\underline{\mathbf{X}}} : \underline{\underline{\mathbf{Y}}} = X_{ij} Y_{ji}$	-	double inner product,
${}^3\underline{\underline{\mathbf{X}}} \vdots {}^3\underline{\underline{\mathbf{Y}}} = X_{ijk} Y_{kji}$	-	tripple inner product,
$\mathbf{x} \otimes \mathbf{y} = x_i y_j \mathbf{e}_i \otimes \mathbf{e}_j$	-	dyadic product.

Operators on tensor variables are:

$\nabla = \dfrac{\partial}{\partial x_k} \mathbf{e}_k$	-	"nabla" operator
$\nabla \cdot \mathbf{x} = \nabla_i x_i$	-	divergence operator,
$\nabla \otimes \mathbf{x} = \nabla_i x_j \mathbf{e}_i \otimes \mathbf{e}_j$	-	gradient operator,
${}^3\underline{\underline{\mathbf{X}}}^{LC} = X_{ijk}^{LC} = X_{jik}$	-	left conjugation,
${}^3\underline{\underline{\mathbf{X}}}^{RC} = X_{ijk}^{RC} = X_{ikj}$	-	right conjugation.

Matrices are defined as:

$\underline{\mathrm{x}}$	-	column,
$\underline{\underline{\mathrm{X}}}$	-	matrix .

Operators on matrix quantities are:

$\underline{\underline{\mathrm{X}}}\,\underline{\underline{\mathrm{Y}}}$	-	matrix product,
$\underline{\underline{\mathrm{X}}}^T$	-	matrix transpose,
$\underline{\underline{\mathrm{X}}}^{-1}$	-	matrix inverse.

2 Higher-Order Continuum Theory

Modeling the mechanical behaviour of heterogeneous materials represents an essential issue in engineering. In recent years investigation of the relations between mechanical properties of material and its microstructure became very attractive topic, considering that almost all materials are heterogeneous at lower scales. Depending on the material microstructure, size effects can be observed, resulting in a different mechanical behaviour [81-83]. Unfortunately, classical continuum theory cannot capture such effects, since it does not contain an internal length scale. Obviously, extension towards higher-order continuum theory is reasonable. First significant work in extension to the higher-order continuum theory originates from Cosserat brothers [84], which gave a first systematic review for a three-dimensional solid. In their contribution, they introduced additional rotational degrees of freedom at the microlevel, along with a non-symmetric stress tensor and a higher-order couple stress tensor. Unfortunately, potential of this generalization was not recognized until the early sixties of the last century. Important developments in higher-order theories during the 1960's were achieved by Mindlin [24, 25, 85, 86], Koiter [87], Toupin [23, 88] and Eringen [89]. Further extension of the Cosserat theory has been done by accounting for not only local rotations, but also stretch gradients. Pioneering achievements in this full second-gradient theory were established in [25, 26] with introduction of double stress tensor as the work conjugate to the second derivative of the displacement field. Also, there are approaches introducing a material with microstructure [24, 90], where each point of the microstructure has its own degrees of freedom. In the last few decades advantages of the higher-order theories have been recognized as valuable tool for modeling of material elastoplasticity derived within a gradient dependent plasticity as well as for damage modeling. Due to higher-order gradients available, description of localization phenomena and material softening is possible without loss of ellipticity of governing equations. Furthermore, with introduction of an intrinsic length scale, size effects, which can be very often observed in experimental investigations, can be efficiently described by means of numerical algorithms. Gradient plasticity and damage models are discussed in [34, 81, 91-94]. Within this research a simplified form of gradient elasticity theory will be presented, where the constitutive law includes the Laplacian of the strains together with only one additional material parameter describing internal material length scale. This theory was

proposed by Altan and Aifantis [95], and its applicability in modeling of the size effects was further demonstrated in [96, 97]. For more details on the review of a gradient continua, see [98, 99].

2.1 Small strain second-gradient continuum formulation

In a classical small strain continuum theory kinematical behaviour at time *t* is described by the displacement field $\mathbf{u}$. According to the geometrical linearity adopted, all the quantities are expressed on the reference configuration. Symmetric part of the displacement field gradient denotes the strain tensor defined as

$$\underline{\boldsymbol{\varepsilon}} = \varepsilon_{ij} = \frac{1}{2}\left(u_{i,j} + u_{j,i}\right). \tag{2.1}$$

In the second-gradient continuum theory, the strain gradient ${}^3\underline{\boldsymbol{\eta}}$ is defined to be gradient of the strain tensor $\underline{\boldsymbol{\varepsilon}}$, as follows

$${}^3\underline{\boldsymbol{\eta}} = \eta_{ijk} = \varepsilon_{jk,i} = \nabla \otimes \underline{\boldsymbol{\varepsilon}}, \tag{2.2}$$

symmetric in the two last indices [26]. Accordingly, in a higher-order theory the strain energy density function is dependent on the strain and strain gradient, $W = W\left(\underline{\boldsymbol{\varepsilon}}, {}^3\underline{\boldsymbol{\eta}}\right)$. The variation of strain energy density is than equal to

$$\delta W = \frac{\partial W}{\partial \underline{\boldsymbol{\varepsilon}}} : \delta \underline{\boldsymbol{\varepsilon}} + \frac{\partial W}{\partial {}^3\underline{\boldsymbol{\eta}}} : \delta {}^3\underline{\boldsymbol{\eta}}, \tag{2.3}$$

which can be expressed as

$$\delta W = \underline{\boldsymbol{\sigma}} : \delta \underline{\boldsymbol{\varepsilon}} + {}^3\underline{\boldsymbol{\mu}} \vdots \delta {}^3\underline{\boldsymbol{\eta}}. \tag{2.4}$$

In Eq. (2.4), $\underline{\boldsymbol{\sigma}} = \sigma_{ij} = \sigma_{ji}$ is Cauchy stress tensor, and ${}^3\underline{\boldsymbol{\mu}} = \mu_{kji} = \mu_{jki}$ represents third-order double stress tensor. In further derivation, writing relation (2.4) in terms of displacement gradients, it is transformed to

$$\delta W = \underline{\boldsymbol{\sigma}} : \left(\nabla \otimes \left(\delta \mathbf{u}\right)\right) + {}^3\underline{\boldsymbol{\mu}} \vdots \left[\nabla \otimes \left(\nabla \otimes \left(\delta \mathbf{u}\right)\right)\right]. \tag{2.5}$$

The first term on the right side of Eq. (2.5) can be expressed as

$$\underline{\boldsymbol{\sigma}} : \left(\nabla \otimes \left(\delta \mathbf{u}\right)\right) = \nabla \cdot \left(\underline{\boldsymbol{\sigma}} \cdot \delta \mathbf{u}\right) - \left(\nabla \cdot \underline{\boldsymbol{\sigma}}\right) \cdot \delta \mathbf{u}, \tag{2.6}$$

while the second one can be extended to

$$\begin{aligned} {}^3\underline{\boldsymbol{\mu}} \vdots \left[\nabla \otimes \left(\nabla \otimes \left(\delta \mathbf{u}\right)\right)\right] &= \nabla \cdot \left[{}^3\underline{\boldsymbol{\mu}} : \left(\nabla \otimes \left(\delta \mathbf{u}\right)\right)\right] - \left(\nabla \cdot {}^3\underline{\boldsymbol{\mu}}\right) : \left(\nabla \otimes \left(\delta \mathbf{u}\right)\right) \\ &= \nabla \cdot \left[{}^3\underline{\boldsymbol{\mu}} : \left(\nabla \otimes \left(\delta \mathbf{u}\right)\right)\right] - \nabla \cdot \left(\delta \mathbf{u} \cdot \left(\nabla \cdot {}^3\underline{\boldsymbol{\mu}}\right)\right) + \left(\nabla \cdot \left(\nabla \cdot {}^3\underline{\boldsymbol{\mu}}\right)\right) \cdot \delta \mathbf{u}. \end{aligned} \tag{2.7}$$

Inserting Eqs. (2.6) and (2.7) into (2.5) we obtain

$$\begin{aligned}\delta W = \nabla\cdot\left(\underline{\boldsymbol{\sigma}}\cdot\delta\mathbf{u}\right) - \left(\nabla\cdot\underline{\boldsymbol{\sigma}}\right)\cdot\delta\mathbf{u} + \nabla\cdot\left[{}^{3}\underline{\boldsymbol{\mu}} : \left(\nabla\otimes\left(\delta\mathbf{u}\right)\right)\right] - \\ - \nabla\cdot\left(\delta\mathbf{u}\cdot\left(\nabla\cdot{}^{3}\underline{\boldsymbol{\mu}}\right)\right) + \left(\nabla\cdot\left(\nabla\cdot{}^{3}\underline{\boldsymbol{\mu}}\right)\right)\cdot\delta\mathbf{u}.\end{aligned} \tag{2.8}$$

Furhermore, variation of the internal work is defined as

$$\delta W^{\text{int}} = \int_V \delta W \mathrm{d}V\,. \tag{2.9}$$

Applying divergence theorem to the internal work variation, the previous relation can be transformed as

$$\begin{aligned}\delta W^{\text{int}} = \int_A \left[\mathbf{n}\cdot\left(\underline{\boldsymbol{\sigma}} - \left(\nabla\cdot{}^{3}\underline{\boldsymbol{\mu}}\right)\right)\cdot\delta\mathbf{u}\right]\mathrm{d}A - \int_V \left\{\left[\nabla\cdot\left(\underline{\boldsymbol{\sigma}} - \left(\nabla\cdot{}^{3}\underline{\boldsymbol{\mu}}\right)\right)\right]\cdot\delta\mathbf{u}\right\}\mathrm{d}V + \\ + \int_A \left[\left(\mathbf{n}\cdot{}^{3}\underline{\boldsymbol{\mu}}\right) : \left(\nabla\otimes\left(\delta\mathbf{u}\right)\right)\right]\mathrm{d}A,\end{aligned} \tag{2.10}$$

where $\mathbf{n}$ is unit outward normal to the surface A of the body. In (2.10), full gradient of the displacement variation $\nabla\otimes\left(\delta\mathbf{u}\right)$ is decomposed into surface and normal gradient in the way

$$\nabla\otimes\left(\delta\mathbf{u}\right) = \nabla^{A}\otimes\left(\delta\mathbf{u}\right) + \mathbf{n}\otimes D\otimes\left(\delta\mathbf{u}\right), \tag{2.11}$$

where the surface gradient is defined as

$$\nabla^{A} = \nabla\cdot\left(\underline{\mathbf{I}} - \mathbf{n}\otimes\mathbf{n}\right), \tag{2.12}$$

and the normal gradient operator is given as

$$D = \mathbf{n}\cdot\nabla\,. \tag{2.13}$$

In Eq. (2.12), $\underline{\mathbf{I}}$ is a second-order unit tensor. Applying the aforementioned decomposition on the last subintegral term in (2.10) the following identity is obtained

$$\left(\mathbf{n}\cdot{}^{3}\underline{\boldsymbol{\mu}}\right) : \left(\nabla\otimes\left(\delta\mathbf{u}\right)\right) = \left(\mathbf{n}\cdot{}^{3}\underline{\boldsymbol{\mu}}\right) : \left(\nabla^{A}\otimes\left(\delta\mathbf{u}\right)\right) + \mathbf{n}\cdot\left(\mathbf{n}\cdot{}^{3}\underline{\boldsymbol{\mu}}\right)\cdot\left(D\otimes\left(\delta\mathbf{u}\right)\right). \tag{2.14}$$

Using product rule of differentiation the first term on the right hand side of Eq. (2.14) can be defined as

$$\left(\mathbf{n}\cdot{}^{3}\underline{\boldsymbol{\mu}}\right) : \left(\nabla^{A}\otimes\left(\delta\mathbf{u}\right)\right) = \nabla^{A}\cdot\left(\left(\mathbf{n}\cdot{}^{3}\underline{\boldsymbol{\mu}}\right)\cdot\delta\mathbf{u}\right) - \nabla^{A}\cdot\left(\mathbf{n}\cdot{}^{3}\underline{\boldsymbol{\mu}}\right)\cdot\delta\mathbf{u}\,, \tag{2.15}$$

where the last term on the right side is expressed through independent variation $\delta\mathbf{u}$. The first term on the right side of Eq. (2.15) can be transformed via surface divergence theorem to

$$\nabla^{A}\cdot\left(\left(\mathbf{n}\cdot{}^{3}\underline{\boldsymbol{\mu}}\right)\cdot\delta\mathbf{u}\right) = \left(\nabla^{A}\cdot\mathbf{n}\right)\otimes\mathbf{n}\cdot\left(\mathbf{n}\cdot{}^{3}\underline{\boldsymbol{\mu}}\right)\cdot\delta\mathbf{u}\,. \tag{2.16}$$

Inserting Eqs. (2.14)-(2.16) into Eq. (2.10), variation of the internal work is obtained as

$$\delta W^{\text{int}} = \int_A \left\{ \left[\mathbf{n} \cdot \left(\underline{\boldsymbol{\sigma}} - \left(\nabla \cdot {}^3\underline{\boldsymbol{\mu}} \right) \right) + \left(\nabla^A \cdot \mathbf{n} \right) \otimes \mathbf{n} \cdot \left(\mathbf{n} \cdot {}^3\underline{\boldsymbol{\mu}} \right) - \nabla^A \cdot \left(\mathbf{n} \cdot {}^3\underline{\boldsymbol{\mu}} \right) \right] \cdot \delta \mathbf{u} \right\} \mathrm{d}A -$$
$$- \int_V \left\{ \left[\nabla \cdot \left(\underline{\boldsymbol{\sigma}} - \left(\nabla \cdot {}^3\underline{\boldsymbol{\mu}} \right) \right) \right] \cdot \delta \mathbf{u} \right\} \mathrm{d}V + \tag{2.17}$$
$$+ \int_A \left[\left(\mathbf{n} \cdot {}^3\underline{\boldsymbol{\mu}} \cdot \mathbf{n} \right) \cdot \left(D \otimes \left(\delta \mathbf{u} \right) \right) \right] \mathrm{d}A.$$

According to (2.17), variation of the external work is expressed as

$$\delta W^{\text{ext}} = \int_A \left(\mathbf{t} \cdot \delta \mathbf{u} \right) \mathrm{d}A + \int_A \left[\boldsymbol{\tau} \cdot \left(D \otimes \left(\delta \mathbf{u} \right) \right) \right] \mathrm{d}A, \tag{2.18}$$

where the body forces are neglected. In Eq. (2.18), $\mathbf{t}$ and $\boldsymbol{\tau}$ are traction and double surface traction, respectively. Using principle of virtual work

$$\delta W^{\text{int}} = \delta W^{\text{ext}}, \tag{2.19}$$

for any domain V and for arbitrary variations of $\delta \mathbf{u}$ and $D \otimes \delta \mathbf{u}$, the equilibrium equation can be defined as

$$\nabla \cdot \left(\underline{\boldsymbol{\sigma}} - \left(\nabla \cdot {}^3\underline{\boldsymbol{\mu}} \right) \right) = \mathbf{0}. \tag{2.20}$$

Contribution of the external loads acting on the surface A, as described in Eq. (2.18) is consisting of the surface traction

$$\mathbf{t} = \mathbf{n} \cdot \left(\underline{\boldsymbol{\sigma}} - \left(\nabla \cdot {}^3\underline{\boldsymbol{\mu}} \right) \right) + \left(\nabla^A \cdot \mathbf{n} \right) \otimes \mathbf{n} \cdot \left(\mathbf{n} \cdot {}^3\underline{\boldsymbol{\mu}} \right) - \nabla^A \cdot \left(\mathbf{n} \cdot {}^3\underline{\boldsymbol{\mu}} \right), \tag{2.21}$$

and the double surface traction

$$\boldsymbol{\tau} = \mathbf{n} \cdot {}^3\underline{\boldsymbol{\mu}} \cdot \mathbf{n}. \tag{2.22}$$

Introducing a second-order tensor of effective stress in the form

$$\underline{\tilde{\boldsymbol{\sigma}}} = \underline{\boldsymbol{\sigma}} - \left(\nabla \cdot {}^3\underline{\boldsymbol{\mu}} \right), \tag{2.23}$$

the equilibrium equation (2.20) can be further rewritten in the usual form of a classical continuum as

$$\nabla \cdot \underline{\tilde{\boldsymbol{\sigma}}} = \mathbf{0}. \tag{2.24}$$

2.1.1 Aifantis form of gradient elasticity theory

In a simplified higher-order continuum theory developed by Mindlin and Eshel [26], where material is considered as microhomogeneous, three forms of strain energy density are introduced. The difference between various forms of strain energy function relies on handling the strain gradient introduced. In form I, additional terms are represented as a second displacement gradients. In form II, higher-order terms are grouped into strain gradient tensor. Form III is based on decomposition of second-order terms into symmetric part as second-

gradient of displacement or strain gradient and rotations gradients. General equations arising from strain energy function are not form-dependent, but only form II gives symmetric stress tensor. Based on the aforementioned, Aifantis proposed a modified case of Mindlin's form II in [95, 100, 101], as declared in [33]. In Mindlin's work [26] strain energy density defined in terms of the strain and strain gradient for a linear elastic isotropic material is defined as

$$W\left(\varepsilon_{ij},\eta_{ijk}\right)=\frac{1}{2}\lambda\varepsilon_{ii}\varepsilon_{jj}+\mu\varepsilon_{ij}\varepsilon_{ij}+a_1\eta_{iik}\eta_{kjj}+a_2\eta_{ijj}\eta_{ikk}+a_3\eta_{iik}\eta_{jjk}+a_4\eta_{ijk}\eta_{ijk}+a_5\eta_{ijk}\eta_{kji}\,, \tag{2.25}$$

where for the sake of clarity index notation has been used. In (2.25) λ and μ are Lamé constants, while $a_1 \ldots a_5$ are gradient coefficients. The experimental determination of five gradient coefficients is rather complex and delicate task. On the other hand, numerical implementation of Mindlin's theory requires computationally expensive and demanding numerical algorithms. To simplify computational and experimental burden, Aifantis has proposed a special case of form II, where gradient coefficients $a_1 = a_2 = a_5 = 0$. With this in mind, the strain energy function (2.25) may be written in the form

$$W\left(\varepsilon_{ij},\eta_{ijk}\right)=\frac{1}{2}\lambda\varepsilon_{ii}\varepsilon_{jj}+\mu\varepsilon_{ij}\varepsilon_{ij}+a_3\eta_{iik}\eta_{jjk}+a_4\eta_{ijk}\eta_{ijk}\,. \tag{2.26}$$

An explicit form of (2.26) introduced in [95, 100, 101] is expressed as

$$W=\frac{1}{2}\lambda\varepsilon_{ii}\varepsilon_{jj}+\mu\varepsilon_{ij}\varepsilon_{ij}+l^2\left(\frac{1}{2}\lambda\varepsilon_{ii,k}\varepsilon_{jj,k}+\mu\varepsilon_{ij,k}\varepsilon_{ij,k}\right), \tag{2.27}$$

where l^2 represents microstructural parameter or material length scale. Finally, using work conjugate variables and by means of (2.4) and (2.27) the following identities can be established

$$\sigma_{ij}=\frac{\partial W}{\partial\varepsilon_{ij}}=\lambda\varepsilon_{pp}\delta_{ij}+2\mu\varepsilon_{ij}=\left(\lambda\,\mathrm{tr}\underline{\boldsymbol{\varepsilon}}\right)\otimes\underline{\mathbf{I}}+2\mu\underline{\boldsymbol{\varepsilon}}\,, \tag{2.28}$$

$$\mu_{kji}=\frac{\partial W}{\partial\eta_{kji}}=l^2\left(\lambda\varepsilon_{pp}\delta_{ij}+2\mu\varepsilon_{ij}\right)_{,k}=l^2\left[\left(\lambda\,\mathrm{tr}\left(\nabla\otimes\underline{\boldsymbol{\varepsilon}}\right)\right)\otimes\underline{\mathbf{I}}+2\mu\left(\nabla\otimes\underline{\boldsymbol{\varepsilon}}\right)\right], \tag{2.29}$$

$$\begin{aligned}\tilde{\sigma}_{ij}&=\lambda\varepsilon_{pp}\delta_{ij}+2\mu\varepsilon_{ij}-l^2\left(\lambda\varepsilon_{pp}\delta_{ij}+2\mu\varepsilon_{ij},\right)_{,kk}\\&=\left(\lambda\,\mathrm{tr}\underline{\boldsymbol{\varepsilon}}\right)\otimes\underline{\mathbf{I}}+2\mu\underline{\boldsymbol{\varepsilon}}-l^2\left[\nabla^2\left(\left(\lambda\,\mathrm{tr}\underline{\boldsymbol{\varepsilon}}\right)\otimes\underline{\mathbf{I}}+2\mu\underline{\boldsymbol{\varepsilon}}\right)\right].\end{aligned} \tag{2.30}$$

2.2 Large strain second-gradient continuum formulation

As it is well known, the small strain formulation is limited to the modeling of simple material responses. A more complex material behavior including elastoplastic strain localization and

softening cannot be modeled accurately. Therefore an extension of the proposed formulation towards large strain framework is desirable. In a classical continuum theory, motion and/or deformation of the body are described by the "motion function" ψ describing nonlinear deformation mapping, which carries an arbitrary material point *X* at time t_0 from the reference (undeformed or initial) configuration to the current configuration at time t. In this manner, position of the material point is marked by position vector $\underline{\mathbf{X}}$ in reference configuration and $\underline{\mathbf{x}}$ in current configuration. Hence, the motion function of the material point *X* may be written as

$$\mathbf{x} = \psi\left(\mathbf{X}, t\right). \tag{2.31}$$

In a large strain framework displacement field pointing from the reference position of the material point to its current position is characterized by

$$\mathbf{u}\left(\mathbf{X}, t\right) = \psi\left(\mathbf{X}, t\right) - \mathbf{X} = \mathbf{x} - \mathbf{X}. \tag{2.32}$$

The spatial derivative of the motion function ψ results in a deformation gradient

$$\underline{\mathbf{F}} = \frac{\partial \psi\left(\mathbf{X}, t\right)}{\partial \mathbf{X}} = \frac{\partial \mathbf{x}}{\partial \mathbf{X}} = \nabla_0 \otimes \mathbf{x} = \underline{\mathbf{I}} + \nabla_0 \otimes \mathbf{u}. \tag{2.33}$$

In Eq. (2.33) ∇_0 denotes "nabla" operator with respect to the reference configuration. In the second-order continuum theory derived within this thesis a higher-order continuum variable appears, describing gradient of the deformation gradient, or shorter, second-order gradient

$${}^3\underline{\mathbf{G}} = \frac{\partial}{\partial \mathbf{X}}\left(\frac{\partial \psi\left(\mathbf{X}, t\right)}{\partial \mathbf{X}}\right) = \nabla_0 \otimes \underline{\mathbf{F}} = \nabla_0 \otimes \nabla_0 \otimes \mathbf{x}, \tag{2.34}$$

with symmetry property $G_{ijk} = G_{kji}$. Following small strain second-order theory described before, as stated in (2.4) variation of strain energy density $W = W\left(\underline{\mathbf{F}}, {}^3\underline{\mathbf{G}}\right)$ equals to

$$\delta W = \underline{\mathbf{P}} : \delta \underline{\mathbf{F}} + {}^3\underline{\mathbf{Q}} \vdots \delta {}^3\underline{\mathbf{G}}. \tag{2.35}$$

In (2.35) first Piola-Kirchhoff stress tensor $\underline{\mathbf{P}}$ and double stress tensor ${}^3\underline{\mathbf{Q}}$ appear. Again, $Q_{ijk} = Q_{kji}$ associated to symmetry of the second-order gradient ${}^3\underline{\mathbf{G}}$. The first Piola-Kirchhoff stress tensor, as an energy conjugate to the deformation gradient expresses the stress relative to the reference configuration. In other words, it relates forces in the current configuration to the areas in the reference configuration (a two-point tensor). In general, it is not symmetric. For infinitesimal deformations and rotations, it is identical to the Cauchy stress. Similar to the small strain case, (2.35) is rewritten by means of displacement variation as

$$\delta W = \underline{\mathbf{P}} : \left(\nabla_0 \otimes \left(\delta \mathbf{u}\right)\right) + {}^3\underline{\mathbf{Q}} \vdots \nabla_0 \otimes \left(\nabla_0 \otimes \left(\delta \mathbf{u}\right)\right). \tag{2.36}$$

Using transformations presented in (2.6) and (2.7), relation (2.36) can be rearranged into

$$\begin{aligned} \delta W = {} & \nabla_0 \cdot \left(\underline{\mathbf{P}} \cdot \delta \mathbf{u}\right) - \left(\nabla_0 \cdot \underline{\mathbf{P}}\right) \cdot \delta \mathbf{u} + \nabla_0 \cdot \left[{}^3\underline{\mathbf{Q}} : \left(\nabla_0 \otimes \left(\delta \mathbf{u}\right)\right)\right] - \\ & - \nabla_0 \cdot \left(\delta \mathbf{u} \cdot \left(\nabla_0 \cdot {}^3\underline{\mathbf{Q}}\right)\right) + \left(\nabla_0 \cdot \left(\nabla_0 \cdot {}^3\underline{\mathbf{Q}}\right)\right) \cdot \delta \mathbf{u}. \end{aligned} \tag{2.37}$$

Applying divergence theorem to Eq. (2.37) and inserting into (2.9), the variation of the work done by the internal forces is equal to

$$\begin{aligned} \delta W^{\text{int}} = {} & \int_{A_0} \left[\mathbf{N} \cdot \left(\underline{\mathbf{P}} - \left(\nabla_0 \cdot {}^3\underline{\mathbf{Q}}\right)\right) \cdot \delta \mathbf{u} \right] \mathrm{d}A_0 - \int_{V_0} \left\{ \left[\nabla_0 \cdot \left(\underline{\mathbf{P}} - \left(\nabla_0 \cdot {}^3\underline{\mathbf{Q}}\right)\right)\right] \cdot \delta \mathbf{u} \right\} \mathrm{d}V_0 + \\ & + \int_{A_0} \left[\left(\mathbf{N} \cdot {}^3\underline{\mathbf{Q}}\right) : \left(\nabla_0 \otimes \left(\delta \mathbf{u}\right)\right)\right] \mathrm{d}A_0, \end{aligned} \tag{2.38}$$

where integration is performed over the body in reference configuration. Also, in (2.38) $\mathbf{N}$ is unit outward normal to the surface A_0 in material configuration. Since full gradient of displacement variation $\nabla_0 \otimes \left(\delta \mathbf{u}\right)$ cannot be determined only on a surface A_0, decomposition into a surface gradient by means of

$$\nabla_0^A = \nabla_0 \cdot \left(\underline{\mathbf{I}} - \mathbf{N} \otimes \mathbf{N}\right), \tag{2.39}$$

and a normal gradient using operator

$$D_0 = \mathbf{N} \cdot \nabla_0 \tag{2.40}$$

is performed in a manner described by relations (2.14)-(2.16). After these rearrangements the variation of internal work becomes

$$\begin{aligned} \delta W^{\text{int}} = {} & \int_{A_0} \left\{ \left[\mathbf{N} \cdot \left(\underline{\mathbf{P}} - \left(\nabla_0 \cdot {}^3\underline{\mathbf{Q}}\right)\right) + \left(\nabla_0^A \cdot \mathbf{N}\right) \otimes \mathbf{N} \cdot \left(\mathbf{N} \cdot {}^3\underline{\mathbf{Q}}\right) - \nabla_0^A \cdot \left(\mathbf{N} \cdot {}^3\underline{\mathbf{Q}}\right) \right] \cdot \delta \mathbf{u} \right\} \mathrm{d}A_0 - \\ & - \int_{V_0} \left\{ \left[\nabla_0 \cdot \left(\underline{\mathbf{P}} - \left(\nabla_0 \cdot {}^3\underline{\mathbf{Q}}\right)\right)\right] \cdot \delta \mathbf{u} \right\} \mathrm{d}V_0 + \\ & + \int_{A_0} \left[\left(\mathbf{N} \cdot {}^3\underline{\mathbf{Q}} \cdot \mathbf{N}\right) \cdot \left(D_0 \otimes \left(\delta \mathbf{u}\right)\right)\right] \mathrm{d}A_0. \end{aligned} \tag{2.41}$$

From the principle of virtual work, variation of work done by external forces is assumed to be similar to (2.18), with respect to the initial configuration

$$\delta W^{\text{ext}} = \int_{A_0} \left(\mathbf{t} \cdot \delta \mathbf{u}\right) \mathrm{d}A_0 + \int_{A_0} \left[\boldsymbol{\tau} \cdot \left(D_0 \otimes \left(\delta \mathbf{u}\right)\right)\right] \mathrm{d}A_0 . \tag{2.42}$$

Using (2.19), for arbitrary domain V_0 and displacement variations $\delta \mathbf{u}$ and $D \otimes \delta \mathbf{u}$ the equilibrium is obtained as follows

$$\nabla_0 \cdot \left(\underline{\mathbf{P}} - \left(\nabla_0 \cdot {}^3\underline{\mathbf{Q}}\right)\right) = \mathbf{0} . \tag{2.43}$$

Furthermore, in a straightforward manner, external loads acting on the surface A_0 are declared as surface traction

$$\mathbf{t} = \mathbf{N} \cdot \left(\underline{\mathbf{P}} - \left(\nabla_0 \cdot {}^3\underline{\mathbf{Q}} \right) \right) + \left(\nabla_0^A \cdot \mathbf{N} \right) \otimes \mathbf{N} \cdot \left(\mathbf{N} \cdot {}^3\underline{\mathbf{Q}} \right) - \nabla_0^A \cdot \left(\mathbf{N} \cdot {}^3\underline{\mathbf{Q}} \right) \tag{2.44}$$

and double surface traction

$$\boldsymbol{\tau} = \mathbf{N} \cdot {}^3\underline{\mathbf{Q}} \cdot \mathbf{N} \,. \tag{2.45}$$

Finally, introducing the effective first Piola-Kirchhoff stress defined as

$$\underline{\tilde{\mathbf{P}}} = \underline{\mathbf{P}} - \left(\nabla \cdot {}^3\underline{\mathbf{Q}} \right), \tag{2.46}$$

equilibrium equation (2.43) can be reformulated to

$$\nabla_0 \cdot \underline{\tilde{\mathbf{P}}} = \mathbf{0} \,. \tag{2.47}$$

3 C^1 continuous displacement based finite element formulation

For the solution of the practical problems analytical solutions for higher-order continua may be obtained only for a few very simple problems. Consequently, finding solution to the problem using a numerical analysis, for example, finite element method is necessary. Higher-order displacement gradients invoked in the virtual work statement lead to a higher-order differential equation. Numerical solution of this governing equation requires a higher interpolation scheme, where C^1 continuity has to be ensured. In the finite element framework this brings necessity for a higher-order finite element formulation supporting additional degrees of freedom [102, 103]. On the other hand, structural complexity of the element also increases [104, 105]. Increased complexity of the finite element formulation as well as inconvenient numerical implementation are the main reasons that these elements are not too attractive for practical use. Therefore, many efforts have been undertaken trying to simulate gradient problems compensating requirement for C^1 interpolations. In this field many methods have been developed, for example, implicit methods [106, 107], mixed formulations where kinematic relation between displacements and displacement derivatives is enforced by Lagrange multipliers [31, 37, 39], or by penalty functions [32, 36, 37] and micromorphic continuum formulations with Lagrange multipliers [38] or penalty parameters [108-110]. Unfortunately, alternative approaches suffer from a several drawbacks, resulting in locking and unphysical results. Despite simplified approach, again, high number of degrees of freedom has to be used. Considering all the difficulties mentioned, mixed finite element formulations show a poor behavior compared to C^1 finite elements [32, 111, 112]. Despite numerical complexity, C^1 finite elements are used in a gradient plasticity problems for approximation of the plastic strain measure [34, 113-115] and for investigation of the crack tip fields [31, 33]. There are also three-dimensional C^1 finite element formulations applied in gradient elasticity problems, as described in [111, 116]. A comprehensive state-of-the-art of C^1 continuous methods is given in [117]. In this thesis, C^1 triangular finite element will be used. In contrast to the mixed formulation mostly applied, here only one-field interpolation describing the displacement distribution is used, which yields the displacements and their

derivatives as nodal values. The element formulation has already been used in a gradient elasticity problems in [32], in a linear elastic fracture mechanics [33], and for a plate bending problems [118], where it was originally developed. In this research, the element will be applied in the strain gradient multiscale procedure [119].

3.1 Small strain finite element formulation

3.1.1 Weak formulation

The two-dimensional (2D) strain gradient triangular FE shown in Figure 3.1 has three nodes, each with twelve degrees of freedom (DOF). Nodal degrees of freedom are two displacements and their first and second order derivatives with respect to the Cartesian coordinates. Here the element is called C1PE3, describing C^1 continuity and a plane strain state. The element displacement field is approximated by a complete fifth-order polynomial with 21 coefficients, and therefore 21 equations are required for their description. Displacement field is defined as

$$\begin{aligned} u = {} & a_1 + a_2 x_1 + a_3 x_2 + a_4 x_1^2 + a_5 x_1 x_2 + a_6 x_2^2 + a_7 x_1^3 + a_8 x_1^2 x_2 + a_9 x_1 x_2^2 + a_{10} x_2^3 + \\ & + a_{11} x_1^4 + a_{12} x_1^3 x_2 + a_{13} x_1^2 x_2^2 + a_{14} x_1 x_2^3 + a_{15} x_2^4 + a_{16} x_1^5 + a_{17} x_1^4 x_2 + a_{18} x_1^3 x_2^2 + \\ & + a_{19} x_1^2 x_2^3 + a_{20} x_1 x_2^4 + a_{21} x_2^5. \end{aligned} \tag{3.1}$$

By means of the element degrees of freedom, only 18 equations can be defined, which means that system of equations is three times undefined. According to [118, 120], the remaining three equations are obtained from the condition that the normal derivative of the displacement along the element edge is constrained to vary as a cubic polynomial. In this way, the element interpolation function is transformed to the condensed polynomial of fifth order which may be defined by only 18 nodal values per displacement components corresponding to 6 values per node.

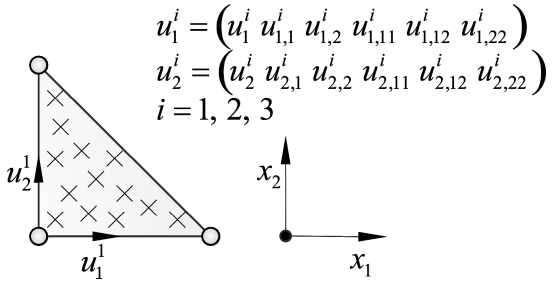

Figure 3.1 C^1 triangular finite element

The weak form of the equilibrium equation (2.20) expressed through the principle of virtual work may be presented as

$$\int_A \left(\underline{\boldsymbol{\sigma}} : \delta \underline{\boldsymbol{\varepsilon}} + {}^3\underline{\boldsymbol{\mu}} \vdots \delta {}^3\underline{\boldsymbol{\eta}} \right) \mathrm{d}A = \int_s \left(\mathbf{t} \cdot \delta \mathbf{u} \right) \mathrm{d}s + \int_s \left[\underline{\mathbf{T}} : \left(\nabla \otimes \left(\delta \mathbf{u} \right) \right) \right] \mathrm{d}s \,, \tag{3.2}$$

where s represents closed boundary line of the surface area A. Also, in the second integral term on the right side of (3.2), double traction tensor $\underline{\mathbf{T}} = \boldsymbol{\tau} \otimes \mathbf{n}$ is introduced. Discrete form of the field variables in the weak form (3.2) is introduced by interpolation of nodal values within the domain of an element using shape functions. Due to C^1 continuous interpolations adopted in the element formulation only displacement field needs to be discretized, while remaining gradient terms can be easily computed through shape function derivatives. Firstly, we start with interpolation of the displacement field $\underline{\mathrm{u}}$ inside an element written in a matrix notation as

$$\underline{\mathrm{u}} = \underline{\underline{\mathrm{N}}}\, \underline{\mathrm{v}} \,. \tag{3.3}$$

In (3.3), $\underline{\underline{\mathrm{N}}}$ is a matrix of the shape functions, given by

$$\underline{\underline{\mathrm{N}}} = \begin{pmatrix} N_1 \dots N_6 & \underline{0} & N_7 \dots N_{12} & \underline{0} & N_{13} \dots N_{18} & \underline{0} \\ \underline{0} & N_1 \dots N_6 & \underline{0} & N_7 \dots N_{12} & \underline{0} & N_{13} \dots N_{18} \end{pmatrix}, \tag{3.4}$$

where $\underline{0}$ represents zero row vector with dimensions (1×6). Interpolation polynomials $N_1 \dots N_{18}$, and element geometry definition are explained in Appendix A. Further, $\underline{\mathrm{v}}$ is a vector of the nodal degrees of freedom described above. Strain, and higher-order gradients are obtained by using shape function derivatives as follows

$$\underline{\boldsymbol{\varepsilon}} = \begin{pmatrix} \varepsilon_{11} \\ \varepsilon_{22} \\ 2\varepsilon_{12} \end{pmatrix} = \underline{\underline{\mathrm{B}}}_{\varepsilon}\, \underline{\mathrm{v}} \,, \tag{3.5}$$

$$\underline{\boldsymbol{\eta}} = \begin{pmatrix} \eta_{111} \\ \eta_{222} \\ \eta_{221} \\ \eta_{112} \\ 2\eta_{121} \\ 2\eta_{212} \end{pmatrix} = \begin{pmatrix} u_{1,11} \\ u_{2,22} \\ u_{1,22} \\ u_{2,11} \\ 2u_{1,21} \\ 2u_{2,12} \end{pmatrix} = \underline{\underline{\mathrm{B}}}_{\eta}\, \underline{\mathrm{v}} \,. \tag{3.6}$$

In (3.6) second derivatives of the displacement are grouped into the vector $\underline{\boldsymbol{\eta}}$ according to [79]. Substituting discrete form of the field variables into Eq. (3.2) leads to

$$\int_A \left(\underline{\boldsymbol{\sigma}} : \left(\underline{\underline{\mathrm{B}}}_{\varepsilon}\, \delta \underline{\mathrm{v}} \right) + {}^3\underline{\boldsymbol{\mu}} \vdots \left(\underline{\underline{\mathrm{B}}}_{\eta}\, \delta \underline{\mathrm{v}} \right) \right) \mathrm{d}A = \int_s \left(\mathbf{t} \cdot \left(\underline{\underline{\mathrm{N}}}\, \delta \underline{\mathrm{v}} \right) \right) \mathrm{d}s + \int_s \left[\underline{\mathbf{T}} : \left(\left(\nabla \otimes \underline{\underline{\mathrm{N}}} \right) \delta \underline{\mathrm{v}} \right) \right] \mathrm{d}s \,, \tag{3.7}$$

where the following identities hold

$$\delta \underline{\mathrm{u}} = \underline{\underline{\mathrm{N}}}\, \delta \underline{\mathrm{v}} \,, \tag{3.8}$$

$$\delta\underline{\varepsilon} = \underline{\underline{B}}_{\varepsilon}\delta\underline{v}\,, \tag{3.9}$$

$$\delta\underline{\eta} = \underline{\underline{B}}_{\eta}\delta\underline{v}\,. \tag{3.10}$$

Since in a general case, material and geometrical nonlinearities are involved, relation (3.7) should be solved in an incrementally-iterative procedure, namely Newton-Rhapson algorithm. Hence, (3.7) is transformed into the incremental form in the interval $\left(t^{i-1}, t^{i}\right)$, where t^{i-1} represents the time increment of the last converged equilibrium state, and t^{i} is a new affine equilibrium state obtained in an iterative procedure using the following relations

$$\underline{u}^{i} = \underline{u}^{i-1} + \Delta\underline{u}\,, \tag{3.11}$$

$$\underline{\boldsymbol{\sigma}}^{i} = \underline{\boldsymbol{\sigma}}^{i-1} + \Delta\underline{\boldsymbol{\sigma}}\,, \tag{3.12}$$

$${}^{3}\underline{\boldsymbol{\mu}}^{i} = {}^{3}\underline{\boldsymbol{\mu}}^{i-1} + \Delta^{3}\underline{\boldsymbol{\mu}}\,. \tag{3.13}$$

Herein $\Delta\underline{u}$ denotes iterative correction of the displacement vector, while the stress increment $\Delta\underline{\boldsymbol{\sigma}}$ and the double stress increment $\Delta^{3}\underline{\boldsymbol{\mu}}$ are computed by the linearized incremental constitutive relations

$$\Delta\underline{\boldsymbol{\sigma}} = {}^{4}\underline{\mathbf{C}}_{\sigma\varepsilon} : \Delta\underline{\boldsymbol{\varepsilon}} + {}^{5}\underline{\mathbf{C}}_{\sigma\eta} \vdots \Delta^{3}\underline{\boldsymbol{\eta}}\,, \tag{3.14}$$

$$\Delta^{3}\underline{\boldsymbol{\mu}} = {}^{5}\underline{\mathbf{C}}_{\mu\varepsilon} : \Delta\underline{\boldsymbol{\varepsilon}} + {}^{6}\underline{\mathbf{C}}_{\mu\eta} \vdots \Delta^{3}\underline{\boldsymbol{\eta}}\,, \tag{3.15}$$

with stress tensor components represented in a matrix form as

$$\underline{\sigma} = \begin{pmatrix} \sigma_{11} \\ \sigma_{22} \\ \sigma_{12} \end{pmatrix} \tag{3.16}$$

and

$$\underline{\mu} = \begin{pmatrix} \mu_{111} \\ \mu_{222} \\ \mu_{221} \\ \mu_{112} \\ \mu_{121} \\ \mu_{122} \end{pmatrix}. \tag{3.17}$$

In (3.14) and (3.15) ${}^{4}\underline{\mathbf{C}}_{\sigma\varepsilon}$, ${}^{5}\underline{\mathbf{C}}_{\sigma\eta}$, ${}^{5}\underline{\mathbf{C}}_{\mu\varepsilon}$, ${}^{6}\underline{\mathbf{C}}_{\mu\eta}$ are consistent material tangent stiffness matrices. Generalized constitutive relations (3.14) and (3.15) include contributions of both first and higher-order gradients in a calculation of the stress fields. This approach will be particularly useful in multiscale computations, where the influence of the heterogeneous microstructure described by the RVE will be carried by the matrices ${}^{5}\underline{\mathbf{C}}_{\sigma\eta}$ and ${}^{5}\underline{\mathbf{C}}_{\mu\varepsilon}$. In other words, for a

homogeneous material these matrices are equal to zero. Transformation of (3.12)-(3.15) into a matrix representation, along with external tractions, and substitution into (3.7), using some straightforward manipulation, obtains the following finite element relation

$$\begin{aligned}&\left[\int_A \left(\underline{\underline{B}}_\varepsilon^T \underline{\underline{C}}_{\sigma\varepsilon} \underline{\underline{B}}_\varepsilon + \underline{\underline{B}}_\varepsilon^T \underline{\underline{C}}_{\sigma\eta} \underline{\underline{B}}_\eta + \underline{\underline{B}}_\eta^T \underline{\underline{C}}_{\mu\varepsilon} \underline{\underline{B}}_\varepsilon + \underline{\underline{B}}_\eta^T \underline{\underline{C}}_{\mu\eta} \underline{\underline{B}}_\eta\right) \mathrm{d}A\right] \Delta \underline{v} = \\ &\int_s \left(\underline{\underline{N}}^T \underline{t} + \left(\nabla \otimes \underline{\underline{N}}\right)^T \underline{T}\right) \mathrm{d}s - \int_A \left(\underline{\underline{B}}_\varepsilon^T \underline{\sigma}^{i-1} + \underline{\underline{B}}_\eta^T \underline{\mu}^{i-1}\right) \mathrm{d}A.\end{aligned} \tag{3.18}$$

As obvious, the finite element relation derived can be represented in a classical nonlinear manner as

$$\underline{\underline{K}}\, \Delta \underline{v} = \underline{F}_\mathrm{e} - \underline{F}_\mathrm{i}\,. \tag{3.19}$$

In this case element stiffness matrix $\underline{\underline{K}}$ consists of the following parts

$$\underline{\underline{K}} = \underline{\underline{K}}_{\sigma\varepsilon} + \underline{\underline{K}}_{\sigma\eta} + \underline{\underline{K}}_{\mu\varepsilon} + \underline{\underline{K}}_{\mu\eta}\,, \tag{3.20}$$

where particular identities are defined as

$$\underline{\underline{K}}_{\sigma\varepsilon} = \int_A \left(\underline{\underline{B}}_\varepsilon^T \underline{\underline{C}}_{\sigma\varepsilon} \underline{\underline{B}}_\varepsilon\right) \mathrm{d}A\,, \tag{3.21}$$

$$\underline{\underline{K}}_{\sigma\eta} = \int_A \left(\underline{\underline{B}}_\varepsilon^T \underline{\underline{C}}_{\sigma\eta} \underline{\underline{B}}_\eta\right) \mathrm{d}A\,, \tag{3.22}$$

$$\underline{\underline{K}}_{\mu\varepsilon} = \int_A \left(\underline{\underline{B}}_\eta^T \underline{\underline{C}}_{\mu\varepsilon} \underline{\underline{B}}_\varepsilon\right) \mathrm{d}A\,, \tag{3.23}$$

$$\underline{\underline{K}}_{\mu\eta} = \int_A \left(\underline{\underline{B}}_\eta^T \underline{\underline{C}}_{\mu\eta} \underline{\underline{B}}_\eta\right) \mathrm{d}A\,. \tag{3.24}$$

The nodal force vectors of external and internal forces on the right side of Eq. (3.19) are

$$\underline{F}_\mathrm{e} = \int_s \left(\underline{\underline{N}}^T \underline{t} + \left(\nabla \otimes \underline{\underline{N}}\right)^T \underline{T}\right) \mathrm{d}s\,, \tag{3.25}$$

$$\underline{F}_\mathrm{i} = \int_A \left(\underline{\underline{B}}_\varepsilon^T \underline{\sigma}^{i-1} + \underline{\underline{B}}_\eta^T \underline{\mu}^{i-1}\right) \mathrm{d}A\,, \tag{3.26}$$

respectively.

3.1.2 Aifantis strain gradient finite element formulation

In a special case of Mindlin's form II proposed by Aifantis the finite element derivation procedure described in section 3.1.1 remains. Firstly, we introduce grouping of higher-order variables according to form II required for derivation of the relevant finite element matrices. Displacement field inside an element is approximated by the same interpolation polynomials

$\underline{\underline{\mathrm{N}}}$, according to (3.3). Strain field is described by first derivatives of the shape functions (3.5) , while higher-order gradients are now expressed as a gradients of the strain field as

$$\underline{\varepsilon}_{x_1} = \begin{pmatrix} \varepsilon_{11,1} \\ \varepsilon_{22,1} \\ 2\varepsilon_{12,1} \end{pmatrix} = \begin{pmatrix} u_{1,11} \\ u_{2,21} \\ u_{1,21} + u_{2,11} \end{pmatrix} = \underline{\underline{\mathrm{B}}}_{\eta_1} \underline{\mathrm{v}}, \tag{3.27}$$

$$\underline{\varepsilon}_{x_2} = \begin{pmatrix} \varepsilon_{11,2} \\ \varepsilon_{22,2} \\ 2\varepsilon_{12,2} \end{pmatrix} = \begin{pmatrix} u_{1,12} \\ u_{2,22} \\ u_{1,22} + u_{2,12} \end{pmatrix} = \underline{\underline{\mathrm{B}}}_{\eta_2} \underline{\mathrm{v}}. \tag{3.28}$$

In (3.27) and (3.28) matrices $\underline{\underline{\mathrm{B}}}_{\eta_1}$ and $\underline{\underline{\mathrm{B}}}_{\eta_2}$ contain gradients of the strain matrix $\underline{\underline{\mathrm{B}}}$ with respect to x_1 and x_2, respectively. Cauchy stress tensor has the widely known form

$$\underline{\sigma} = \underline{\underline{\mathrm{C}}}_{\sigma\varepsilon} \underline{\underline{\mathrm{B}}}_{\varepsilon} \underline{\mathrm{v}}. \tag{3.29}$$

In further derivation, double stress vectors are introduced, as work conjugates to $\underline{\varepsilon}_{x_1}$ and $\underline{\varepsilon}_{x_2}$, as established in (2.29)

$$\underline{\mu}_{x_1} = \begin{pmatrix} \mu_{111} \\ \mu_{122} \\ \mu_{112} \end{pmatrix} = l^2 \underline{\underline{\mathrm{C}}}_{\sigma\varepsilon} \underline{\underline{\mathrm{B}}}_{\eta_1} \underline{\mathrm{v}}, \tag{3.30}$$

$$\underline{\mu}_{x_2} = \begin{pmatrix} \mu_{211} \\ \mu_{222} \\ \mu_{212} \end{pmatrix} = l^2 \underline{\underline{\mathrm{C}}}_{\sigma\varepsilon} \underline{\underline{\mathrm{B}}}_{\eta_2} \underline{\mathrm{v}}. \tag{3.31}$$

On the basis of (3.30) and (3.31) it can be seen that double stress tensors in Aifantis theory are related to the strain gradients via the same elasticity matrix relating classical continuum measures, Cauchy stress and strain, multiplied by the microstructural parameter l^2. This significantly simplifies problems regarding experimental determination of a higher-order constitutive model, since classical stress-strain experimental data are sufficient. Only unknown material parameter is l^2, which is also material dependent. Even though Aifantis gradient elasticity theory assumes linear elastic material behaviour (linear finite element equation is sufficient), for the sake of completeness nonlinear equation will be derived here. Once again, we start with the weak form of the principle of virtual work (3.2). Discrete form of (3.2) is achieved by means of (3.3), (3.5), (3.27) and (3.28) which is then expressed as

$$\begin{aligned} &\int_A \left(\underline{\boldsymbol{\sigma}} : \left(\underline{\underline{\mathrm{B}}}_{\varepsilon} \delta\underline{\mathrm{v}} \right) + {}^3\underline{\boldsymbol{\mu}}_{x_1} \vdots \left(\underline{\underline{\mathrm{B}}}_{\eta_1} \delta\underline{\mathrm{v}} \right) + {}^3\underline{\boldsymbol{\mu}}_{x_2} \vdots \left(\underline{\underline{\mathrm{B}}}_{\eta_2} \delta\underline{\mathrm{v}} \right) \right) \mathrm{d}A = \\ &\int_s \left(\mathbf{t} \cdot \left(\underline{\underline{\mathrm{N}}} \delta\underline{\mathrm{v}} \right) \right) \mathrm{d}s + \int_s \left[\underline{\mathbf{T}} : \left(\left(\nabla \otimes \underline{\underline{\mathrm{N}}} \right) \delta\underline{\mathrm{v}} \right) \right] \mathrm{d}s, \end{aligned} \tag{3.32}$$

in a similar form as in (3.7). In (3.32) variations of strain gradients $\underline{\varepsilon}_{x_1}$ and $\underline{\varepsilon}_{x_2}$ are defined in an analogous way as in (3.10). Next step is linearization of (3.32). As the first step, transformation into the incremental form in the interval $\left(t^{i-1}, t^{i}\right)$ is necessary. The new affine equilibrium state in the moment t^{i} is obtained using incremental updates (3.11), (3.12) and the following identities for double stress tensors

$$ {}^{3}\underline{\boldsymbol{\mu}}_{x_1}^{i} = {}^{3}\underline{\boldsymbol{\mu}}_{x_1}^{i-1} + \Delta\,{}^{3}\underline{\boldsymbol{\mu}}_{x_1}, \tag{3.33} $$

$$ {}^{3}\underline{\boldsymbol{\mu}}_{x_2}^{i} = {}^{3}\underline{\boldsymbol{\mu}}_{x_2}^{i-1} + \Delta\,{}^{3}\underline{\boldsymbol{\mu}}_{x_2}. \tag{3.34} $$

Stress increments $\Delta\underline{\boldsymbol{\sigma}}$, $\Delta\,{}^{3}\underline{\boldsymbol{\mu}}_{x_1}$ and $\Delta\,{}^{3}\underline{\boldsymbol{\mu}}_{x_2}$ are computed by the linearized incremental constitutive relations

$$ \Delta\underline{\boldsymbol{\sigma}} = {}^{4}\underline{\mathbf{C}}_{\sigma\varepsilon} : \Delta\underline{\boldsymbol{\varepsilon}}, \tag{3.35} $$

$$ \Delta\,{}^{3}\underline{\boldsymbol{\mu}}_{x_1} = l^2\left({}^{4}\underline{\mathbf{C}}_{\sigma\varepsilon} : \Delta\underline{\boldsymbol{\varepsilon}}_{x_1}\right), \tag{3.36} $$

$$ \Delta\,{}^{3}\underline{\boldsymbol{\mu}}_{x_2} = l^2\left({}^{4}\underline{\mathbf{C}}_{\sigma\varepsilon} : \Delta\underline{\boldsymbol{\varepsilon}}_{x_2}\right). \tag{3.37} $$

As already mentioned, in a stress update relations (3.35)-(3.37) only classical stress-strain material matrix ${}^{4}\underline{\mathbf{C}}_{\sigma\varepsilon}$ is used. Substitution of (3.12) and (3.33)-(3.37) into (3.32), after some classical finite element mathematical manipulations the following relationship is obtained

$$ \begin{aligned} &\left[\int_A \left[\underline{\underline{\mathrm{B}}}_{\varepsilon}^{T}\underline{\underline{\mathrm{C}}}_{\sigma\varepsilon}\underline{\underline{\mathrm{B}}}_{\varepsilon} + l^2\left(\underline{\underline{\mathrm{B}}}_{\eta_1}^{T}\underline{\underline{\mathrm{C}}}_{\sigma\varepsilon}\underline{\underline{\mathrm{B}}}_{\eta_1} + \underline{\underline{\mathrm{B}}}_{\eta_2}^{T}\underline{\underline{\mathrm{C}}}_{\sigma\varepsilon}\underline{\underline{\mathrm{B}}}_{\eta_2}\right)\right]\mathrm{d}A\right]\Delta\underline{\mathrm{v}} = \\ &\int_s \left(\underline{\underline{\mathrm{N}}}^{T}\,\underline{\mathrm{t}} + \left(\nabla\otimes\underline{\underline{\mathrm{N}}}\right)^{T}\underline{\mathrm{T}}\right)\mathrm{d}s - \int_A \left(\underline{\underline{\mathrm{B}}}_{\varepsilon}^{T}\underline{\sigma}^{i-1} + \underline{\underline{\mathrm{B}}}_{\eta_1}^{T}\underline{\mu}_{x_1}^{i-1} + \underline{\underline{\mathrm{B}}}_{\eta_2}^{T}\underline{\mu}_{x_2}^{i-1}\right)\mathrm{d}A. \end{aligned} \tag{3.38} $$

Equation (3.38) can be easily derived in the form of Eq. (3.19) with introduction of usual finite element matrix variables. Therefore, the stiffness matrix of the element is defined by the relation

$$ \underline{\underline{\mathrm{K}}} = \underline{\underline{\mathrm{K}}}_{l} + l^2\left(\underline{\underline{\mathrm{K}}}_{x_1} + \underline{\underline{\mathrm{K}}}_{x_2}\right), \tag{3.39} $$

consisting of the submatrices

$$ \underline{\underline{\mathrm{K}}}_{l} = \int_A \left(\underline{\underline{\mathrm{B}}}_{\varepsilon}^{T}\underline{\underline{\mathrm{C}}}_{\sigma\varepsilon}\underline{\underline{\mathrm{B}}}_{\varepsilon}\right)\mathrm{d}A, \tag{3.40} $$

$$ \underline{\underline{\mathrm{K}}}_{x_1} = \int_A \left(\underline{\underline{\mathrm{B}}}_{\eta_1}^{T}\underline{\underline{\mathrm{C}}}_{\sigma\varepsilon}\underline{\underline{\mathrm{B}}}_{\eta_1}\right)\mathrm{d}A, \tag{3.41} $$

$$ \underline{\underline{\mathrm{K}}}_{x_2} = \int_A \left(\underline{\underline{\mathrm{B}}}_{\eta_2}^{T}\underline{\underline{\mathrm{C}}}_{\sigma\varepsilon}\underline{\underline{\mathrm{B}}}_{\eta_2}\right)\mathrm{d}A. \tag{3.42} $$

Nodal force vector of the external contributions is already derived in (3.25), while internal nodal force vector takes the following form

$$\underline{\mathrm{F}}_{\mathrm{i}} = \int_A \left(\underline{\underline{\mathrm{B}}}_{\varepsilon}^T \underline{\sigma}^{i-1} + \underline{\underline{\mathrm{B}}}_{\eta_1}^T \underline{\mu}_{x_1}^{i-1} + \underline{\underline{\mathrm{B}}}_{\eta_2}^T \underline{\mu}_{x_2}^{i-1} \right) \mathrm{d}A \,. \tag{3.43}$$

3.2 Large strain finite element formulation

In the sequel, generalization of the C^1 continuous finite element formulation to a geometrical nonlinearity will be derived, also discussed in the author's paper [121]. As usual in finite element framework for solving problems in solid mechanics, total Lagrange approach has been adopted, where all quantities are formulated with respect to the undeformed configuration. Displacement field is approximated by the same interpolation functions as defined in (3.3). Here, deformation gradient written in a matrix notation is represented as

$$\underline{\mathrm{F}} = \begin{pmatrix} F_{11} \\ F_{22} \\ F_{12} \\ F_{21} \end{pmatrix} = \begin{pmatrix} 1+u_{1,1} \\ 1+u_{2,2} \\ u_{1,2} \\ u_{2,1} \end{pmatrix} = \underline{\underline{\mathrm{B}}}_F \underline{\mathrm{v}} \,, \tag{3.44}$$

in accordance with (2.33). It is clear that matrix $\underline{\underline{\mathrm{B}}}_F$ contains appropriate combination of the first derivatives of the shape function matrix $\underline{\underline{\mathrm{N}}}$. Next, gradient of the deformation gradient in matrix form may be expressed in the form

$$\underline{\mathrm{G}} = \begin{pmatrix} G_{111} \\ G_{221} \\ G_{211} \\ G_{121} \\ G_{112} \\ G_{222} \\ G_{212} \\ G_{122} \end{pmatrix} = \begin{pmatrix} F_{11,1} \\ F_{22,1} \\ F_{12,1} \\ F_{21,1} \\ F_{11,2} \\ F_{22,2} \\ F_{12,2} \\ F_{21,2} \end{pmatrix} = \begin{pmatrix} u_{1,11} \\ u_{2,21} \\ u_{1,21} \\ u_{2,11} \\ u_{1,12} \\ u_{2,22} \\ u_{1,22} \\ u_{2,12} \end{pmatrix} = \underline{\underline{\mathrm{B}}}_G \underline{\mathrm{v}} \,, \tag{3.45}$$

where matrix $\underline{\underline{\mathrm{B}}}_G$ is composed of second derivatives of the interpolations functions. Since the sequence of derivatives is arbitrary, it can be seen that $G_{221} = G_{122}$ and $G_{211} = G_{112}$, which explains symmetry property discussed in Section 2.2. Exploiting this, second derivatives of the displacement field can be expressed in a reduced matrix form, of a dimension (6×1). This is the case in Eq. (3.6), where mixed second derivatives are expressed as only one member

per displacement component, multiplied by two. Using large strain second gradient continuum theory discussed in Section 2.2, the weak form of the equilibrium equation (2.43) expressed through the principle of virtual work may be presented as

$$\int_{A_0}\left(\underline{\mathbf{P}}:\delta\underline{\mathbf{F}}+{}^{3}\underline{\mathbf{Q}}\vdots\delta{}^{3}\underline{\mathbf{G}}\right)\mathrm{d}A_0=\int_{s_0}\left(\mathbf{t}\cdot\delta\mathbf{u}\right)\mathrm{d}s_0+\int_{s_0}\left[\underline{\mathbf{T}}:\left(\nabla_0\otimes\left(\delta\mathbf{u}\right)\right)\right]\mathrm{d}s_0\,. \tag{3.46}$$

Taking variations of a deformation gradient (3.44) and a second-order gradient (3.45) as explained earlier, by means of (3.3), relation (3.46) can be easily transformed into

$$\int_{A_0}\left(\underline{\mathbf{P}}:\left(\underline{\underline{\mathbf{B}}}_F\delta\mathrm{v}\right)+{}^{3}\underline{\mathbf{Q}}\vdots\left(\underline{\underline{\mathbf{B}}}_G\delta\mathrm{v}\right)\right)\mathrm{d}A_0=\int_{s_0}\left(\mathbf{t}\cdot\left(\underline{\underline{\mathbf{N}}}\delta\mathrm{v}\right)\right)\mathrm{d}s_0+\int_{s_0}\left[\underline{\mathbf{T}}:\left(\left(\nabla_0\otimes\underline{\underline{\mathbf{N}}}\right)\delta\mathrm{v}\right)\right]\mathrm{d}s_0\,. \tag{3.47}$$

The next step is linearization of (3.47). Since this procedure has been comprehensively explained Section 3.1, the details will be omitted here. Generalized consistently linearized constitutive relations used in linearization are obtained as follows

$$\Delta\underline{\mathbf{P}}={}^{4}\underline{\mathbf{C}}_{PF}:\Delta\underline{\mathbf{F}}+{}^{5}\underline{\mathbf{C}}_{PG}\vdots\Delta{}^{3}\underline{\mathbf{G}}\,, \tag{3.48}$$

$$\Delta{}^{3}\underline{\mathbf{Q}}={}^{5}\underline{\mathbf{C}}_{QF}:\Delta\underline{\mathbf{F}}+{}^{6}\underline{\mathbf{C}}_{QG}\vdots\Delta{}^{3}\underline{\mathbf{G}}\,. \tag{3.49}$$

In (3.48) and (3.49), the components of the first Piola-Kirchhoff stress are

$$\underline{\mathrm{P}}=\begin{pmatrix}P_{11}\\P_{22}\\P_{12}\\P_{21}\end{pmatrix}, \tag{3.50}$$

and double stress vector is written as

$$\underline{\mathrm{Q}}=\begin{pmatrix}Q_{111}\\Q_{122}\\Q_{112}\\Q_{121}\\Q_{211}\\Q_{222}\\Q_{212}\\Q_{221}\end{pmatrix}. \tag{3.51}$$

After mathematical rearrangements explained previously finite element equation can be defined as

$$\begin{aligned}&\left[\int_{A_0}\left(\underline{\underline{\mathrm{B}}}_F^T\underline{\underline{\mathrm{C}}}_{PF}\underline{\underline{\mathrm{B}}}_F+\underline{\underline{\mathrm{B}}}_F^T\underline{\underline{\mathrm{C}}}_{PG}\underline{\underline{\mathrm{B}}}_G+\underline{\underline{\mathrm{B}}}_G^T\underline{\underline{\mathrm{C}}}_{QF}\underline{\underline{\mathrm{B}}}_F+\underline{\underline{\mathrm{B}}}_G^T\underline{\underline{\mathrm{C}}}_{QG}\underline{\underline{\mathrm{B}}}_G\right)\mathrm{d}A_0\right]\Delta\underline{\mathrm{v}}=\\&\int_{s_0}\left(\underline{\underline{\mathrm{N}}}^T\underline{\mathrm{t}}+\left(\nabla\otimes\underline{\underline{\mathrm{N}}}\right)^T\underline{\mathrm{T}}\right)\mathrm{d}s_0-\int_{A_0}\left(\underline{\underline{\mathrm{B}}}_F^T\underline{\mathrm{P}}^{i-1}+\underline{\underline{\mathrm{B}}}_G^T\underline{\mathrm{Q}}^{i-1}\right)\mathrm{d}A_0.\end{aligned} \tag{3.52}$$

From (3.52) extraction of the finite element equation in the form (3.19) is straightforward. The element stiffness matrix consists of four counterparts, as follows

$$\underline{\underline{\mathrm{K}}} = \underline{\underline{\mathrm{K}}}_{PF} + \underline{\underline{\mathrm{K}}}_{PG} + \underline{\underline{\mathrm{K}}}_{QF} + \underline{\underline{\mathrm{K}}}_{QG} . \tag{3.53}$$

The submatrices in Eq. (3.53) are defined as

$$\underline{\underline{\mathrm{K}}}_{PF} = \int_{A_0} \left(\underline{\underline{\mathrm{B}}}_F^T \underline{\underline{\mathrm{C}}}_{PF} \underline{\underline{\mathrm{B}}}_F \right) \mathrm{d}A_0 , \tag{3.54}$$

$$\underline{\underline{\mathrm{K}}}_{PG} = \int_{A_0} \left(\underline{\underline{\mathrm{B}}}_F^T \underline{\underline{\mathrm{C}}}_{PG} \underline{\underline{\mathrm{B}}}_G \right) \mathrm{d}A_0 , \tag{3.55}$$

$$\underline{\underline{\mathrm{K}}}_{QF} = \int_{A_0} \left(\underline{\underline{\mathrm{B}}}_G^T \underline{\underline{\mathrm{C}}}_{QF} \underline{\underline{\mathrm{B}}}_F \right) \mathrm{d}A_0 , \tag{3.56}$$

$$\underline{\underline{\mathrm{K}}}_{QG} = \int_{A_0} \left(\underline{\underline{\mathrm{B}}}_G^T \underline{\underline{\mathrm{C}}}_{QG} \underline{\underline{\mathrm{B}}}_G \right) \mathrm{d}A_0 . \tag{3.57}$$

In addition, the nodal force vector is equal to

$$\underline{\mathrm{F}}_{\mathrm{i}} = \int_{A_0} \left(\underline{\underline{\mathrm{B}}}_F^T \underline{\mathrm{P}}^{i-1} + \underline{\underline{\mathrm{B}}}_G^T \underline{\mathrm{Q}}^{i-1} \right) \mathrm{d}A_0 . \tag{3.58}$$

3.3 Physical interpretation of nodal degrees of freedom

The derived finite element has twelve degrees of freedom per a node, where, besides the displacements, first and second derivatives are also available as nodal degrees of freedom. Such a high number of degrees of freedom obviously complicates element formulation, raising matrix dimensionality (number of rows and columns) of the intrinsic element fields. On the first sight, availability of higher-order derivatives at the node gives to the element extreme flexibility for achievement of various deformation modes, even by a single element, which would not be possible for a classical C^0 elements without some additional constraint equations or large number of finite elements. But, on the other hand, dealing with all these derivatives represents delicate and quite demanding task. For example, definition of the boundary conditions such as clamp or essential constraints requires appropriate dealing with all the derivatives. In this case, boundary conditions regarding derivatives are not specifically restricted only on an outside boundary of the numerical model. For some problems, there might be necessary for constraining derivatives through the whole model to obtain correct results. Furthermore, establishment of a straight edge when using C^1 finite element discretization is not anymore a straightforward task compared to C^0 finite elements. Basically, if derivatives are not appropriately handled, the consequences are unpredictable. Assuming

that displacement degrees of freedom are easily resolved, deformed shape should lead to some realistic behaviour, but it is not guaranteed. Without correct derivative boundary conditions the boundaries and throughout the model, distribution of the displacements as well as displacement gradients through the model cannot be taken as reliable, leading also to the wrong stress distributions. So, in order to cope with this problems, clear physical interpretation of each nodal degree of freedom is required.

Displacement components u_1 and u_2 are inherent from classical finite elements and further discussion about them is not necessary. First derivatives $u_{1,1}$ and $u_{2,2}$ represent longitudinal or lateral strains, which can be easily visualized, and no significant difficulties managing them in boundary condition setting should appear. Also, the twist degrees of freedom $u_{1,2}$ and $u_{2,1}$ are generally known from local continuum mechanics theory and their use in boundary conditions can be resolved without any issues. If required, their combination constraints shear strain. Dealing with second derivatives, which usually do not come as a nodal variables, becomes more difficult. Hence, in the following discussion, physical meaning of each second derivative will be graphically visualized. Nodal variables $u_{1,11}$ and $u_{2,22}$ are physically interpreted as the rates of the change of normal strains in x_1 and x_2 directions, respectively. As shown in Figs. 3.2 and 3.3, if we prescribe only this components on a square model, we can see the movement of an interior material in the loading direction. Next, nodal degrees of freedom $u_{1,22}$ and $u_{2,11}$ are solely prescribed on a square model represented in Figs. 3.4 and 3.5, respectively. It can be observed that they physically represent curvatures. Thus, these variables should be constrained when establishment of a straight edge is required. Prescribing only mixed second derivatives $u_{1,21}$ and $u_{2,12}$ on a square model gives deformation responses presented in Figs. 3.6 and 3.7. For a straight edge this components should be constrained, too. To appropriately describe bending of the material, mixed second derivatives in combination with curvatures should be prescribed or released, depending on the problem, to achieve correct distribution of the displacement gradients.

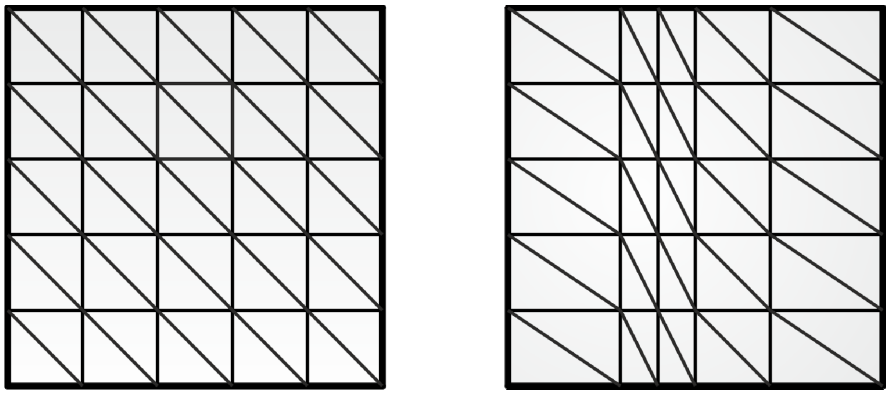

Figure 3.2 Physical interpretation of nodal degree of freedom $u_{1,11}$

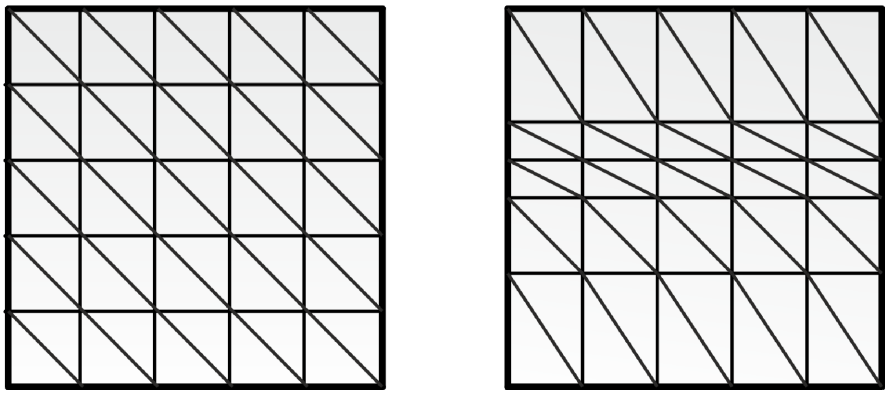

Figure 3.3 Physical interpretation of nodal degree of freedom $u_{2,22}$

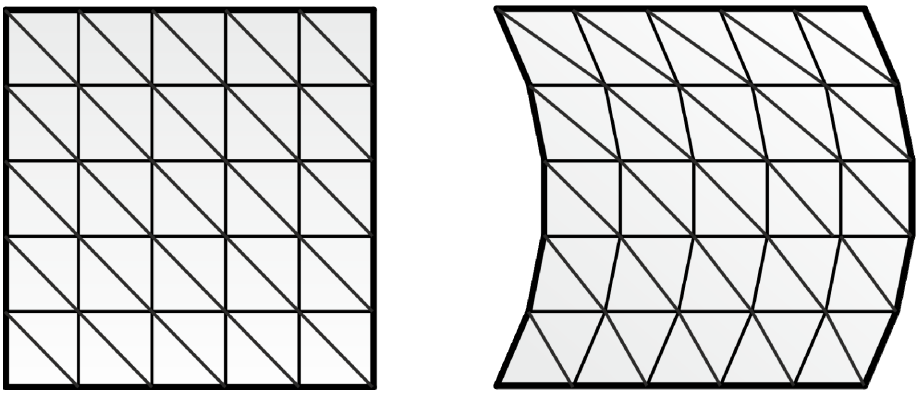

Figure 3.4 Physical interpretation of nodal degree of freedom $u_{1,22}$

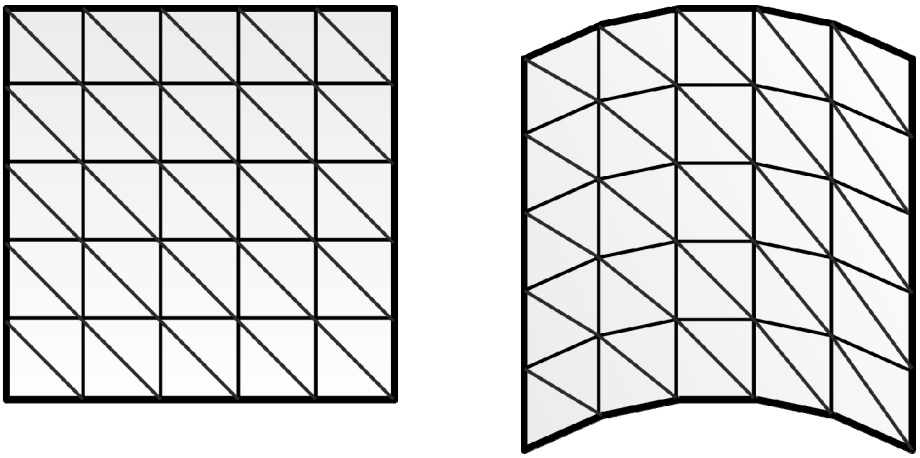

Figure 3.5 Physical interpretation of nodal degree of freedom $u_{2,11}$

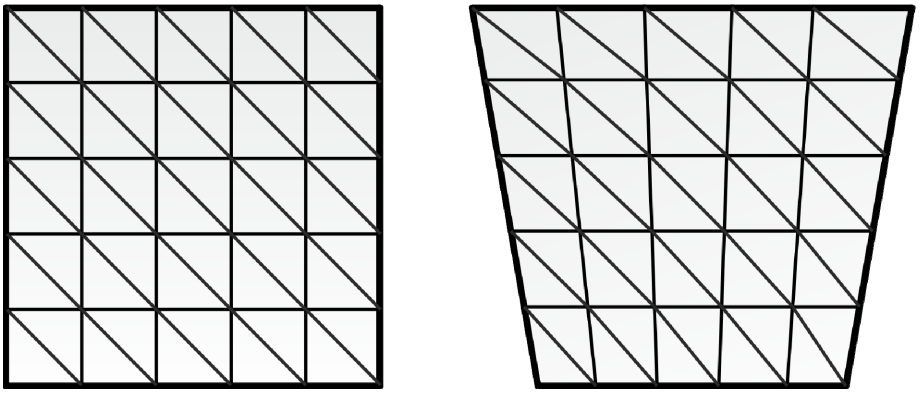

Figure 3.6 Physical interpretation of nodal degree of freedom $u_{1,21}$

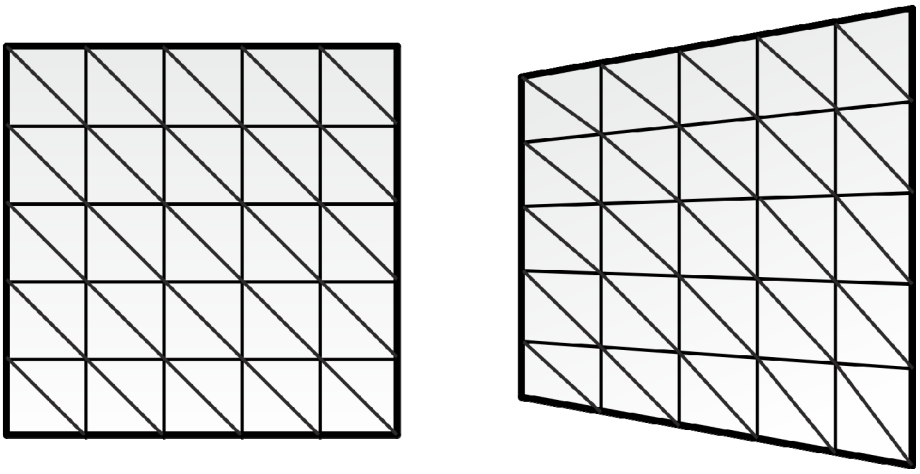

Figure 3.7 Physical interpretation of nodal degree of freedom $u_{2,12}$

3.4 Numerical implementation of the finite element formulations into commercial software

3.4.1 ABAQUS implementation

The nonlinear solution to the system of equations (3.19) has been carried out using commercial finite element software ABAQUS/Standard [122]. Nonlinear solver available in ABAQUS/Standard is utilized via user-defined element subroutine UEL, written in FORTRAN programming language. Essentially, ABAQUS/Standard calls user element coding for each finite element, computing element's contribution to the nodal residual force vector and global system stiffness matrix. It also assembles full system of equations, calculating iterative corrections to the solution variables. Implementation of user elements requires obeying ABAQUS/Standard conventions [123], replacing commercially offered numerical codes by the codes developed on your own. ABAQUS/Standard conventions involve input data required, matrix dimensionality and names, output variables, etc… In development of user finite elements, if possible, ABAQUS/Standard predefined degrees of freedom are usually used, shown in Table 3.1.

Table 3.1 ABAQUS predefined nodal degrees of freedom

1	x_1 displacement
2	x_2 displacement
3	x_3 displacement
4	Rotation about the x_1 axis, in radians
5	Rotation about the x_2 axis, in radians
6	Rotation about the x_3 axis, in radians
7	Warping amplitude (for open-section beam elements)
8	Pore pressure, hydrostatic fluid pressure, or acoustic pressure
9	Electric potential
10	Connector material flow (units of length)
11-30	Temperatures (or normalized concentration in mass diffusion analysis)

For development of a classical C^0 continuous finite elements used for problems in solid mechanics degrees of freedom listed in Table 3.1 are in the most cases sufficient. But, for C^1

finite element developed in this thesis ABAQUS/Standard does not offer first and second derivatives of displacement as an essential nodal variables. However, in user coding predefined degrees of freedom can be also used for other purposes, which gives possibility, e. g., to use rotations, warping amplitude and other degrees of freedom as derivatives of displacement. In our case, since twelve nodal variables are necessary, nodal temperatures have to be used. Unfortunately, to invoke nodal temperature degrees of freedom (NT11-NT30), thermal analysis should be performed. This means that numerical analysis using derived C^1 finite element cannot be conducted as a purely mechanical problem within ABAQUS/Standard framework.

Hence, in order to compute nonlinear problems discretized by the aforementioned C^1 finite element using ABAQUS/Standard solver, fully coupled thermal-stress analysis has to be conducted, though mechanical problems are solved, similar as in [124, 125] for solving XFEM problems. In order to define nodal degrees of freedom, ABAQUS/Standard predefined displacements degrees of freedom 1 and 2 are utilized as displacements, while derivatives degrees of freedom are employed through the nodal temperatures NT11-NT20. During fully coupled thermal-stress analysis nodal temperatures are integrated using a backward-difference scheme, and the nonlinear coupled system is solved using Newton's method. There are two implementation methods of Newton's method available in ABAQUS/Standard, an exact or an approximate. In an exact implementation a nonsymmetric stiffness matrix is constructed representing system of coupled equations as follows

$$\begin{pmatrix} \underline{\underline{K}}_{uu} & \underline{\underline{K}}_{u\theta} \\ \underline{\underline{K}}_{\theta u} & \underline{\underline{K}}_{\theta\theta} \end{pmatrix} \begin{pmatrix} \Delta\underline{u} \\ \Delta\underline{\theta} \end{pmatrix} = \begin{pmatrix} \underline{R}_u \\ \underline{R}_\theta \end{pmatrix}. \tag{3.59}$$

In (3.59) $\Delta\underline{u}$ and $\Delta\underline{\theta}$ are respective corrections to the incremental displacement and temperature, which in this case represents displacement derivatives. In Eq. (3.59), $\underline{\underline{K}}_{uu}$, $\underline{\underline{K}}_{u\theta}$, $\underline{\underline{K}}_{\theta u}$ and $\underline{\underline{K}}_{\theta\theta}$ are submatrices of the fully coupled global stiffness matrix, while $\underline{R}_u$ and $\underline{R}_\theta$ are the mechanical and thermal residual vectors, respectively. For solution of system of equations (3.59) unsymmetrical matrix storage and solution scheme are required, where mechanical and thermal equations are solved simultaneously. If there is a weak coupling between the mechanical and thermal solutions, an approximate Newton's method can be utilized. This method can be applied if the components in the off-diagonal submatrices are small compared to the components in the diagonal submatrices. A less costly solution may be obtained by setting the off-diagonal submatrices to zero obtaining an approximate set of equations

$$\begin{pmatrix} \underline{\underline{\mathrm{K}}}_{uu} & \underline{\underline{0}} \\ \underline{\underline{0}} & \underline{\underline{\mathrm{K}}}_{\theta\theta} \end{pmatrix} \begin{pmatrix} \Delta\underline{\mathrm{u}} \\ \Delta\underline{\theta} \end{pmatrix} = \begin{pmatrix} \Delta\underline{\mathrm{R}}_{u} \\ \Delta\underline{\mathrm{R}}_{\theta} \end{pmatrix}, \tag{3.60}$$

since with this approximation thermal and mechanical equations can be solved separately, with fewer equations to consider in each subproblem. This modified form of Newton's method does not affect solution accuracy since the fully coupled effect is considered through the residual vector at each increment in time. The rate of convergence strongly depends on the magnitude of the coupling effect, so more iterations are generally needed to achieve equilibrium compared to the exact implementation of Newton's method. Also, when the coupling is significant, the exact implementation of Newton's method is required. In the C^1 finite element formulation intended for implementation coupling between displacements and displacement derivatives is obviously strong. Thus, contributions of the submatrices $\underline{\underline{\mathrm{K}}}_{u\theta}$ and $\underline{\underline{\mathrm{K}}}_{\partial u}$ cannot be neglected. Considering this, the exact implementation of Newton's method seems to be logical choice. For more details about coupled analysis procedures in ABAQUS/Standard, see [123].

3.4.2 Numerical integration of element stiffness matrix

As it is well-known, numerical formulation using area coordinates is common for a triangular finite elements, due to simplicity and numerical performance. However, area coordinates used in [33, 118] and the integration approach by means of analytical Eisenberg-Malvern formula are generally not suitable for use in the multiscale framework, where the constitutive matrix and the stress tensor have to be calculated at every macroscopic integration point. Therefore, for this purpose, stiffness matrix of the C1PE3 element should be integrated e. g., by the Gauss Legendre numerical integration method. Exact evaluation of the stiffness matrix requires a scheme to be able to integrate a polynomial up to the eighth degree, with the error of order $O\left(h^9\right)$. The full integration scheme developed in [126] requires 25 Gauss points, and it is $O\left(h^{10}\right)$ accurate. But such numerical scheme is a computationally expensive, and its application in a multiscale procedure is extremely unattractive.

Nevertheless, in the finite element practice full integration can usually be avoided and a less accurate schemes are often sufficient. In [34], a 16 Gauss point scheme, which is $O\left(h^8\right)$ accurate has been derived. According to [127], for no loss of convergence it is enough that the scheme employed is able to integrate exactly a polynomial of degree $2\left(p-m\right)$, or the error

has to be of the order $O\left(h^{2(p-m)+1}\right)$. In the aforementioned formulas, p is the degree of the complete polynomial used in the interpolation, and m is the highest order of the derivatives present in the problem. For the finite element used in the research $p=5$ and $m=2$, thus $O\left(h^{7}\right)$ is necessary. The reduced integration technique with 13 Gauss points can be found in [128, 129], satisfying required accuracy. It has been already applied in [30, 32, 130]. This integration procedure is adopted as the most efficient. Additional rigid body (zero energy) modes are not induced and the highest possible accuracy for the number of integration points used is achieved.

3.5 Finite element verification

To demonstrate validity of the finite element formulations derived, several patch tests have been performed on some usual benchmark examples. The patch test has historically been used to check the completeness and stability properties of the finite elements, which are the necessary and sufficient conditions for convergence of a finite element formulation. The basic idea of a linear patch test is that discretization is constructed in such way that at least one node lies in the interior of the numerical model. Boundary conditions prescribed on the boundaries should be consistent with a uniform state of strain and stress. Accordingly, interior results must satisfy the imposed solution exactly, describing a uniform state of deformation and stress.

Linear patch test is usually sufficient for the elements constructed in the framework of a classical continuum. But, for a higher-order continuum finite element formulations used in this research linear patch test only does not suffice. In contrast to the elements derived for a classical continuum which should satisfy only the well-known linear patch test, the strain gradient based elements should pass the quadratic patch test in order to be able to solve the second gradient boundary value problem accurately. For the triangular finite element developed within this thesis a quadratic patch test is also desirable. In a quadratic patch test element's ability to reproduce a quadratic displacement, linear strain and constant gradient of the strain field is tested. Since in Aifantis strain gradient elasticity theory microstructural parameter l^2 appears, it is convenient to check influence of the microstructural parameter on the element performance and behaviour.

3.5.1 Pure shear test

Firstly, linear patch test has been performed through the pure shear test, where small strain theory has been adopted. Rectangular model used in the example has dimensions 0.24×0.12. It has been discretized by 10 finite elements as shown in Figure 3.8, where discretization has been applied according to [131].

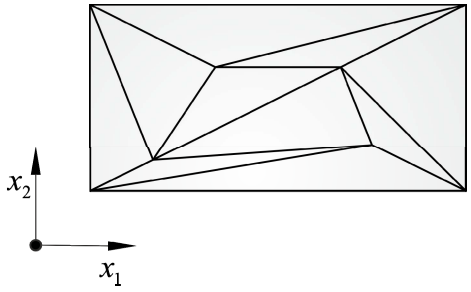

Figure 3.8 Finite element discretization for a pure shear problem

Material parameters used are Young's modulus $E = 10^6$ and Poisson's ratio $\nu = 0.25$. On the boundary nodes of the model displacement field is imposed in the form

$$u_1 = u_0 \left(x_1 + \frac{1}{2} x_2 \right), \tag{3.61}$$

$$u_2 = u_0 \left(x_2 + \frac{1}{2} x_1 \right). \tag{3.62}$$

According to the element's nodal degrees of freedom first and second derivatives of (3.61) and (3.62) should be prescribed too. The value of u_0 has been taken from [132], where $u_0 = 0.001$. Analytical solution of this problem with the used dimensions and displacement field are as follows: $\sigma_{11} = 1333$, $\sigma_{22} = 1333$, $\tau_{12} = 400$, and $\gamma_{12} = 0.001$. After numerical analysis, numerical results obtained correspond exactly to the analytical solutions.

3.5.2 Cook's beam

The next example considered is a Cook's beam. The beam is loaded by the continuous load on the right edge, as presented in Figure 3.9. Plane stress and small strains are assumed. Finite element model is discretised by the 12 finite elements, according to Figure 3.9. Material properties used in the example are Young's modulus $E = 1$ and Poisson's ratio $\nu = 0.33$. Loading value $F = 1$ and thickness of the beam $t = 0.1$ are again taken from [132]. In this example influence of the reduced Gauss-Legendre scheme on performance of the element has been tested. Table 3.2 shows the results of the vertical displacement at point A.

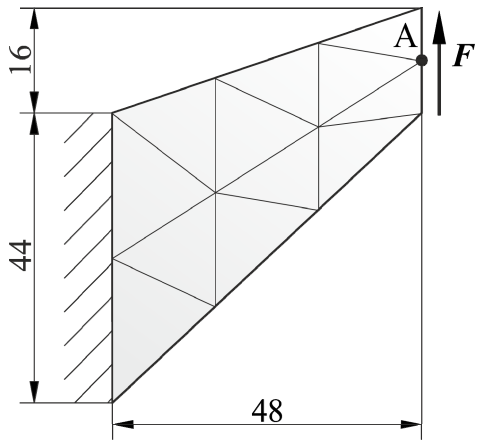

Figure 3.9 Cooke's beam

Table 3.2 Vertical displacement at point A

	Vertical displacement at point A
C1PE3 (25 integration points)	23.84
C1PE3 (13 integration points)	23.86
Exact	23.96

From Table 3.2 it is clear that both integration schemes show good agreement with an exact solution. As usual, reduced scheme gives more compliant behaviour, but in this case influence is almost negligible. It should be noted that such good performance is demonstrated with 12 elements only.

3.5.3 Cantilever beam bending problem

In the next benchmark test cantilever beam subjected to a bending is studied. This test is used to assess the sensitivity of the element to the geometric distortions. The mesh used for the patch test is taken from [133] and presented in Figure 3.10. As can be seen, this patch test is originally intended for the quadrilateral elements; therefore default discretization is adjusted to the triangular finite elements, as shown in Figs. 3.11 and 3.12.

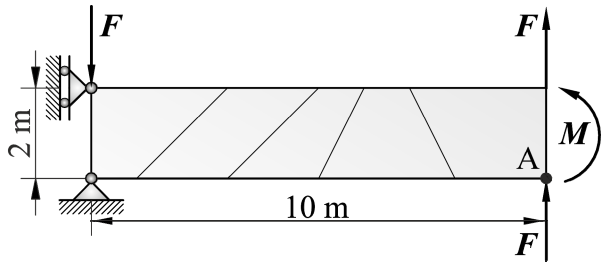

Figure 3.10 Cantilever beam subjected to bending

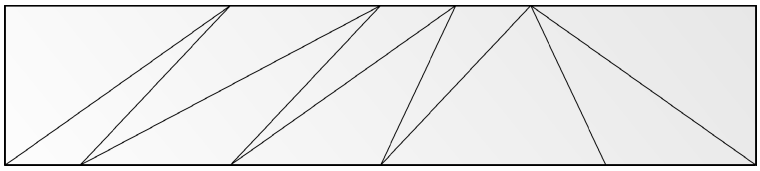

Figure 3.11 Distorded mesh 1

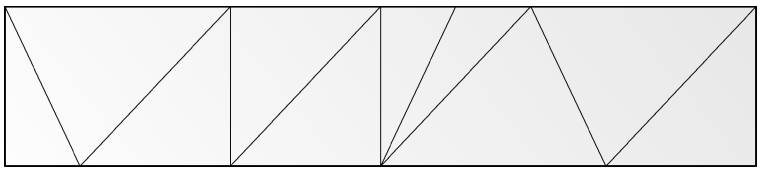

Figure 3.12 Distorded mesh 2

Two loading cases are studied herein. One is the case with the linear bending caused by concentrated forces $F = 150\,\mathrm{N}$ and the other is the case with the pure bending caused by applied bending moment $M = 2000\,\mathrm{Nmm}$. The elasticity modulus and Poisson's ratio of the beam are 1500 MPa and 0.25, respectively. To impose boundary conditions for C1PE3 element on the left edge, except displacements, which are straightforward it was necessary to define first and second derivatives of displacements. On the left edge, which remains straight, first derivatives of both displacements are supressed. Furthermore, all second derivatives in the normal direction to the edge as well as mixed second derivatives in both directions need to be constrained. The results of the vertical displacement at point A for two load cases are shown in Table 3.3 and Table 3.4 with reference solution according to [134].

Table 3.3 Vertical displacement of cantilever beam at point A loaded by a concentrated force

	Vertical displacement at point A
Distorted mesh1	102.044
Distorted mesh 2	102.295
Exact	102.6

Table 3.4 Vertical displacement of cantilever beam at point A loaded by a bending moment

	Vertical displacement at point A
Distorted mesh1	102.246
Distorted mesh 2	102.503
Exact	100

From the results shown in Tables above it can be clearly seen that the element C1PE3 presented in this research passes the patch test and its performance is satisfactorily even for excessively distorted discretization. The results obtained by distorted mesh 1 show a stiffer behaviour in an almost negligible extent compared to mesh 2 for the both loading cases, which is not usual considering that mesh 1 is more distorted than mesh 2. For a second loading case where beam is loaded by a bending moment both discretizations show small measure of too compliant behaviour.

3.5.4 Influence of the microstructural parameter *l*

In the previous examples a classical continuum theory has been used. In this example Aifantis theory has been employed with microstructural parameter $l > 0$, meaning that the effect of an environment on behavior of some point is taken into consideration (nonlocal theory). Accordingly, element stiffness becomes increased according to (3.39) and the double stress tensors defined by (3.30) and (3.31) are nonzero. Influence of the microstructural parameter on a mechanical behavior of the material has been examined on a membrane with a circular hole subjected to tension as discussed in [131]. Geometry and boundary conditions are presented in Figure 3.13. For the numerical model double symmetry is used, and discretization presented in Figure 3.14 is taken from the literature to achieve better comparability with [131].

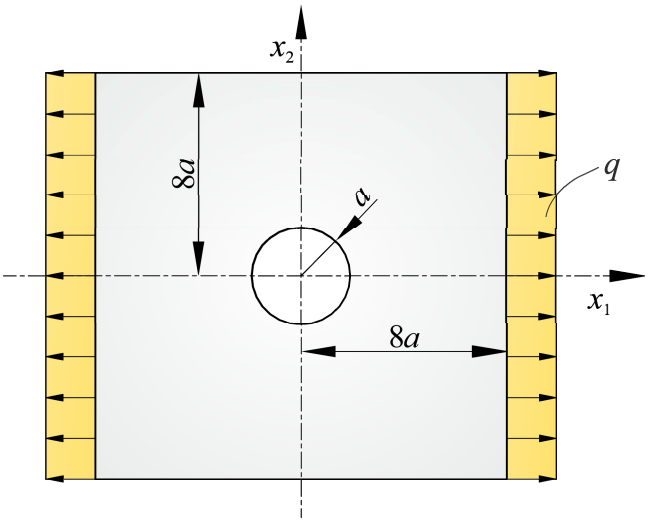

Figure 3.13 Membrane with a circular hole subjected to a tension loading

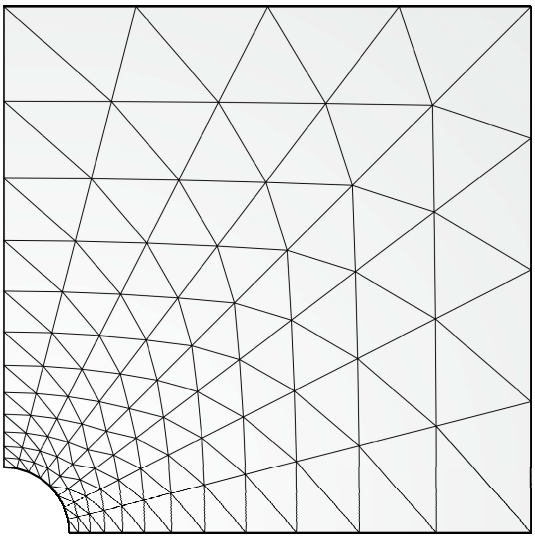

Figure 3.14 Finite element discretization of the membrane

In the presented example the hole radius is set to $a = 1$. Several analyses are conducted, for various $\frac{l}{a}$ ratios, where l was set to $0.01, 0.1, 0.125, 0.167, 0.25, 0.33, 0.5$ and 1 with Poisson's ratios $\nu = 0$ and $\nu = 0.5$. The stress concentration factor (ratio of the maximum effective stress and the nominal stress) is compared to the values from [131] for a plane stress assumption. Performance of the full and reduced integration scheme have been again compared, to study an influence of the integration scheme on the numerical influence of the higher order stiffness matrices $\underline{\underline{\mathbf{K}}}_{x_1}$ and $\underline{\underline{\mathbf{K}}}_{x_2}$. The results obtained are presented in Figs. 3.15 and 3.16.

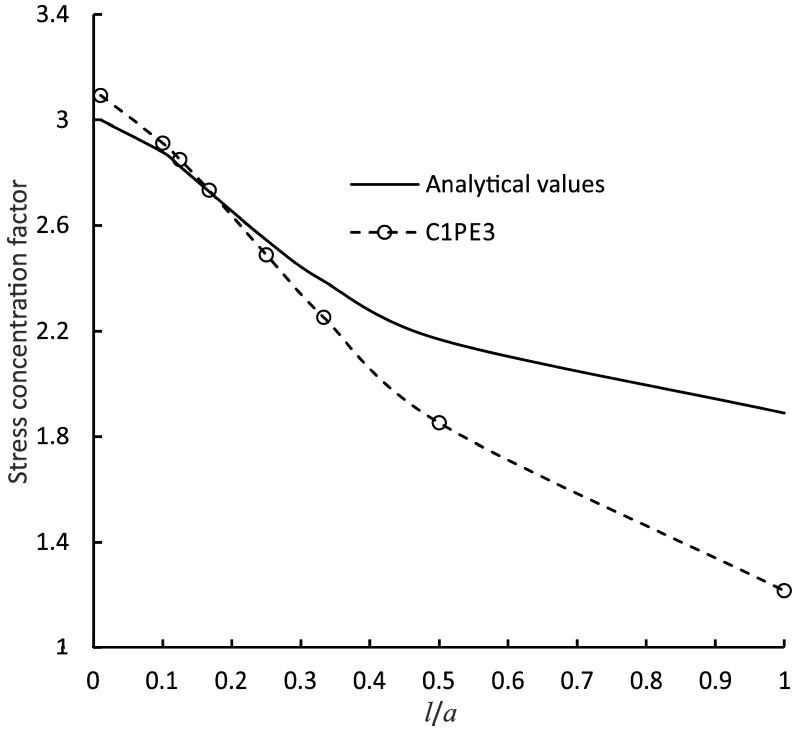

Figure 3.15 Stress concentration factor for a membrane with a hole (ν = 0)

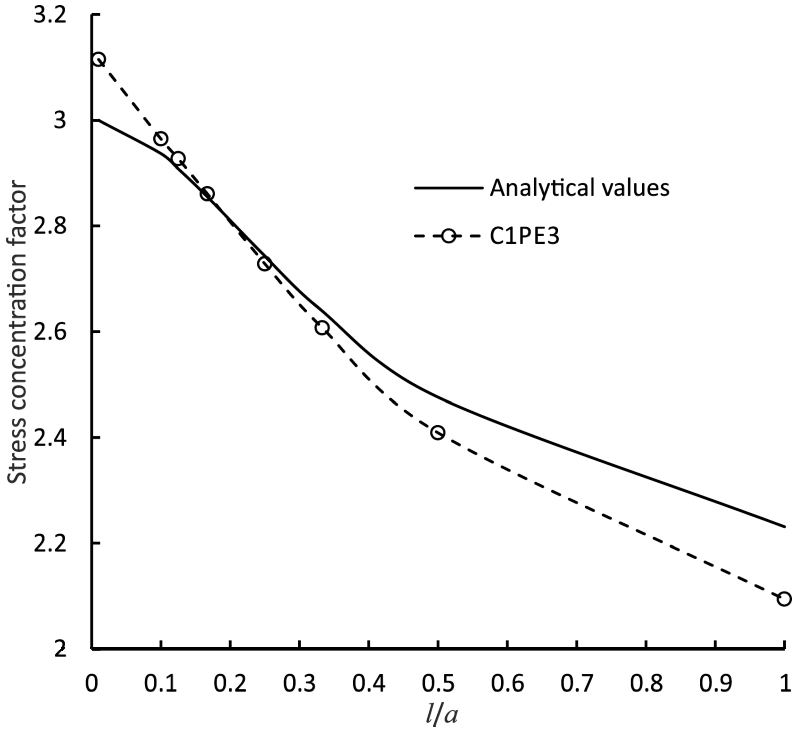

Figure 3.16 Stress concentration factor for a membrane with a hole (ν = 0.5)

In Figures presented above only results obtained by 13 point integration rule have been visualized, since full integration scheme provides identical results. In this way, once more it has been demonstrated that a reduced integration does not have any significant influence on the numerical performance of the finite element, in this case through numerical integration of

the higher order stiffness matrices. The obtained stress concentration factor results show good correspondence with the exact solution for lower values of l. For a higher values of l stress concentration factor has a slightly steeper decrease, but generally, the results are satisfying. To achieve better results, finer discretization around the hole can be used. Besides, real engineering material in general case do not possess limit values of Poisson's ratio 0 and 0.5. Additional comparison of the results to the other finite element formulations can be made using [131].

3.5.5 Quadratic patch test

As already noted, for a finite element formulation based on the nonlocal continuum theory it is necessary to check the element behaviour by the quadratic patch test. Basically, quadratic displacement field is prescribed on the boundaries. The element must be able to reproduce linear distribution of first derivatives of displacement and constant distribution of the second displacement derivatives throughout interior. The finite element model and discretization used in an elastic quadratic patch test has dimensions $a \times a$, as shown in Figure 3.17.

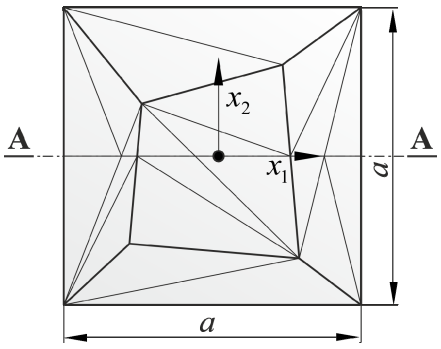

Figure 3.17 Finite element discretization of the quadratic patch test model

In the presented example the side length of square patch is set to $a = 100\,\text{mm}$. The patch configuration is discretized by 22 distorted finite elements. The geometry partitioning zones drawn by the thick line are taken from [131, 135]. Since in this particular example the solution is examined through the middle section A-A, a modified discretization with more distorted elements is performed, in which new nodes are introduced along line A-A, as displayed in Figure 3.17. The nodal connectivity into the elements has been chosen by the worst case scenario to test element robustness. The material model used is taken from [77], and it is similar to a Mindlin's second order gradient linear elastic material model proposed in [25, 26]. Accordingly, the first Piola-Kirchhoff stress tensor and the double stress tensor are given by

$$\underline{\mathbf{P}} = \lambda \operatorname{tr}\left(\nabla \otimes \mathbf{u}\right) \otimes \underline{\mathbf{I}} + 2\mu\left(\nabla \otimes \mathbf{u}\right), \tag{3.63}$$

$${}^{3}\underline{\mathbf{Q}} = \frac{l^2\lambda}{24}\left({}^{3}\underline{\mathbf{G}} : {}^{4}\underline{\mathbf{I}} + {}^{4}\underline{\mathbf{I}} : {}^{3}\underline{\mathbf{G}}\right) + \frac{l^2\mu}{12}{}^{3}\underline{\mathbf{G}} + \frac{l^2\mu}{24}\left({}^{3}\underline{\mathbf{G}}^{LC} + \left({}^{3}\underline{\mathbf{G}}^{LC}\right)^{RC}\right). \tag{3.64}$$

In Eqs. (3.63) and (3.64) λ and μ are Lamé constants, while $\underline{\mathbf{I}}$ and ${}^{4}\underline{\mathbf{I}}$ represent the second- and fourth-order unit tensors. The exponents *LC* and *RC* denote the left and right conjugation, respectively. The microstructural parameter is denoted by l, as a measure of nonlocality with dimension of a length. The material considered is a linear elastic steel, with $\lambda = 121\,154\,\text{MPa}$ and $\mu = 80\,769.2\,\text{MPa}$. On the boundary nodes of the finite element discretized model, displacements are imposed in the form of a quadratic polynomial proposed by [136] and expressed as

$$u_1 = 0.001\left(0.12\,x_1 + 0.14\,x_2 + 0.16\,x_1^2 + 0.18\,x_1x_2 + 0.20\,x_2^2\right), \tag{3.65}$$

$$u_2 = 0.001\left(0.11\,x_1 + 0.13\,x_2 + 0.15\,x_1^2 + 0.10\,x_1x_2 + 0.21\,x_2^2\right), \tag{3.66}$$

as well as their first and second derivatives. Solving the boundary value problem, a linearly varying deformation field and a constant gradient of the deformation field throughout the patch are expected. Here, an influence of the microstructural parameter l (material length scale) on the patch test results has been examined. Several analyses are conducted in which $\frac{l}{a}$ ratio has been varied and it takes the values from 1 up to 5 in order to study its influence on the size-dependent mechanical response (e.g. size effect phenomenon) of the patch predicted by gradient elasticity. The existence of a size effect implies that specimens with the same shape but different sizes show a different mechanical behavior. It is worth mentioning that the size effects could not be captured by classical continuum theories since no constitutive length scale parameters exist in these theories to scale the effects of strain gradients. Figs. 3.18 and 3.19 show the distribution of the first gradient of displacement $u_{1,1}$ and the second gradient of displacement $u_{1,11}$ along line A–A shown in Figure 3.17. Here, due to non-uniform deformation distribution in the quadratic patch test, the influence of the internal material length scale l becomes significant. The diagrams display that the results converge to an exact analytical values with the increase of the length scale parameter, which is in accordance to the phenomenon known in the literature [8]. The linear distribution of $u_{1,1}$ is reproduced for $\frac{l}{a} = 3$, and the constant value of $u_{1,11}$ over the line A–A is achieved for the ratio $\frac{l}{a} = 5$. It should be noted that in Figure 3.19 fine scale is used on the ordinate axis and the highest error

in the value of second-order strain is 1%, which maybe on the first sight is not an impression. Thus, it can be concluded that the proposed triangular finite element employing the second-order large strain theory passes the quadratic patch test under the condition that the material length scale parameters are sufficiently large. This statement also implicates that the element sizes need to be smaller than l. Such observation is in agreement with the results reported in the literature for a number of problems including quadratic patch tests [8], perforated strips under tension [131], notched beams under bending and indentation problems [42]. Therein, it has been found that the strain gradient effects become important if the material length scale parameter l is of the same order of magnitude as the representative length associated with deformation (size of a hole, indenter or otherwise). On the other hand, if the characteristic dimension of non-uniform deformation is much larger than material length scale parameter, strain gradient effects become negligible, and the strain gradient theories degenerate to conventional continuum theories. In the special case of $l = 0$, the linear patch test, usual in a classical continuum mechanics is satisfied, which has also already been proven.

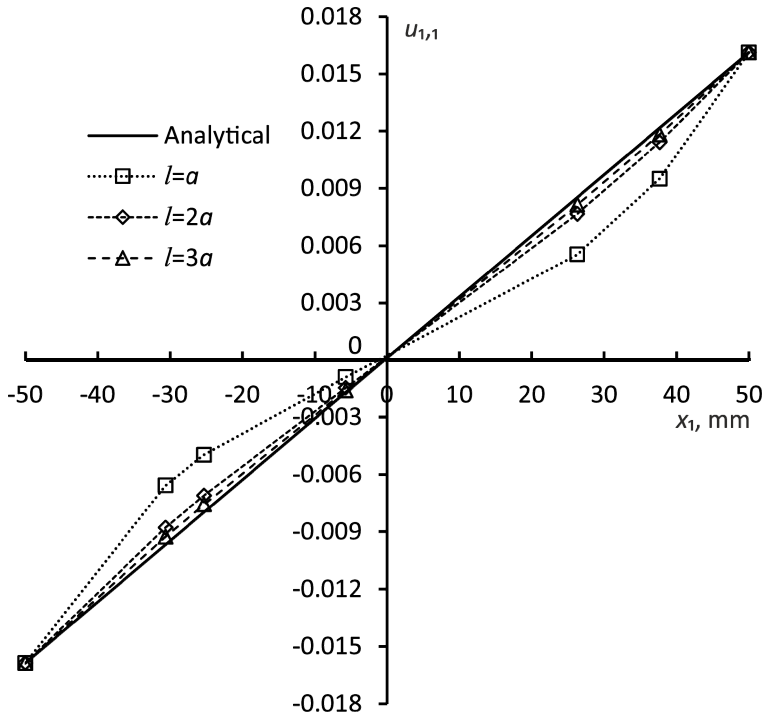

Figure 3.18 Distribution of strain through A-A

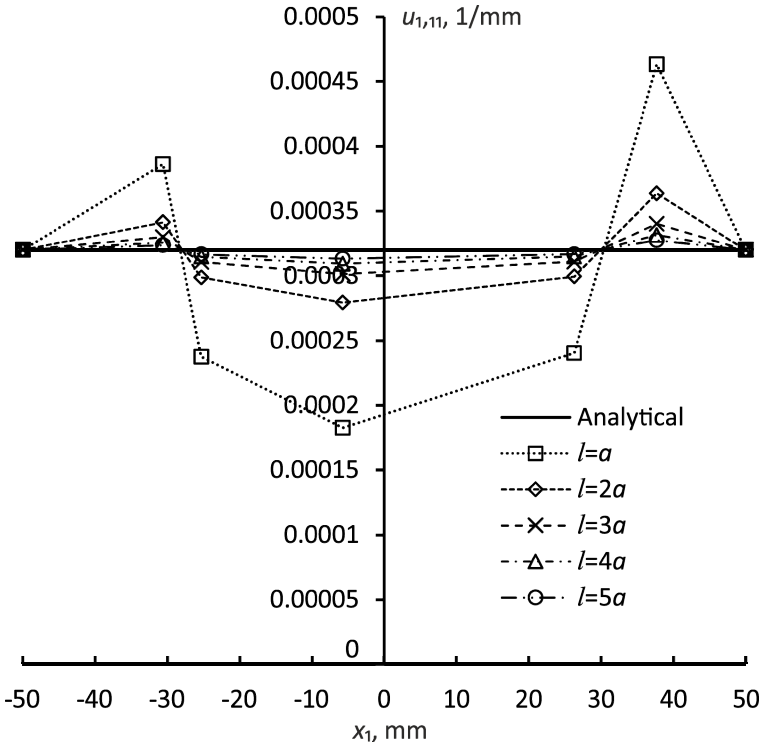

Figure 3.19 Distribution of second-order strain through A-A

3.5.6 Elastic boundary shear layer problem

In order to further verify the accuracy and convergence of the solutions obtained by the developed large strain higher-order triangular finite element, a simple boundary shear layer problem, usually used as a benchmark test in a higher-order formulations e.g. in [10, 77, 79], is analyzed. The schematic presentation of the geometry, boundary conditions and finite element mesh are given in Figure 3.20.

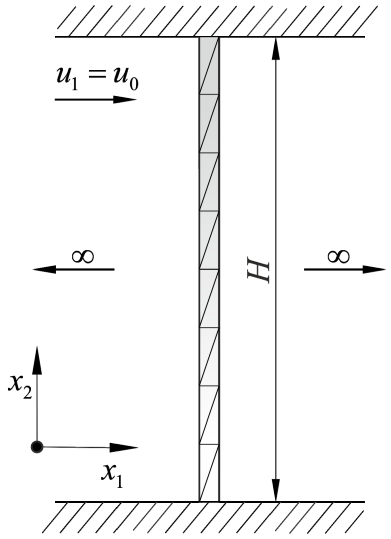

Figure 3.20 Discretization of the shear layer strip

The strip height is $H = 1\,\text{mm}$ in the x_2 direction and it has an infinite length in the horizontal x_1 direction. Since all field quantities are independent of the x_1 direction, the computational model may comprise only the elements row through the height. Five finite element meshes consisting of 2, 4, 8, 16 and 32 elements per height are considered, maintaining the element side length ratio of 2.5. As shown in Figure 3.20, the bottom boundary is fixed, while a horizontal displacement $u_1 = u_0 = 0.03\,\text{mm}$ is imposed on the top boundary. Accordingly, the boundary conditions of the bottom and top clamped edges are prescribed by the displacement and deformation gradient components in the following form:

$$\text{at bottom boundary}\,(x_2 = 0): u_1 = 0,\;\; u_2 = 0,\;\; u_{1,2} = 0\,, \tag{3.67}$$

$$\text{at top boundary}\,(x_2 = H): u_1 = u_0,\; u_2 = 0,\;\; u_{1,2} = 0\,. \tag{3.68}$$

Besides, the condition $u_2 = 0$ is prescribed on the left and right boundary nodes along the height, which are imposed by the periodicity conditions enforcing the independency of x_1. Through the whole strip height, the second displacement derivatives $u_{1,21}$, $u_{2,11}$, $u_{2,21}$ and $u_{2,22}$ are suppressed enabling a horizontal movements of the strip layers. For the sake of comparison, the Mindlin's elastic constitutive model together with a material data are taken from [8]. Thus the first Piola-Kirchhoff stress tensor and the double stress tensor are expressed as

$$\underline{\mathbf{P}} = \lambda\,\mathrm{tr}\left(\nabla \otimes \mathbf{u}\right) \otimes \underline{\mathbf{I}} + 2\mu\left(\nabla \otimes \mathbf{u}\right), \tag{3.69}$$

$$\begin{aligned} {}^3\underline{\mathbf{Q}} = {} & \frac{l^2\mu}{2}\left({}^3\underline{\mathbf{G}} : {}^4\underline{\mathbf{I}} + {}^4\underline{\mathbf{I}} : {}^3\underline{\mathbf{G}}\right) + \frac{l^2\mu}{4}\left({}^3\underline{\mathbf{G}}^{LC} : {}^4\underline{\mathbf{I}} + 2\left({}^3\underline{\mathbf{G}} : {}^4\underline{\mathbf{I}}\right)^{LC} + {}^4\underline{\mathbf{I}} : {}^3\underline{\mathbf{G}}^{RC}\right) + \\ & + l^2\mu\left({}^3\underline{\mathbf{G}}^{LC} : {}^4\underline{\mathbf{I}}\right)^{LC} + l^2\mu\,{}^3\underline{\mathbf{G}} + \frac{l^2\mu}{2}\left({}^3\underline{\mathbf{G}}^{LC} + \left({}^3\underline{\mathbf{G}}^{LC}\right)^{RC}\right). \end{aligned} \tag{3.70}$$

The material data are the shear modulus $\mu = 2000\,\text{MPa}$, the bulk modulus $K = 5000\,\text{MPa}$ and the material length scale $l = 0.05\,\text{mm}$. It should be noted that the material law used fulfills the frame indifference condition, as clarified in [8]. The deformation response of the strip is displayed by a distribution of the shear strain over the height calculated analytically by the expression

$$u_{1,2}\left(x_2\right) = \frac{\sqrt{2}u_0\left(-\sinh\left[\dfrac{H}{\sqrt{2}l}\right] + \sinh\left[\dfrac{H - x_2}{\sqrt{2}l}\right] + \sinh\left[\dfrac{x_2}{\sqrt{2}l}\right]\right)}{-4l + 4l\cosh\left[\dfrac{H}{\sqrt{2}l}\right] - \sqrt{2}H\sinh\left[\dfrac{H}{\sqrt{2}l}\right]}. \tag{3.71}$$

Details about derivation of an analytical relation (3.71) are explained in [8]. Comparison of numerical and analytical results is presented in Figure 3.21.

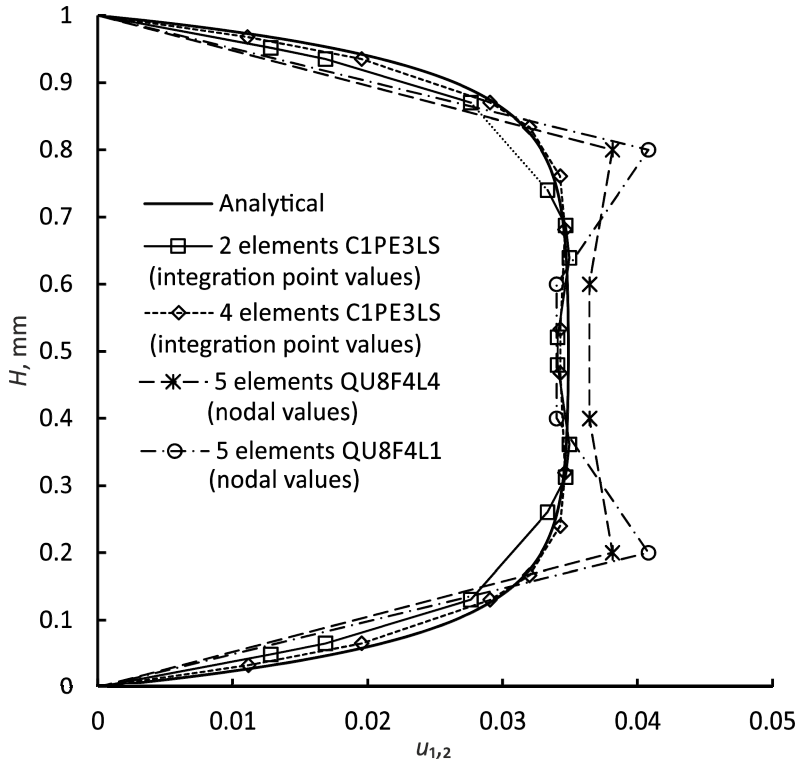

Figure 3.21 Distribution of the shear strain along the height of the strip

The convergence of the numerical solutions obtained by a developed triangular finite element, here labelled as C1PE3LS (Large Strain), towards an analytical result are presented and compared with the solutions obtained by the quadrilateral elements QU8F4L1 and QU8F4L4 based on the mixed formulation taken from [8]. More about QU8F4L1 and QU8F4L4 finite element formulations can be found in [39]. As evident in Figure 3.21, the presented C1PE3LS element converges quickly with a mesh refinement. The analytical solution is achieved only by four C1PE3LS elements, while the results obtained by five elements QU8F4L1 and QU8F4L4 are far from analytical solution. In [8] it has been shown that the twenty elements are needed to reach the analytical values. Thus, conclusion is that the convergence rate of the element C1PE3LS in the presented shear strain computation is much higher than of the tested quadrilateral elements, which is considered as an advantage of the C^1 large strain finite element formulation proposed in this contribution.

However, the number of elements is not the best measure for the convergence assessment. The number of degrees of freedom may be more relevant. However, the data available for comparison, which are displayed in the form of diagrams in [8], are only presented versus the number of elements. The number of degrees of freedom for the

quadrilateral elements could be assessed by using the corresponding element formulation shown in [37-39]. After this consideration, it is to conclude that the solutions obtained by the computational model of the finite element QU8F4L1 reach the analytical values for the discretization of 394 degrees of freedom. In the case of the element QU8F4L4 the convergence is achieved for 454 degrees of freedom. On the contrary, the analytical values are captured only by 72 degrees of freedom, when the triangular finite element C1PE3LS is used.

In addition, analogous to the procedure in [8], the traction and double traction calculated on the top edge of the strip $(x_2 = H)$ have been considered to further evaluate the proposed triangular element. The accuracy and the convergence rate are again tested, and accordingly, the results are compared with an analytical solution and with the values obtained by the QU8F4L1 and QU8F4L4 elements again taken from [8], as shown in Figs. 3.22 and 3.23.

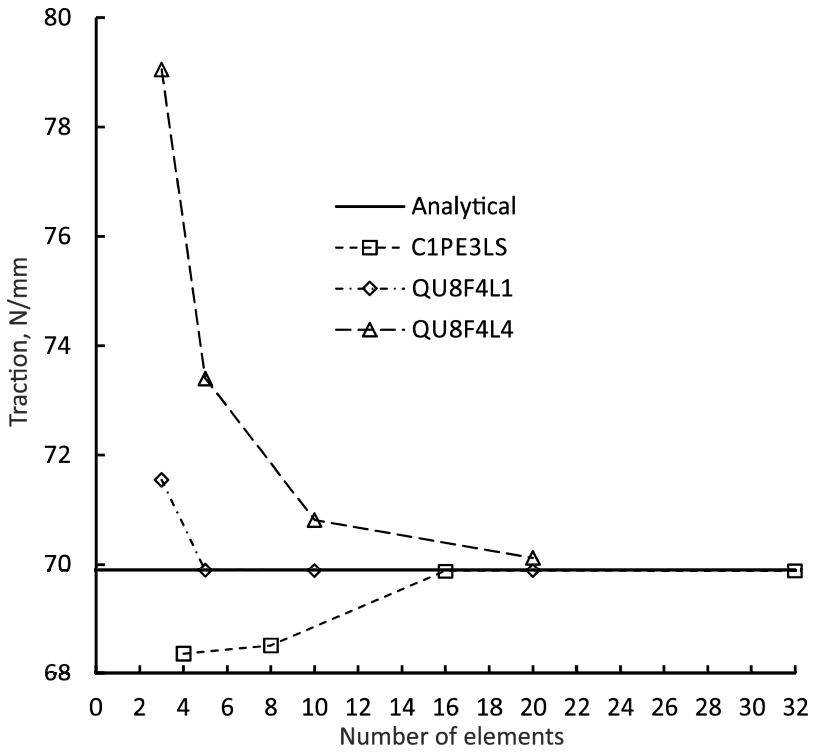

Figure 3.22 Convergence of the boundary traction for different finite element discretization sizes

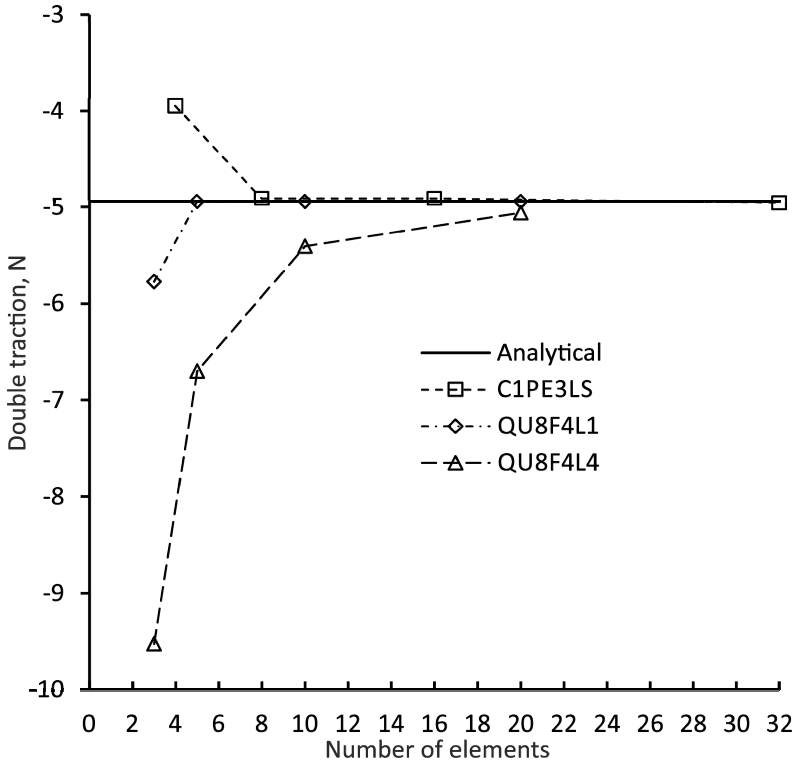

Figure 3.23 Convergence of the boundary double traction for different finite element discretization sizes

It is obvious, that the results obtained by all elements reach the analytical value as the mesh refinement increases. However, the mixed finite element QU8F4L1 exhibits a higher convergence rate than the triangular element C1PE3LS, while the convergence rate for the element QU8F4L4 is slower than that for C1PE3LS. The reason for this slight disadvantage of the triangular finite element could be its relatively less efficient computation of the boundary traction because the element employs a full displacement formulation. Therein, the mixed formulation should generally have an advantage because the deformation gradient components are interpolation functions. If the number of elements is replaced by the number of degrees of freedom, as mentioned above, the conclusion is similar. The element QU8F4L1 shows the best performance because the analytical values are reached with only 109 degrees of freedom, while the solutions obtained by the triangular C1PE3LS element converge if the mesh with 216 degrees of freedom is used. To achieve the convergence using the element QU8F4L4, the mesh with 454 degrees of freedom is needed.

In spite of this disadvantage and bearing in mind its excellent behavior in the previous example, the C^1 large strain triangular finite element can be considered as efficient enough for the modeling of second-order large strain boundary value problems.

4 Homogenization of heterogeneous materials

All materials are heterogeneous at various scales of observation. In the framework of a mechanical exploitation of the material, material heterogeneities are interesting ultimately through their influence on a non-uniform response and microstructure evolution which have profound impact on a continuum mechanical response at engineering scales. In a classical local continuum approach many materials can be treated as homogeneous continua through separation of the scale of the problem under consideration and the scale at which actual heterogeneities affect physical processes as plasticity, nucleation and growth of damage, phase transformation, etc. Generally speaking, description of the microstructural phenomena leads to a better understanding of the macroscopic behavior. But, one cannot assume that effective material model is of the same type as the model used for the microconstituents, with an exception of linear elastic material at small strains where the superposition principle holds.

Until a few years ago, the determination of effective, homogeneous material properties could only be done by either conducting experiments on an existing material sample or by semi-analytical methods in very few cases, making rather strong assumptions on the mechanical variables or the microstructure. Unfortunately, this class of methods does not necessarily reflect the physical processes occurring at the lower scales, leading quite often to an inaccurate results. In order to accurately predict the mechanical response of the evolving microstructure, multiscale approach is required, integrating physical understanding of material behavior at various physical scales. Rapid increase of computational power boosted by innovative solutions in numerical modeling has enabled detailed quantification of the mechanical response of materials across multiple scales for a nonlinear processes. Using multiscale setting we are able to develop a constitutive models applicable at engineering scales using detailed information obtained from finer scales through application of newly developed class of computational homogenization methods.

The overall concept of computational homogenization is developed in [137-139] and its main attention is determination of the effective properties of a heterogeneous media. Computational homogenization allows incorporation of the microstructure into a standard continuum model turning standard boundary value problem into a nested boundary value problem, containing a macroscale and a microscale level. In such scheme an explicit

macroscopic material model is not available. Instead, it is provided by a locally attached microscopic boundary value problem driven by macroscopic quantities. However, finer scale geometry (microstructure) is often unknown, so statistical assumptions have to be made. The macroscopic properties are determined by a homogenization process acting on the effective, homogenized sample of material called statistically representative volume element (RVE), see for example [140-143]. The resulting effective material is supposed to represent all macroscopic properties of the microheterogeneous structure and enables to restrict the computational effort to the smallest, still representative, material sample. Firstly developed concepts of computational homogenization techniques are built within a standard local continuum mechanics, where the behaviour of a material point depends only on the first gradient of the displacement field, referred to as first-order homogenization. Unfortunately, first-order micro-macro computational approaches, as well as conventional homogenization methods, have some major disadvantages. As first, despite the fact that first-order homogenization technique accounts an influence of the heterogeneous microstructure by explicit modeling of the microconstituents, it cannot take into account the absolute size of the microstructure. Consequently, geometrical size effects cannot be accounted for. On the other hand, from mathematical point of view first-order approach relies on the intrinsic assumption of uniformity of the macroscopic stress as strain fields appointed to RVE. Due to uniformity assumption first-order homogenization is not appropriate for problems dealing with high gradients, where the macroscopic fields can vary rapidly.

To overcome these shortcomings, a second-order computational homogenization procedure, as extension of the classical computational homogenization has been proposed [27, 57, 97, 144, 145]. To derive second-order homogenization, a nonlocal continuum theory satisfying C^1 continuity has to be used at the macroscale. In this way the first and the second gradient of the displacement field at the macrolevel are prescribed through essential boundary conditions on the RVE. At the microscale, RVE is still treated as an ordinary continuum, described by a standard continuum theory using well known constitutive equations. From the solution of the RVE boundary value problem, stress-, double stress tensor and constitutive matrices giving higher-order macrocontinuum constitutive behaviour are extracted from a homogenization procedure.

The micro–macro algorithm derived within this thesis consists of two models representing two different levels. The first level represents the macromodel, discretized by a previously derived triangular finite elements. As the second level, the microstructure is presented by the representative volume element, which is in this Chapter discretized by a C^0

quadrilateral four-node finite elements. The macroscopic quantities are denoted by the subscript "M", while the microscopic values are labelled with the subscript "m". In every macrolevel integration point of the structural mesh, the RVE microanalysis is performed. The macrolevel displacement gradients are transformed into the RVE boundary nodal displacements using corresponding boundary conditions. After solving the RVE boundary value problem, the stress, the double stress and the constitutive matrices are obtained by a homogenization procedure.

4.1 Small strain second-order computational homogenization

4.1.1 Macro-to-micro scale transition

In a small strain second-order computational homogenization scheme the RVE boundary displacement field is defined by Taylor series expansion as

$$\mathbf{u}_{\mathrm{m}} = \underline{\boldsymbol{\varepsilon}}_{\mathrm{M}} \cdot \mathbf{x} + \frac{1}{2}\left(\mathbf{x} \cdot {}^{3}\underline{\boldsymbol{\eta}}_{\mathrm{M}} \cdot \mathbf{x}\right) + \mathbf{r}\,. \tag{4.1}$$

In (4.1), $\mathbf{x}$ represents representative volume spatial coordinate, and $\mathbf{r}$ is microstructural fluctuation field, i.e., the microlevel contribution to the RVE displacement field. In homogenization, general principle which needs to be satisfied says that volume average of the variables at the lower scale must be equal to the variables at the coarse scale. To satisfy this rule, the volume average of the microstrain, derived from Eq. (4.1) is expressed as

$$\frac{1}{V}\int_{V}\left(\nabla_{\mathrm{m}} \otimes \mathbf{u}_{\mathrm{m}}\right)\mathrm{d}V = \frac{1}{V}\int_{V}\underline{\boldsymbol{\varepsilon}}_{\mathrm{m}}\,\mathrm{d}V = \underline{\boldsymbol{\varepsilon}}_{\mathrm{M}} + \frac{1}{V}\int_{V}\left({}^{3}\underline{\boldsymbol{\eta}}_{\mathrm{M}} \cdot \mathbf{x}\right)\mathrm{d}V + \frac{1}{V}\int_{V}\left(\nabla_{\mathrm{m}} \otimes \mathbf{r}\right)\mathrm{d}V\,, \tag{4.2}$$

where V represents the RVE volume. To satisfy the condition that the macrostrain is equal to the volume average of the microstrain, the second and third terms on the right-hand side of Eq. (4.2) should vanish. To eliminate the second integral, the coordinate system origin should be set into the centroid of RVE (first moment of area about the centroid equal to zero), as presented in Figure 4.1 for a 2D case. To enforce the mentioned equality, the third integral may be transformed by using divergence theorem and set to zero as

$$\frac{1}{V}\int_{V}\left(\nabla_{\mathrm{m}} \otimes \mathbf{r}\right)\mathrm{d}V = \frac{1}{V}\int_{\Gamma}\left(\mathbf{n} \otimes \mathbf{r}\right)\mathrm{d}\Gamma = \underline{\mathbf{0}}\,, \tag{4.3}$$

with Γ representing RVE boundary.

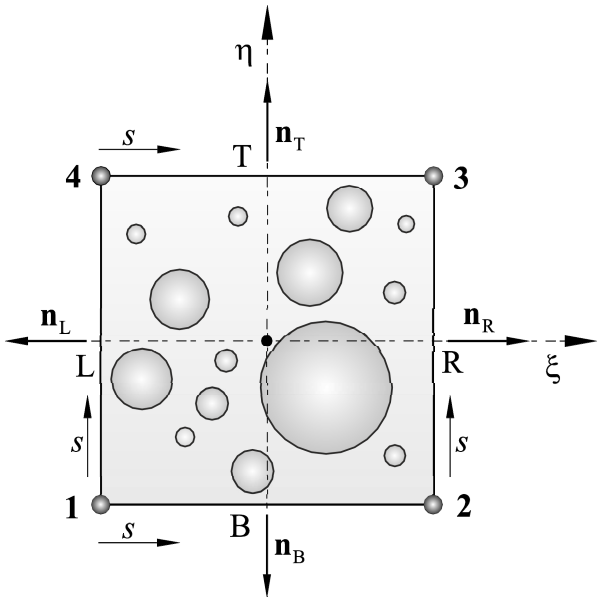

Figure 4.1 Representative volume element

In further derivation, volume average of the microlevel second-order strain should be related to the macrolevel second-order strain. But, preservation of C^0 continuous boundary value problem at the microlevel excludes higher-order variables appearing at the macroscale. In other words, microlevel second-order strain cannot be related to the macrolevel conjugate since it is not available in a standard continuum. To resolve this issue, in [27] alternative approach has been proposed where a second-order gradient on the C^0 continuous RVE is represented as the first moment of the first gradient in the way

$$ {}^3\underline{\boldsymbol{\eta}}_{\mathrm{m}} = \int_V \left(\underline{\boldsymbol{\varepsilon}}_{\mathrm{m}} \otimes \mathbf{x} + \mathbf{x} \otimes \underline{\boldsymbol{\varepsilon}}_{\mathrm{m}} \right) \mathrm{d}V \,. \tag{4.4} $$

The approach proposed in relation (4.4) has also been accepted in the later publications [18, 19, 30, 79]. Substitution of gradient of (4.1) into (4.4) allows to write

$$ \begin{aligned} \int_V \left(\underline{\boldsymbol{\varepsilon}}_{\mathrm{m}} \otimes \mathbf{x} + \mathbf{x} \otimes \underline{\boldsymbol{\varepsilon}}_{\mathrm{m}} \right) \mathrm{d}V = {}^3\underline{\boldsymbol{\eta}}_{\mathrm{M}} \cdot \left(\int_V \left(\mathbf{x} \otimes \mathbf{x} \right) \mathrm{d}V \right) + \int_V \left(\left(\nabla_{\mathrm{m}} \otimes \mathbf{r} \right) \otimes \mathbf{x} \right) \mathrm{d}V + \\ + \left(\int_V \left(\mathbf{x} \otimes \mathbf{x} \right) \mathrm{d}V \right) \cdot {}^3\underline{\boldsymbol{\eta}}_{\mathrm{M}} + \int_V \left(\mathbf{x} \otimes \left(\nabla_{\mathrm{m}} \otimes \mathbf{r} \right) \right) \mathrm{d}V . \end{aligned} \tag{4.5} $$

In Eq. (4.5) first member of a gradient expression of (4.1) has been left out of consideration using once again first moment of area about centroid. Furthermore, integral relations in parentheses are the second moment of area, $\underline{\mathbf{J}}$. Using the fact that in this thesis only square geometry of RVE is considered, second-moment of area for the RVE of side length L is

$$ \underline{\mathbf{J}} = \frac{L^4}{12} \otimes \underline{\mathbf{I}} \,. \tag{4.6} $$

In a multiscale setting it is usual that scale transition is performed over the RVE boundary Γ, thus, it is preferable to rearrange Eq. (4.5) to the terms defined only on the RVE boundary. The rearrangement can be done using mathematical manipulations

$$\left(\nabla_{\mathrm{m}} \otimes \mathbf{k}\right) \otimes \mathbf{x} = \nabla_{\mathrm{m}} \otimes \left(\mathbf{k} \otimes \mathbf{x}\right) - \left(\underline{\mathbf{I}} \otimes \mathbf{k}\right)^{RC}, \tag{4.7}$$

$$\mathbf{x} \otimes \left(\nabla_{\mathrm{m}} \otimes \mathbf{k}\right) = \left(\mathbf{x} \otimes \mathbf{k}\right) \otimes \nabla_{\mathrm{m}} - \left(\underline{\mathbf{I}} \otimes \mathbf{k}\right)^{RC}, \tag{4.8}$$

for arbitrary $\mathbf{k}$. In Eqs. (4.7) and (4.8) exponent *RC* represents right conjugation defined in Chapter 1.5.

Substitution of (4.7) and (4.8) into Eq. (4.5) gives

$$\begin{aligned}
&\int_V \left(\nabla_{\mathrm{m}} \otimes \left(\mathbf{u}_{\mathrm{m}} \otimes \mathbf{x}\right) - \left(\underline{\mathbf{I}} \otimes \mathbf{u}_{\mathrm{m}}\right)^{RC} + \left(\mathbf{x} \otimes \mathbf{u}_{\mathrm{m}}\right) \otimes \nabla_{\mathrm{m}} - \left(\underline{\mathbf{I}} \otimes \mathbf{u}_{\mathrm{m}}\right)^{RC}\right) \mathrm{d}V = \\
&{}^3\underline{\boldsymbol{\eta}}_{\mathrm{M}} \cdot \underline{\mathbf{J}} + \underline{\mathbf{J}} \cdot {}^3\underline{\boldsymbol{\eta}}_{\mathrm{M}} + \int_V \left(\nabla_{\mathrm{m}} \otimes \left(\mathbf{r} \otimes \mathbf{x}\right) - \left(\underline{\mathbf{I}} \otimes \mathbf{r}\right)^{RC}\right) \mathrm{d}V + \\
&+ \int_V \left(\left(\mathbf{x} \otimes \mathbf{r}\right) \otimes \nabla_{\mathrm{m}} - \left(\underline{\mathbf{I}} \otimes \mathbf{r}\right)^{RC}\right) \mathrm{d}V.
\end{aligned} \tag{4.9}$$

In further derivation Eq. (4.9) can be arranged in a more convenient way grouping similar variables

$$\begin{aligned}
&\int_V \left(\nabla_{\mathrm{m}} \otimes \left(\mathbf{u}_{\mathrm{m}} \otimes \mathbf{x}\right) + \left(\mathbf{x} \otimes \mathbf{u}_{\mathrm{m}}\right) \otimes \nabla_{\mathrm{m}} - 2\left(\underline{\mathbf{I}} \otimes \mathbf{u}_{\mathrm{m}}\right)^{RC}\right) \mathrm{d}V = \\
&{}^3\underline{\boldsymbol{\eta}}_{\mathrm{M}} \cdot \underline{\mathbf{J}} + \underline{\mathbf{J}} \cdot {}^3\underline{\boldsymbol{\eta}}_{\mathrm{M}} + \int_V \left(\nabla_{\mathrm{m}} \otimes \left(\mathbf{r} \otimes \mathbf{x}\right) + \left(\mathbf{x} \otimes \mathbf{r}\right) \otimes \nabla_{\mathrm{m}} - 2\left(\underline{\mathbf{I}} \otimes \mathbf{r}\right)^{RC}\right) \mathrm{d}V.
\end{aligned} \tag{4.10}$$

Application of divergence theorem to the volume integrals in (4.10) gives

$$\begin{aligned}
&\int_\Gamma \left(\mathbf{n} \otimes \left(\mathbf{u}_{\mathrm{m}} \otimes \mathbf{x}\right) + \left(\mathbf{x} \otimes \mathbf{u}_{\mathrm{m}}\right) \otimes \mathbf{n}\right) \mathrm{d}\Gamma - 2\int_V \left(\underline{\mathbf{I}} \otimes \mathbf{u}_{\mathrm{m}}\right)^{RC} \mathrm{d}V = \\
&{}^3\underline{\boldsymbol{\eta}}_{\mathrm{M}} \cdot \underline{\mathbf{J}} + \underline{\mathbf{J}} \cdot {}^3\underline{\boldsymbol{\eta}}_{\mathrm{M}} + \int_\Gamma \left(\mathbf{n} \otimes \left(\mathbf{r} \otimes \mathbf{x}\right) + \left(\mathbf{x} \otimes \mathbf{r}\right) \otimes \mathbf{n}\right) \mathrm{d}\Gamma - 2\int_V \left(\underline{\mathbf{I}} \otimes \mathbf{r}\right)^{RC} \mathrm{d}V.
\end{aligned} \tag{4.11}$$

Next, (4.11) can be rearranged more conveniently as

$$\begin{aligned}
{}^3\underline{\boldsymbol{\eta}}_{\mathrm{M}} \cdot \underline{\mathbf{J}} + \underline{\mathbf{J}} \cdot {}^3\underline{\boldsymbol{\eta}}_{\mathrm{M}} = &\int_\Gamma \left(\mathbf{n} \otimes \left(\mathbf{u}_{\mathrm{m}} \otimes \mathbf{x}\right) + \left(\mathbf{x} \otimes \mathbf{u}_{\mathrm{m}}\right) \otimes \mathbf{n}\right) \mathrm{d}\Gamma - \\
&- \int_\Gamma \left(\mathbf{n} \otimes \left(\mathbf{r} \otimes \mathbf{x}\right) + \left(\mathbf{x} \otimes \mathbf{r}\right) \otimes \mathbf{n}\right) \mathrm{d}\Gamma - \\
&- 2\int_V \left(\underline{\mathbf{I}} \otimes \mathbf{u}_{\mathrm{m}}\right)^{RC} \mathrm{d}V + 2\int_V \left(\underline{\mathbf{I}} \otimes \mathbf{r}\right)^{RC} \mathrm{d}V.
\end{aligned} \tag{4.12}$$

In orde to simplify form of Eq. (4.12), displacement term in the first volume integral on the right side can be expressed through (4.1)

$$2\int_V \left(\underline{\mathbf{I}} \otimes \mathbf{u}_{\mathrm{m}}\right)^{RC} \mathrm{d}V = 2\int_V \left(\underline{\mathbf{I}} \otimes \left(\underline{\boldsymbol{\varepsilon}}_{\mathrm{M}} \cdot \mathbf{x} + \frac{1}{2}\left(\mathbf{x} \cdot {}^3\underline{\boldsymbol{\eta}}_{\mathrm{M}} \cdot \mathbf{x}\right) + \mathbf{r}\right)\right)^{RC} \mathrm{d}V, \tag{4.13}$$

which is transformed into

$$2\int_V \left(\underline{\mathbf{I}}\otimes\mathbf{u}_{\mathrm{m}}\right)^{RC}\mathrm{d}V = 2\left[\underline{\mathbf{I}}\otimes\left(\int_V \mathbf{x}\,\mathrm{d}V\right)\cdot\underline{\boldsymbol{\varepsilon}}_{\mathrm{M}}\right]^{RC} + \\ + \left[\underline{\mathbf{I}}\otimes\left(\int_V (\mathbf{x}\otimes\mathbf{x})\mathrm{d}V\right) : {}^{3}\underline{\boldsymbol{\eta}}_{\mathrm{M}}^{RC}\right]^{RC} + 2\int_V \left(\underline{\mathbf{I}}\otimes\mathbf{r}\right)^{RC}\mathrm{d}V. \tag{4.14}$$

Once again, using definition of the first and second moment of area, Eq. (4.14) is simplified to

$$2\int_V \left(\underline{\mathbf{I}}\otimes\mathbf{u}_{\mathrm{m}}\right)^{RC}\mathrm{d}V = \left(\underline{\mathbf{I}}\otimes\underline{\mathbf{J}} : {}^{3}\underline{\boldsymbol{\eta}}_{\mathrm{M}}^{RC}\right)^{RC} + 2\int_V \left(\underline{\mathbf{I}}\otimes\mathbf{r}\right)^{RC}\mathrm{d}V\,. \tag{4.15}$$

Substitution of (4.15) into (4.12) yields the following relationship

$${}^{3}\underline{\boldsymbol{\eta}}_{\mathrm{M}}\cdot\underline{\mathbf{J}} + \underline{\mathbf{J}}\cdot{}^{3}\underline{\boldsymbol{\eta}}_{\mathrm{M}} = \int_\Gamma \left(\mathbf{n}\otimes\left(\mathbf{u}_{\mathrm{m}}\otimes\mathbf{x}\right) + \left(\mathbf{x}\otimes\mathbf{u}_{\mathrm{m}}\right)\otimes\mathbf{n}\right)\mathrm{d}\Gamma - \\ - \int_\Gamma \left(\mathbf{n}\otimes\left(\mathbf{r}\otimes\mathbf{x}\right) + \left(\mathbf{x}\otimes\mathbf{r}\right)\otimes\mathbf{n}\right)\mathrm{d}\Gamma - \left(\underline{\mathbf{I}}\otimes\underline{\mathbf{J}} : {}^{3}\underline{\boldsymbol{\eta}}_{\mathrm{M}}^{RC}\right)^{RC}, \tag{4.16}$$

which after rearrangement is given by

$${}^{3}\underline{\boldsymbol{\eta}}_{\mathrm{M}}\cdot\underline{\mathbf{J}} + \underline{\mathbf{J}}\cdot{}^{3}\underline{\boldsymbol{\eta}}_{\mathrm{M}} + \left(\underline{\mathbf{I}}\otimes\underline{\mathbf{J}} : {}^{3}\underline{\boldsymbol{\eta}}_{\mathrm{M}}^{RC}\right)^{RC} = \int_\Gamma \left(\mathbf{n}\otimes\left(\mathbf{u}_{\mathrm{m}}\otimes\mathbf{x}\right) + \left(\mathbf{x}\otimes\mathbf{u}_{\mathrm{m}}\right)\otimes\mathbf{n}\right)\mathrm{d}\Gamma - \\ - \int_\Gamma \left(\mathbf{n}\otimes\left(\mathbf{r}\otimes\mathbf{x}\right) + \left(\mathbf{x}\otimes\mathbf{r}\right)\otimes\mathbf{n}\right)\mathrm{d}\Gamma. \tag{4.17}$$

Finally, Eq. (4.6) should be inserted into (4.17), leaving a macrolevel second-order gradient on the left side of the equation, defined only by the microlevel terms integrated over the RVE boundary. Hence, Eq. (4.17) is defined as

$$\frac{L^4}{12}{}^{3}\underline{\boldsymbol{\eta}}_{\mathrm{M}} + \frac{L^4}{12}{}^{3}\underline{\boldsymbol{\eta}}_{\mathrm{M}} + \frac{L^4}{12}\left(\underline{\mathbf{I}}\otimes\underline{\mathbf{I}} : {}^{3}\underline{\boldsymbol{\eta}}_{\mathrm{M}}^{RC}\right)^{RC} = \int_\Gamma \left(\mathbf{n}\otimes\left(\mathbf{u}_{\mathrm{m}}\otimes\mathbf{x}\right) + \left(\mathbf{x}\otimes\mathbf{u}_{\mathrm{m}}\right)\otimes\mathbf{n}\right)\mathrm{d}\Gamma - \\ - \int_\Gamma \left(\mathbf{n}\otimes\left(\mathbf{r}\otimes\mathbf{x}\right) + \left(\mathbf{x}\otimes\mathbf{r}\right)\otimes\mathbf{n}\right)\mathrm{d}\Gamma. \tag{4.18}$$

Multiplying Eq. (4.18) by inverse of second moment of area $\frac{12}{L^4}$ allows to write

$$2\,{}^{3}\underline{\boldsymbol{\eta}}_{\mathrm{M}} + \left(\underline{\mathbf{I}}\otimes\underline{\mathbf{I}} : {}^{3}\underline{\boldsymbol{\eta}}_{\mathrm{M}}^{RC}\right)^{RC} = \frac{12}{L^4}\left[\int_\Gamma \left(\mathbf{n}\otimes\left(\mathbf{u}_{\mathrm{m}}\otimes\mathbf{x}\right) + \left(\mathbf{x}\otimes\mathbf{u}_{\mathrm{m}}\right)\otimes\mathbf{n}\right)\mathrm{d}\Gamma - \right. \\ \left. - \int_\Gamma \left(\mathbf{n}\otimes\left(\mathbf{r}\otimes\mathbf{x}\right) + \left(\mathbf{x}\otimes\mathbf{r}\right)\otimes\mathbf{n}\right)\mathrm{d}\Gamma\right]. \tag{4.19}$$

Relation (4.19) should be satisfied regardless to the particular microfluctuation field $\mathbf{r}$ giving constraint equation

$$\int_\Gamma \left(\mathbf{n}\otimes\left(\mathbf{r}\otimes\mathbf{x}\right) + \left(\mathbf{x}\otimes\mathbf{r}\right)\otimes\mathbf{n}\right)\mathrm{d}\Gamma = {}^{3}\underline{\mathbf{0}}\,. \tag{4.20}$$

Any RVE boundary conditions used must explicitly satisfy relations (4.3) and (4.20). In this thesis displacement boundary conditions and generalized periodic boundary conditions will be used. Derivation of the boundary conditions used on the RVE will be discussed later. The displacement boundary conditions obey an assumption that $\mathbf{r} = \mathbf{0}, \forall \mathbf{x} \in \Gamma$, which yields automatic satisfaction of the two aforementioned constraints. The generalized periodic boundary conditions assume identical microfluctuation field on the opposite RVE sides, as defined in Figure 4.1, resulting in

$$\mathbf{r}_{\mathrm{R}}(s) = \mathbf{r}_{\mathrm{L}}(s), \tag{4.21}$$

$$\mathbf{r}_{\mathrm{T}}(s) = \mathbf{r}_{\mathrm{B}}(s), \tag{4.22}$$

where *s* is a local coordinate along the edge and the subscripts L, R, T and B stand for the left, right, top and bottom boundaries of the RVE. From Eqs. (4.21) and (4.22), it is obvious that relation (4.3) is satisfied [8], considering $\mathbf{n}_{\mathrm{L}}(s) = -\mathbf{n}_{\mathrm{R}}(s)$ and $\mathbf{n}_{\mathrm{T}}(s) = -\mathbf{n}_{\mathrm{B}}(s)$. Relation (4.20) must be prescribed on two RVE edges only, due to periodicity (4.21) and (4.22). Consequently, Eq. (4.20) can be simplified to

$$\int_{\Gamma_{\mathrm{L}}} \mathbf{r}_{\mathrm{L}} \, \mathrm{d}\Gamma = \mathbf{0}, \tag{4.23}$$

$$\int_{\Gamma_{\mathrm{B}}} \mathbf{r}_{\mathrm{B}} \, \mathrm{d}\Gamma = \mathbf{0}. \tag{4.24}$$

After substitution of microfluctuations for the left and bottom edge of the RVE defined on the basis of (4.1) into (4.23) and (4.24), the following expressions are obtained

$$\int_{\Gamma_{\mathrm{L}}} \mathbf{u}_{\mathrm{L}} \, \mathrm{d}\Gamma = \underline{\boldsymbol{\varepsilon}}_{\mathrm{M}} \cdot \int_{\Gamma_{\mathrm{L}}} \mathbf{x}_{\mathrm{L}} \, \mathrm{d}\Gamma + \frac{1}{2} {}^{3}\underline{\boldsymbol{\eta}}_{\mathrm{M}} : \int_{\Gamma_{\mathrm{L}}} (\mathbf{x}_{\mathrm{L}} \otimes \mathbf{x}_{\mathrm{L}}) \, \mathrm{d}\Gamma, \tag{4.25}$$

$$\int_{\Gamma_{\mathrm{B}}} \mathbf{u}_{\mathrm{B}} \, \mathrm{d}\Gamma = \underline{\boldsymbol{\varepsilon}}_{\mathrm{M}} \cdot \int_{\Gamma_{\mathrm{B}}} \mathbf{x}_{\mathrm{B}} \, \mathrm{d}\Gamma + \frac{1}{2} {}^{3}\underline{\boldsymbol{\eta}}_{\mathrm{M}} : \int_{\Gamma_{\mathrm{B}}} (\mathbf{x}_{\mathrm{B}} \otimes \mathbf{x}_{\mathrm{B}}) \, \mathrm{d}\Gamma. \tag{4.26}$$

Numerical implementation of constraints (4.25) and (4.26) will be discussed in a subsequent sections.

4.1.2 Boundary conditions on microstructural level

As generally known, boundary conditions on microstructural level are used for transformation of the displacements gradients at a macrolevel material point into nodal degrees of freedom on the RVE boundaries. In second-order homogenization scheme considered in this research and for a small strain assumption used in this section, $\underline{\boldsymbol{\varepsilon}}_{\mathrm{M}}$ and ${}^{3}\underline{\boldsymbol{\eta}}_{\mathrm{M}}$ at a macrolevel material

point are transformed by means of boundary conditions into nodal displacement in x_1 and x_2 direction on the RVE boundaries. From the literature review [7, 53, 146, 147] it has been recognized that displacement- and periodicity boundary conditions give reasonable homogenized results for a heterogeneous materials. More precisely, periodic boundary conditions have been proven as the most versatile, giving the best homogenized results and the most realistic RVE deformation response [7, 53].

Values prescribed to the boundary nodes are dependent on the nodal position, which is expressed by a coordinate matrix. For every macrolevel displacement gradient coordinate matrix is required to transform macrogradients into RVE boundary displacements, which means that two coordinate matrices should be derived. For derivation of the coordinate matrices displacements of an *i*th node are expanded into components depending on macroscale gradients (3.5) and (3.6) according to (4.1)

$$\begin{aligned}\left(u_1\right)_i = &\left(u_{1,1}\right)_{\mathrm{M}}\left(x_1\right)_i + \frac{1}{2}\left(u_{1,2}+u_{2,1}\right)_{\mathrm{M}}\left(x_2\right)_i + \frac{1}{2}\left(u_{1,11}\right)_{\mathrm{M}}\left(x_1^2\right)_i + \\ &+\frac{1}{2}\left(u_{1,21}\right)_{\mathrm{M}}\left(x_1x_2\right)_i + \frac{1}{2}\left(u_{1,22}\right)_{\mathrm{M}}\left(x_2^2\right)_i,\end{aligned} \tag{4.27}$$

$$\begin{aligned}\left(u_2\right)_i = &\frac{1}{2}\left(u_{1,2}+u_{2,1}\right)_{\mathrm{M}}\left(x_1\right)_i + \left(u_{2,2}\right)_{\mathrm{M}}\left(x_2\right)_i + \frac{1}{2}\left(u_{2,11}\right)_{\mathrm{M}}\left(x_1^2\right)_i + \\ &+\frac{1}{2}\left(u_{2,12}\right)_{\mathrm{M}}\left(x_1x_2\right)_i + \frac{1}{2}\left(u_{2,22}\right)_{\mathrm{M}}\left(x_2^2\right)_i.\end{aligned} \tag{4.28}$$

It can be noticed that in (4.27) and (4.28) microfluctuation field is supressed. Dealing with microfluctuation field constitutes a major distinction between displacement and generalized periodic boundary conditions. Relations (4.27) and (4.28) can be transformed into a matrix form as

$$\begin{aligned}\underline{\mathrm{u}}_i = \begin{pmatrix}u_1\\u_2\end{pmatrix}_i &= \frac{1}{2}\begin{pmatrix}2x_1 & 0 & x_2\\ 0 & 2x_2 & x_1\end{pmatrix}_i \underline{\varepsilon}_{\mathrm{M}} + \\ &+\frac{1}{4}\begin{pmatrix}2x_1^2 & 0 & 2x_2^2 & 0 & x_1x_2 & 0\\ 0 & 2x_2^2 & 0 & 2x_1^2 & 0 & x_1x_2\end{pmatrix}_i \underline{\eta}_{\mathrm{M}}.\end{aligned} \tag{4.29}$$

From (4.29) coordinate matrices of an *i*th node can be extracted in the form

$$\underline{\underline{\mathrm{D}}}_i = \frac{1}{2}\begin{pmatrix}2x_1 & 0 & x_2\\ 0 & 2x_2 & x_1\end{pmatrix}^T, \tag{4.30}$$

$$\underline{\underline{\mathrm{H}}}_i = \frac{1}{4}\begin{pmatrix}2x_1^2 & 0 & 2x_2^2 & 0 & x_1x_2 & 0\\ 0 & 2x_2^2 & 0 & 2x_1^2 & 0 & x_1x_2\end{pmatrix}^T, \tag{4.31}$$

as introduced in [79]. Introducing coordinate matrices (4.30) and (4.31), the displacements of a single node on the RVE boundary are represented by

$$\underline{\mathrm{u}}_i = \underline{\underline{\mathrm{D}}}_i^T \underline{\varepsilon}_\mathrm{M} + \underline{\underline{\mathrm{H}}}_i^T \underline{\eta}_\mathrm{M} . \tag{4.32}$$

To suppress rigid body movements of RVE, corner node 1 shown in Figure 4.1 can be fixed. In that case all prescribed displacements are defined relatively to the node 1. This can be done by subtraction of coordinate matrices of node 1 from all remaining coordinate matrices of the nodes whose displacements are being prescribed. Thus, Eq. (4.32) is defined as

$$\underline{\mathrm{u}}_i = \left(\underline{\underline{\mathrm{D}}}_i^T - \underline{\underline{\mathrm{D}}}_1\right)\underline{\varepsilon}_\mathrm{M} + \left(\underline{\underline{\mathrm{H}}}_i^T - \underline{\underline{\mathrm{H}}}_1\right)\underline{\eta}_\mathrm{M} . \tag{4.33}$$

In the case of displacement boundary conditions (4.33) is extended onto all RVE boundary nodes giving

$$\underline{\mathrm{u}}_\mathrm{b} = \underline{\underline{\mathrm{D}}}^T \underline{\varepsilon}_\mathrm{M} + \underline{\underline{\mathrm{H}}}^T \underline{\eta}_\mathrm{M} . \tag{4.34}$$

In Eq. (4.34) coordinate matrices are assembled in the way

$$\underline{\underline{\mathrm{D}}}^T = \left(\underline{\underline{\mathrm{D}}}_1^T \quad \underline{\underline{\mathrm{D}}}_2^T \quad \cdots \quad \underline{\underline{\mathrm{D}}}_n^T\right), \tag{4.35}$$

$$\underline{\underline{\mathrm{H}}}^T = \left(\underline{\underline{\mathrm{H}}}_1^T \quad \underline{\underline{\mathrm{H}}}_2^T \quad \cdots \quad \underline{\underline{\mathrm{H}}}_n^T\right), \tag{4.36}$$

with n as a number of boundary nodes. In coordinate matrix assemblies (4.35) and (4.36) rigid body motions are accounted for.

As already mentioned, in relation (4.34) microfluctuations have been supressed on all boundary nodes. This is the main reason that displacement boundary conditions provide stiffer RVE behaviour compared to the generalized periodic boundary conditions, which are derived below. When using generalized periodic boundary conditions, according to Figure 4.1 only corner nodal displacements are prescribed, with account of rigid body motions elimination. Hence, we can write

$$\underline{\mathrm{u}}_i = \underline{\underline{\mathrm{D}}}_i^T \underline{\varepsilon}_\mathrm{M} + \underline{\underline{\mathrm{H}}}_i^T \underline{\eta}_\mathrm{M}, \ i = 2,3,4 . \tag{4.37}$$

The remaining boundary nodes have a related degrees of freedom according to periodicity assumptions (4.21) and (4.22). Basically, the pairs of nodes on opposite sides of RVE $\left(\mathrm{R} \leftrightarrow \mathrm{L}, \mathrm{T} \leftrightarrow \mathrm{B}\right)$ need to be defined. This implicates regular nodal distribution on the opposite sides of RVE, which in practical sense can aggravate discretization of highly irregular microstructures. There is also an approach of prescribing periodicity conditions on irregular meshes by application of polynomial interpolation [22]. To impose periodicity of microfluctuations on the RVE boundaries periodicity equations need to be derived. Firstly,

microfluctuations of every RVE edge are expressed by means of Eqs. (4.1) and (4.32) in matrix form as

$$\underline{r}_R = \underline{u}_R - \underline{\underline{D}}_R^T \underline{\varepsilon}_M - \underline{\underline{H}}_R^T \underline{\eta}_M , \tag{4.38}$$

$$\underline{r}_L = \underline{u}_L - \underline{\underline{D}}_L^T \underline{\varepsilon}_M - \underline{\underline{H}}_L^T \underline{\eta}_M , \tag{4.39}$$

$$\underline{r}_T = \underline{u}_T - \underline{\underline{D}}_T^T \underline{\varepsilon}_M - \underline{\underline{H}}_T^T \underline{\eta}_M , \tag{4.40}$$

$$\underline{r}_B = \underline{u}_B - \underline{\underline{D}}_B^T \underline{\varepsilon}_M - \underline{\underline{H}}_B^T \underline{\eta}_M . \tag{4.41}$$

Substituting (4.38)-(4.41) into (4.21) and (4.22) the following relations are obtained

$$\underline{u}_R - \underline{\underline{D}}_R^T \underline{\varepsilon}_M - \underline{\underline{H}}_R^T \underline{\eta}_M = \underline{u}_L - \underline{\underline{D}}_L^T \underline{\varepsilon}_M - \underline{\underline{H}}_L^T \underline{\eta}_M , \tag{4.42}$$

$$\underline{u}_T - \underline{\underline{D}}_T^T \underline{\varepsilon}_M - \underline{\underline{H}}_T^T \underline{\eta}_M = \underline{u}_B - \underline{\underline{D}}_B^T \underline{\varepsilon}_M - \underline{\underline{H}}_B^T \underline{\eta}_M . \tag{4.43}$$

After straightforward manipulations periodicity equations (4.42) and (4.43) are finally defined as

$$\underline{u}_R - \underline{u}_L = \left(\underline{\underline{D}}_R^T - \underline{\underline{D}}_L^T \right) \underline{\varepsilon}_M + \left(\underline{\underline{H}}_R^T - \underline{\underline{H}}_L^T \right) \underline{\eta}_M , \tag{4.44}$$

$$\underline{u}_T - \underline{u}_B = \left(\underline{\underline{D}}_T^T - \underline{\underline{D}}_B^T \right) \underline{\varepsilon}_M + \left(\underline{\underline{H}}_T^T - \underline{\underline{H}}_B^T \right) \underline{\eta}_M . \tag{4.45}$$

On the basis of (4.44) and (4.45) it is clear that in generalized periodic boundary conditions boundary nodes do not have explicitly prescribed values of displacements, but rather relative ratio of displacements on opposite edges, with exception of the corner nodes. The fact that only relative RVE response is determined gives an additional compliance to the RVE behaviour. Accordingly, homogenized results are also more compliant and realistic in comparison to displacement boundary conditions where microfluctuation field is supressed on the RVE boundaries by explicit prescribing of nodal values. It is known that imposition of equation constraints within the finite element framework introduces dependent degrees of freedom in the numerical model. Generally, the choice of dependent and independent variables is free. In Eqs. (4.44) and (4.45) nodal displacements of two RVE edges must be also treated as dependent and eliminated from global RVE system of equations. The choice of dependent and independent nodes in this case is not completely mandatory, because nodal displacements of two RVE edges are bounded by integral relations (4.25) and (4.26). In this thesis left and bottom edge will be bounded by the microfluctuation integral relations, which with introduction of coordinate matrices are defined as

$$\int_{\Gamma_L} \underline{u}_L \, d\Gamma = \left(\int_{\Gamma_L} D_L^T \, d\Gamma \right) \underline{\varepsilon}_M + \left(\int_{\Gamma_L} \underline{\underline{H}}_L^T \, d\Gamma \right) \underline{\eta}_M , \tag{4.46}$$

$$\int_{\Gamma_B} \underline{u}_B \, d\Gamma = \left(\int_{\Gamma_B} D_B^T \, d\Gamma \right) \underline{\varepsilon}_M + \left(\int_{\Gamma_B} \underline{\underline{H}}_B^T \, d\Gamma \right) \underline{\eta}_M . \tag{4.47}$$

After that, it is obvious that in periodicity equations only right and top edge can be treated as dependent.

4.1.3 Micro-to-macro scale transition

After solving RVE boundary value problem homogenization of the stress tensors and calculation of the constitutive matrices is performed. In homogenization of stress inconsistency is expected, since C^0 continuity is preserved on the microstructural level. Due to continuity degradation double stress appearing at the macrolevel does not exist as a solution variable in RVE boundary value problem. However, it will be shown that macrolevel double stress can be homogenized, but not as a true volume average of its microconjugate. The starting point for stress homogenization is Hill-Mandel energy condition, which says that volume average of the work variation done on the RVE must be equal to the work variation at the macrostructural material point. Mathematically speaking this is elaborated as

$$\frac{1}{V} \int_V \delta W_m \, dV = \delta W_M , \tag{4.48}$$

which is decomposed as

$$\frac{1}{V} \int_V \left(\underline{\boldsymbol{\sigma}}_m : \delta \underline{\boldsymbol{\varepsilon}}_m \right) dV = \underline{\boldsymbol{\sigma}}_M : \delta \underline{\boldsymbol{\varepsilon}}_M + {}^3\underline{\boldsymbol{\mu}}_M \vdots \delta^3 \underline{\boldsymbol{\eta}}_M . \tag{4.49}$$

Furthermore, for the variation of the work done at the microlevel we can write

$$\frac{1}{V} \int_V \delta W_m \, dV = \frac{1}{V} \int_V \left(\underline{\boldsymbol{\sigma}}_m : \left(\nabla_m \otimes \delta \mathbf{u}_m \right) \right) dV = \frac{1}{V} \int_\Gamma \left(\mathbf{n} \cdot \underline{\boldsymbol{\sigma}}_m \cdot \delta \mathbf{u}_m \right) d\Gamma = \frac{1}{V} \int_\Gamma \left(\mathbf{t} \cdot \delta \mathbf{u}_m \right) d\Gamma . \tag{4.50}$$

After that, in the last boundary integral of (4.50) variation of displacement field (4.1) on the RVE boundaries can be inserted

$$\frac{1}{V} \int_V \delta W_m \, dV = \frac{1}{V} \int_\Gamma \left(\mathbf{t} \cdot \left(\delta \underline{\boldsymbol{\varepsilon}}_M \cdot \mathbf{x} + \frac{1}{2} \left(\mathbf{x} \cdot \delta^3 \underline{\boldsymbol{\eta}}_M \cdot \mathbf{x} \right) + \delta \mathbf{r} \right) \right) d\Gamma , \tag{4.51}$$

which can be arranged into

$$\begin{aligned} \frac{1}{V} \int_V \delta W_m \, dV = & \left(\frac{1}{V} \int_\Gamma \left(\mathbf{t} \otimes \mathbf{x} \right) d\Gamma \right) : \delta \underline{\boldsymbol{\varepsilon}}_M + \left(\frac{1}{2V} \int_\Gamma \left(\mathbf{x} \otimes \mathbf{t} \otimes \mathbf{x} \right) d\Gamma \right) \vdots \delta^3 \underline{\boldsymbol{\eta}}_M + \\ & + \frac{1}{V} \int_\Gamma \left(\mathbf{t} \cdot \delta \mathbf{r} \right) d\Gamma . \end{aligned} \tag{4.52}$$

Comparing relation (4.52) to (4.49), it can be easily seen following equalities are valid

$$\underline{\boldsymbol{\sigma}}_{\mathrm{M}} = \frac{1}{V}\int_{\Gamma}\left(\mathbf{t}\otimes\mathbf{x}\right)\mathrm{d}\Gamma\,, \tag{4.53}$$

$$^{3}\underline{\boldsymbol{\mu}}_{\mathrm{M}} = \frac{1}{2V}\int_{\Gamma}\left(\mathbf{x}\otimes\mathbf{t}\otimes\mathbf{x}\right)\mathrm{d}\Gamma \tag{4.54}$$

and

$$\frac{1}{V}\int_{\Gamma}\left(\mathbf{t}\cdot\delta\mathbf{r}\right)\mathrm{d}\Gamma = 0\,. \tag{4.55}$$

Integral condition (4.55) must be proven before exploiting (4.53) and (4.54). In the case of displacement boundary conditions $\mathbf{r}=\mathbf{0},\forall\mathbf{x}\in\Gamma$ which clearly satisfies (4.55). For generalized periodic boundary conditions microfluctuation of the corner nodes are supressed (4.37). With account of integrals (4.23) and (4.24), as well as periodicity (4.21) and (4.22), integral condition (4.55) is again confirmed.

In the limit case, the infinitesimal force $\mathbf{t}\mathrm{d}\Gamma$ in (4.53) and (4.54) may be represented as RVE boundary nodal force of an *i*th node, $\underline{\mathrm{f}}_{\mathrm{b}}^{i}$ [7]. Accordingly, homogenized stress tensors integrated over RVE boundary can be defined as a matrix product of the coordinate matrices and nodal forces over RVE boundary

$$\underline{\sigma}_{\mathrm{M}} = \frac{1}{V}\underline{\underline{\mathrm{D}}}\,\underline{\mathrm{f}}_{\mathrm{b}}\,, \tag{4.56}$$

$$\underline{\mu}_{\mathrm{M}} = \frac{1}{V}\underline{\underline{\mathrm{H}}}\,\underline{\mathrm{f}}_{\mathrm{b}}\,. \tag{4.57}$$

As a matter of convenience, homogenized stress tensors can be derived as volume integrals over RVE. For Cauchy stress tensor this means that

$$\underline{\boldsymbol{\sigma}}_{\mathrm{M}} = \frac{1}{V}\int_{V}\underline{\boldsymbol{\sigma}}_{\mathrm{m}}\,\mathrm{d}V\,. \tag{4.58}$$

To confirm Eq. (4.58), the microlevel Cauchy stress tensor can be written as

$$\underline{\boldsymbol{\sigma}}_{\mathrm{m}} = \left(\nabla_{\mathrm{m}}\cdot\underline{\boldsymbol{\sigma}}_{\mathrm{m}}\right)\otimes\mathbf{x} + \underline{\boldsymbol{\sigma}}_{\mathrm{m}}\cdot\left(\nabla_{\mathrm{m}}\otimes\mathbf{x}\right) = \nabla_{\mathrm{m}}\cdot\left(\underline{\boldsymbol{\sigma}}_{\mathrm{m}}\otimes\mathbf{x}\right). \tag{4.59}$$

Since homogenization is performed after finding RVE equilibrium, well-known static equilibrium equation holds $\nabla_{\mathrm{m}}\cdot\underline{\boldsymbol{\sigma}}_{\mathrm{m}}=\mathbf{0}$, as well as $\nabla_{\mathrm{m}}\otimes\mathbf{x}=\underline{\mathbf{I}}$. Inserting (4.59) into (4.58) we obtain

$$\underline{\boldsymbol{\sigma}}_{\mathrm{M}} = \frac{1}{V}\int_{V}\left(\nabla_{\mathrm{m}}\cdot\left(\underline{\boldsymbol{\sigma}}_{\mathrm{m}}\otimes\mathbf{x}\right)\right)\mathrm{d}V = \frac{1}{V}\int_{\Gamma}\left(\mathbf{n}\cdot\underline{\boldsymbol{\sigma}}_{\mathrm{m}}\otimes\mathbf{x}\right)\mathrm{d}\Gamma = \frac{1}{V}\int_{\Gamma}\left(\mathbf{t}\otimes\mathbf{x}\right)\mathrm{d}\Gamma\,, \tag{4.60}$$

which confirms (4.53). Volume integral for double stress can be found using divergence theorem on Eq. (4.54)

$$ {}^{3}\underline{\boldsymbol{\mu}}_{\mathrm{M}} = \frac{1}{2V}\int_{\Gamma}\left(\mathbf{x}\otimes\mathbf{t}\otimes\mathbf{x}\right)\mathrm{d}\Gamma = \frac{1}{2V}\int_{\Gamma}\left(\mathbf{x}\otimes\left(\mathbf{n}\cdot\underline{\boldsymbol{\sigma}}\right)\otimes\mathbf{x}\right)\mathrm{d}\Gamma = \frac{1}{2V}\int_{V}\left(\nabla_{\mathrm{m}}\cdot\left(\mathbf{x}\otimes\underline{\boldsymbol{\sigma}}\otimes\mathbf{x}\right)\right)\mathrm{d}V\,. \tag{4.61} $$

Subintegral term of (4.61) can be extended to

$$ \nabla_{\mathrm{m}}\cdot\left(\mathbf{x}\otimes\underline{\boldsymbol{\sigma}}\otimes\mathbf{x}\right) = \mathbf{x}\otimes\left(\nabla_{\mathrm{m}}\cdot\underline{\boldsymbol{\sigma}}\right)\otimes\mathbf{x} + \left(\nabla_{\mathrm{m}}\otimes\mathbf{x}\right)\cdot\underline{\boldsymbol{\sigma}}\otimes\mathbf{x} + \mathbf{x}\otimes\underline{\boldsymbol{\sigma}}\cdot\left(\nabla_{\mathrm{m}}\otimes\mathbf{x}\right). \tag{4.62} $$

Substituting relation (4.62) into (4.61) double stress is expressed as

$$ {}^{3}\underline{\boldsymbol{\mu}}_{\mathrm{M}} = \frac{1}{2V}\int_{V}\left(\underline{\boldsymbol{\sigma}}_{\mathrm{m}}\otimes\mathbf{x} + \mathbf{x}\otimes\underline{\boldsymbol{\sigma}}_{\mathrm{m}}\right)\mathrm{d}V\,. \tag{4.63} $$

It can be concluded that higher-order stress in a classical continuum is physically interpreted as a first moment of Cauchy stress tensor, analogously to definition used for a second-order strain (4.4). To complete scale transition procedure, macroscopic constitutive matrices need to be derived. Variations of stress tensors at the macrolevel written in the matrix form are

$$ \delta\underline{\sigma}_{\mathrm{M}} = \frac{1}{V}\underline{\underline{\mathrm{D}}}\left(\delta\underline{\mathrm{f}}_{\mathrm{b}}\right), \tag{4.64} $$

$$ \delta\underline{\mu}_{\mathrm{M}} = \frac{1}{V}\underline{\underline{\mathrm{H}}}\left(\delta\underline{\mathrm{f}}_{\mathrm{b}}\right). \tag{4.65} $$

Next, variation of RVE boundary nodal force $\delta\underline{\mathrm{f}}_{\mathrm{b}}$ can be extracted from global RVE system of equations, $\underline{\underline{\mathrm{K}}}\underline{\mathrm{u}} = \underline{\mathrm{f}}$. By means of the topological projection matrices $\underline{\underline{\mathrm{P}}}_{\mathrm{a}}$ and $\underline{\underline{\mathrm{P}}}_{\mathrm{b}}$, denoting internal and boundary contributions, respectively, finite element equation can be subdivided into submatrices

$$ \underline{\underline{\mathrm{K}}} = \begin{pmatrix} \underline{\underline{\mathrm{K}}}_{\mathrm{aa}} & \underline{\underline{\mathrm{K}}}_{\mathrm{ab}} \\ \underline{\underline{\mathrm{K}}}_{\mathrm{ba}} & \underline{\underline{\mathrm{K}}}_{\mathrm{bb}} \end{pmatrix} = \begin{pmatrix} \underline{\underline{\mathrm{P}}}_{\mathrm{a}}\underline{\underline{\mathrm{K}}}\,\underline{\underline{\mathrm{P}}}_{\mathrm{a}}^{T} & \underline{\underline{\mathrm{P}}}_{\mathrm{a}}\underline{\underline{\mathrm{K}}}\,\underline{\underline{\mathrm{P}}}_{\mathrm{b}}^{T} \\ \underline{\underline{\mathrm{P}}}_{\mathrm{b}}\underline{\underline{\mathrm{K}}}\,\underline{\underline{\mathrm{P}}}_{\mathrm{a}}^{T} & \underline{\underline{\mathrm{P}}}_{\mathrm{b}}\underline{\underline{\mathrm{K}}}\,\underline{\underline{\mathrm{P}}}_{\mathrm{b}}^{T} \end{pmatrix}, \tag{4.66} $$

$$ \underline{\mathrm{u}} = \begin{pmatrix} \underline{\mathrm{u}}_{\mathrm{a}} \\ \underline{\mathrm{u}}_{\mathrm{b}} \end{pmatrix} = \begin{pmatrix} \underline{\underline{\mathrm{P}}}_{\mathrm{a}}\underline{\mathrm{u}} \\ \underline{\underline{\mathrm{P}}}_{\mathrm{b}}\underline{\mathrm{u}} \end{pmatrix}, \tag{4.67} $$

$$ \underline{\mathrm{f}} = \begin{pmatrix} \underline{\mathrm{f}}_{\mathrm{a}} \\ \underline{\mathrm{f}}_{\mathrm{b}} \end{pmatrix} = \begin{pmatrix} \underline{\underline{\mathrm{P}}}_{\mathrm{a}}\underline{\mathrm{f}} \\ \underline{\underline{\mathrm{P}}}_{\mathrm{b}}\underline{\mathrm{f}} \end{pmatrix}. \tag{4.68} $$

For a nonlinear problems variation of finite element equation partitioned by (4.66)-(4.68) is

$$ \begin{pmatrix} \underline{\underline{\mathrm{K}}}_{\mathrm{aa}} & \underline{\underline{\mathrm{K}}}_{\mathrm{ab}} \\ \underline{\underline{\mathrm{K}}}_{\mathrm{ba}} & \underline{\underline{\mathrm{K}}}_{\mathrm{bb}} \end{pmatrix} \begin{pmatrix} \delta\underline{\mathrm{u}}_{\mathrm{a}} \\ \delta\underline{\mathrm{u}}_{\mathrm{b}} \end{pmatrix} = \begin{pmatrix} \delta\underline{\mathrm{f}}_{\mathrm{a}} \\ \delta\underline{\mathrm{f}}_{\mathrm{b}} \end{pmatrix}. \tag{4.69} $$

Once RVE equilibrium is reached, $\delta\underline{\mathrm{u}}_{\mathrm{a}} = \underline{0}$. Inserting this in Eq. (4.69), finite element equation is transformed to

$$ \delta\underline{\mathrm{f}}_{\mathrm{b}} = \underline{\underline{\tilde{\mathrm{K}}}}_{\mathrm{bb}}\delta\underline{\mathrm{u}}_{\mathrm{b}}\,. \tag{4.70} $$

In (4.70), $\underline{\underline{\tilde{K}}}_{bb}$ represents condensed RVE stiffness matrix, where stiffness is described by the contributions of external nodes only. It is written in the form

$$\underline{\underline{\tilde{K}}}_{bb} = \underline{\underline{K}}_{bb} - \underline{\underline{K}}_{ba}\underline{\underline{K}}_{aa}^{-1}\underline{\underline{K}}_{ab}. \tag{4.71}$$

Now variation of the external nodal forces (4.70) can be substituted into variations of stresses (4.64) and (4.65) giving

$$\delta\underline{\sigma}_M = \frac{1}{V}\underline{\underline{D}}\underline{\underline{\tilde{K}}}_{bb}\delta\underline{u}_b, \tag{4.72}$$

$$\delta\underline{\mu}_M = \frac{1}{V}\underline{\underline{H}}\underline{\underline{\tilde{K}}}_{bb}\delta\underline{u}_b. \tag{4.73}$$

In the end, variation of boundary displacements $\delta\underline{u}_b$ can be found in (4.34). By this, we can write

$$\delta\underline{\sigma}_M = \frac{1}{V}\underline{\underline{D}}\underline{\underline{\tilde{K}}}_{bb}\left(\underline{\underline{D}}^T\left(\delta\underline{\varepsilon}_M\right) + \underline{\underline{H}}^T\left(\delta\underline{\eta}_M\right)\right), \tag{4.74}$$

$$\delta\underline{\mu}_M = \frac{1}{V}\underline{\underline{H}}\underline{\underline{\tilde{K}}}_{bb}\left(\underline{\underline{D}}^T\left(\delta\underline{\varepsilon}_M\right) + \underline{\underline{H}}^T\left(\delta\underline{\eta}_M\right)\right). \tag{4.75}$$

Comparing (4.74) and (4.75) to a linearized incremental constitutive relations (3.14) and (3.15), macroscopic constitutive material matrices can be easily extracted in the following form

$$\underline{\underline{C}}_{\sigma\varepsilon} = \frac{1}{V}\underline{\underline{D}}\underline{\underline{\tilde{K}}}_{bb}\underline{\underline{D}}^T, \tag{4.76}$$

$$\underline{\underline{C}}_{\sigma\eta} = \frac{1}{V}\underline{\underline{D}}\underline{\underline{\tilde{K}}}_{bb}\underline{\underline{H}}^T, \tag{4.77}$$

$$\underline{\underline{C}}_{\mu\varepsilon} = \frac{1}{V}\underline{\underline{H}}\underline{\underline{\tilde{K}}}_{bb}\underline{\underline{D}}^T, \tag{4.78}$$

$$\underline{\underline{C}}_{\mu\eta} = \frac{1}{V}\underline{\underline{H}}\underline{\underline{\tilde{K}}}_{bb}\underline{\underline{H}}^T. \tag{4.79}$$

4.1.4 Numerical implementation

The above described micro-macro scheme has been implemented into the FE program ABAQUS/Standard using user subroutines. Analysis of heterogeneous materials using multiscale framework embedded into Abaqus has several advantages. It offers a wide database for solving mechanical or other problems without additional programming. In the second-order homogenization this is very useful for the simulation of a variety of physical processes at the microstructural level. Furthermore, Abaqus extracts many information in the

results file which are needed for the post-processing. For the homogenization purposes, the scale bridging and extraction of the required results can be achieved through a simple user coding. On the other hand, Abaqus allows the customization and development of a user graphical interface, which can enormously speed up preparation and execution of the multiscale analysis by a few button clicks. Finally, the implementation of the derived numerical algorithms into a commercial software makes them to be much more attractive for industrial use. In addition, Abaqus offers also the possibility of the parallelization in the numerical analysis, which can significantly improve computational efficiency, but it is beyond the scope of this thesis.

Similar works concerning the implementation of the multiscale framework comprising first-order homogenization into ABAQUS/Standard has been carried out in [148, 149]. As mentioned, C^1 triangular finite element applied for the macrolevel discretization is embedded by means of the user subroutine UEL, as described in Section 3.4. On the microlevel, RVE is discretized by the C^0 continuous quadrilateral finite element similar to the ABAQUS/Standard element CPE4, which is derived and implemented into the user subroutine UELMAT. UELMAT is an only user subroutine allowing access into the ABAQUS/Standard material library. On this way, access to a wide range of material models available in ABAQUS/Standard is enabled. At the macrolevel, global nonlinear finite element equation is solved, for the incremental displacement $\Delta\underline{V}$. At the macroelement level, displacement gradient increments $\Delta\underline{\varepsilon}_M$ and $\Delta\underline{\eta}_M$ are updated using Eqs. (3.9) and (3.10). RVE boundary displacement increment $\Delta\underline{u}_b$ is calculated by means of Eq. (4.34) for displacement boundary conditions or Eq. (4.37) for periodic boundary conditions. If periodic boundary conditions are used, periodicity equations (4.44) and (4.45), as well as integral conditions (4.46) and (4.47) must be imposed too. At the microlevel, a nonlinear boundary value problem is also solved, where homogenization procedure is conducted by means of Eqs. (4.58), (4.63) and (4.76)-(4.79). After solving RVE boundary value problem using the derived homogenization strategy, the results are transferred to the macrolevel Gauss material point. The presented computational procedure has to be carried out at every finite element integration point exhibiting a nonlinear material behaviour. In the case of a linear material behaviour, homogenization of constitutive matrices is required only once, for example as preprocessing step. Stress variables can be than computed in a classical finite element manner. The computational algorithm proposed is performed only in the frame of ABAQUS/Standard by simultaneous combination of the micro and macro analyses, as it is summarized in the

flowchart in Figure 4.2. Macrolevel UEL subroutine acts as a master routine, it prescribes RVE boundary conditions and runs microlevel analysis as another ABAQUS/Standard boundary value problem. During this period master analysis is paused awaiting for input data provided by a homogenization. More detailed description of the microlevel computations is presented in Table 4.1.

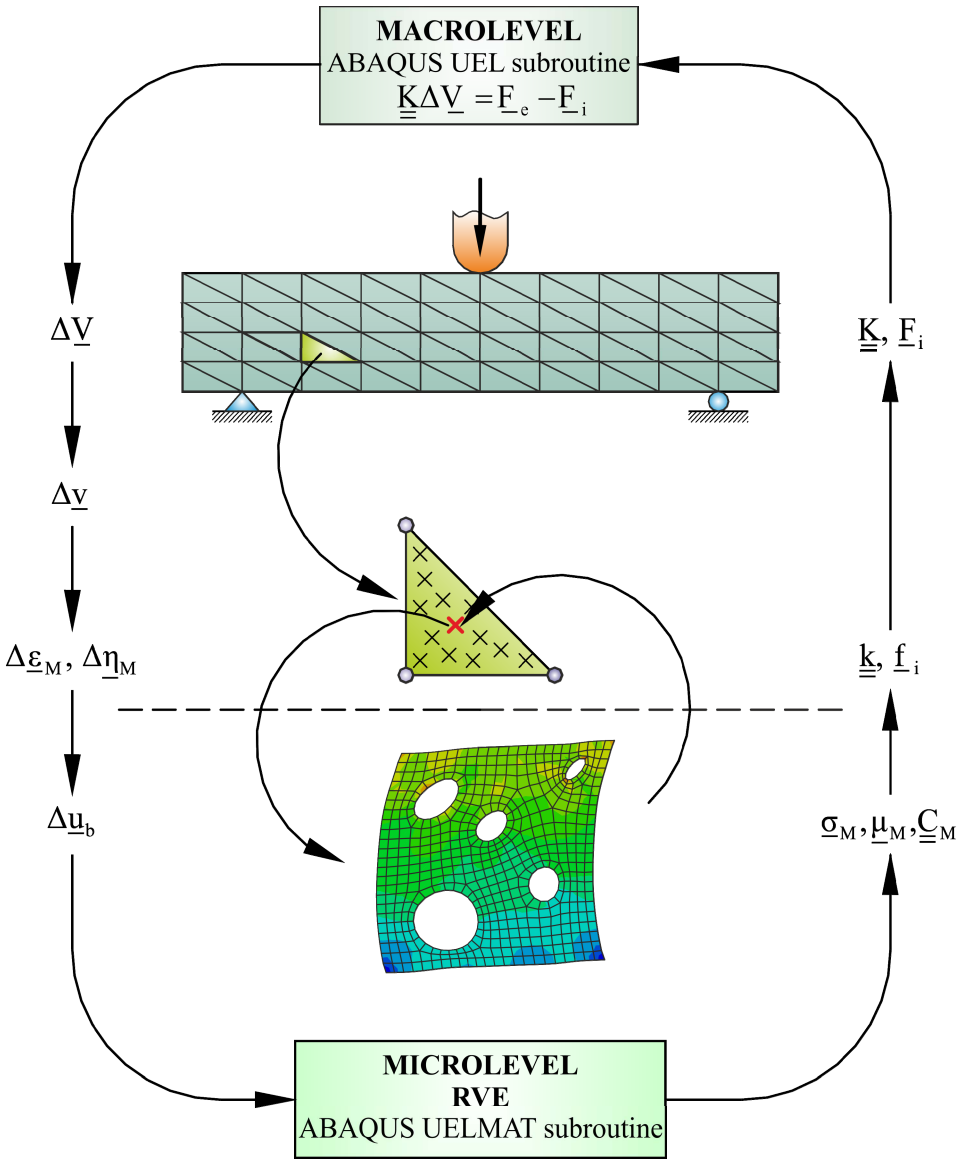

Figure 4.2 Micro-macro small strain multiscale algorithm

Table 4.1 Algorithm of the computations at the microlevel in small strain framework

1. Apply an increment of $\underline{u}_b$
2. If increment = last $\rightarrow$ go to **5**. **else** $\rightarrow$ go to **3**.
3. Solve the RVE boundary value problem in incrementally-iterative procedure
4. If convergence = true $\rightarrow$ go to **1**. **else** $\rightarrow$ go to **3**.
5. In the last increment: **loop** over all elements: **loop** over all integration points: computation of the homogenized stress tensors $\underline{\sigma}_M$ and $\underline{\mu}_M$ assembly of the RVE stiffness matrix, **end loop** **end loop** Assembly of the topological projection matrices $\underline{\underline{P}}_a$ and $\underline{\underline{P}}_b$ Assembly of the coordinate matrices $\underline{\underline{D}}$ and $\underline{\underline{H}}$ Computation of the RVE stiffness submatrices $\underline{\underline{K}}_{aa}$, $\underline{\underline{K}}_{ab}$, $\underline{\underline{K}}_{ba}$, $\underline{\underline{K}}_{bb}$ Computation of the condensed RVE stiffness $\tilde{\underline{\underline{K}}}_{bb}$ Computation of $\underline{\underline{C}}_M$ counterparts $\underline{\underline{C}}_{\sigma\varepsilon}$, $\underline{\underline{C}}_{\sigma\eta}$, $\underline{\underline{C}}_{\mu\varepsilon}$, $\underline{\underline{C}}_{\mu\eta}$
6. End analysis
7. Return to the macrolevel

4.1.5 Numerical evaluation of microfluctuation integral

In the following, numerical implementation of the microfluctuation integral constraints (4.46) and (4.47) is discussed, and various integration techniques for the microfluctuation integral evaluation are considered. In order to numerically implement the above mentioned conditions, several formulas, such as Boole's, Simpson's and trapezoidal integration rule have been considered. The performance of the integration approaches has been verified on a homogeneous unit square model discretized by 4×4 quadrilateral finite elements. The strain gradient component $\eta_{221} = u_{1,22} = 0.02 \frac{1}{\text{mm}}$ has been imposed on the boundaries. As can be observed from Figure 4.3, the corner nodal displacements are zero. Due to periodic boundary conditions, Eqs. (4.44) and (4.45) also result in zero. Thus, from numerical point static equilibrium is already achieved, since no loading is applied to the model using only corner

displacements and periodicity equations. Consequently, the required deformed shape cannot be achieved by periodic boundary conditions without implementation of the integral condition. This also points to the fact that without microfluctuation constraint all components of second-order strain ${}^{3}\underline{\boldsymbol{\eta}}_{\mathrm{M}}$ cannot be prescribed at the microlevel.

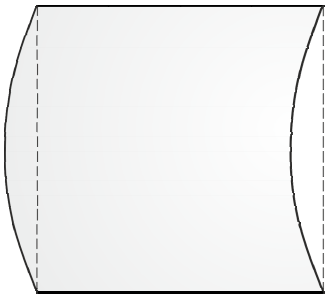

Figure 4.3 Deformed shape of the model for second-order srain component $u_{1,22}$

As expected, every integration technique used computes integral expressions exactly. On the other hand, the deformed shapes of the model differ, and only trapezoidal rule gives an exact deformation corresponding to Figure 4.3, as it is shown in Figure 4.4.

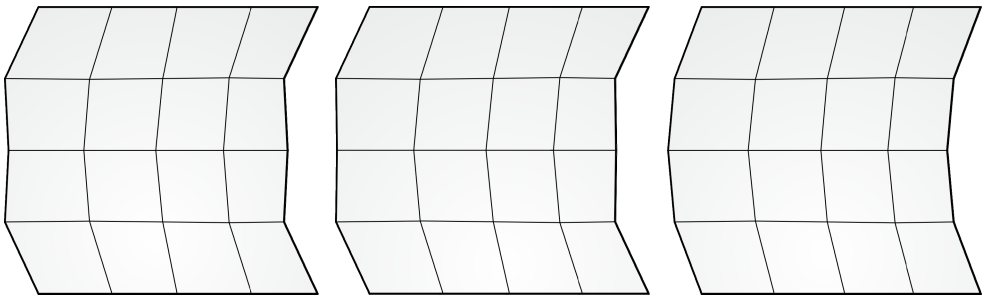

a) **b)** **c)**

Figure 4.4 Comparison of deformed model shapes obtained by various numerical integration techniques: a) Boole's rule, b) Simpson's rule, c) trapezoidal rule

Since in this problem we are dealing with a homogeneous material, microfluctuation filed is vanished. In other words, left and right edge must be smoothly curved, which is the case only in Figure 4.4c. The trapezoidal rule describes smooth edge shapes, while the Boole's and Simpson's formulas preserve zigzag arrangement of the nodes on the left and right edges due to the unfavourable weight pattern subjected to the nodes. It should be mentioned that finer meshes give analogous deformed shapes. Trapezoidal rule has again been verified on the simple example taken from [10]. To finally disengage other numerical methods accuracy of the results obtained has also been checked by the Simpson's formula. Computational model is a square of the side length $10\,\mu\mathrm{m}$ with an eccentric hole of radius $2\,\mu\mathrm{m}$ subjected to the

second-order strain components $\eta_{221} = 0.02\frac{1}{\mu m}$ and $\eta_{222} = 0.02\frac{1}{\mu m}$. Elasticity modulus E and Poisson's ratio ν taken are 175 GPa and 0.3, respectively. The deformed shapes presented in Figs. 4.5 and 4.6 show a good agreement with the reference solution [10].

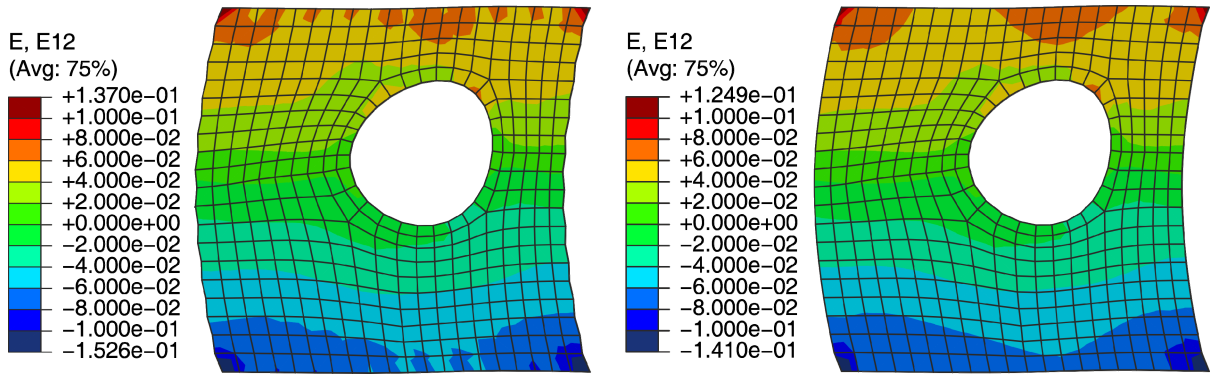

a) **b)**

Figure 4.5 Deformed shapes for second-order strain component $u_{1,22}$: a) Simpson rule, b) trapezoidal rule

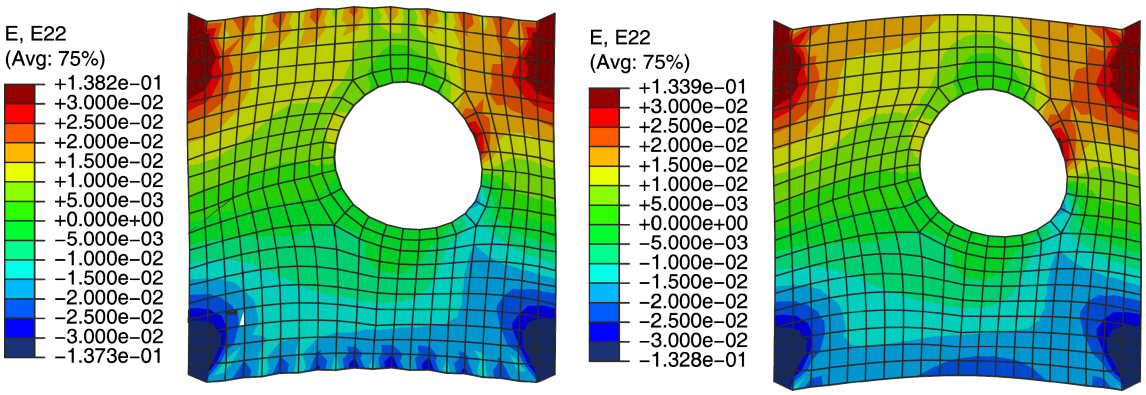

a) **b)**

Figure 4.6 Deformed shapes for second-order strain component $u_{2,22}$: a) Simpson rule, b) trapezodial rule

It is confirmed one more time that trapezoidal rule provides physically consistent deformed shapes compared to Simpson's rule. The same example is considered in [30]. Results obtained are the same, but contour plots are not comparable, because in the thesis contour scale has been adjusted to match to the reference contour plots in [10]. There are several minor discrepancies which are results of the different theories used, and of the finite element meshes that are similar, but not identical. A large strain theory has been used in the reference solution in contrast to the small theory applied here. Although the number of elements on the edges of the computational models is equivalent, here a slightly finer mesh around the hole is used. In

spite of some discrepancies, comparison of the present results with the reference solutions verifies the accuracy of the numerical implementation of the boundary conditions as well as the physically based behavior of a heterogeneous model. In both loading cases the artificial stress concentrations are noticed at the corners of the models, which are the consequence of the fluctuations at the corners set to zero. The second reason for this artificial phenomenon may be the missing of a surface integral enforcing zero microfluctuation field [10].

4.2 Large strain second-order computational homogenization

4.2.1 Macro-to-micro scale transition

Once small strain micro-macro methodology has been derived, extension to a large strain theory is mostly a straightforward step [121]. The formulation can also be considered as a direct extension of the small strain formulation presented in the previous section, which is also presented in author's work [30]. According to the nonlocal continuum theory, the small strain variables are replaced by the large strain values defined with respect to the macroscopic reference configuration. In a large strain second-order computational homogenization scheme Taylor series expansion describing the RVE boundary displacement field is written as

$$\mathbf{u}_{\mathrm{m}} = \mathbf{x} - \mathbf{X} = \left(\underline{\mathbf{F}}_{\mathrm{M}} - \underline{\mathbf{I}}\right) \cdot \mathbf{X} + \frac{1}{2}\left(\mathbf{X} \cdot {}^{3}\underline{\mathbf{G}}_{\mathrm{M}} \cdot \mathbf{X}\right) + \mathbf{r}\,. \tag{4.80}$$

In (4.80) distinction among initial and current RVE spatial coordinate exist. To satisfy equality between volume average of microlevel deformation gradient and macrolevel deformation gradient, (4.80) is transformed to

$$\frac{1}{V_0}\int_{V_0} \underline{\mathbf{F}}_{\mathrm{m}}\,\mathrm{d}V = \frac{1}{V_0}\int_{V_0} \left(\nabla_{0\mathrm{m}} \otimes \mathbf{x}\right)\mathrm{d}V_0 = \underline{\mathbf{F}}_{\mathrm{M}} + \frac{1}{V_0}\int_{V_0} \left({}^{3}\underline{\mathbf{G}}_{\mathrm{M}} \cdot \mathbf{X}\right)\mathrm{d}V_0 + \frac{1}{V_0}\int_{V_0} \left(\nabla_{0\mathrm{m}} \otimes \mathbf{r}\right)\mathrm{d}V_0\,. \tag{4.81}$$

In (4.81) second-order unit tensor which arises from gradient of $\left(\mathbf{x} - \mathbf{X}\right)$, but it disappears since on the right side unit tensor appears in $\left(\underline{\mathbf{F}}_{\mathrm{M}} - \underline{\mathbf{I}}\right)$, so it has been left out of consideration. As usual in a large strain theory adopting Lagrange approach, all operators are taken at initial configuration. Based on this, V_0 represents initial RVE volume, $\nabla_{0\mathrm{m}}$ is „nabla" operator in the reference configuration at the microscale. As already known, second and third integral member of (4.81) should vanish. Second integral vanishes using principle of the first moment of area about the centroid, as presented in Figure 4.1. The third integral may be transformed by using divergence theorem and set to zero in the way

$$\frac{1}{V_0}\int_{V_0}\left(\nabla_{0\mathrm{m}}\otimes\mathbf{r}\right)\mathrm{d}V_0=\frac{1}{V_0}\int_{\Gamma_0}\left(\mathbf{N}\otimes\mathbf{r}\right)\mathrm{d}\Gamma_0=\underline{\mathbf{0}}, \tag{4.82}$$

with Γ_0 representing RVE boundary in reference configuration. Next issue is relation between volume average of the microlevel second-order deformation gradient and macrolevel second-order deformation gradient. As in a small strain case, preservation of C^0 continuous boundary value problem at the microlevel excludes gradient of the deformation gradient, which precludes direct relation to its macroconjugate. Adopting alternative approach proposed in [27] second-order deformation gradient at the microstructural level can be defined as

$${}^3\underline{\mathbf{G}}_{\mathrm{m}}=\int_{V_0}\left(\underline{\mathbf{F}}_{\mathrm{m}}\otimes\mathbf{X}+\mathbf{X}\otimes\underline{\mathbf{F}}_{\mathrm{m}}\right)\mathrm{d}V_0\,. \tag{4.83}$$

Substitution of gradient of (4.80) into (4.83) gives the following

$$\begin{aligned}\int_{V_0}\left(\underline{\mathbf{F}}_{\mathrm{m}}\otimes\mathbf{X}+\mathbf{X}\otimes\underline{\mathbf{F}}_{\mathrm{m}}\right)\mathrm{d}V_0={}&{}^3\underline{\mathbf{G}}_{\mathrm{M}}\cdot\mathbf{J}+\int_{V_0}\left(\left(\nabla_{0\mathrm{m}}\otimes\mathbf{r}\right)\otimes\mathbf{X}\right)\mathrm{d}V_0+\mathbf{J}\cdot{}^3\underline{\mathbf{G}}_{\mathrm{M}}+\\&+\int_{V_0}\left(\mathbf{X}\otimes\left(\nabla_{0\mathrm{m}}\otimes\mathbf{r}\right)\right)\mathrm{d}V_0.\end{aligned} \tag{4.84}$$

Detailed derivation has been discussed in Section 4.1.1, so only some crucial steps will be presented. Using mathematical manipulation (4.7) and (4.8) along with divergence theorem, volume integrals in Eq. (4.84) can be transformed into surface integrals over Γ_0

$$\begin{aligned}&\int_{\Gamma_0}\left(\mathbf{N}\otimes\left(\mathbf{x}\otimes\mathbf{X}\right)+\left(\mathbf{X}\otimes\mathbf{x}\right)\otimes\mathbf{N}\right)\mathrm{d}\Gamma_0-2\int_{V_0}\left(\underline{\mathbf{I}}\otimes\mathbf{x}\right)^{RC}\mathrm{d}V_0=\\&{}^3\underline{\mathbf{G}}_{\mathrm{M}}\cdot\underline{\mathbf{J}}+\underline{\mathbf{J}}\cdot{}^3\underline{\mathbf{G}}_{\mathrm{M}}+\int_{\Gamma_0}\left(\mathbf{N}\otimes\left(\mathbf{r}\otimes\mathbf{X}\right)+\left(\mathbf{X}\otimes\mathbf{r}\right)\otimes\mathbf{N}\right)\mathrm{d}\Gamma_0-2\int_{V_0}\left(\underline{\mathbf{I}}\otimes\mathbf{r}\right)^{RC}\mathrm{d}V_0.\end{aligned} \tag{4.85}$$

After rearrangement (4.85) is represented as

$$\begin{aligned}{}^3\underline{\mathbf{G}}_{\mathrm{M}}\cdot\underline{\mathbf{J}}+\underline{\mathbf{J}}\cdot{}^3\underline{\mathbf{G}}_{\mathrm{M}}={}&\int_{\Gamma_0}\left(\mathbf{N}\otimes\left(\mathbf{x}\otimes\mathbf{X}\right)+\left(\mathbf{X}\otimes\mathbf{x}\right)\otimes\mathbf{N}\right)\mathrm{d}\Gamma_0-\\&-\int_{\Gamma_0}\left(\mathbf{N}\otimes\left(\mathbf{r}\otimes\mathbf{X}\right)+\left(\mathbf{X}\otimes\mathbf{r}\right)\otimes\mathbf{N}\right)\mathrm{d}\Gamma_0-\\&-2\int_{V_0}\left(\underline{\mathbf{I}}\otimes\mathbf{x}\right)^{RC}\mathrm{d}V_0+2\int_{V_0}\left(\underline{\mathbf{I}}\otimes\mathbf{r}\right)^{RC}\mathrm{d}V_0.\end{aligned} \tag{4.86}$$

In further simplification the first volume integral on the right side of (4.86) can be expressed through (4.80)

$$2\int_{V_0}\left(\underline{\mathbf{I}}\otimes\mathbf{x}\right)^{RC}\mathrm{d}V_0=2\int_{V_0}\left(\underline{\mathbf{I}}\otimes\left(\left(\underline{\mathbf{F}}_{\mathrm{M}}-\underline{\mathbf{I}}\right)\cdot\mathbf{X}+\frac{1}{2}\left(\mathbf{X}\cdot{}^3\underline{\mathbf{G}}_{\mathrm{M}}\cdot\mathbf{X}\right)+\mathbf{r}+\mathbf{X}\right)\right)^{RC}\mathrm{d}V_0 \tag{4.87}$$

which is transformed into

$$2\int_{V_0}\left(\underline{\mathbf{I}}\otimes\mathbf{x}\right)^{RC}\mathrm{d}V_0 = 2\left[\underline{\mathbf{I}}\otimes\left(\int_{V_0}\mathbf{X}\,\mathrm{d}V_0\right)\cdot\underline{\mathbf{F}}_{\mathrm{M}}\right]^{RC} - 2\left[\underline{\mathbf{I}}\otimes\left(\int_{V_0}\mathbf{X}\,\mathrm{d}V_0\right)\cdot\underline{\mathbf{I}}\right]^{RC} + \\ + \left[\underline{\mathbf{I}}\otimes\left(\int_{V_0}\left(\mathbf{X}\otimes\mathbf{X}\right)\mathrm{d}V_0\right):{}^{3}\underline{\mathbf{G}}_{\mathrm{M}}^{RC}\right]^{RC} + 2\int_{V_0}\left(\underline{\mathbf{I}}\otimes\mathbf{r}\right)^{RC}\mathrm{d}V_0 + \\ + 2\left[\underline{\mathbf{I}}\otimes\left(\int_{V_0}\mathbf{X}\,\mathrm{d}V_0\right)\right]^{RC}. \tag{4.88}$$

In relation (4.88) first, second and the last member vanish due to reasons mentioned above, which simplifies (4.88) to

$$2\int_{V_0}\left(\underline{\mathbf{I}}\otimes\mathbf{x}\right)^{RC}\mathrm{d}V_0 = \left(\underline{\mathbf{I}}\otimes\underline{\mathbf{J}}:{}^{3}\underline{\mathbf{G}}_{\mathrm{M}}^{RC}\right)^{RC} + 2\int_{V_0}\left(\underline{\mathbf{I}}\otimes\mathbf{r}\right)^{RC}\mathrm{d}V_0\,. \tag{4.89}$$

Substitution of (4.89) into (4.86) after some straightforward manipulations explained for small strain case gives

$${}^{3}\underline{\mathbf{G}}_{\mathrm{M}}\cdot\underline{\mathbf{J}}+\underline{\mathbf{J}}\cdot{}^{3}\underline{\mathbf{G}}_{\mathbf{M}}+\left(\underline{\mathbf{I}}\otimes\underline{\mathbf{J}}:{}^{3}\underline{\mathbf{G}}_{\mathrm{M}}^{RC}\right)^{RC} = \int_{\Gamma_0}\left(\mathbf{N}\otimes\left(\mathbf{x}\otimes\mathbf{X}\right)+\left(\mathbf{X}\otimes\mathbf{x}\right)\otimes\mathbf{N}\right)\mathrm{d}\Gamma_0 - \\ -\int_{\Gamma_0}\left(\mathbf{N}\otimes\left(\mathbf{r}\otimes\mathbf{X}\right)+\left(\mathbf{X}\otimes\mathbf{r}\right)\otimes\mathbf{N}\right)\mathrm{d}\Gamma_0. \tag{4.90}$$

Inserting of second moment of area (4.6) into (4.90), we get after some calculus the final expression

$$2\,{}^{3}\underline{\mathbf{G}}_{\mathrm{M}}+\left(\underline{\mathbf{I}}\otimes\underline{\mathbf{I}}:{}^{3}\underline{\mathbf{G}}_{\mathrm{M}}^{RC}\right)^{RC} = \frac{12}{L^4}\left[\int_{\Gamma_0}\left(\mathbf{N}\otimes\left(\mathbf{x}\otimes\mathbf{X}\right)+\left(\mathbf{X}\otimes\mathbf{x}\right)\otimes\mathbf{N}\right)\mathrm{d}\Gamma_0 - \right. \\ \left. -\int_{\Gamma_0}\left(\mathbf{N}\otimes\left(\mathbf{r}\otimes\mathbf{X}\right)+\left(\mathbf{X}\otimes\mathbf{r}\right)\otimes\mathbf{N}\right)\mathrm{d}\Gamma_0\right]. \tag{4.91}$$

Since relation (4.91) should be satisfied regardless to a particular microfluctuation field $\mathbf{r}$ the following constraint equation must be satisfied

$$\int_{\Gamma_0}\left(\mathbf{N}\otimes\left(\mathbf{r}\otimes\mathbf{X}\right)+\left(\mathbf{X}\otimes\mathbf{r}\right)\otimes\mathbf{N}\right)\mathrm{d}\Gamma_0 = {}^{3}\underline{\mathbf{0}}\,. \tag{4.92}$$

In the large strain extension of a small strain framework the same boundary conditions on RVE will be used. Any RVE boundary conditions used must explicitly satisfy relations (4.82) and (4.92). Details about discussion regarding averaging constraints can be found in Section 4.1.1. Analogously to the generalized periodic boundary conditions in a small strain case microfluctuation integral constraint (4.92) must be prescribed on two RVE edges only, where integration is now performed on initial configuration

$$\int_{\Gamma_L} \mathbf{r}_L \, d\Gamma_0 = \mathbf{0}, \tag{4.93}$$

$$\int_{\Gamma_B} \mathbf{r}_B \, d\Gamma_0 = \mathbf{0}. \tag{4.94}$$

In a similar way, after substitution of (4.80) relations (4.93) and (4.94) are expressed as

$$\int_{\Gamma_L} \mathbf{u}_L \, d\Gamma_0 = \left(\underline{\mathbf{F}}_M - \underline{\mathbf{I}}\right) \cdot \int_{\Gamma_L} \mathbf{X}_L \, d\Gamma_0 + \frac{1}{2} {}^3\underline{\mathbf{G}}_M : \int_{\Gamma_L} \left(\mathbf{X}_L \otimes \mathbf{X}_L\right) d\Gamma_0, \tag{4.95}$$

$$\int_{\Gamma_B} \mathbf{u}_B \, d\Gamma_0 = \left(\underline{\mathbf{F}}_M - \underline{\mathbf{I}}\right) \cdot \int_{\Gamma_B} \mathbf{X}_B \, d\Gamma_0 + \frac{1}{2} {}^3\underline{\mathbf{G}}_M : \int_{\Gamma_B} \left(\mathbf{X}_B \otimes \mathbf{X}_B\right) d\Gamma_0. \tag{4.96}$$

4.2.2 Boundary conditions on microstructural level

In Section 4.1.2 the most important facts about characteristics and a general behaviour of various boundary conditions have been mentioned. Since in a large strain formulation displacement gradients at the macrolevel are differently shaped, new coordinate matrices need to be derived. Again, for derivation of a coordinate matrices displacements of an *i*th node are expanded into components depending on a macroscale gradients (3.44) and (3.45) according to (4.80)

$$\begin{aligned}(u_1)_i = {} & (u_{1,1})_M (X_1)_i + (u_{1,2})_M (X_2)_i + \frac{1}{2}(u_{1,11})_M (X_1^2)_i + \\ & + \frac{1}{2}(u_{1,12})_M (X_1 X_2)_i + \frac{1}{2}(u_{1,21})_M (X_2 X_1)_i + \frac{1}{2}(u_{1,22})_M (X_2^2)_i,\end{aligned} \tag{4.97}$$

$$\begin{aligned}(u_2)_i = {} & (u_{2,1})_M (X_1)_i + (u_{2,2})_M (X_2)_i + \frac{1}{2}(u_{2,11})_M (X_1^2)_i + \\ & + \frac{1}{2}(u_{2,12})_M (X_1 X_2)_i + \frac{1}{2}(u_{2,21})_M (X_2 X_1)_i + \frac{1}{2}(u_{2,22})_M (X_2^2)_i.\end{aligned} \tag{4.98}$$

On the basis of an extended second-order deformation gradient ${}^3\underline{\mathbf{G}}_M$ compared to ${}^3\underline{\boldsymbol{\eta}}_M$, quadratic terms in (4.97) and (4.98) have also an extended form in comparison to (4.27) and (4.28). Relations (4.97) and (4.98) in a matrix form are written as

$$\begin{aligned}\underline{\mathrm{u}}_i = \begin{pmatrix} u_1 \\ u_2 \end{pmatrix}_i = {} & \begin{pmatrix} X_1 & 0 & X_2 & 0 \\ 0 & X_2 & 0 & X_1 \end{pmatrix}_i \underline{\mathrm{F}}_M + \\ & + \frac{1}{2}\begin{pmatrix} X_1^2 & 0 & X_1X_2 & 0 & X_1X_2 & 0 & X_2^2 & 0 \\ 0 & X_1X_2 & 0 & X_1^2 & 0 & X_2^2 & 0 & X_1X_2 \end{pmatrix}_i \underline{\mathrm{G}}_M.\end{aligned} \tag{4.99}$$

From (4.99) coordinate matrices of an *i*th node can be extracted in the form

$$\underline{\underline{\mathrm{D}}}_i = \begin{pmatrix} X_1 & 0 & X_2 & 0 \\ 0 & X_2 & 0 & X_1 \end{pmatrix}^T, \tag{4.100}$$

$$\underline{\underline{\mathrm{H}}}_i = \frac{1}{2}\begin{pmatrix} X_1^2 & 0 & X_1X_2 & 0 & X_1X_2 & 0 & X_2^2 & 0 \\ 0 & X_1X_2 & 0 & X_1^2 & 0 & X_2^2 & 0 & X_1X_2 \end{pmatrix}^T. \tag{4.101}$$

The shape of coordinate matrices can be confirmed in [77]. With introduction of the coordinate matrices (4.100) and (4.101), displacements of a single node on the RVE boundary are recast to

$$\underline{\mathrm{u}}_i = \underline{\underline{\mathrm{D}}}_i^T \underline{\mathrm{F}}_\mathrm{M} + \underline{\underline{\mathrm{H}}}_i^T \underline{\mathrm{G}}_\mathrm{M}, \tag{4.102}$$

with account of rigid body movements elimination. Periodicity equation arising in generalized periodic boundary conditions remains the same, with appropriate macroscale gradients used

$$\underline{\mathrm{u}}_\mathrm{R} - \underline{\mathrm{u}}_\mathrm{L} = \left(\underline{\underline{\mathrm{D}}}_\mathrm{R}^T - \underline{\underline{\mathrm{D}}}_\mathrm{L}^T\right)\underline{\mathrm{F}}_\mathrm{M} + \left(\underline{\underline{\mathrm{H}}}_\mathrm{R}^T - \underline{\underline{\mathrm{H}}}_\mathrm{L}^T\right)\underline{\mathrm{G}}_\mathrm{M}, \tag{4.103}$$

$$\underline{\mathrm{u}}_\mathrm{T} - \underline{\mathrm{u}}_\mathrm{B} = \left(\underline{\underline{\mathrm{D}}}_\mathrm{T}^T - \underline{\underline{\mathrm{D}}}_\mathrm{B}^T\right)\underline{\mathrm{F}}_\mathrm{M} + \left(\underline{\underline{\mathrm{H}}}_\mathrm{T}^T - \underline{\underline{\mathrm{H}}}_\mathrm{B}^T\right)\underline{\mathrm{G}}_\mathrm{M}. \tag{4.104}$$

After introduction coordinate matrices in a large strain framework, integral conditions (4.95) and (4.96) become defined as

$$\int_{\Gamma_\mathrm{L}} \underline{\mathrm{u}}_\mathrm{L}\, \mathrm{d}\Gamma_0 = \left(\int_{\Gamma_\mathrm{L}} \mathrm{D}_\mathrm{L}^T\, \mathrm{d}\Gamma_0\right)\underline{\mathrm{F}}_\mathrm{M} + \left(\int_{\Gamma_\mathrm{L}} \underline{\underline{\mathrm{H}}}_\mathrm{L}^T\, \mathrm{d}\Gamma_0\right)\underline{\mathrm{G}}_\mathrm{M}, \tag{4.105}$$

$$\int_{\Gamma_\mathrm{B}} \underline{\mathrm{u}}_\mathrm{B}\, \mathrm{d}\Gamma_0 = \left(\int_{\Gamma_\mathrm{B}} \mathrm{D}_\mathrm{B}^T\, \mathrm{d}\Gamma_0\right)\underline{\mathrm{F}}_\mathrm{M} + \left(\int_{\Gamma_\mathrm{B}} \underline{\underline{\mathrm{H}}}_\mathrm{B}^T\, \mathrm{d}\Gamma_0\right)\underline{\mathrm{G}}_\mathrm{M}. \tag{4.106}$$

Remaining details regarding derivation of above mentioned relations and their numerical implementation has already been discussed for a small strain case. The choice of an appropriate method for numerical implementation of (4.105) and (4.106) has been tested in Section 4.1.5.

4.2.3 Micro-to-macro scale transition

Homogenization of microvariables and transition to the macrolevel keeps all the steps explained in Section 4.1.3. In a large strain extent again in homogenization of double stress inconsistency is expected, since C^0 continuity is preserved on the microstructural level. The resulting relations have the same shape as in a small strain theory, replaced by an appropriate large strain conjugates. Hill-Mandel energy condition has already been defined in (4.49). Using first Piola-Kirchhoff stress tensor as an energy conjugate to the deformation gradient

and double stress as an energy conjugate to the second-order deformation gradient, Hill-Mandel is defined by the relation

$$\frac{1}{V_0}\int_{V_0}\left(\underline{\mathbf{P}}_{\mathrm{m}} : \delta\underline{\mathbf{F}}_{\mathrm{m}}\right)\mathrm{d}V_0 = \underline{\mathbf{P}}_{\mathrm{M}} : \delta\underline{\mathbf{F}}_{\mathrm{M}} + {}^{3}\underline{\mathbf{Q}}_{\mathrm{M}} \vdots \delta^{3}\underline{\mathbf{G}}_{\mathrm{M}}\,. \tag{4.107}$$

Variation of the work done at the microlevel can be further elaborated as follows

$$\frac{1}{V}\int_{V}\delta W_{\mathrm{m}}\,\mathrm{d}V = \frac{1}{V_0}\int_{V_0}\left(\underline{\mathbf{P}}_{\mathrm{m}} : \left(\nabla_{\mathrm{m}} \otimes \delta\mathbf{x}\right)\right)\mathrm{d}V_0 = \frac{1}{V_0}\int_{\Gamma_0}\left(\mathbf{N}\cdot\underline{\mathbf{P}}_{\mathrm{m}}\cdot\delta\mathbf{x}\right)\mathrm{d}\Gamma_0 = \frac{1}{V_0}\int_{\Gamma}\left(\mathbf{t}\cdot\delta\mathbf{x}\right)\mathrm{d}\Gamma_0\,. \tag{4.108}$$

In (4.108), stress vector $\mathbf{t}$ is expressed as $\mathbf{t} = \underline{\mathbf{P}}\cdot\mathbf{N}$. In the last boundary integral of (4.108) substitution of variation of a current coordinate (4.80) on the RVE boundaries gives

$$\frac{1}{V_0}\int_{V_0}\delta W_{\mathrm{m}}\,\mathrm{d}V_0 = \frac{1}{V_0}\int_{\Gamma_0}\left(\mathbf{t}\cdot\left(\delta\underline{\mathbf{F}}_{\mathrm{M}}\cdot\mathbf{X} + \frac{1}{2}\left(\mathbf{X}\cdot\delta^{3}\underline{\mathbf{G}}_{\mathrm{M}}\cdot\mathbf{X}\right) + \delta\mathbf{r}\right)\right)\mathrm{d}\Gamma_0\,, \tag{4.109}$$

which is rearranged into

$$\begin{aligned}\frac{1}{V_0}\int_{V_0}\delta W_{\mathrm{m}}\,\mathrm{d}V_0 = {} & \left(\frac{1}{V_0}\int_{\Gamma_0}\left(\mathbf{t}\otimes\mathbf{X}\right)\mathrm{d}\Gamma_0\right) : \delta\underline{\mathbf{F}}_{\mathrm{M}} + \left(\frac{1}{2V_0}\int_{\Gamma_0}\left(\mathbf{X}\otimes\mathbf{t}\otimes\mathbf{X}\right)\mathrm{d}\Gamma_0\right)\vdots\delta^{3}\underline{\mathbf{G}}_{\mathrm{M}} + \\ & + \frac{1}{V_0}\int_{\Gamma_0}\left(\mathbf{t}\cdot\delta\mathbf{r}\right)\mathrm{d}\Gamma_0.\end{aligned} \tag{4.110}$$

On the basis of the aforementioned principles explained for a small strain assumption the following identities are defined

$$\underline{\mathbf{P}}_{\mathrm{M}} = \frac{1}{V_0}\int_{\Gamma_0}\left(\mathbf{t}\otimes\mathbf{X}\right)\mathrm{d}\Gamma_0\,, \tag{4.111}$$

$${}^{3}\underline{\mathbf{Q}}_{\mathrm{M}} = \frac{1}{2V_0}\int_{\Gamma_0}\left(\mathbf{X}\otimes\mathbf{t}\otimes\mathbf{X}\right)\mathrm{d}\Gamma_0\,, \tag{4.112}$$

and

$$\frac{1}{V_0}\int_{\Gamma_0}\left(\mathbf{t}\cdot\delta\mathbf{r}\right)\mathrm{d}\Gamma_0 = 0\,. \tag{4.113}$$

Integral condition (4.113) has already been proven to vanish for both cases of boundary conditions used in this research. Matrix notation of (4.111) and (4.112) is elaborated as

$$\underline{\mathrm{P}}_{\mathrm{M}} = \frac{1}{V_0}\underline{\underline{\mathrm{D}}}\,\underline{\mathrm{f}}_{\mathrm{b}}\,, \tag{4.114}$$

$$\underline{\mathrm{Q}}_{\mathrm{M}} = \frac{1}{V_0}\underline{\underline{\mathrm{H}}}\,\underline{\mathrm{f}}_{\mathrm{b}}\,. \tag{4.115}$$

Volume integral expression of (4.111) can be derived by the mathematical manipulation of (4.59) demonstrating that

$$\underline{\mathbf{P}}_{\mathrm{M}} = \frac{1}{V_0}\int_{V_0} \underline{\mathbf{P}}_{\mathrm{m}}\, \mathrm{d}V_0 \,. \tag{4.116}$$

Also, by mathematical manipulation of (4.61)-(4.63), double stress is formulated as

$$^{3}\underline{\underline{\mathbf{Q}}}_{\mathrm{M}} = \frac{1}{2V_0}\int_{V_0} \left(\underline{\mathbf{P}}_{\mathrm{m}} \otimes \mathbf{X} + \mathbf{X} \otimes \underline{\mathbf{P}}_{\mathrm{m}}\right) \mathrm{d}V_0 \,. \tag{4.117}$$

Once again higher-order stress is physically interpreted as a first moment of first Piola-Kirchhoff stress tensor. To derive macroscopic constitutive operators static condensation procedure should be employed, according to steps described in (4.64)-(4.75). After that, macroscopic tangents are extracted in the form

$$\underline{\underline{\mathbf{C}}}_{PF} = \frac{1}{V_0}\underline{\underline{\mathbf{D}}}\,\underline{\underline{\tilde{\mathbf{K}}}}_{\mathrm{bb}}\underline{\underline{\mathbf{D}}}^{T} \,, \tag{4.118}$$

$$\underline{\underline{\mathbf{C}}}_{PG} = \frac{1}{V_0}\underline{\underline{\mathbf{D}}}\,\underline{\underline{\tilde{\mathbf{K}}}}_{\mathrm{bb}}\underline{\underline{\mathbf{H}}}^{T} \,, \tag{4.119}$$

$$\underline{\underline{\mathbf{C}}}_{QF} = \frac{1}{V_0}\underline{\underline{\mathbf{H}}}\,\underline{\underline{\tilde{\mathbf{K}}}}_{\mathrm{bb}}\underline{\underline{\mathbf{D}}}^{T} \,, \tag{4.120}$$

$$\underline{\underline{\mathbf{C}}}_{QG} = \frac{1}{V_0}\underline{\underline{\mathbf{H}}}\,\underline{\underline{\tilde{\mathbf{K}}}}_{\mathrm{bb}}\underline{\underline{\mathbf{H}}}^{T} \,. \tag{4.121}$$

4.2.4 Numerical implementation

Large strain multiscale framework has been implemented into the finite element software ABAQUS/Standard using mostly the same principles in subroutine programming as in a small strain setting, shown in Figure 4.7. C^1 finite element used for discretization of the macrolevel problem is here labelled as C1PE3LS, and it is explained in Section 3.2, coded as UEL subroutine. At the microlevel RVE is discretized by the plane strain quadrilateral finite element CPE4 from the ABAQUS/Standard element library, where C^0 continuous interpolations are employed. Such an approach takes advantage of the fact that the algorithms employ geometrical nonlinearities, and so the different material models available in ABAQUS/Standard can be used. As is common for nonlinear problems, an incremental-iterative procedure is performed. Accordingly, the load applied at the macrolevel is divided into increments, and in this setting, microlevel computations are performed as a series of *restart* analyses. The *restart* analysis methodology available in ABAQUS/Standard relies on the basic assumptions of large strain theory, where a new loading increment is imposed on the last equilibrated configuration. In each macroscale computational step, an increment of

boundary displacements is imposed on a last converged RVE configuration. After several iterative steps and satisfying the convergence criterions, the RVE output data are mapped at macroscale integration points.

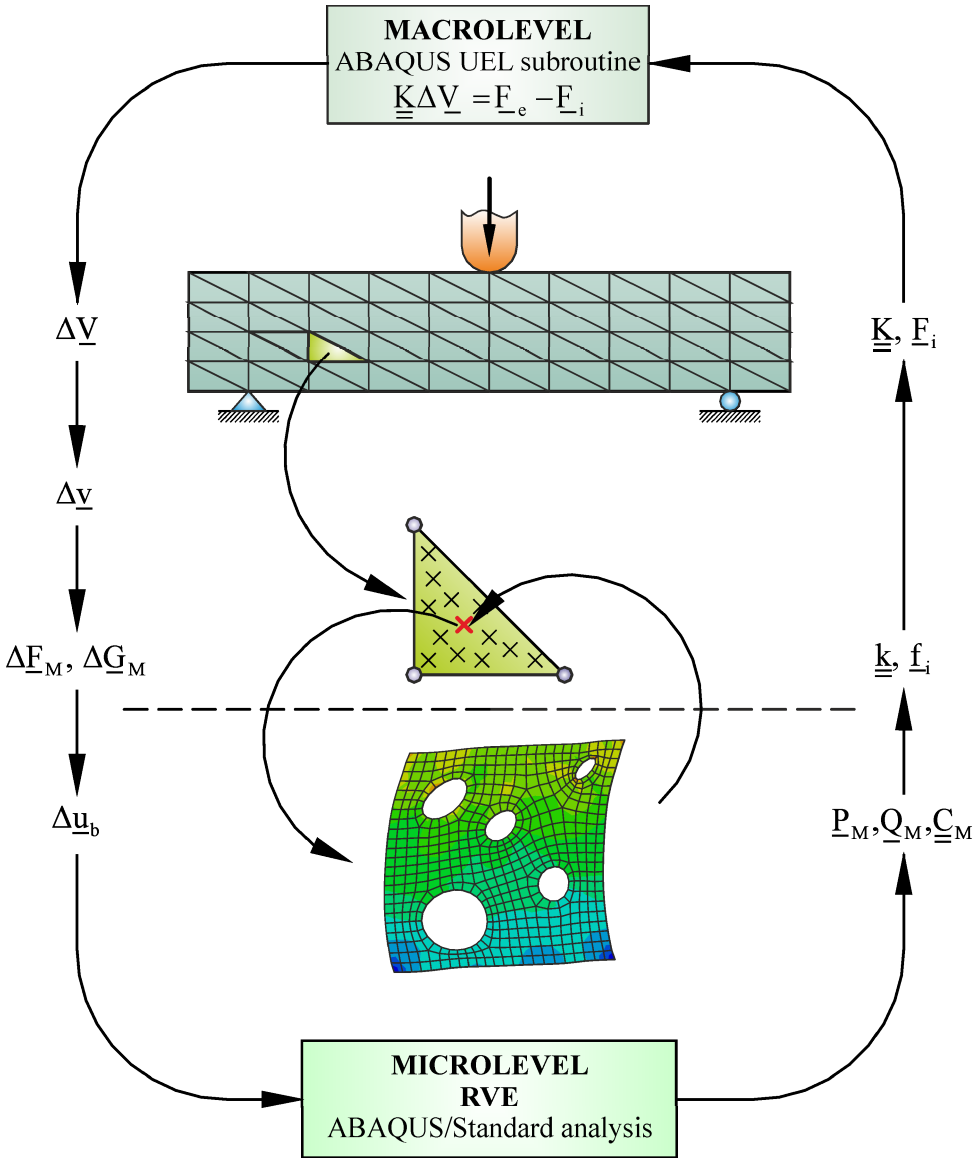

Figure 4.7 Micro-macro large strain multiscale algorithm

In this computational procedure, each new converged increment at the macrolevel creates a completely new set of RVE output databases. It is obvious that such an approach requires significant memory consumption, which increases with finer loading incrementation at the macroscale. Moreover, the RVE response is divided in several files depending on the number of load increments at the macroscale. The complete unified response history of the RVE assigned to a single integration point at the macrolevel should be derived through the *join* command available in ABAQUS/Standard. Several problems arise during the implementation

of the described two-scale computational procedure in Abaqus. The first is that the first Piola-Kirchhoff stress tensor required at the macrolevel integration point is not available as a solution variable in ABAQUS/Standard. Hence, before any averaging, Cauchy stress tensor, which is obtained as the solution stress in ABAQUS/Standard, must be properly transformed as

$$\underline{\mathbf{P}}_{\mathrm{m}} = J\,\underline{\boldsymbol{\sigma}}_{\mathrm{m}}\,\underline{\mathbf{F}}_{\mathrm{m}}^{-T}\,, \tag{4.122}$$

where $J = \det \underline{\mathbf{F}}_{\mathrm{m}}$. The second problem is that for derivation of the macrolevel tangent stiffness matrices the condensed RVE stiffness $\tilde{\mathbf{K}}_{\mathrm{bb}}$ is required. The consistent material matrices used for the integration of the RVE stiffness in the case of finite strains with small volume changes are expressed in ABAQUS/Standard by the relation

$${}^{4}\underline{\mathbf{C}}_{\mathrm{Abaqus}} = \frac{\partial \Delta \underline{\boldsymbol{\sigma}}}{\partial \Delta \underline{\boldsymbol{\varepsilon}}^{\mathrm{L}}}\,, \tag{4.123}$$

with $\underline{\boldsymbol{\varepsilon}}^{\mathrm{L}}$ as a logarithmic strain. But, to obtain the homogenized tangent matrices for the macroscale, RVE stiffness should be integrated by the material constitutive matrix defined as

$${}^{4}\underline{\mathbf{C}}_{PF} = \frac{\partial \Delta \underline{\mathbf{P}}_{\mathrm{m}}}{\partial \Delta \underline{\mathbf{F}}_{\mathrm{m}}}\,, \tag{4.124}$$

consistent with the macrolevel requirements. Therefore, the transformation of Eq. (4.123) into Eq. (4.124) is required. Accordingly, the consistent material matrix defined in Eq. (4.124) can be expressed as

$${}^{4}\underline{\mathbf{C}}_{PF} = \frac{\partial \Delta \underline{\mathbf{P}}_{\mathrm{m}}}{\partial \Delta \underline{\mathbf{F}}_{\mathrm{m}}} = \frac{\partial \Delta \underline{\mathbf{P}}_{\mathrm{m}}}{\partial \Delta \underline{\boldsymbol{\sigma}}_{\mathrm{m}}} \frac{\partial \Delta \underline{\boldsymbol{\sigma}}_{\mathrm{m}}}{\partial \Delta \underline{\boldsymbol{\varepsilon}}_{\mathrm{m}}^{\mathrm{L}}} \frac{\partial \Delta \underline{\boldsymbol{\varepsilon}}_{\mathrm{m}}^{\mathrm{L}}}{\partial \Delta \underline{\mathbf{F}}_{\mathrm{m}}}\,. \tag{4.125}$$

In Eq. (4.125), by using the chain rule, the first term can be simplified to

$$\frac{\partial \Delta \underline{\mathbf{P}}_{\mathrm{m}}}{\partial \Delta \underline{\boldsymbol{\sigma}}_{\mathrm{m}}} = \frac{\partial \left(J\,\underline{\mathbf{F}}_{\mathrm{m}}^{-1} \Delta \underline{\boldsymbol{\sigma}}_{\mathrm{m}} \right)}{\partial \Delta \underline{\boldsymbol{\sigma}}_{\mathrm{m}}} = J\,\underline{\mathbf{F}}_{\mathrm{m}}^{-1}\,, \tag{4.126}$$

giving the transformation formula for the RVE material constitutive material matrix

$${}^{4}\underline{\mathbf{C}}_{PF} = J\,\underline{\mathbf{F}}_{\mathrm{m}}^{-1}\,{}^{4}\underline{\mathbf{C}}_{\mathrm{Abaqus}} \frac{\partial \Delta \underline{\boldsymbol{\varepsilon}}_{\mathrm{m}}^{\mathrm{L}}}{\partial \Delta \underline{\mathbf{F}}_{\mathrm{m}}}\,. \tag{4.127}$$

Thus, after completion of the RVE analysis using only the capabilities of ABAQUS/Standard, Python script extracts the nodal and integration point results from ABAQUS/Standard output database (*.odb*) into an external *.dat* files. The extracted results are read into a "*dummy*" analysis solving the same RVE boundary value problem, but in this case conducted by the UELMAT subroutine. The analysis is considered as "*dummy*" because the equilibrated results

from the external files are read in, and the elements behavior is fully determined. The purpose of this analysis is homogenization of the macrovariables. First, Cauchy stress tensor is transformed into first Piola-Kirchhoff stress tensor. Thereafter, the stresses can be averaged for the macroscale according (4.116) and (4.117). As the second, the material matrix in a form of (4.123) calculated in every integration point should be transformed according to relation (4.127). Afterwards, transformed material matrix is used to integrate the RVE stiffness and homogenization of the macroscale materials matrices. It should be stressed out that the main reason for the "*dummy*" UELMAT analysis is an extraction of the material constitutive matrix calculated by ABAQUS/Standard, which can only be accessed through UELMAT subroutine. A description of the steps performed at the microscale is presented in Table 4.2.

All multiscale computations calculated within this research were performed on a workstation possessing 8 CPUs with a clock speed of 3.7 GHz and 64 GB of RAM memory. It is clear that the CPU time in the homogenization procedure greatly depends on the RVE size and discretization. As an illustration, the complete microscale computation of an RVE discretized by 500 first-order quadrilateral finite elements takes approximately 10 seconds. The majority of the computational effort is spent on the calculation of the condensed RVE stiffness. If only the stress is homogenized, the computational time is almost unaffected. The Abaqus output database file for the RVE considered requires approximately 3 MB of disk space. In a multiscale context, where one macroscale element comprises 13 material points, this means that up to 30 MB of disk space is required for all RVEs. For practical problems, the saving of all RVEs data through all increments can use a memory of few tens of gigabytes.

Table 4.2 Algorithm of the computations at the microlevel in large strain framework

Abaqus restart analysis - read last converged results from restart file

1. Apply an increment of $\underline{u}_b$

2. If increment = last $\rightarrow$ go to **5**.
else $\rightarrow$ go to **3**.

3. Solve the RVE boundary value problem

4. If convergence = true
$\rightarrow$ write a new restart increment
$\rightarrow$ go to **1**.
else $\rightarrow$ go to **3**.

5. In the last increment:
write nodal and integration point results into external .dat files

6. End analysis

7. Start Abaqus UELMAT analysis

8. Homogenization procedure
Loop over all elements
Loop over all integration points
read converged results read from *.*dat* files
transformation of the Cauchy stress tensor
computation of the homogenized stress tensors $\underline{P}_M$ and $\underline{Q}_M$
transformation of material matrix at the integration point
assembly of the RVE stiffness matrix
End loop
End loop
Assembly of the topological projection matrices $\underline{\underline{P}}_a$ and $\underline{\underline{P}}_b$
Assembly of the coordinate matrices $\underline{\underline{D}}$ and $\underline{\underline{H}}$
Computation of the RVE stiffness submatrices $\underline{\underline{K}}_{aa}$, $\underline{\underline{K}}_{ab}$, $\underline{\underline{K}}_{ba}$, $\underline{\underline{K}}_{bb}$
Computation of the condensed RVE stiffness $\tilde{\underline{\underline{K}}}_{bb}$
Computation of $\underline{\underline{C}}_M$ counterparts $\underline{\underline{C}}_{PF}$, $\underline{\underline{C}}_{PG}$, $\underline{\underline{C}}_{QF}$, $\underline{\underline{C}}_{QG}$

9. End analysis

10. Return to the macrolevel

4.3 Numerical examples

4.3.1 Shear layer problem

As the first example, a simple shear of a heterogeneous strip under boundary constraints is modeled, which is widely used as a benchmark problem in the literature, e.g. in [10, 30, 75, 79]. The strip height is $h = 10\,\text{mm}$, and it has an infinite length in the horizontal direction, as shown in Figure 4.8a. Therefore, the macroscale computational model may comprise only an elements row through the height. Four finite element meshes consisting of 2, 4, 8 and 16 elements per height are considered, maintaining the element side length ratio of 2.5.

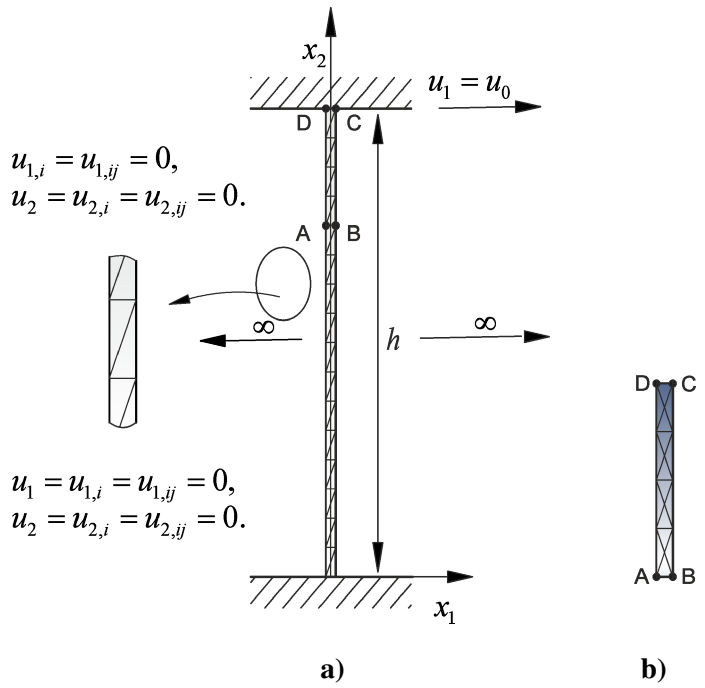

Figure 4.8 Discretization of the macroscopic model: a) shear layer strip, b) submodel

The material considered is an hypothetical example of a steel with a porous microstructure consisting of an elastoplastic matrix with linear isotropic hardening. Young's modulus E is taken as 210 GPa, and Poisson's ratio is set to 0.3. The yield stress of $\sigma_{\text{Y}} = 250$ MPa and the constant elastoplastic tangent modulus of $E_{\text{T}} = 250$ MPa are assumed. The square RVE with the side length of 0.2 mm discretized by 508 quadrilateral finite elements is presented in Figure 4.9. It consists of randomly distributed voids, with the void ratio of 0.13 and the average void radius of 0.043 mm.

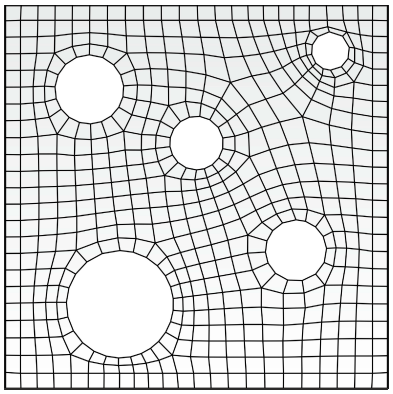

Figure 4.9 RVE presenting steel with porous microstructure with 13% of porosity

The boundary conditions of the top and bottom clamped edges are described in Figure 4.8a by displacement components and their derivatives, where $i, j = 1,2$. The left and right edge are bounded by periodicity conditions, thereby enforcing the independency of x_1. At the top edge the horizontal displacement u_0 is prescribed. The loading cases corresponding to several horizontal displacements of u_0 are considered. The results obtained by the displacement and periodic boundary conditions on the RVE are compared. The shear strain distribution over the height of the strip for different finite element meshes is presented in Figure 4.10 for the displacement of $u_0 = 0.005\,\text{mm}$. In this case, linear displacement and periodicity boundary conditions on the RVE are considered. Since there are no significant differences in a shear strain distribution for both RVE boundary conditions imposed, the results in Figure 4.10 are given only for the periodic boundary conditions. As expected, the finer mesh is more able to capture boundary shear layer, as well as the pure shear in the middle of the strip. From Figure 4.10 it is evident that the discretization consisting of 16 elements per height can be taken as the limit case discretization for the description of middle pure shear because there are only slight differences between the values obtained by 8 and 16 elements per height. However, the differences in the boundary layer responses near the top and bottom clamped edges are still significant, and a further convergence check in that area is needed.

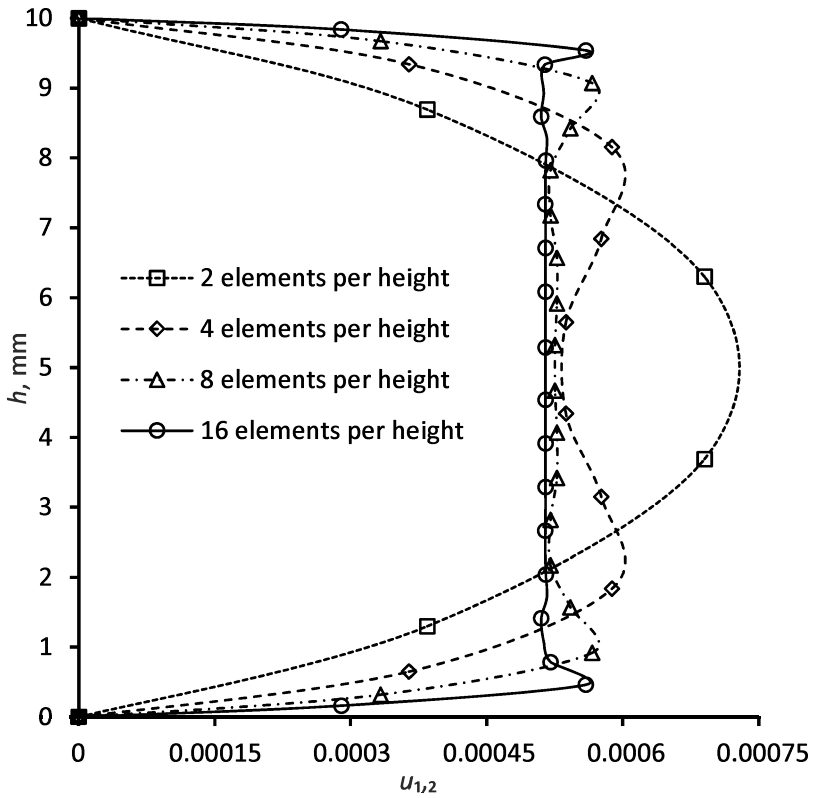

Figure 4.10 Distribution of displacement gradient $u_{1,2}$ for u_0=0.005 mm

Therefore, to discretize a boundary layer area with more elements, the well-known submodeling technique has been used. Accordingly, the submodel of the height of 2.5 mm, describing the boundary layer deformation responses, is discretized by 16 finite elements as presented in Figure 4.8b. The submodel boundary conditions are taken from the uniform strip discretization of 16 elements per height. Figure 4.11 represents the comparison of the shear strain distribution over the boundary layer area calculated by both the global model and the submodel. As can be seen, the submodel results are in good agreement with the global model predictions. By using a significantly larger number of elements in the submodel discretization, the solutions are only slightly improved. The distribution of a second-order strain $u_{1,22}$ over the discretized global model is presented in Figure 4.12, and compared to the values computed with the finer discretized submodel in the vicinity of the upper clamp. As evident, a good agreement of the values obtained by both computational models is achieved.

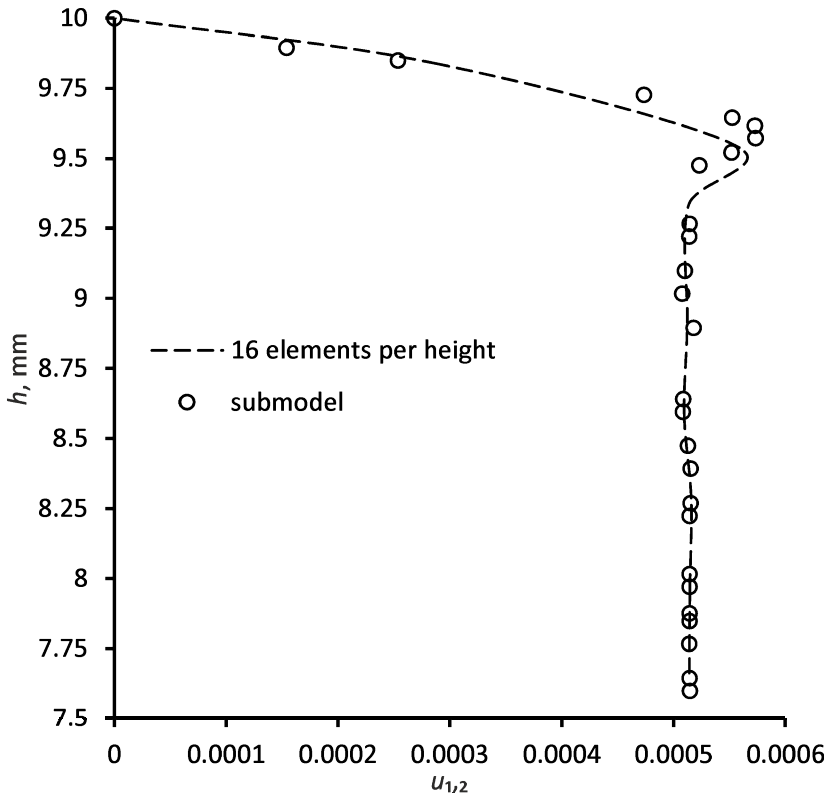

Figure 4.11 Comparison of displacement gradient $u_{1,2}$ obtained by the global model and the submodel for u_0=0.005 mm

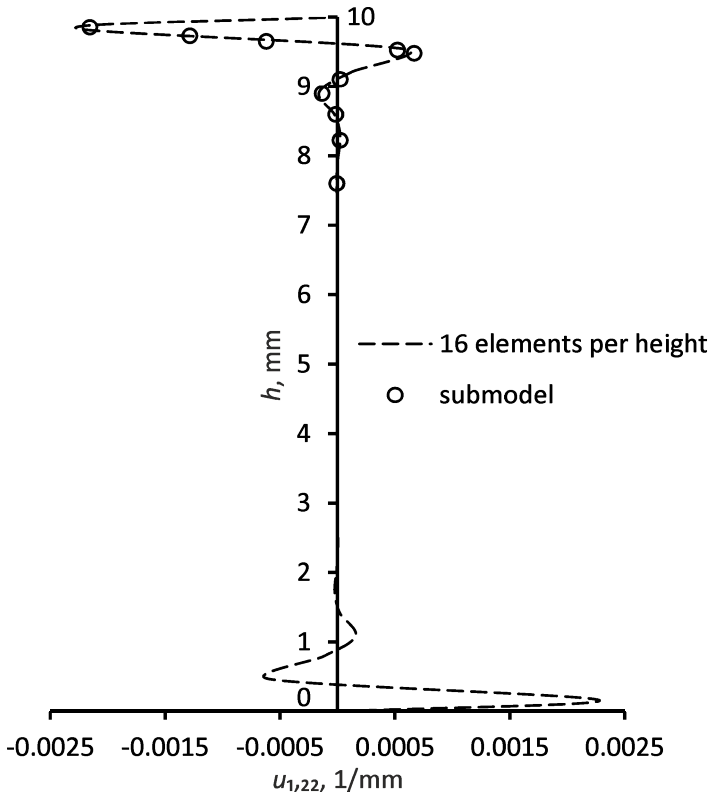

Figure 4.12 Comparison of second-order displacement gradient $u_{1,22}$ obtained by the global model and the submodel for u_0=0.005 mm

After convergence study described above, it can be concluded that the finite element mesh of the shear layer strip consisting of 16 triangular finite elements per height can be used for further consideration of the strip deformation responses. The rigorous constraining boundary conditions at the top and bottom edges cause very small strains close to the boundary, but they result in a high gradients of the second-order strain $u_{1,22}$. It this particular case the curve in Figure 4.12 can be considered as the derivative of the curve displayed in Figure 4.10. The comparison of the presented curves proves this statement, which confirms the accuracy of the computations. It should be noted that $u_{1,22}$ is a nodal degree of freedom of the triangular finite element applied at the macrolevel. The distributions of the shear microstrain through the strip height, presented on the deformed RVEs for the displacement and periodic boundary conditions, are shown in Figure 4.13.

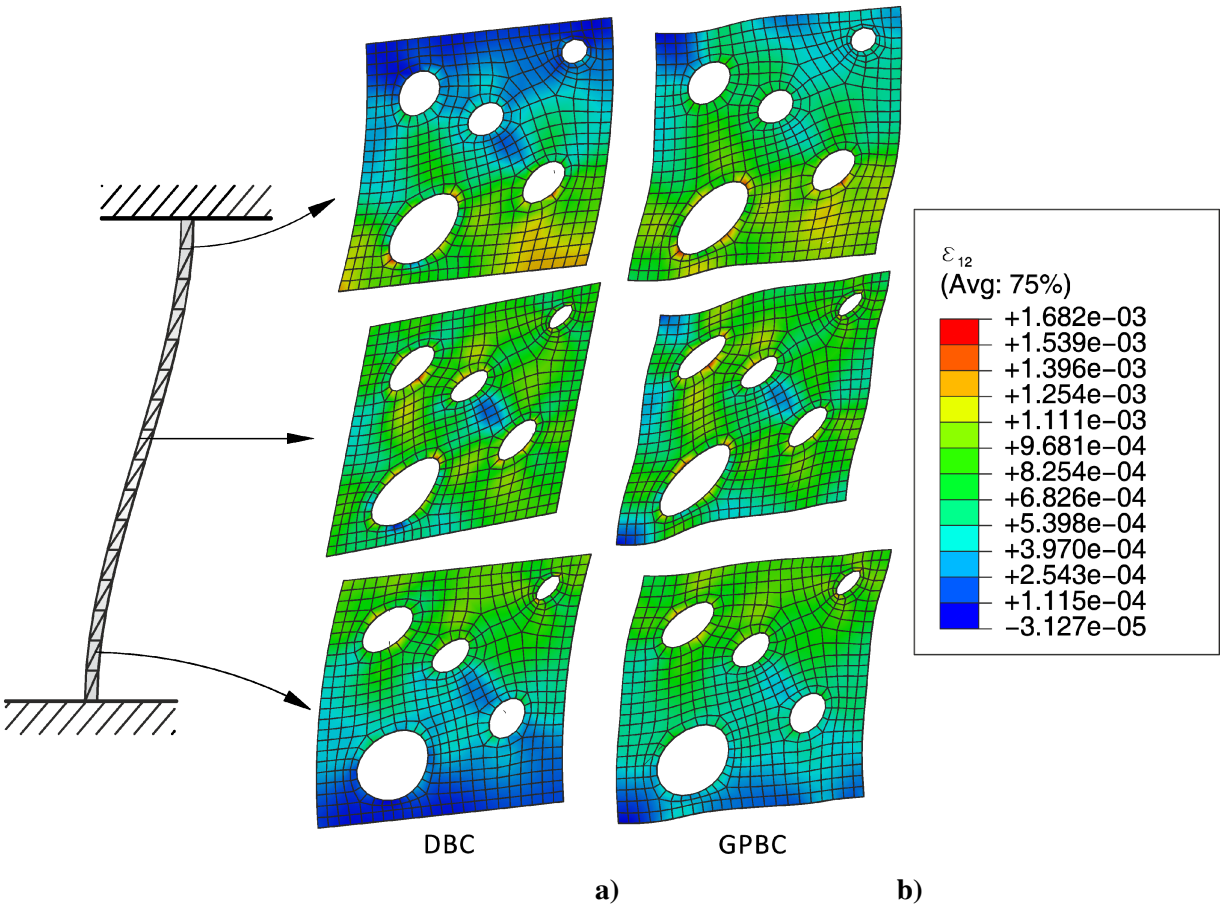

Figure 4.13 Distribution of the shear microstrain on selected RVE-s over the strip for u_0=0.005 mm: a) displacement b. c., b) generalized periodic b. c.

As can be observed, at the bottom layer as well as at the top layer, the strain gradients are noticeable, while in the middle of the strip pure shear is dominant. The distinctions between different boundary conditions applied are obvious. The stiffer RVE response is obtained when

the linear displacement boundary conditions are used, due to the introduced microfluctuation assumption. It should be stressed that a more realistic results are obtained for the periodic boundary conditions.

In addition, the deformation responses of the shear layer under several prescribed displacements u_0 and generalized periodic boundary conditions have been considered. The distributions of displacement gradients $u_{1,2}$ and $u_{1,22}$ through the height of the strip are shown in Figs. 4.14 and 4.15. From Figure 4.14, it is evident that the width of a boundary layer, described by the change of the shear strain, increases with the progressing of the prescribed displacement u_0, as expected. On the other hand, the middle strip zone of the pure shear reduces when the loading increases. It is clear that the shape of the curves is significantly influenced by the boundary conditions at the strip edges. Here, according to the C^1 finite element nodal degrees of freedom used, boundary conditions including a second-order derivatives are imposed, which is different of the shear layer example available in the literature [18, 27, 79]. The curves presented in Figure 4.15 clearly display the derivatives of the curves from Figure 4.14, which is in an accordance with the previous discussion. As evident from Figure 4.15, gradients significantly change in the boundary zones, where their peaks increase with the increasing of the prescribed displacements. Therein, the width of the boundary layer increases as the loading progresses. It should be noted that the second-order strain in this case describes the curvature of the strip, which disappears in the middle strip zone, as expected. It can be concluded that the realistic deformation response of the shear layer is again confirmed.

In order to completely verify behaviour of multiscale algorithms developed in this research large strain multiscale analysis has also been conducted. Displacement of the upper clamp has been increased to $u_0 = 0.1\,\mathrm{mm}$. The computed large strain deformation responses are compared with the results obtained by the small strain computation. The distribution of the shear strain component $u_{1,2}$ along the height of the strip is presented in Figure 4.16 for both the large strain and a small strain regimes. The analogous diagram presenting the second-order strain component $u_{1,22}$ is shown in Figure 4.17. It is obvious that only slight differences are exhibited between the large strain and the small strain responses, which proves that the elastoplastic response may be accurately captured in the small strain analysis, too. In accordance with displacement gradients distributions presented, there are no significant differences between the distributions of the equivalent plastic strain over the selected RVEs

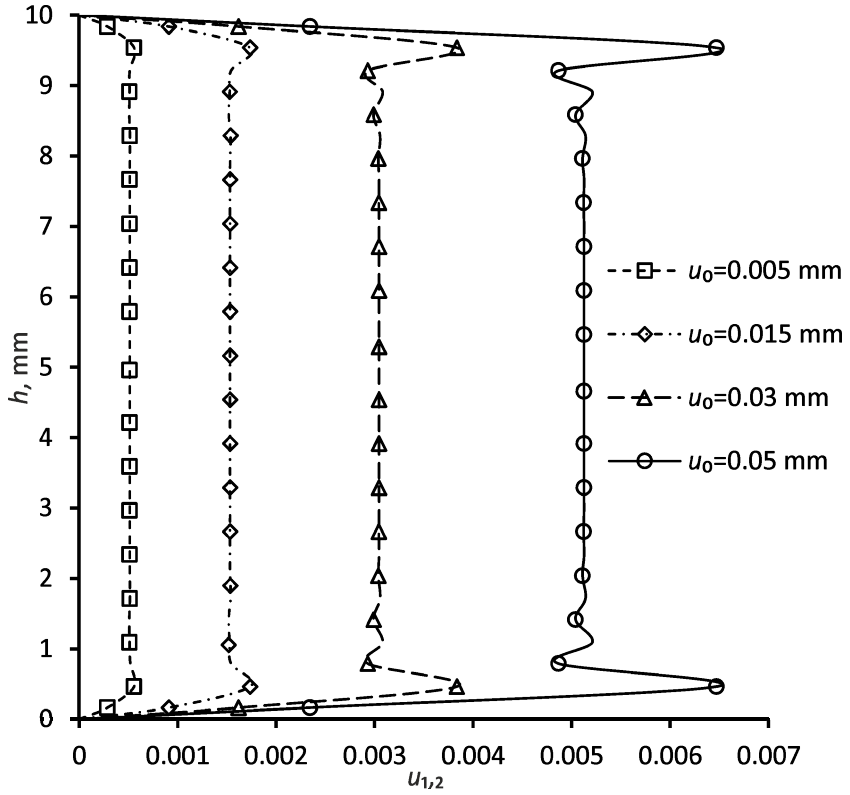

Figure 4.14 Distribution of displacement gradient $u_{1,2}$ for several displacements of u_0, mm

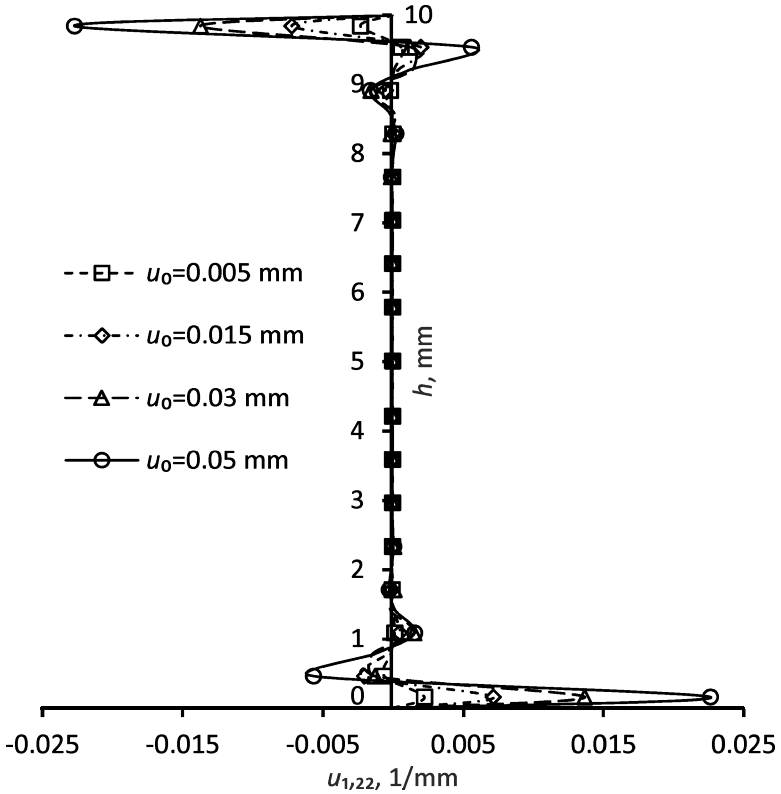

Figure 4.15 Distribution of second-order displacement gradient $u_{1,22}$ for several displacements of u_0, mm

along the height of the strip obtained by the small strain and the large strain computations, as shown in Figure 4.18. As evident from Figure 4.18, three characteristic zones can again be distinguished. The RVEs positioned at the bottom and top of the strip remain mostly elastic, while the microstructural plastic zones are much more developed in the middle of the strip. However, the distinction between the deformation responses of the RVE associated to the pure shear zone at the mid-height of the strip is visible. Here, the RVE rotation is clearly evident which may be considered as the result of the large strain formulation. Since the RVE boundary conditions in the large strain homogenization approach are derived using the deformation gradient, which employs the rotational and stretching mechanisms, as well as the second-order gradient, these deformation responses are correctly transferred at the microstructural level. On contrary, in the small strain context the RVE behavior is determined by the strain and the second-order strain, which is in accordance with the theoretical principles of small strain theory considering the mechanical behavior on the reference configuration only. To exhibit more significant large strain response and to obtain larger differences between small strain and large strain computations, either upper edge displacement should be increased or a material with higher porosity should be considered.

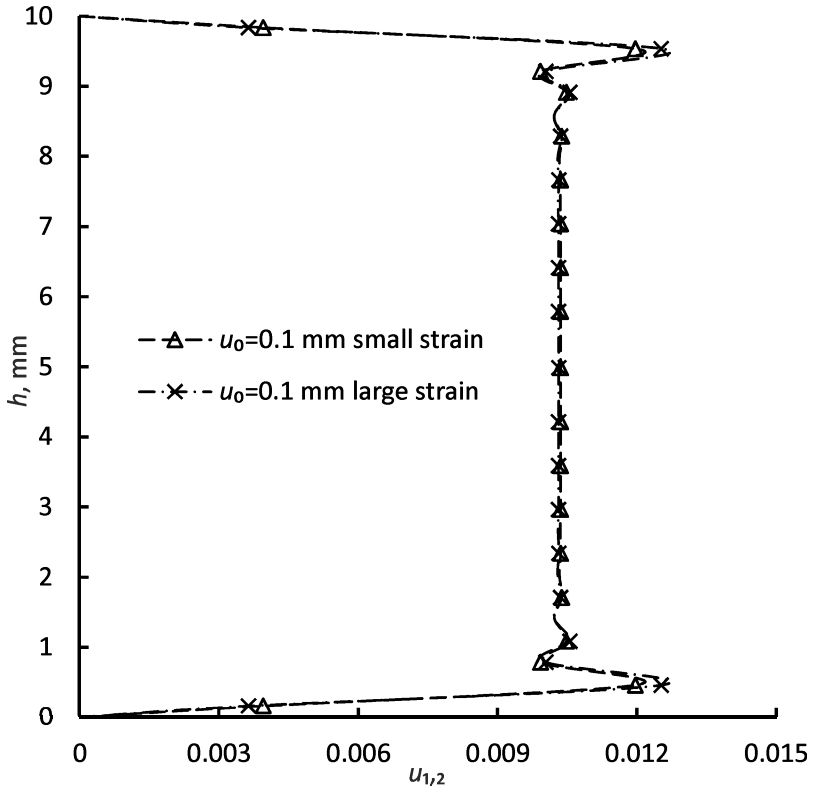

Figure 4.16 Distribution of displacement gradient $u_{1,2}$ for u_0=0.1 mm

Furthermore, Figure 4.19 shows the equivalent plastic strain distribution over the RVE located in the middle of the strip, for the loading cases corresponding to various displacement of u_0, where the development of a shear band is described. It is obvious that the shear band is firstly developed in a vertical direction, between the largest voids, and then it spreads across the RVE with the increase of the prescribed displacement. The shear band development is accompanied with the further deformation of the RVE, as shown in Figure 4.19d.

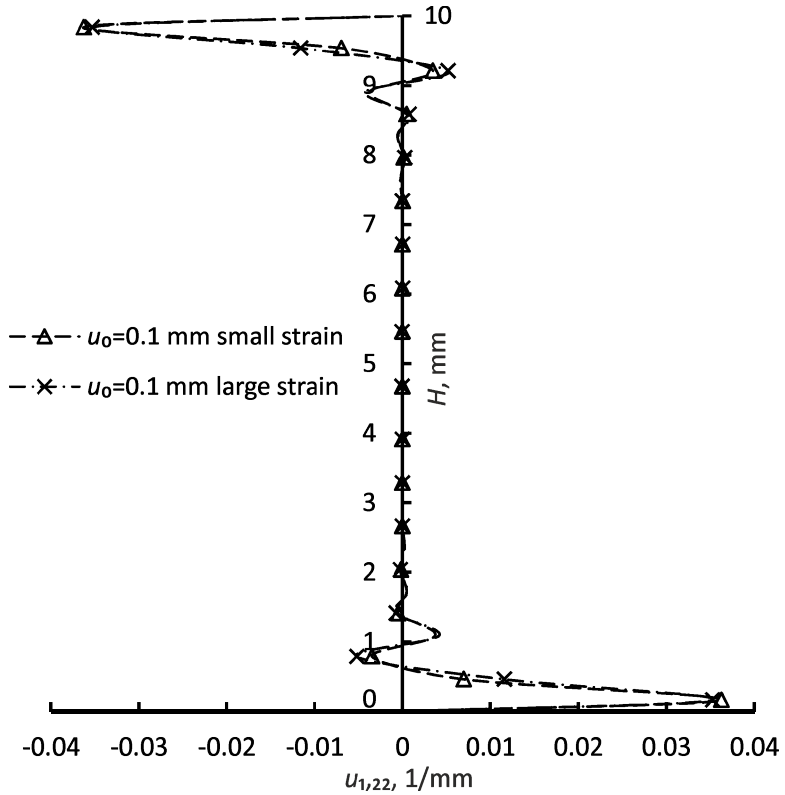

Figure 4.17 Distribution of second-order displacement gradient $u_{1,22}$ for u_0=0.1 mm

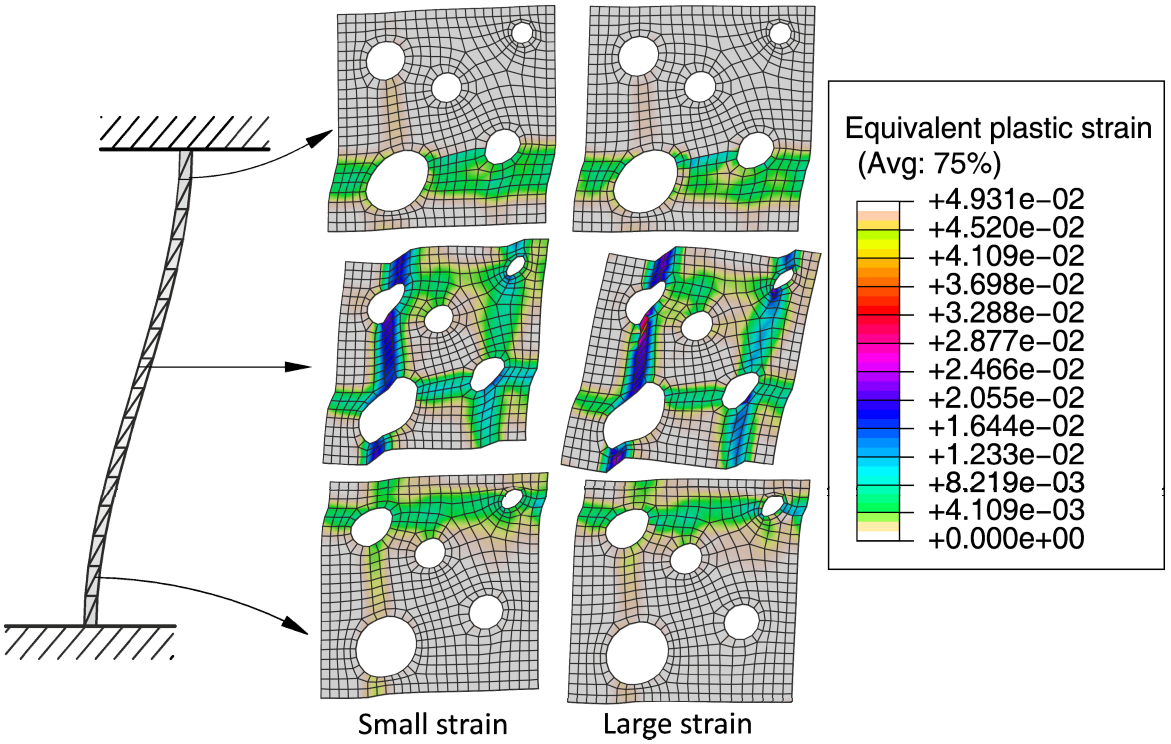

Figure 4.18 Distribution of equivalent plastic strain along the height of the strip for u_0=0.1 mm

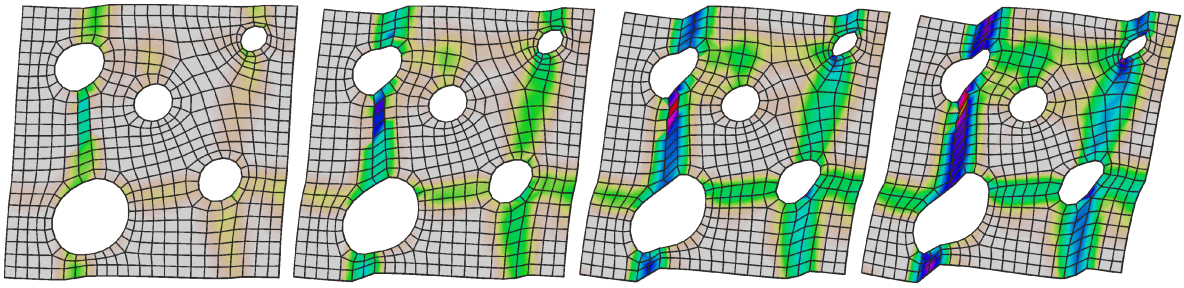

a) **b)** **c)** **d)**

Figure 4.19 Distribution of the equivalent plastic strain on RVE located in the middle of the strip for several loading cases: a) u_0=0.03 mm, b) u_0=0.05 mm, c) u_0=0.075 mm, d) u_0=0.1 mm

4.3.2 Rectangular strip under bending

Next example where multiscale procedure has been tested is a rectangular strip with a length and height of 0.2 m and a thickness of 1 m subjected to bending. The deformation response of a square model discretized by 16 plane strain triangular finite elements is studied, as shown in Figure 4.20a.

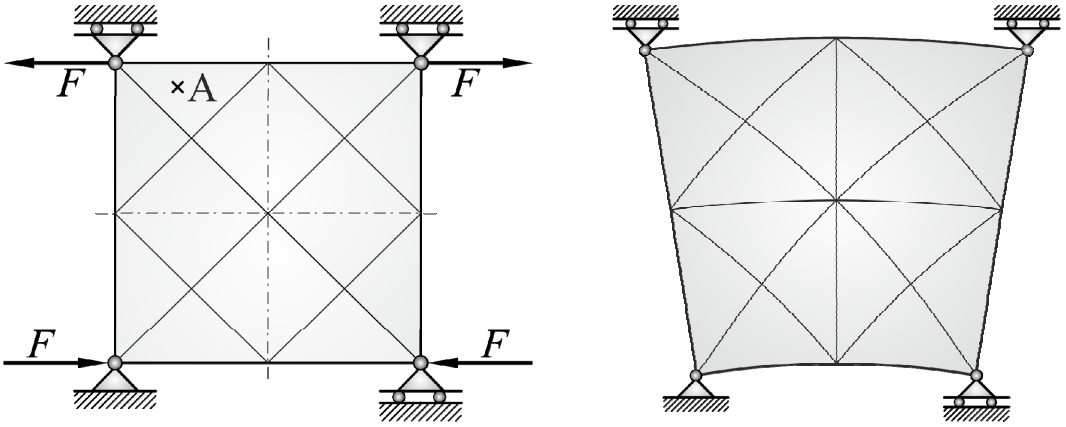

a) b)

Figure 4.20 Strip subjected to bending: a) discretization and loading, b) deformed configuration

The loading and boundary conditions are imposed, which yield the deformed configuration of the macro model displaying constant curvature. The second mixed derivatives and the second derivatives of the normal displacement are suppressed in all nodes. The material considered is an hypothetical example of a steel with a porous microstructure which has been used in the shear layer problem in Section 4.3.1. This computational problem is analogous to the pure bending example already discussed in [8], where it was shown that the second-order approach is needed to determine the deformation pattern accurately. Here the deformation responses are considered using both small strain and the large strain multiscale computational approaches, where next to microstructural cell with 13% of porosities presented in Figure 3.1, cell with 27% randomly distributed voids is analyzed, with geometry displayed in Figure 4.21.

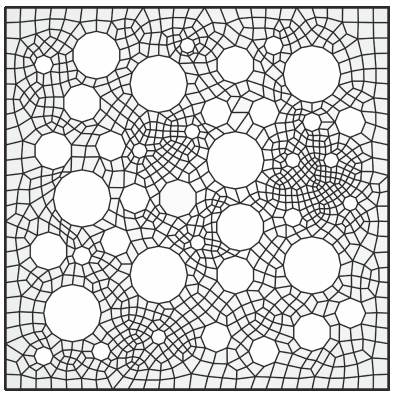

Figure 4.21 RVE presenting steel with porous microstructure with 27% of porosity

The side length of the both RVEs is taken to be $0.2\,\text{mm}$. For comparison, a homogeneous material has also been considered. RVE with 13% voids of an average radius of $0.043\,\text{mm}$ is discretized by 508 quadrilateral finite elements, whereas the discretization of the

microstructural cell with 27% voids with the average radius of $0.0086\,\text{mm}$ is performed using 1198 elements.

The moment-curvature diagram presenting the deformation responses for different computational variants is shown in Figure 4.22. The diagram shows that the stiffness of the analyzed specimens is significantly decreased when the porosity is increased from 13% to 27 % in both small strain and large strain regimes, as expected. Accordingly, for the same curvature the bending moment is significantly reduced if the porosity is increased. It is also evident that the bending moment at a certain curvature is reduced if the large strain elasto-plastic structural computation is performed. It should be stressed that the computational results display the realistic structural behavior, which demonstrates the accuracy of the proposed computational algorithms. Unfortunately, the results cannot be compared with other numerical solutions because they are not available in literature for the heterogeneous microstructure considered. The distribution of the effective plastic strain over the deformed RVEs at the integration point A, shown in Figure 4.20a, are presented in Figs. 4.23 and 4.24. Two different values of bending moments associated to different curvatures, for the both porosities are considered. It is obvious in Figure 4.22 that at the bending moment of $1160\,\text{kNm}$ the structure consisting of 13% porosity remains in an elastic range, while in the case of 27% voids a nonlinear response is displayed.

Figure 4.23 shows that the microstructural shear bands between voids are developed in both the small strain and the large strain regimes. At the bending moment level of $1800\,\text{kNm}$ in RVE with 13% porosity the plastic zones occur only in a small local domains around the voids in the case of a small strain computation. On contrary, in large strain setting spread of plastic zones resulting with the shear bands appears. As obvious, the differences in the elastoplastic behavior are exhibited when the analyses assuming small strain and large strain are performed and compared. Both approaches detect the plastic initiation at the same location, while the plastic localization and the development of shear bands are much more clearly visible in the case of large strain. The RVE obeying the large strain theory is being slightly rotated, which is inherent from the deformation gradient imposed.

It should be noticed that deformed RVEs are not able to demonstrate the macroscopic curvature pattern because a very large ratio between microscopic and macroscopic side length has been chosen. As may be seen in Figure 4.22, both heterogeneous microstructures considered are loaded almost to the macrostructural limit point, and no curvature appears on the RVE. Thus, it is to conclude that the chosen academic materials exhibit too stiff behavior.

The microscopic curvature would be more pronounced, if a larger RVE size would be used. It is known that the determination of the RVE represents an important issue in the homogenization concept. This is particularly important in the second-order homogenization approach, where the nonlocal influence is in direct correlation to the RVE size. However, the RVE determination and its influence on the structural responses is beyond the scope of this thesis and may be found in [78, 140, 150].

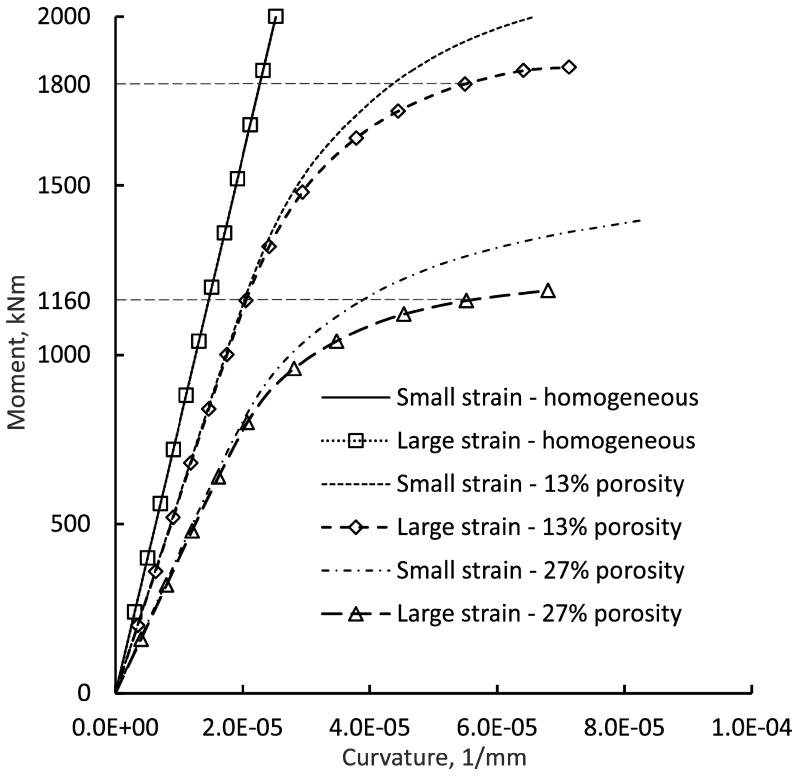

Figure 4.22 Moment-curvature diagram

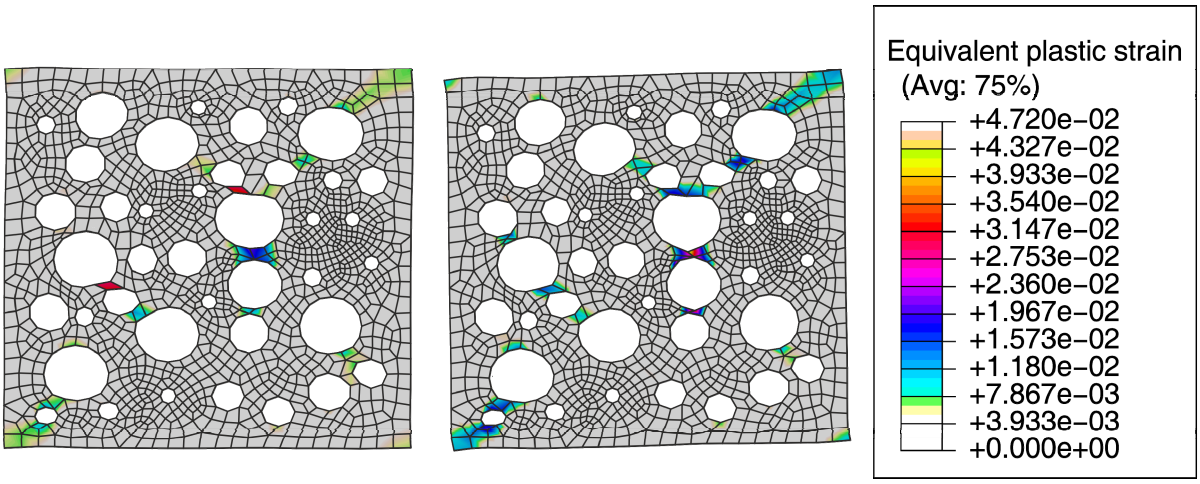

a) **b)**

Figure 4.23 Distribution of effective plastic strain over RVE at integration point A for bending moment of 1160 kNm and porosity of 27%: a) small strain response, b) large strain response

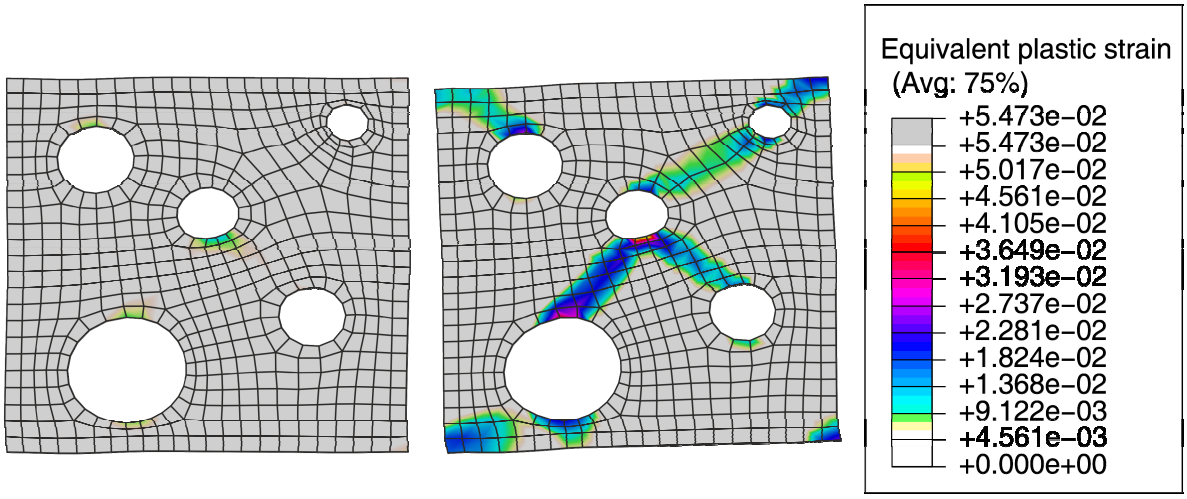

a) **b)**

Figure 4.24 Distribution of effective plastic strain over RVE at integration point A for bending moment of 1800 kNm and porosity of 13%: a) small strain response, b) large strain response

5 C^1 continuous second-order computational homogenization

In the previous chapter a second-order homogenization approach used in the literature [18, 19, 29, 77, 80] has been derived. As a contribution to this C^1-C^0 approach, in this thesis a new C^1 finite element has been derived and used for discretization of a macroscale continuum. Numerical implementation of the scheme has been done into commercial software package ABAQUS/Standard. Even though second-order computational homogenization approach has a many advantages, continuity degradation which brings simplified boundary value problem at the microlevel and an increased numerical efficiency also suffers from several drawbacks, also revealed in [10]. The problem is in the scale transition methodology where C^1-C^0 transition introduces inconsistencies. First inconsistency arises in a volume averaging of the second-order macrolevel gradient, which cannot be related to the microlevel higher-order gradient as a true volume average. Secondly, after resolving Hill-Mandel energy condition, homogenized double stress requires a modified definition at the microstructural level. Also, corner nodes fluctuations are fixed to zero, which consequently leads to an artificial stress concentrations due to strain concentrations in the corners of RVE.

There are several approaches offering solutions to this issues [10, 17, 75, 80], but inconsistencies in a mathematical approach of second-order homogenization still remain. Besides, multiscale modeling of the material softening as well as damage initiation and propagation is mostly done within first-order homogenization approach [151-155]. To enhance numerical accuracy of damage calculations, gradient terms have also been introduced. Noteworthy to mention, in a multiscale damage modeling there are other issues to be solved regarding questionable representativeness of the RVE [71, 150, 156]. It is important to mention, that besides computational and mathematical aspects, preservation of C^0 continuity at the microlevel is also motivated by an experimental determination of constitutive material behaviour, because higher-order continuity at the microlevel also draws gradient dependent constitutive theories requiring experimental material data relating second-order variables. The above mentioned discussion indicates, that for an efficient micro-macro

algorithm comprising second-order homogenization scheme, a higher-order continuum should be introduced at the microlevel.

Hence, in this chapter a new multiscale algorithm based on the second-order computational homogenization is developed. In comparison to the actual multiscale developments employing second-order computational homogenization, a new algorithm preserves C^1 continuity at the microlevel. Microstructure is described by the Aifantis strain gradient elasticity theory assuming linear elastic material behavior and small strains. Since in Aifantis theory only one gradient parameter l^2 appears, issues regarding description of a higher-order microconstituental material behavior can be solved in a straightforward manner. In a new multiscale setting scale transition methodology is derived. Since in a new scheme complementary continuum theories are used at both scales, each macrolevel displacement gradient can be derived as a true volume average of its microconjugate. In a macro-to-micro transition, gradient displacement and gradient generalized periodic boundary conditions are derived. In the same way, in C^1 homogenization each macrolevel stress tensor is derived as a true volume average of its microconjugate.

5.1 Macro-to-micro scale transition

In a newly developed scheme homogenization principles still need to be satisfied. Starting point is a Taylor series expansion of the RVE displacement field depending on the macroscale displacement gradients (3.5), (3.27) and (3.28) which leads to

$$\mathbf{u}_{\mathrm{m}} = \underline{\boldsymbol{\varepsilon}}_{\mathrm{M}} \cdot \mathbf{x} + \frac{1}{2}\left[\mathbf{x} \cdot \left(\nabla \otimes \underline{\boldsymbol{\varepsilon}}_{\mathrm{M}}\right) \cdot \mathbf{x}\right] + \mathbf{r} \,. \tag{5.1}$$

Expressing volume average of the microlevel gradients the following identities are obtained

$$\frac{1}{V}\int_V \left(\nabla_{\mathrm{m}} \otimes \mathbf{u}_{\mathrm{m}}\right) \mathrm{d}V = \frac{1}{V}\int_V \underline{\boldsymbol{\varepsilon}}_{\mathrm{m}} \mathrm{d}V = \underline{\boldsymbol{\varepsilon}}_{\mathrm{M}} + \frac{1}{V}\int_V \left(\left(\nabla \otimes \underline{\boldsymbol{\varepsilon}}_{\mathrm{M}}\right) \cdot \mathbf{x}\right) \mathrm{d}V + \frac{1}{V}\int_V \left(\nabla_{\mathrm{m}} \otimes \mathbf{r}\right) \mathrm{d}V \,. \tag{5.2}$$

Using the same principles as before, the second term on the right side of (5.2) vanishes and last integral term is cast into

$$\frac{1}{V}\int_V \left(\nabla_{\mathrm{m}} \otimes \mathbf{r}\right) \mathrm{d}V = \frac{1}{V}\int_\Gamma \left(\mathbf{n} \otimes \mathbf{r}\right) \mathrm{d}\Gamma = \underline{\mathbf{0}} \,, \tag{5.3}$$

as in (4.3). In a new scheme second-order microlevel gradient can be computed, which is written as

$$\frac{1}{V}\int_V \left(\nabla_{\mathrm{m}} \otimes \underline{\boldsymbol{\varepsilon}}_{\mathrm{m}}\right) \mathrm{d}V = \nabla \otimes \underline{\boldsymbol{\varepsilon}}_{\mathrm{M}} + \frac{1}{V}\int_V \left(\nabla_{\mathrm{m}} \otimes \left(\nabla_{\mathrm{m}} \otimes \mathbf{r}\right)\right) \mathrm{d}V \,. \tag{5.4}$$

From (5.4) another integral relation on the microfluctuation field arises which can be recast using divergence theorem similar as in (5.3)

$$\frac{1}{V}\int_V \left(\nabla_{\mathrm{m}} \otimes \left(\nabla_{\mathrm{m}} \otimes \mathbf{r}\right)\right) \mathrm{d}V = \frac{1}{V}\int_\Gamma \left(\mathbf{n} \otimes \left(\nabla_{\mathrm{m}} \otimes \mathbf{r}\right)\right) \mathrm{d}\Gamma = {}^3\underline{\mathbf{0}}\,. \tag{5.5}$$

In C^1 macro-to-micro transition, there is a clear advantage over classical C^1-C^0 approach, which is brought by consistency of macro- and microgradients. No special assumptions and no long lasting mathematical manipulations are required. On the microlevel gradient displacement- and gradient generalized periodic boundary conditions will be utilized. Basically, these are the same boundary conditions used before. The term „gradient“ makes distinction in a way that not only displacements, but also all displacements gradients used as a nodal degrees of freedom are prescribed, or constrained by periodicity equations. Since in the case of gradient displacement boundary conditions microfluctuation field on the RVE boundaries is suppressed, (5.3) and (5.5) are satisfied without any actions. Based on the periodicity assumptions which have already been declared in the previous chapters, relations (5.3) and (5.5) are also fulfilled.

5.1.1 Boundary conditions on microstructural level

To derive efficient boundary conditions, coordinate matrices are required. The displacement polynomial prescribed from the macrolevel to an *i*th node of RVE is proposed in the following form

$$\begin{aligned}\left(u_1\right)_i = \left(u_{1,1}\right)_{\mathrm{M}}\left(x_1\right)_i + \frac{1}{2}\left(u_{1,2}+u_{2,1}\right)_{\mathrm{M}}\left(x_2\right)_i + \frac{1}{2}\left(u_{1,11}\right)_{\mathrm{M}}\left(x_1^2\right)_i + \\ + \frac{1}{2}\left(u_{1,12}\right)_{\mathrm{M}}\left(x_1x_2\right)_i + \frac{1}{2}\left(u_{1,21}\right)_{\mathrm{M}}\left(x_2x_1\right)_i + \frac{1}{2}\left(u_{1,22}\right)_{\mathrm{M}}\left(x_2^2\right)_i,\end{aligned} \tag{5.6}$$

$$\begin{aligned}\left(u_2\right)_i = \frac{1}{2}\left(u_{1,2}+u_{2,1}\right)_{\mathrm{M}}\left(x_1\right)_i + \left(u_{2,2}\right)_{\mathrm{M}}\left(x_2\right)_i + \frac{1}{2}\left(u_{2,11}\right)_{\mathrm{M}}\left(x_1^2\right)_i + \\ + \frac{1}{2}\left(u_{2,12}\right)_{\mathrm{M}}\left(x_1x_2\right)_i + \frac{1}{2}\left(u_{2,21}\right)_{\mathrm{M}}\left(x_2x_1\right)_i + \frac{1}{2}\left(u_{2,22}\right)_{\mathrm{M}}\left(x_2^2\right)_i.\end{aligned} \tag{5.7}$$

Relations (5.6) and (5.7) should be rewritten in a matrix form using displacement gradients (3.5), (3.27) and (3.28), inherent to Aifantis theory. A minor difficulty arises in a matrix transformation of (5.6) and (5.7). As known, the shear term in the strain tensor is composed of two components. Due to symmetry of the strain tensor linear part of RVE displacement field $\left(u_{1,2}\right)_{\mathrm{M}} x_2$ can be easily established taking one half of $\frac{1}{2}\left(u_{1,2}+u_{2,1}\right)_{\mathrm{M}}$. The same is valid for $\left(u_{2,1}\right)_{\mathrm{M}} x_1$. But second derivatives of the shear strain lose this symmetry property

$\left(u_{1,21} \neq u_{2,11} \text{ and } u_{1,22} \neq u_{2,12}\right)$. Eqs. (5.6) and (5.7) cannot be reproduced through coordinate matrices because in a matrix multiplication derivatives of shear term include two components, and it is not possible to invalidate only single term. However, since order of derivatives is irrelevant, (5.6) and (5.7) are assumed in the following form

$$\begin{aligned}\left(u_1\right)_i = &\left(u_{1,1}\right)_{\mathrm{M}}\left(x_1\right)_i + \frac{1}{2}\left(u_{1,2}+u_{2,1}\right)_{\mathrm{M}}\left(x_2\right)_i + \frac{1}{2}\left(u_{1,11}\right)_{\mathrm{M}}\left(x_1^2\right)_i + \\ &+\left(u_{1,21}\right)_{\mathrm{M}}\left(x_1x_2\right)_i + \frac{1}{2}\left(u_{1,22}\right)_{\mathrm{M}}\left(x_2^2\right)_i,\end{aligned} \tag{5.8}$$

$$\begin{aligned}\left(u_2\right)_i = &\frac{1}{2}\left(u_{1,2}+u_{2,1}\right)_{\mathrm{M}}\left(x_1\right)_i + \left(u_{2,2}\right)_{\mathrm{M}}\left(x_2\right)_i + \frac{1}{2}\left(u_{2,11}\right)_{\mathrm{M}}\left(x_1^2\right)_i + \\ &+\left(u_{2,12}\right)_{\mathrm{M}}\left(x_1x_2\right)_i + \frac{1}{2}\left(u_{2,22}\right)_{\mathrm{M}}\left(x_2^2\right)_i.\end{aligned} \tag{5.9}$$

Polynomials (5.8) and (5.9) maybe rewritten as

$$\begin{aligned}\begin{pmatrix}u_1\\u_2\end{pmatrix}_i = &\begin{pmatrix}x_1 & 0 & \frac{1}{2}x_2\\ 0 & x_2 & \frac{1}{2}x_1\end{pmatrix}_i \underline{\varepsilon}_{\mathrm{M}} + \\ &+\begin{pmatrix}\frac{1}{2}x_1^2 & -\frac{1}{2}x_2^2 & 0\\ 0 & x_1x_2 & \frac{1}{2}x_1^2\end{pmatrix}_i \left(\underline{\varepsilon}_{,1}\right)_{\mathrm{M}} + \begin{pmatrix}x_1x_2 & 0 & \frac{1}{2}x_2^2\\ -\frac{1}{2}x_1^2 & \frac{1}{2}x_2^2 & 0\end{pmatrix}_i \left(\underline{\varepsilon}_{,2}\right)_{\mathrm{M}},\end{aligned} \tag{5.10}$$

for a single node of RVE. To derive coordinate matrices, matrix terms in (5.10) must be extended on all nodal degrees of freedom of C^1 finite element, according to Figure 3.1. This finally leads to

$$\underline{\mathrm{u}}_i = \underline{\underline{\mathrm{D}}}_i^T \underline{\varepsilon}_{\mathrm{M}} + \left(\underline{\underline{\mathrm{H}}}_1^T\right)_i \left(\underline{\varepsilon}_{,1}\right)_{\mathrm{M}} + \left(\underline{\underline{\mathrm{H}}}_2^T\right)_i \left(\underline{\varepsilon}_{,2}\right)_{\mathrm{M}}. \tag{5.11}$$

The coordinate matrices used in (5.11) are defined as

$$\underline{\underline{\underline{\mathrm{D}}}}_i = \begin{pmatrix} x_1 & 0 & \frac{1}{2}x_2 \\ 1 & 0 & 0 \\ 0 & 0 & \frac{1}{2} \\ 0 & 0 & 0 \\ 0 & 0 & 0 \\ 0 & 0 & 0 \\ 0 & x_2 & \frac{1}{2}x_1 \\ 0 & 0 & \frac{1}{2} \\ 0 & 1 & 0 \\ 0 & 0 & 0 \\ 0 & 0 & 0 \\ 0 & 0 & 0 \end{pmatrix}^T, \tag{5.12}$$

$$\left(\underline{\underline{\underline{\mathrm{H}}}}_1\right)_i = \begin{pmatrix} \frac{1}{2}x_1^2 & -\frac{1}{2}x_2^2 & 0 \\ x_1 & 0 & 0 \\ 0 & -x_2 & 0 \\ 1 & 0 & 0 \\ 0 & 0 & 0 \\ 0 & -1 & 0 \\ 0 & x_1x_2 & \frac{1}{2}x_1^2 \\ 0 & x_2 & x_1 \\ 0 & x_1 & 0 \\ 0 & 0 & 1 \\ 0 & 1 & 0 \\ 0 & 0 & 0 \end{pmatrix}^T, \tag{5.13}$$

and

$$\left(\underline{\underline{\mathrm{H}}}_2\right)_i = \begin{pmatrix} x_1x_2 & 0 & \frac{1}{2}x_2^2 \\ x_2 & 0 & 0 \\ x_1 & 0 & x_2 \\ 0 & 0 & 0 \\ 1 & 0 & 0 \\ 0 & 0 & 1 \\ -\frac{1}{2}x_1^2 & \frac{1}{2}x_2^2 & 0 \\ -x_1 & 0 & 0 \\ 0 & x_2 & 0 \\ -1 & 0 & 0 \\ 0 & 0 & 0 \\ 0 & 1 & 0 \end{pmatrix}^T . \tag{5.14}$$

Rigid body movements can be suppressed by an analogous procedure as in C^1-C^0 homogenization. Caution should be taken here in the sense of physical interpretation of a nodal degrees of freedom. In other words, rigid body motions can be removed only on displacement degrees of freedom, while remaining derivatives are not influenced by this action. With introduction of coordinate matrices periodicity equations are derived in the same manner as in Section 4.1.2 taking the similar form

$$\underline{\mathrm{u}}_\mathrm{R} - \underline{\mathrm{u}}_\mathrm{L} = \left(\underline{\underline{\mathrm{D}}}_\mathrm{R}^T - \underline{\underline{\mathrm{D}}}_\mathrm{L}^T\right)\underline{\varepsilon}_\mathrm{M} + \left[\left(\underline{\underline{\mathrm{H}}}_1^T\right)_\mathrm{R} - \left(\underline{\underline{\mathrm{H}}}_1^T\right)_\mathrm{L}\right]\left(\underline{\varepsilon}_{,1}\right)_\mathrm{M} + \left[\left(\underline{\underline{\mathrm{H}}}_2^T\right)_\mathrm{R} - \left(\underline{\underline{\mathrm{H}}}_2^T\right)_\mathrm{L}\right]\left(\underline{\varepsilon}_{,2}\right)_\mathrm{M}, \tag{5.15}$$

$$\underline{\mathrm{u}}_\mathrm{T} - \underline{\mathrm{u}}_\mathrm{B} = \left(\underline{\underline{\mathrm{D}}}_\mathrm{T}^T - \underline{\underline{\mathrm{D}}}_\mathrm{B}^T\right)\underline{\varepsilon}_\mathrm{M} + \left[\left(\underline{\underline{\mathrm{H}}}_1^T\right)_\mathrm{T} - \left(\underline{\underline{\mathrm{H}}}_1^T\right)_\mathrm{B}\right]\left(\underline{\varepsilon}_{,1}\right)_\mathrm{M} + \left[\left(\underline{\underline{\mathrm{H}}}_2^T\right)_\mathrm{T} - \left(\underline{\underline{\mathrm{H}}}_2^T\right)_\mathrm{B}\right]\left(\underline{\varepsilon}_{,2}\right)_\mathrm{M}. \tag{5.16}$$

Periodicity equations in C^1 homogenization make relations not only between displacements, but also between first and second derivatives available as a nodal degrees of freedom. This makes periodicity equation more consistent compared to C^1-C^0 homogenization due to introduction of a higher-order continuum at the microlevel. It also gives possibility to prescribe a full second-order gradient from the macrolevel on the RVE boundaries, without microfluctuation integral. In Section 4.1.1 it has been mentioned that Eq. (5.3) is satisfied automatically considering RVE geometry and periodicity of microfluctuations. So, analogy should be possible in C^1 homogenization regarding Eqs. (5.3) and (5.5). By author's experience this is not the case in C^1 homogenization. To prove the previous statement, unit square model made of homogeneous material has been subjected to a combination of loadings $2\varepsilon_{12} = \varepsilon_{11,2} = 2\varepsilon_{12,2} = 0.1$. To impose the loading on model boundaries, both gradient boundary conditions have been used. If integral relations (5.3) and (5.5) are automatically satisfied

based on the periodicity and the geometry of RVE, deformed shape and distribution of gradients on the model should be equal without any particular prescription of constraints, which is considered here as the second case. The third case has been considered where (5.3) and (5.5) are explicitly imposed on the RVE boundaries. Due to periodicity, integrals must be imposed on two edges only, which is in a matrix form expressed as

$$\int_{\Gamma_L} \underline{u}_L \, d\Gamma = \left(\int_{\Gamma_L} D_L^T \, d\Gamma \right) \underline{\varepsilon}_M + \left(\int_{\Gamma_L} \left(\underline{\underline{H}}_1^T \right)_L d\Gamma \right) \left(\underline{\varepsilon}_{,1} \right)_M + \left(\int_{\Gamma_L} \left(\underline{\underline{H}}_2^T \right)_L d\Gamma \right) \left(\underline{\varepsilon}_{,2} \right)_M , \tag{5.17}$$

$$\int_{\Gamma_B} \underline{u}_B \, d\Gamma = \left(\int_{\Gamma_B} D_B^T \, d\Gamma \right) \underline{\varepsilon}_M + \left(\int_{\Gamma_B} \left(\underline{\underline{H}}_1^T \right)_B d\Gamma \right) \left(\underline{\varepsilon}_{,1} \right)_M + \left(\int_{\Gamma_B} \left(\underline{\underline{H}}_2^T \right)_B d\Gamma \right) \left(\underline{\varepsilon}_{,2} \right)_M . \tag{5.18}$$

The results for distribution of displacement gradients $u_{1,21}$; $u_{2,11}$ and $u_{2,12}$ for gradient displacement and gradient generalized periodic boundary conditions are presented in Figs. 5.1, 5.2 and 5.3.

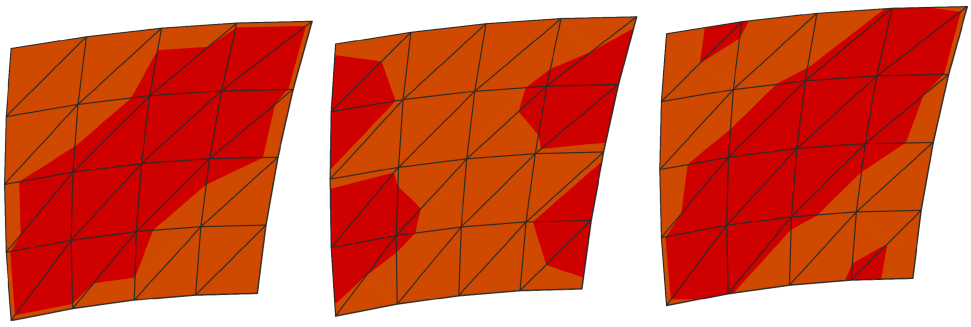

a) **b)** **c)**

Figure 5.1 Distribution of $u_{1,21}$: a) gradient displacement b. c., b) gradient generalized periodic b. c. without microfluctuation integral, c) gradient generalized periodic b. c. with microfluctuation integral

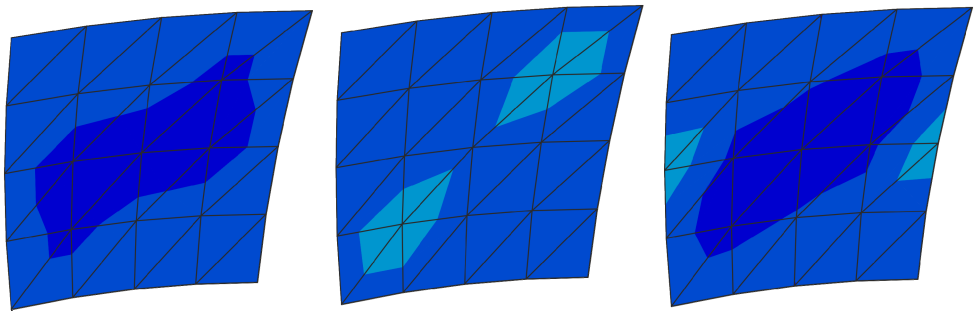

a) **b)** **c)**

Figure 5.2 Distribution of $u_{2,11}$: a) gradient displacement b. c., b) gradient generalized periodic b. c. without microfluctuation integral, c) gradient generalized periodic b. c. with microfluctuation integral

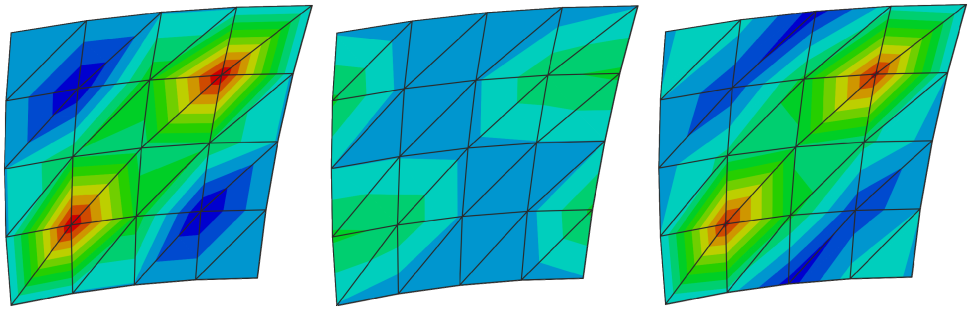

a) **b)** **c)**

Figure 5.3 Distribution of $u_{2,12}$: a) gradient displacement b. c., b) gradient generalized periodic b. c. without microfluctuation integral, c) gradient generalized periodic b. c. with microfluctuation integral

Distribution of shear strain which is also imposed on the boundaries is not displayed here since in this example there is no significant difference in distribution. But, distribution of all second-order strains considered reveals distribution disagreements. It is clear that without explicit imposition of microfluctuation integrals (5.3) and (5.5), results vary in comparison to gradient displacement boundary conditions and periodic conditions where integral relations have been explicitly imposed. These disagreements come even more pronounced for stochastic loading cases and heterogeneous geometries when distribution of the strains differs, which in the worst case leads unphysical deformation responses. With incorrect deformed shapes neither homogenized results cannot be expected to be right. It can be concluded that in C^1 homogenization integrals (5.3) and (5.5) must be explicitly imposed and fulfilled to get meaningful deformed shapes and consequently homogenized solutions, which was not the case in C^1-C^0 homogenization. This can be explained by the fact that in C^1-C^0

homogenization microfluctuation integral (4.20) or (4.92), which provides micro-macro relation of the second-order gradients requires that microfluctuation field vanishes in an averaged sense. By imposing this constraint, integral equation (4.3) is included retroactively.

5.1.2 Effect of microfluctutation integral in C^1 homogenization

Once the necessity of explicit imposition of microfluctuation integrals (5.3) and (5.5) has been confirmed, an effect of integral constraint has been tested. It has been mentioned that in C^1-C^0 homogenization microfluctuation integral in combination with supressed microfluctuations at corner nodes causes localizations and artificial stress concentrations, as confirmed in Section 4.1.5. The problem of corner concentrations has been mostly solved in [10], where microfluctuation constraint is imposed as a volume integral, giving more compliant results. But again, it has been stressed that a relaxed constraints are necessary, because strain concentrations are not fully resolved. Deformation responses are again tested in C^1 homogenization, on the same example of a voided model as in Section 4.1.5, with trapezoidal rule as an only choice of numerical integration scheme. Both loading cases by $u_{1,22}$ and $u_{2,22}$ are examined.

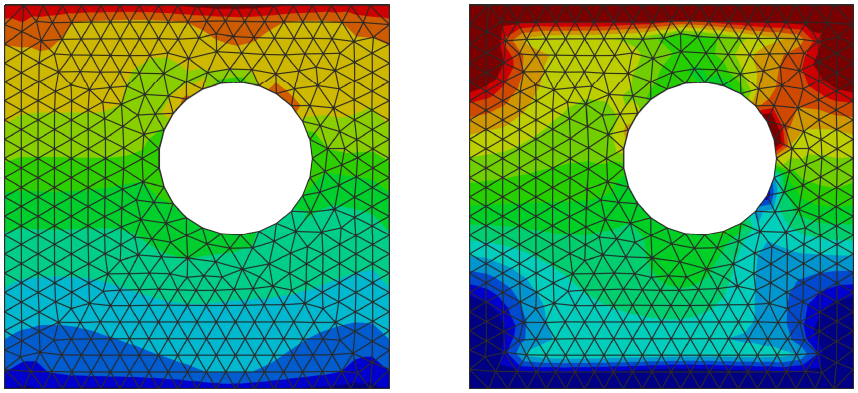

a) **b)**

Figure 5.4 Distribution of strain contours: a) ε_{12} for loading by second-order strain component $u_{1,22}$, b) ε_{22} for loading by second-order strain component $u_{2,22}$

Deformation responses in Figure 5.4 are equivalent to the one presented in Section 4.1.5 and they are not the topic of interest. Of particular interest is a distribution of displacement gradients. There are obvious differences in contour distributions presented in Figure 5.4 in contrary to Figs. 4.5b and 4.6b. In Figs. 5.4a and 5.4b, there is no more strain localizations appearing at the corners. Strains are now equally spreading from the corners through the whole length of the upper and bottom edge of the model. By this, smooth change of strains

from bottom to top is accomplished. Contours presented in Figure 5.4 show very strong similarity to the distributions presented in [10], where such compliant results are obtained by constraining microfluctuation field through whole volume of the model. Considering that equivalent compliant behaviour is obtained only by surface integral, this is one great advantage which comes with consistency of a scale transition in C^1 homogenization.

5.2 Micro-to-macro scale transition

After successfull derivation of consistent macro-to-micro transition, consistency of stress homogenization is also expected due to a second-order stress tensors defined in Aifantis theory, which are a constitutive part of the work done on the microstructural level. By the vrtue of the equivalent continuum theories used at the both scales, Hill-Mandel energy condition has equivalent terms on both sides of equation, which can be experienced in the first-order homogenization only. Using the principle (4.48), Hill-Mandel energy condition takes the form

$$\frac{1}{V}\int_V \left(\underline{\boldsymbol{\sigma}}_{\mathrm{m}} : \delta\underline{\boldsymbol{\varepsilon}}_{\mathrm{m}} + {}^3\underline{\boldsymbol{\mu}}_{\mathrm{m}} \vdots \left(\nabla_{\mathrm{m}} \otimes \delta\underline{\boldsymbol{\varepsilon}}_{\mathrm{m}}\right)\right) \mathrm{d}V = \underline{\boldsymbol{\sigma}}_{\mathrm{M}} : \delta\underline{\boldsymbol{\varepsilon}}_{\mathrm{M}} + {}^3\underline{\boldsymbol{\mu}}_{\mathrm{M}} \vdots \left(\nabla \otimes \delta\underline{\boldsymbol{\varepsilon}}_{\mathrm{M}}\right). \tag{5.19}$$

Left side of Eq. (5.19) is expanded using gradients at the microlevel based on (5.1) and can be written as

$$\begin{aligned} &\frac{1}{V}\int_V W_{\mathrm{m}}\,\mathrm{d}V = \frac{1}{V}\int_V \left(\underline{\boldsymbol{\sigma}}_{\mathrm{m}} : \delta\underline{\boldsymbol{\varepsilon}}_{\mathrm{m}} + {}^3\underline{\boldsymbol{\mu}}_{\mathrm{m}} \vdots \left(\nabla_{\mathrm{m}} \otimes \delta\underline{\boldsymbol{\varepsilon}}_{\mathrm{m}}\right)\right)\mathrm{d}V = \\ &\frac{1}{V}\int_V \left[\underline{\boldsymbol{\sigma}}_{\mathrm{m}} : \left(\delta\underline{\boldsymbol{\varepsilon}}_{\mathrm{M}} + \left(\nabla \otimes \delta\underline{\boldsymbol{\varepsilon}}_{\mathrm{M}}\right)\cdot\mathbf{x} + \nabla_{\mathrm{m}} \otimes \delta\mathbf{r}\right) + {}^3\underline{\boldsymbol{\mu}}_{\mathrm{m}} \vdots \left(\nabla \otimes \delta\underline{\boldsymbol{\varepsilon}}_{\mathrm{M}} + \nabla_{\mathrm{m}} \otimes \left(\nabla_{\mathrm{m}} \otimes \delta\mathbf{r}\right)\right)\right]\mathrm{d}V. \end{aligned} \tag{5.20}$$

By simple rearrangement, (5.20) can be expressed in a more convenient manner

$$\begin{aligned} \frac{1}{V}\int_V W_{\mathrm{m}}\,\mathrm{d}V = &\left(\frac{1}{V}\int_V \underline{\boldsymbol{\sigma}}_{\mathrm{m}}\,\mathrm{d}V\right) : \delta\underline{\boldsymbol{\varepsilon}}_{\mathrm{M}} + \frac{1}{V}\int_V \left(\underline{\boldsymbol{\sigma}}_{\mathrm{m}} : \left(\nabla_{\mathrm{m}} \otimes \delta\mathbf{r}\right)\right)\mathrm{d}V + \\ &+\left(\frac{1}{V}\int_V \left({}^3\underline{\boldsymbol{\mu}}_{\mathrm{m}} + \underline{\boldsymbol{\sigma}}_{\mathrm{m}} \otimes \mathbf{x}\right)\mathrm{d}V\right) \vdots \left(\nabla \otimes \delta\underline{\boldsymbol{\varepsilon}}_{\mathrm{M}}\right) + \frac{1}{V}\int_V \left[{}^3\underline{\boldsymbol{\mu}}_{\mathrm{m}} \vdots \left(\nabla_{\mathrm{m}} \otimes \left(\nabla_{\mathrm{m}} \otimes \delta\mathbf{r}\right)\right)\right]\mathrm{d}V. \end{aligned} \tag{5.21}$$

In Eq. (5.21), integral members containing microfluctuations should vanish for further derivation. Using divergence theorem volume integrals transform into surface integrals and they are read as

$$\frac{1}{V}\int_V \begin{pmatrix} \underline{\boldsymbol{\sigma}}_{\mathrm{m}} : \left(\nabla_{\mathrm{m}} \otimes \delta\mathbf{r}\right) \\ {}^3\underline{\boldsymbol{\mu}}_{\mathrm{m}} \vdots \left(\nabla_{\mathrm{m}} \otimes \left(\nabla_{\mathrm{m}} \otimes \delta\mathbf{r}\right)\right) \end{pmatrix} \mathrm{d}V = \frac{1}{V}\int_\Gamma \begin{pmatrix} \mathbf{n}\cdot\underline{\boldsymbol{\sigma}}_{\mathrm{m}}\cdot\delta\mathbf{r} \\ \mathbf{n}\cdot{}^3\underline{\boldsymbol{\mu}}_{\mathrm{m}} : \left(\nabla_{\mathrm{m}} \otimes \delta\mathbf{r}\right) \end{pmatrix} \mathrm{d}\Gamma = 0. \tag{5.22}$$

Equality (5.22) can be confirmed by the fact that microfluctuations do not contribute to the work performed on the RVE due to periodicity assumptions. Besides, corner microfluctuations are supressed, which in combination with (5.3) and (5.5) once more proves statement (5.22). With this in mind, (5.21) turns into

$$\frac{1}{V}\int_V W_{\mathrm{m}}\,\mathrm{d}V = \left(\frac{1}{V}\int_V \underline{\boldsymbol{\sigma}}_{\mathrm{m}}\,\mathrm{d}V\right) : \delta\underline{\boldsymbol{\varepsilon}}_{\mathrm{M}} + \left(\frac{1}{V}\int_V \left({}^3\underline{\boldsymbol{\mu}}_{\mathrm{m}} + \underline{\boldsymbol{\sigma}}_{\mathrm{m}} \otimes \mathbf{x}\right)\mathrm{d}V\right) \vdots \left(\nabla \otimes \delta\underline{\boldsymbol{\varepsilon}}_{\mathrm{M}}\right). \tag{5.23}$$

Comparing (5.23) to the right side of (5.19) the following equalities can be extracted

$$\underline{\boldsymbol{\sigma}}_{\mathrm{M}} = \frac{1}{V}\int_V \underline{\boldsymbol{\sigma}}_{\mathrm{m}}\,\mathrm{d}V\,, \tag{5.24}$$

$${}^3\underline{\boldsymbol{\mu}}_{\mathrm{M}} = \frac{1}{V}\int_V \left({}^3\underline{\boldsymbol{\mu}}_{\mathrm{m}} + \underline{\boldsymbol{\sigma}}_{\mathrm{m}} \otimes \mathbf{x}\right)\mathrm{d}V\,. \tag{5.25}$$

In Eq. (5.25) two terms appears on the right side. The first member is a second-order stress at the microlevel. Next to him Cauchy stress also appears, multiplied by the position vector. In C^1-C^0 homogenization only the second-term can be used, and it replaces the second-order stress completely. Here in C^1 homogenization this second term basically represents contribution of the heterogeneities to the second-order stress tensors. Homogenized stress tensors can be derived also as a surface integrals taking into account work done at the microstructural level defined as

$$\frac{1}{V}\int_V \left(\underline{\boldsymbol{\sigma}}_{\mathrm{m}} : \delta\underline{\boldsymbol{\varepsilon}}_{\mathrm{m}} + {}^3\underline{\boldsymbol{\mu}}_{\mathrm{m}} \vdots \left(\nabla_{\mathrm{m}} \otimes \delta\underline{\boldsymbol{\varepsilon}}_{\mathrm{m}}\right)\right)\mathrm{d}V = \frac{1}{V}\int_\Gamma \left(\mathbf{t}\cdot\delta\mathbf{u}_{\mathrm{m}} + \left(\boldsymbol{\tau}\otimes\mathbf{n}\right) : \left(\nabla_{\mathrm{m}} \otimes \delta\mathbf{u}_{\mathrm{m}}\right)\right)\mathrm{d}\Gamma\,. \tag{5.26}$$

Substitution of (5.1) into (5.26) gives

$$\begin{aligned}
&\frac{1}{V}\int_\Gamma \left(\mathbf{t}\cdot\delta\mathbf{u}_{\mathrm{m}} + \left(\boldsymbol{\tau}\otimes\mathbf{n}\right) : \left(\nabla_{\mathrm{m}} \otimes \delta\mathbf{u}_{\mathrm{m}}\right)\right)\mathrm{d}\Gamma = \\
&\frac{1}{V}\int_\Gamma \left[\mathbf{t}\cdot\left(\delta\underline{\boldsymbol{\varepsilon}}_{\mathrm{M}}\cdot\mathbf{x} + \frac{1}{2}\left(\mathbf{x}\cdot\left(\nabla\otimes\delta\underline{\boldsymbol{\varepsilon}}_{\mathrm{M}}\right)\cdot\mathbf{x}\right) + \delta\mathbf{r}\right)\right]\mathrm{d}\Gamma + \\
&+\frac{1}{V}\int_\Gamma \left[\left(\boldsymbol{\tau}\otimes\mathbf{n}\right) : \left(\delta\underline{\boldsymbol{\varepsilon}}_{\mathrm{M}} + \left(\nabla\otimes\delta\underline{\boldsymbol{\varepsilon}}_{\mathrm{M}}\right)\cdot\mathbf{x} + \nabla_{\mathrm{m}}\otimes\delta\mathbf{r}\right)\right]\mathrm{d}\Gamma.
\end{aligned} \tag{5.27}$$

Relation (5.27) can be conveniently arranged by grouping of variables to

$$\begin{aligned}
&\frac{1}{V}\int_\Gamma \left(\mathbf{t}\cdot\delta\mathbf{u}_{\mathrm{m}} + \left(\boldsymbol{\tau}\otimes\mathbf{n}\right) : \left(\nabla_{\mathrm{m}} \otimes \delta\mathbf{u}_{\mathrm{m}}\right)\right)\mathrm{d}\Gamma = \left(\frac{1}{V}\int_\Gamma \left(\mathbf{t}\otimes\mathbf{x} + \boldsymbol{\tau}\otimes\mathbf{n}\right)\mathrm{d}\Gamma\right) : \delta\underline{\boldsymbol{\varepsilon}}_{\mathrm{M}} + \frac{1}{V}\int_\Gamma \mathbf{t}\cdot\delta\mathbf{r}\,\mathrm{d}\Gamma + \\
&+\left(\frac{1}{V}\int_\Gamma \left(\frac{1}{2}\left(\mathbf{x}\otimes\mathbf{t}\otimes\mathbf{x}\right) + \boldsymbol{\tau}\otimes\mathbf{n}\otimes\mathbf{x}\right)\mathrm{d}\Gamma\right) \vdots \left(\nabla\otimes\delta\underline{\boldsymbol{\varepsilon}}_{\mathrm{M}}\right) + \frac{1}{V}\int_\Gamma \left(\left(\boldsymbol{\tau}\otimes\mathbf{n}\right) : \left(\nabla_{\mathrm{m}}\otimes\delta\mathbf{r}\right)\right)\mathrm{d}\Gamma.
\end{aligned} \tag{5.28}$$

Integral members containing microfluctuation disappears, which already has been proven. This leads (5.28) to

$$\frac{1}{V}\int_{\Gamma}\left(\mathbf{t}\cdot\delta\mathbf{u}_{\mathrm{m}}+\left(\boldsymbol{\tau}\otimes\mathbf{n}\right):\left(\nabla_{\mathrm{m}}\otimes\delta\mathbf{u}_{\mathrm{m}}\right)\right)\mathrm{d}\Gamma=\left(\frac{1}{V}\int_{\Gamma}\left(\mathbf{t}\otimes\mathbf{x}+\boldsymbol{\tau}\otimes\mathbf{n}\right)\mathrm{d}\Gamma\right):\delta\underline{\boldsymbol{\varepsilon}}_{\mathrm{M}}+$$
$$+\left(\frac{1}{V}\int_{\Gamma}\left(\frac{1}{2}\left(\mathbf{x}\otimes\mathbf{t}\otimes\mathbf{x}\right)+\boldsymbol{\tau}\otimes\mathbf{n}\otimes\mathbf{x}\right)\mathrm{d}\Gamma\right)\vdots\left(\nabla\otimes\delta\underline{\boldsymbol{\varepsilon}}_{\mathrm{M}}\right). \tag{5.29}$$

After back substitution of Eq. (5.29) into (5.26) and then into (5.19) homogenized stress tensors are found in the form

$$\underline{\boldsymbol{\sigma}}_{\mathrm{M}}=\frac{1}{V}\int_{\Gamma}\left(\mathbf{t}\otimes\mathbf{x}+\boldsymbol{\tau}\otimes\mathbf{n}\right)\mathrm{d}\Gamma, \tag{5.30}$$

$${}^{3}\underline{\boldsymbol{\mu}}_{\mathrm{M}}=\frac{1}{V}\int_{\Gamma}\left(\frac{1}{2}\left(\mathbf{x}\otimes\mathbf{t}\otimes\mathbf{x}\right)+\boldsymbol{\tau}\otimes\mathbf{n}\otimes\mathbf{x}\right)\mathrm{d}\Gamma. \tag{5.31}$$

In a practical use, it is common to calculate homogenized stress values in a matrix form. Following the same principles explained in previous chapters homogenized stresses are

$$\underline{\sigma}_{\mathrm{M}}=\frac{1}{V}\underline{\underline{\mathrm{D}}}\underline{\mathrm{f}}_{\mathrm{b}}, \tag{5.32}$$

$$\left(\underline{\mu}_{x_1}\right)_{\mathrm{M}}=\frac{1}{V}\underline{\underline{\mathrm{H}}}_{1}\underline{\mathrm{f}}_{\mathrm{b}}, \tag{5.33}$$

$$\left(\underline{\mu}_{x_2}\right)_{\mathrm{M}}=\frac{1}{V}\underline{\underline{\mathrm{H}}}_{2}\underline{\mathrm{f}}_{\mathrm{b}}. \tag{5.34}$$

5.2.1 Homogenization of macrolevel constitutive behaviour

To complete a whole micro-macro procedure we need to find macroscopic constitutive tangents. Material behaviour of every microconstituent is described by the constitutive operator $\underline{\underline{\mathrm{C}}}_{\sigma\varepsilon}$. To account contribution of the heterogeneous microstructure on the macroscale, one constitutive operator is obviously insufficient. Therefore, generalized incremental Aifantis macroscopic constitutive relations are used at the macrolevel where every stress tensor is dependent on every macrolevel displacement gradient tensor which results in

$$\Delta\underline{\boldsymbol{\sigma}}_{\mathrm{M}}={}^{4}\underline{\mathbf{C}}_{\sigma\varepsilon}:\Delta\underline{\boldsymbol{\varepsilon}}_{\mathrm{M}}+{}^{5}\underline{\mathbf{C}}_{\sigma\varepsilon_{x_1}}\vdots\Delta\left({}^{3}\underline{\boldsymbol{\varepsilon}}_{,1}\right)_{\mathrm{M}}+{}^{5}\underline{\mathbf{C}}_{\sigma\varepsilon_{x_2}}\vdots\Delta\left({}^{3}\underline{\boldsymbol{\varepsilon}}_{,2}\right)_{\mathrm{M}}, \tag{5.35}$$

$$\Delta\left({}^{3}\underline{\boldsymbol{\mu}}_{x_1}\right)_{\mathrm{M}}={}^{5}\underline{\mathbf{C}}_{\mu_{x_1}\varepsilon}:\Delta\underline{\boldsymbol{\varepsilon}}_{\mathrm{M}}+{}^{6}\underline{\mathbf{C}}_{\mu_{x_1}\varepsilon_{x_1}}\vdots\Delta\left({}^{3}\underline{\boldsymbol{\varepsilon}}_{,1}\right)_{\mathrm{M}}+{}^{6}\underline{\mathbf{C}}_{\mu_{x_1}\varepsilon_{x_2}}\vdots\Delta\left({}^{3}\underline{\boldsymbol{\varepsilon}}_{,2}\right)_{\mathrm{M}}, \tag{5.36}$$

$$\Delta\left({}^{3}\underline{\boldsymbol{\mu}}_{x_2}\right)_{\mathrm{M}}={}^{5}\underline{\mathbf{C}}_{\mu_{x_2}\varepsilon}:\Delta\underline{\boldsymbol{\varepsilon}}_{\mathrm{M}}+{}^{6}\underline{\mathbf{C}}_{\mu_{x_2}\varepsilon_{x_1}}\vdots\Delta\left({}^{3}\underline{\boldsymbol{\varepsilon}}_{,1}\right)_{\mathrm{M}}+{}^{6}\underline{\mathbf{C}}_{\mu_{x_2}\varepsilon_{x_2}}\vdots\Delta\left({}^{3}\underline{\boldsymbol{\varepsilon}}_{,2}\right)_{\mathrm{M}}. \tag{5.37}$$

As shown in (5.35)-(5.37), nine constitutive operators are required in a C^1 homogenization, which more than twice required, compared to C^1-C^0 homogenization. Combination of computationally expensive homogenization procedure along with a complex finite element

formulation sounds unattractive, but all the benefices that come with this framework have been demonstrated in theoretical derivations through Chapter 5, and it will be demonstrated in computational examples afterwards.

In this case on the macrolevel there is no microstructural parameter l^2. Logically, microstructural parameter cannot be used twice, at the micro- and macrolevel. As the second, determination of the microstructural parameter belonging to the heterogeneous microstructure is strongly ambiguous. But that does not mean that nonlocality effects cannot be described on the macrostructure. Basically, microstructural parameter of a microconstituent participates in an assembly of RVE global stiffness matrix. After homogenization, contribution of microstructural parameter is averaged through generalized constitutive operators, though it is not directly observable. Determination of constitutive operators (5.35)-(5.37) follows the same procedure of static condensation of global RVE stiffness and it will be not detailed here. All the necessary information can be found in previous derivations. It should be noticed that in C^1 homogenization RVE stiffness matrix used in condensation procedure in Aifantis theory consists of several parts, according to (3.39). After usual derivation steps, homogenized constitutive matrices are expressed through the condensed RVE stiffness $\tilde{\mathbf{K}}_{\mathrm{bb}}$ and coordinate matrices as

$$\underline{\underline{\mathrm{C}}}_{\sigma\varepsilon} = \frac{1}{V}\underline{\underline{\mathrm{D}}}\,\underline{\underline{\tilde{\mathrm{K}}}}_{\mathrm{bb}}\underline{\underline{\mathrm{D}}}^{T}, \tag{5.38}$$

$$\underline{\underline{\mathrm{C}}}_{\sigma\varepsilon_{x_1}} = \frac{1}{V}\underline{\underline{\mathrm{D}}}\,\underline{\underline{\tilde{\mathrm{K}}}}_{\mathrm{bb}}\underline{\underline{\mathrm{H}}}_{1}^{T}, \tag{5.39}$$

$$\underline{\underline{\mathrm{C}}}_{\sigma\varepsilon_{x_2}} = \frac{1}{V}\underline{\underline{\mathrm{D}}}\,\underline{\underline{\tilde{\mathrm{K}}}}_{\mathrm{bb}}\underline{\underline{\mathrm{H}}}_{2}^{T}, \tag{5.40}$$

$$\underline{\underline{\mathrm{C}}}_{\mu_{x_1}\varepsilon} = \frac{1}{V}\underline{\underline{\mathrm{H}}}_{1}\underline{\underline{\tilde{\mathrm{K}}}}_{\mathrm{bb}}\underline{\underline{\mathrm{D}}}^{T}, \tag{5.41}$$

$$\underline{\underline{\mathrm{C}}}_{\mu_{x_1}\varepsilon_{x_1}} = \frac{1}{V}\underline{\underline{\mathrm{H}}}_{1}\underline{\underline{\tilde{\mathrm{K}}}}_{\mathrm{bb}}\underline{\underline{\mathrm{H}}}_{1}^{T}, \tag{5.42}$$

$$\underline{\underline{\mathrm{C}}}_{\mu_{x_1}\varepsilon_{x_2}} = \frac{1}{V}\underline{\underline{\mathrm{H}}}_{1}\underline{\underline{\tilde{\mathrm{K}}}}_{\mathrm{bb}}\underline{\underline{\mathrm{H}}}_{2}^{T}, \tag{5.43}$$

$$\underline{\underline{\mathrm{C}}}_{\mu_{x_2}\varepsilon} = \frac{1}{V}\underline{\underline{\mathrm{H}}}_{2}\underline{\underline{\tilde{\mathrm{K}}}}_{\mathrm{bb}}\underline{\underline{\mathrm{D}}}^{T}, \tag{5.44}$$

$$\underline{\underline{\mathrm{C}}}_{\mu_{x_2}\varepsilon_{x_1}} = \frac{1}{V}\underline{\underline{\mathrm{H}}}_{2}\underline{\underline{\tilde{\mathrm{K}}}}_{\mathrm{bb}}\underline{\underline{\mathrm{H}}}_{1}^{T}, \tag{5.45}$$

$$\underline{\underline{\mathrm{C}}}_{\mu_{x_2}\varepsilon_{x_2}} = \frac{1}{V}\underline{\underline{\mathrm{H}}}_{2}\underline{\underline{\tilde{\mathrm{K}}}}_{\mathrm{bb}}\underline{\underline{\mathrm{H}}}_{2}^{T}. \tag{5.46}$$

5.3 Derivation of nonlocality effect in C^1 homogenization

After establishing micro-macro computational procedure it is necessary to identify nonlocal effects which occur on the RVE and their influence a mechanical response of the macrostructure. It is known that in C^1-C^0 homogenization RVE size dictates nonlocality effects through homogenized double-stress and constitutive operators. On the other hand, in a material model of here presented C^1 homogenization microstructural parameter is present as an intrinsic variable in combination with RVE size. Both parameters generally can be changed independently giving nonlocality effects which are expressed as a combination of both parameters. Thus, for derivation of a robust multiscale scheme relation between nonlocal influence of the RVE size and parameter l should be identified. With known correlation nonlocal influence of the two parameters can be described by one „effective“ nonlocal parameter. In C^1-C^0 homogenization there is a known nonlocality correlation between Aifantis theory and Mindlin's gradient continuum theory identified by a relation between Aifantis microstructural parameter l and RVE size, derived in [77, 78] as

$$l^2 = \frac{L^2}{12}. \tag{5.47}$$

But unfortunately, (5.47) gives correlation among two gradient approaches and it does not resolve the issue when both parameters are present in a single numerical model. The answer can be found in analytical C^1 homogenization. We can take for example homogeneous RVE of side length L discretized by two C1PE3 finite elements, shown in Figure 5.5.

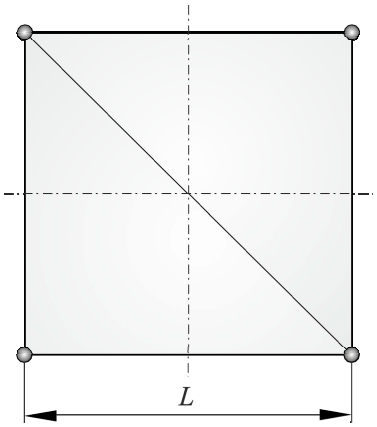

Figure 5.5 Homogeneous RVE discretized by two finite elements

Material considered is linear elastic, with constitutive behaviour defined in (2.28) and (2.29). Global stiffness matrix of the model is also a condensed stiffness $\underline{\underline{\tilde{K}}}_{bb}$, since no internal nodes

are included and no static condensation is needed. After assembly of coordinate matrices based on relations (5.12)-(5.14) we can enter into homogenization formulas (5.38)-(5.46). Due to homogeneity of material, only $\underline{\underline{\mathbf{C}}}_{\sigma\varepsilon}$, $\underline{\underline{\mathbf{C}}}_{\mu_{x_1}\varepsilon_{x_1}}$ and $\underline{\underline{\mathbf{C}}}_{\mu_{x_2}\varepsilon_{x_2}}$ are only non-zero matrices. They are shaped as

$$\underline{\underline{\mathbf{C}}}_{\sigma\varepsilon} = \begin{pmatrix} \lambda+2\mu & \lambda & 0 \\ \lambda & \lambda+2\mu & 0 \\ 0 & 0 & \mu \end{pmatrix}, \tag{5.48}$$

$$\underline{\underline{\mathbf{C}}}_{\mu_{x_1}\varepsilon_{x_1}} = \left(l^2+\frac{L^2}{12}\right)\begin{pmatrix} \lambda+2\mu & \lambda & 0 \\ \lambda & \lambda+2\mu & 0 \\ 0 & 0 & \mu \end{pmatrix}, \tag{5.49}$$

$$\underline{\underline{\mathbf{C}}}_{\mu_{x_2}\varepsilon_{x_2}} = \left(l^2+\frac{L^2}{12}\right)\begin{pmatrix} \lambda+2\mu & \lambda & 0 \\ \lambda & \lambda+2\mu & 0 \\ 0 & 0 & \mu \end{pmatrix}. \tag{5.50}$$

In all homogenized material tangents the usual continuum material matrix (5.48) is being returned, demonstrating validity of the algorithms derived. Material operators (5.49) and (5.50) relating higher-order terms are multiplied by the same constant member, in analogy to (3.30) and (3.31). As can be seen, multiplier appearing in (5.49) and (5.50) consists of known correlation (5.47) and Aifantis microstructural parameter. Its influence on tangent operators (5.49) and (5.50) has the same role as l^2 in (3.30) and (3.31). This brings to the conclusion that a multiplicative member $\left(l^2+\frac{L^2}{12}\right)$ basically represents an "effective" microstructural parameter as an intrinsic variable in C^1 homogenization emerging from the RVE size as well material related Aifantis microstructural parameter l^2. So we can write

$$l_{\text{eff}}^2 = l^2 + \frac{L^2}{12}. \tag{5.51}$$

Relation (5.51) represents Aifantis microstructural parameter in an extended formulation. Therefore, analogical correlation to (5.47) of nonlocality effects in C^1-C^0 and C^1 homogenization emerges in a form

$$l_{\text{eff}}^2 = l^2 + \frac{L_{C^1}^2}{12} = \frac{L_{C^0}^2}{12}. \tag{5.52}$$

In (5.52), L_{C^1} and L_{C^0} stand for RVE sizes in C^1 and C^1-C^0 homogenization, respectively. So, it can be said that (5.52) gives analytical expression for the ratio of the RVE sizes in C^1 and C^1-C^0 homogenization.

5.4 Numerical implementation

Multiscale procedure comprising C^1 homogenization has been implemented into commercial software ABAQUS/Standard using the same principles as for a small strain algorithm detailed in Section 4.1.4. Some basic differences which emerge with C^1 homogenization are displayed

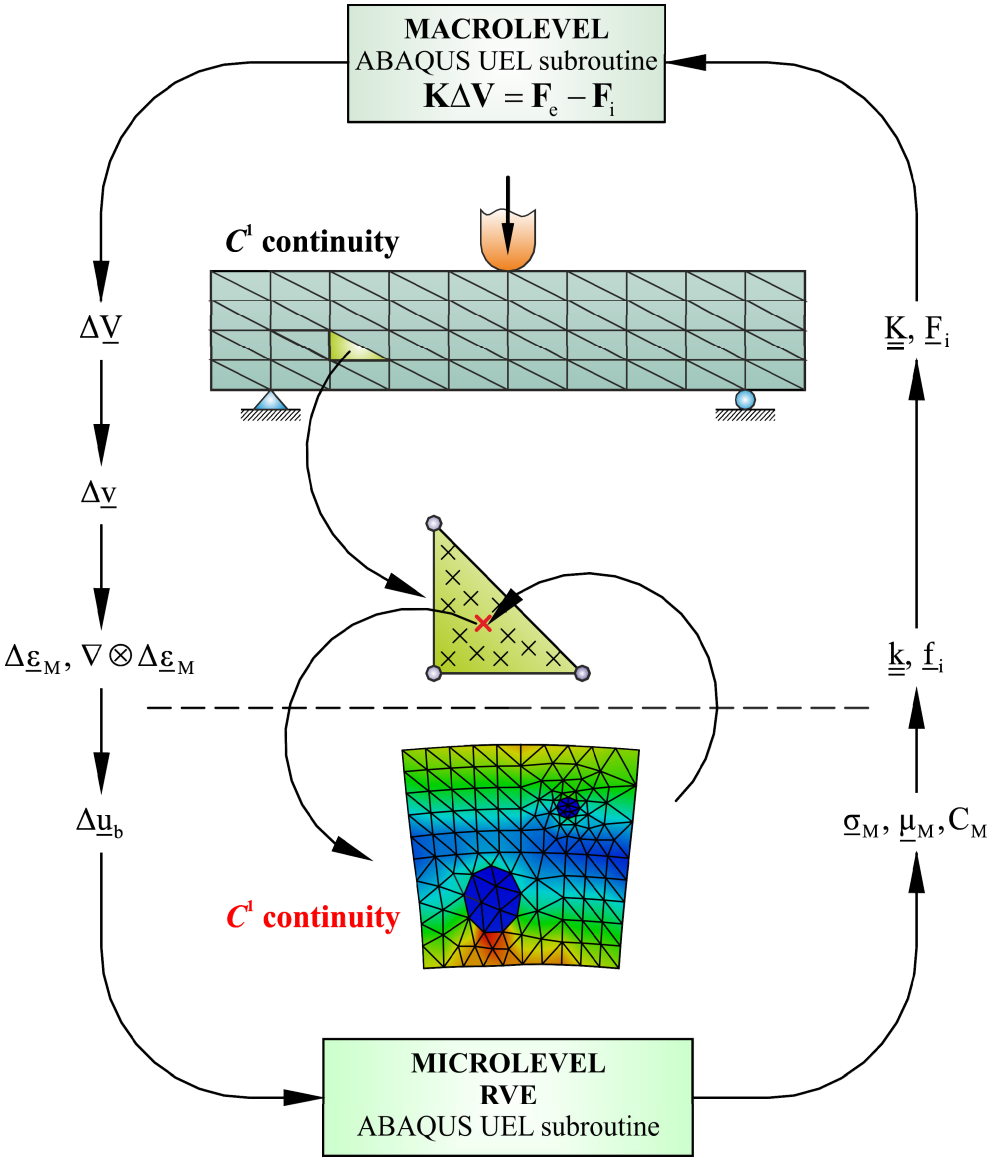

Figure 5.6 Micro-macro C^1 multiscale algorithm

in Figure 5.6. The same C^1 finite element formulation is used for discretization of both levels. UELMAT subroutine which has previously been used for RVE boundary value problem does not support coupled thermal-stress analysis required for implementation of C^1 finite element. Hence, in this framework both scales are numerically implemented by means of UEL subroutine. With UEL subroutine, ABAQUS/Standard material models are not available, and

user coding is required. For a linear elastic material behaviour this does not represent an obstacle. But, in the case of further extension to material nonlinearity, or any other material behaviour, advanced user coding is necessary. Since only a linear elastic behaviour is taken into account, homogenization step for determination of a material matrices can be performed as a preprocessor step which significantly improves speed of the calculations.

It is clear that multiscale scheme in any framework is numerically expensive and time consuming. For such computationally demanding numerical procedure parallelization and cluster computation is a logical options. At the moment of writing this thesis, author did not have a cluster computer available for use, so unfortunately he was not in the opportunity to derive an efficient and robust parallel multiscale code. Nevertheless, to improve the numerical efficiency, "semi-parallelized" code has been developed for all multiscale schemes mentioned in this research. In a default setting multiscale computations are performed in a point-by-point manner. For the C^1 element formulation used in this research this extends computation time per one macroelement enormuously making use of a such advanced procedure impossible in problems where larger amounts of elements is necessary. By „pseudo-parallelization" developed in this thesis computations are performed in a scheme of element-by-element, so this means that 13 RVEs providing homogenized results for 13 material points of one macroscale element are calculated simultaneously. It is important to stress that this scheme consumes considerable amounts of CPU power and RAM memory on a single workstation. In further development of computational procedure combination of „pseudo-parallel" algorithm and e.g. MPI parallelization would make a powerful numerical tool. In conclusion, with a semi-parallelized code, practical problems can be solved on a single workstation by a multiscale procedure within a few hours or days, depending on the size of computational model.

5.5 Convergence properties of C^1 homogenization

After successful derivation of C^1 multiscale procedure, testing of convergence of homogenized results is being performed. Heterogeneous RVE presenting porous steel with 13% of porosity, equivalent to the one used in Section 4.3.1 is now discretized by C1PE3 finite elements. Young's modulus E is taken as 210 GPa, and Poisson's ratio is set to 0.3, as before, but nonlinear behaviour is discarded. Three finite element discretizations have been considered, presented in Figure 5.7. RVE has been subjected to a tension by the strain

component $\varepsilon_{11} = 0.001$ and to bending by the strain gradient component $\varepsilon_{11,2} = 0.001 \frac{1}{\text{mm}}$. For a tension loading convergence of homogenized σ_{11} has been monitored, while for bending loading convergence of homogenized μ_{211} has been tracked. To ensure that convergence is not dependent on a microstructural parameter, two values of l^2 have been considered, $l^2 = 0\,\text{mm}^2$ and $l^2 = 1\,\text{mm}^2$. The results are displayed on diagrams in Figs. 5.8 and 5.9.

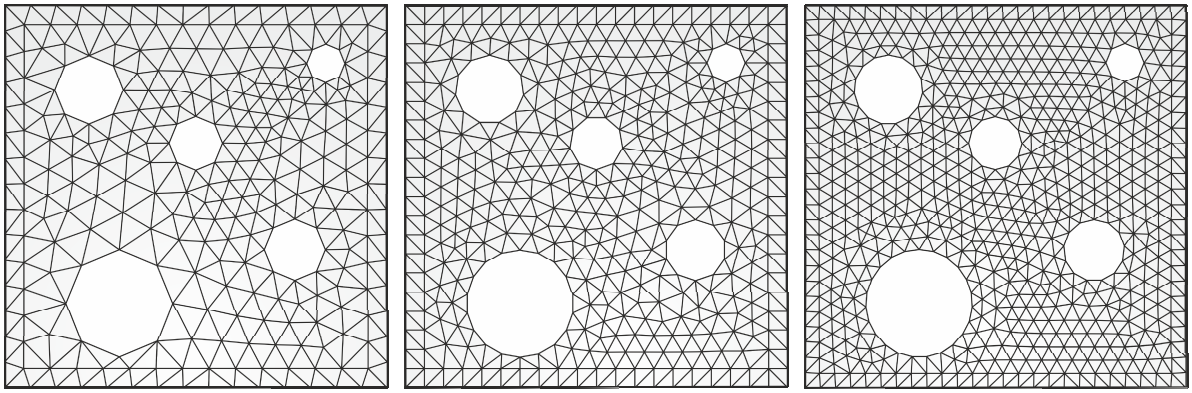

a) **b)** **c)**

Figure 5.7 RVE of side length 0.2 mm discretized by: a) 486, b) 790, c) 1281 C1PE3 finite elements

From the diagrams it can be observed that homogenized stress values are almost constant for all finite element meshes considered. Also, value of l^2 does change only value of homogenized stress, and it is not influenced by the mesh density, which was to expect. It is important to say that the lowest mesh density of 486 elements used is taken as a minimum required for decent description of porosities in the model. Even with this poor mesh homogenized values do not change. Therefore, we can conclude that once optimum mesh density is found, homogenized results will be not affected by the mesh density, thanks to high polynomials used in a finite element formulation.

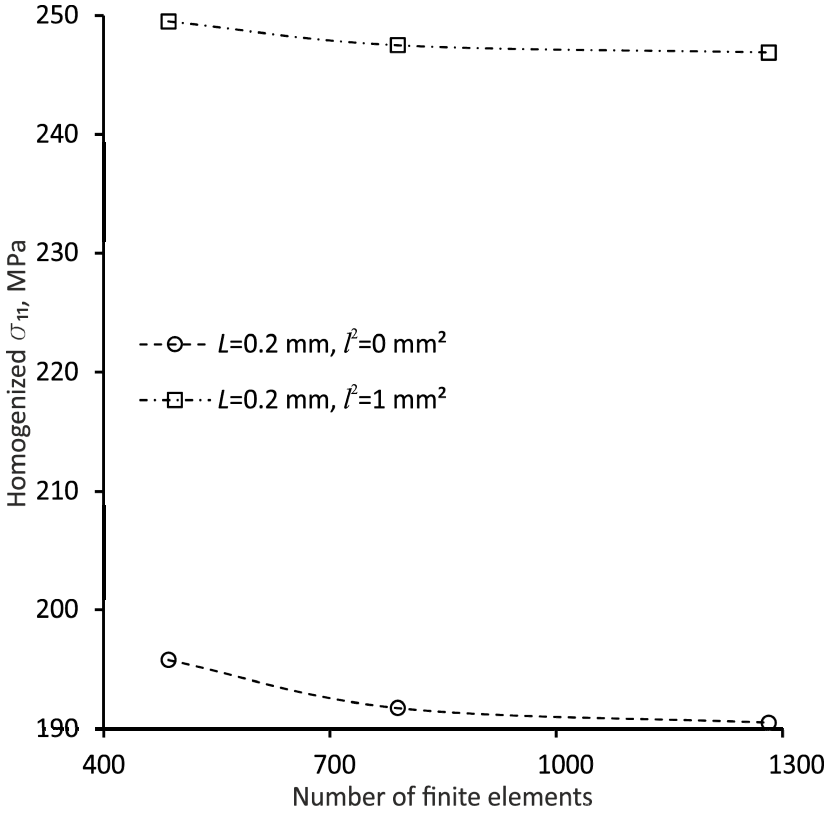

Figure 5.8 Convergence of homogenized σ_{11}

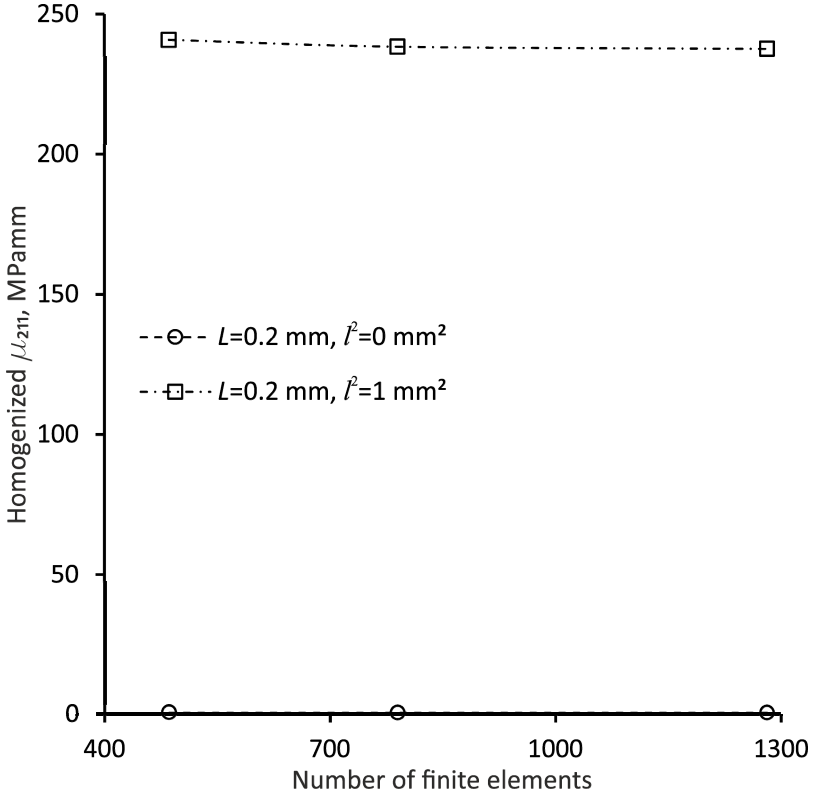

Figure 5.9 Convergence of homogenized μ_{211}

After testing sensitivity of homogenization on mesh density, three RVE sizes representing the same material for several values of l^2 have been compared. RVEs with side lengths of 0.2, 0.5 and 1 mm have been used. They all are presented in Figure 5.10 so that the reader can get a geometrical picture of the microstructure sizes which have been compared. The diagrams presenting the results are shown in Figs. 5.11 and 5.12.

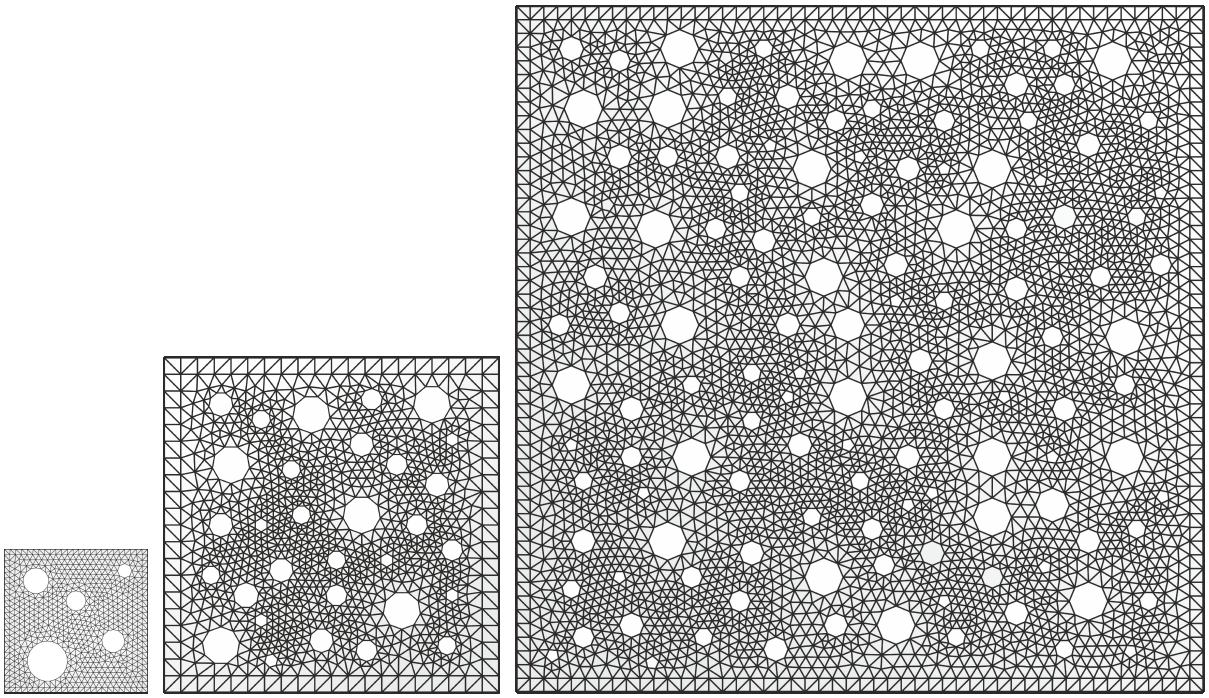

a) **b)** **c)**

Figure 5.10 RVEs presenting porous steel with side length: a) 0.2 mm, b) 0.5 mm, c) 1 mm

As can be seen from Figure 5.11, with slight increase of l homogenized Cauchy stress rises steeply up to the constant value and remains uninfluenced to the change of l. With increase of the RVE size homogenized values change proportionally. Results for RVE sizes of 0.5 and 1 mm are coincident. This brings to the conclusion that RVE size of 0.5 mm can be taken as sufficient if real material would be under test, since with increase of RVE size there is no change in the homogenized response. In Figure 5.12 it can be found that second-order stress has a quadratic change with increase of a microstructural parameter, which is in accordance with constitutive relation (3.31). With change of the RVE size homogenized second-order stress changes accordingly, expressing nonlocal influence. From Figure 5.12 it is clear that determination of the sufficient RVE size on the basis of the second-order stress is dubious due to its constantly changing value with an increase of the RVE size. This issue is also mentioned in [77]. Finally, it can be said that convergence of homogenized results in C^1 homogenization is easily achieved.

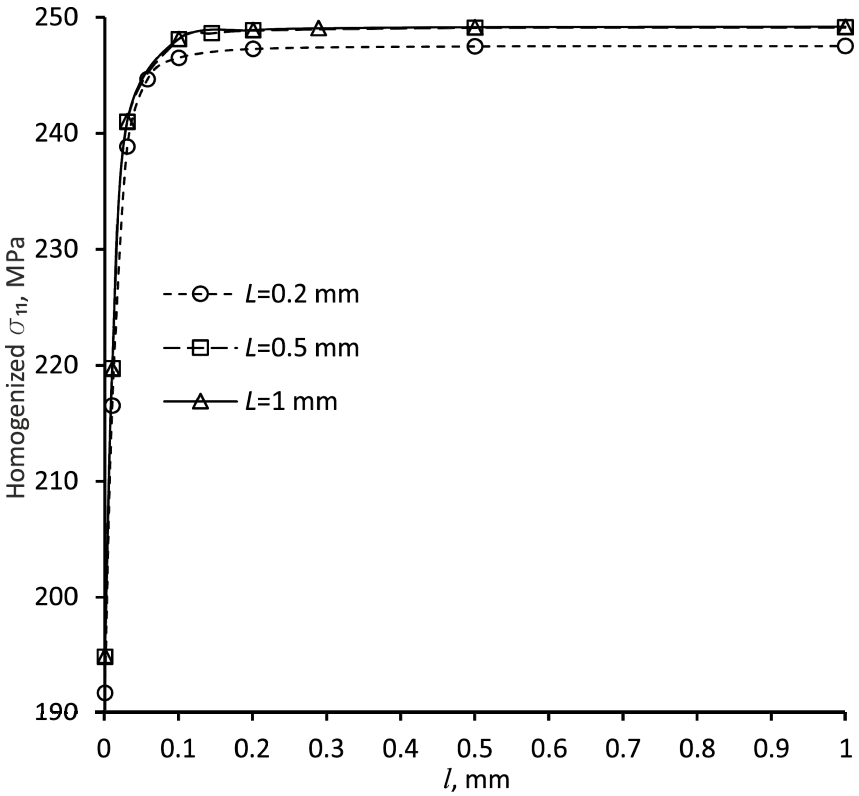

Figure 5.11 Homogenized values of σ_{11} for different RVE sizes and microstructural parameter

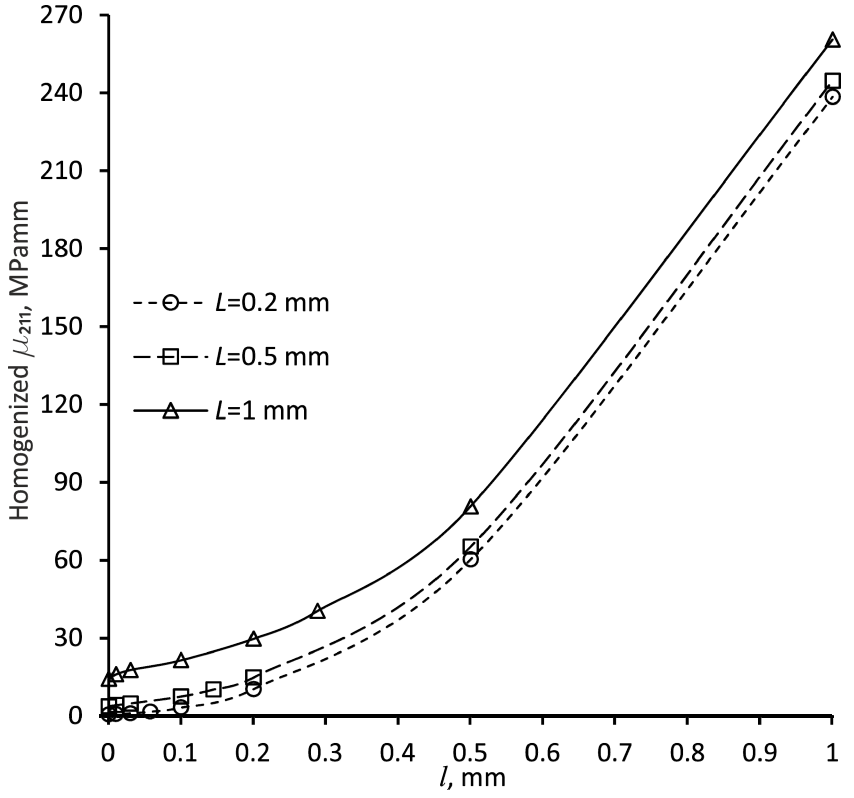

Figure 5.12 Homogenized values of μ_{211} for different RVE sizes and microstructural parameter

5.6 Numerical examples

5.6.1 Shear layer problem

In the first example, widely used shear layer problem has been analyzed. This benchmark test has already been used in this thesis for verification of C^1-C^0 homogenization of a small and a large strain setting in Section 4.3.1. In further testing C^1 multiscale procedure will be compared to C^1-C^0 scheme. To make results obtained by two distinct approaches comparable, Eq. (5.52) is used as a link among them. For $l^2 = 0$, equal RVE sizes in two homogenization approaches must give an equivalent nonlocal behaviour. Macromodel with boundary conditions is found in Figure 4.8a. In example considered here displacement of the upper clamp is $u_0 = 0.005\,\text{mm}$. Again academic porous steel with 13% of porosity has been used, but now nonlinear material behaviour is discarded. RVE of side length $L = 0.2\,\text{mm}$ used in C^1-C^0 homogenization discretized by 508 quadrilateral finite elements has been presented in Figure 4.9 and equivalent discretization of RVE by 790 C1PE3 elements is given in Figure 5.7b. In C^1 homogenization gradient displacement and gradient generalized periodic boundary conditions have been used and compared to C^1-C^0 generalized periodic boundary conditions. Distribution of first and second derivatives through height of the strip is represented in Figs. 5.13 and 5.14. Both Figures show identical results of distributions, proving derived identities in this research. Both type of gradient boundary conditions have shown a consistent behaviour in comparison to C^1-C^0 boundary conditions.

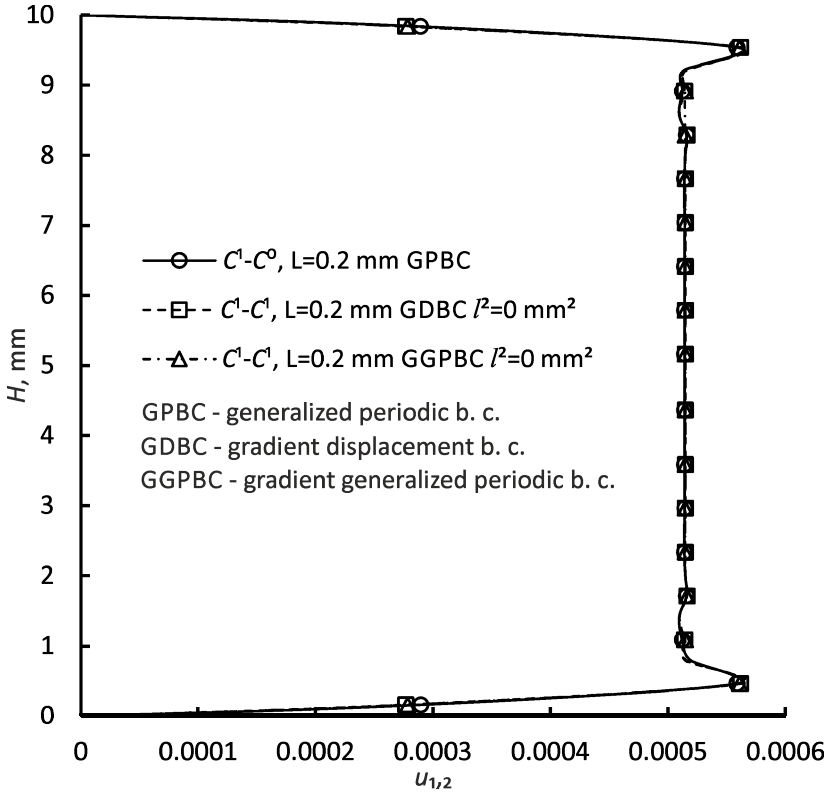

Figure 5.13 Distribution of displacement gradient $u_{1,2}$ for RVE side length 0.2 mm

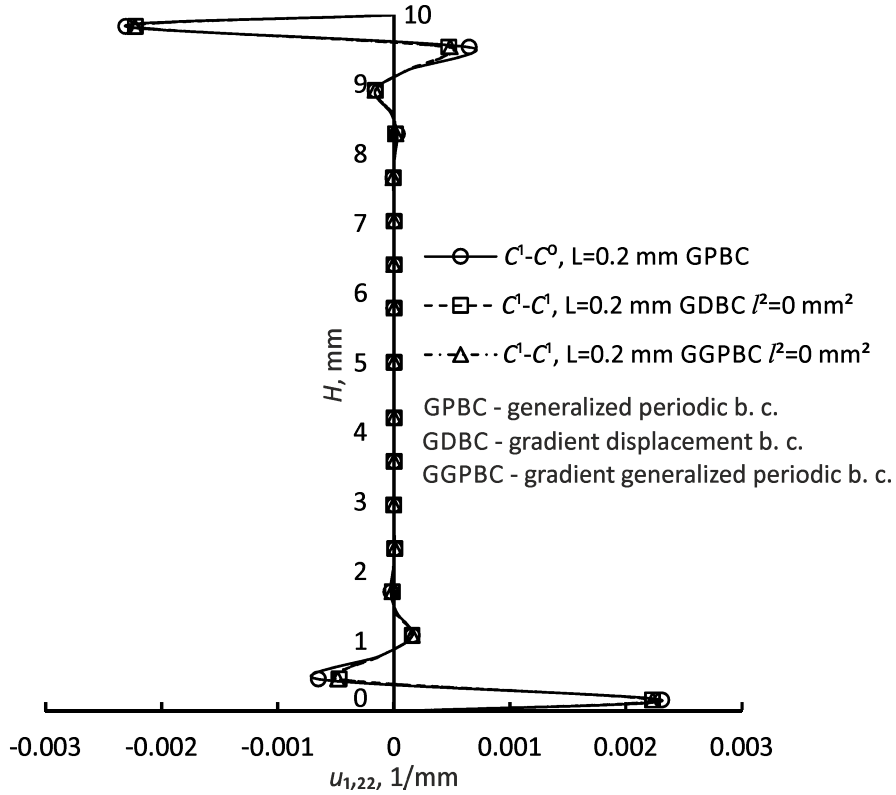

Figure 5.14 Distribution of second-order displacement gradient $u_{1,22}$ for RVE side length 0.2 mm

Now it is necessary to demonstrate that Eq. (5.52) holds also for a non-equal RVE sizes in two homogenization approaches. In this context, two RVEs discretized by quadrilateral finite

elements have been introduced. Figure 5.15 represents RVE of side length 0.5 mm discretized by 1779 finite elements as an equivalent to the one shown in Figure 5.10b.

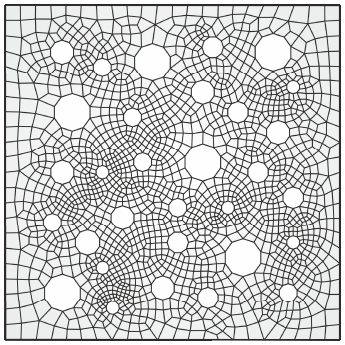

Figure 5.15 RVE of side length 0.5 mm discretized by 1779 finite elements

Figure 5.16 represents RVE of side length 1 mm discretized by 5667 finite elements as an equivalent to the one shown in Figure 5.10c.

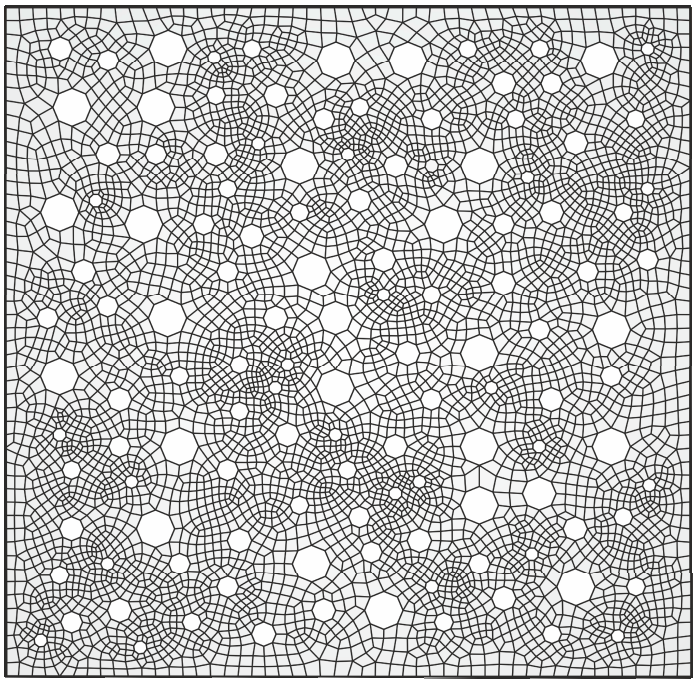

Figure 5.16 RVE of side length 1 mm discretized by 5667 finite elements

In the following figures distribution of the first and second-order derivatives for two homogenization approaches is presented for RVE sizes 0.5 and 1 mm.

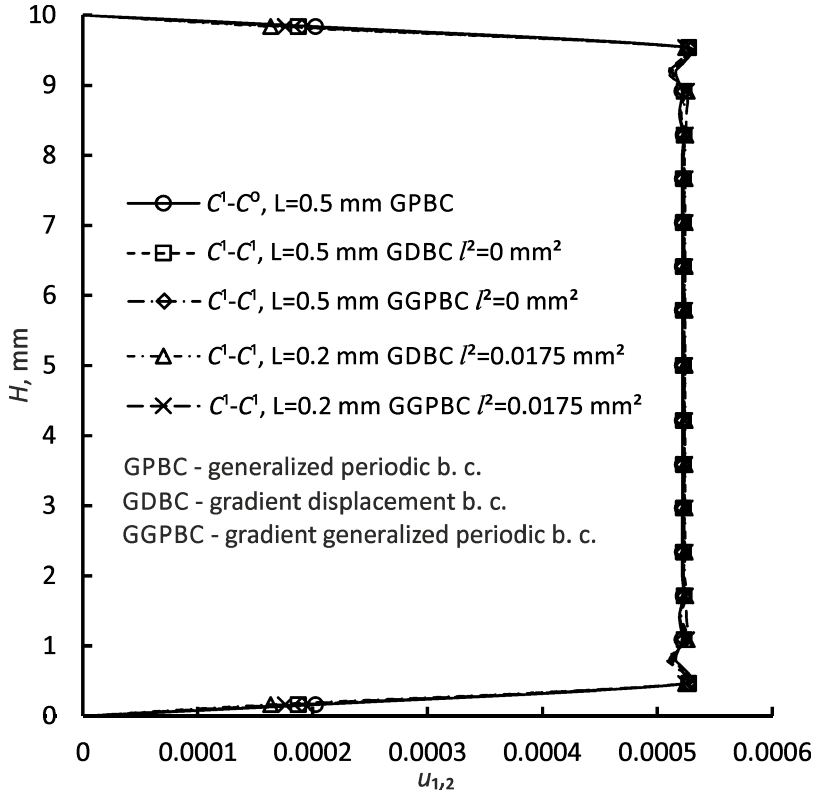

Figure 5.17 Distribution of displacement gradient $u_{1,2}$ for RVE side length size 0.5 mm

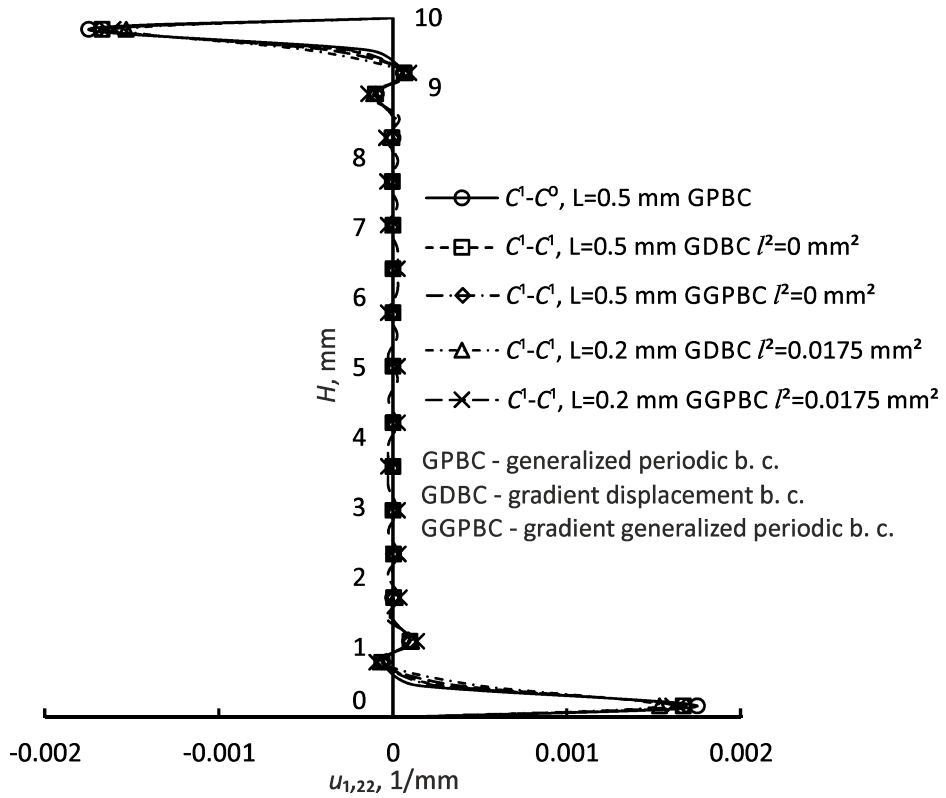

Figure 5.18 Distribution of second-order displacement gradient $u_{1,22}$ for RVE side length 0.5 mm

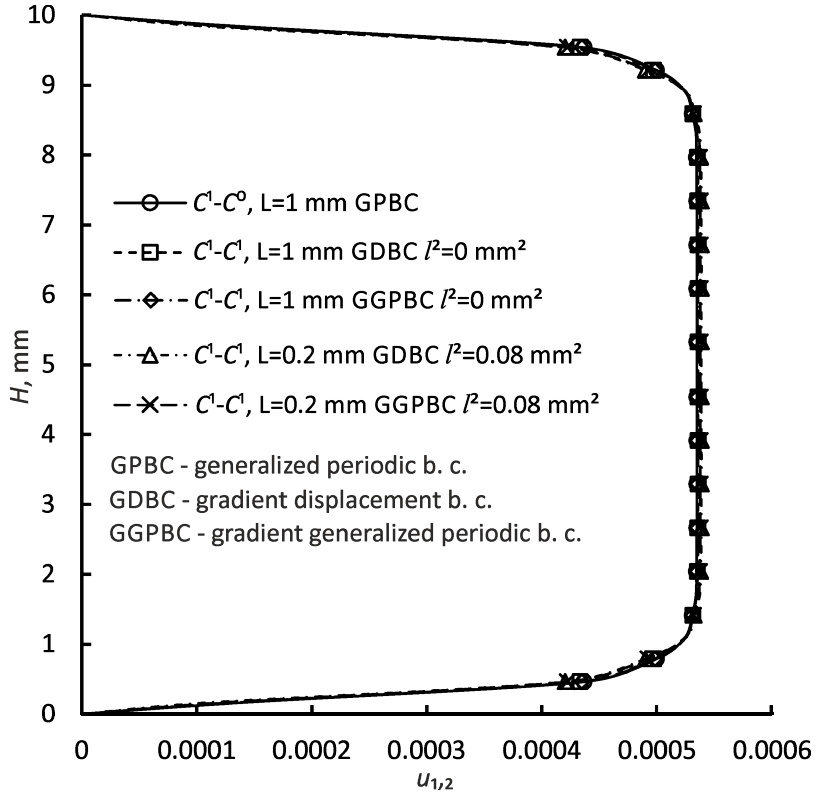

Figure 5.19 Distribution of displacement gradient $u_{1,2}$ for RVE side length 1 mm

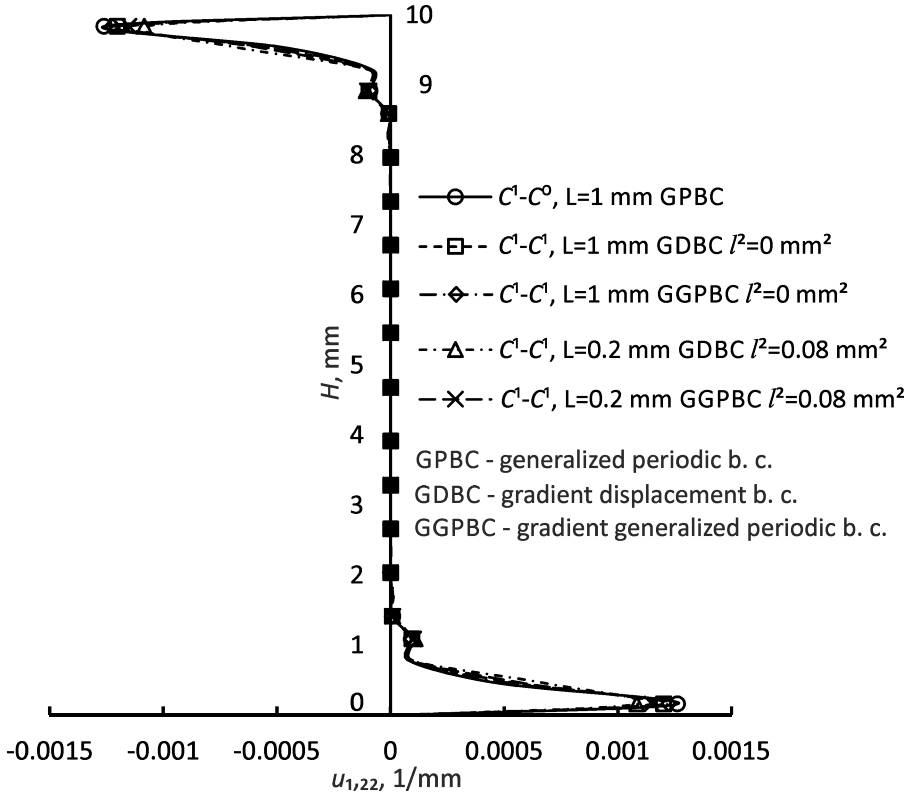

Figure 5.20 Distribution of second-order displacement gradient $u_{1,22}$ for RVE side length 1 mm

Distributions presented in Figs. 5.17-5.20 once again demonstrate validity of derivations in C^1 homogenization in a multiple ways. As first, all the distributions for RVE sizes of 0.5 and 1

mm used in both C^1-C^0 and C^1 homogenization are identical with both types of gradient boundary conditions. As the second, ability of C^1 approach to encompass nonlocal effects by a combination of the RVE size and microstructural parameter l has been demonstrated. For example, in Figs. 5.17 and 5.18 there are results for RVE of side length 0.2 mm used in C^1 homogenization. To recover RVE size difference to 0.5 mm on the basis of Eq. (5.52) appropriate measure of $l^2 = 0.0175\,\mathrm{mm}^2$ is calculated and prescribed to the material model. In Figs. 5.19 and 5.20 besides RVE with a side length 1 mm, five times smaller RVE has been used in C^1 homogenization. To encompass equivalent nonlocal behaviour measure of $l^2 = 0.08\,\mathrm{mm}^2$ has been added into material model. The same effects are achieved by gradient displacement and gradient generalized periodic boundary conditions.

Hence, a conclusion is that C^1 homogenization offers a great numerical advantage, where smaller RVE sizes can be used in computations giving an equivalent material behaviour as several times larger RVE has been considered. Smaller RVE also means faster computational time. This is very important in a static condensation when inverse of $\underline{\underline{\mathrm{K}}}_{aa}$ must be explicitly found, Eq. (4.71). After successfull verification, superiority of C^1 homogenization has been demonstrated in comparative analysis of shear layer problem. Gradient generalized periodic boundary conditions have been used on RVE with $L = 0.2\,\mathrm{mm}$, while microstructural parameter l^2 has been increased gradually. Figs. 5.21 and 5.22 show calculated results.

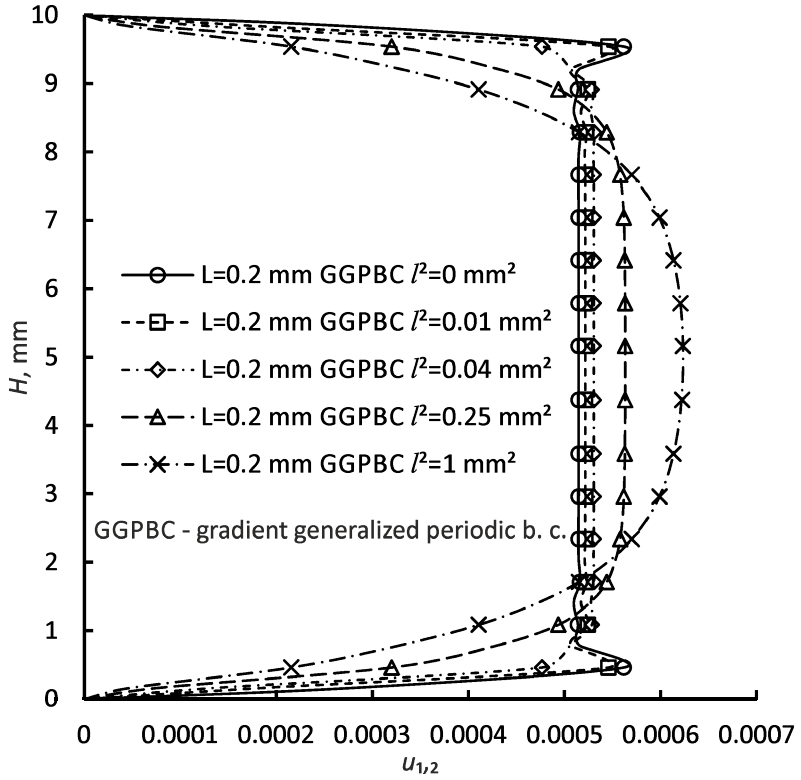

Figure 5.21 Distribution of displacement gradient $u_{1,2}$ for RVE side length 0.2 mm and various microstructural parameter values

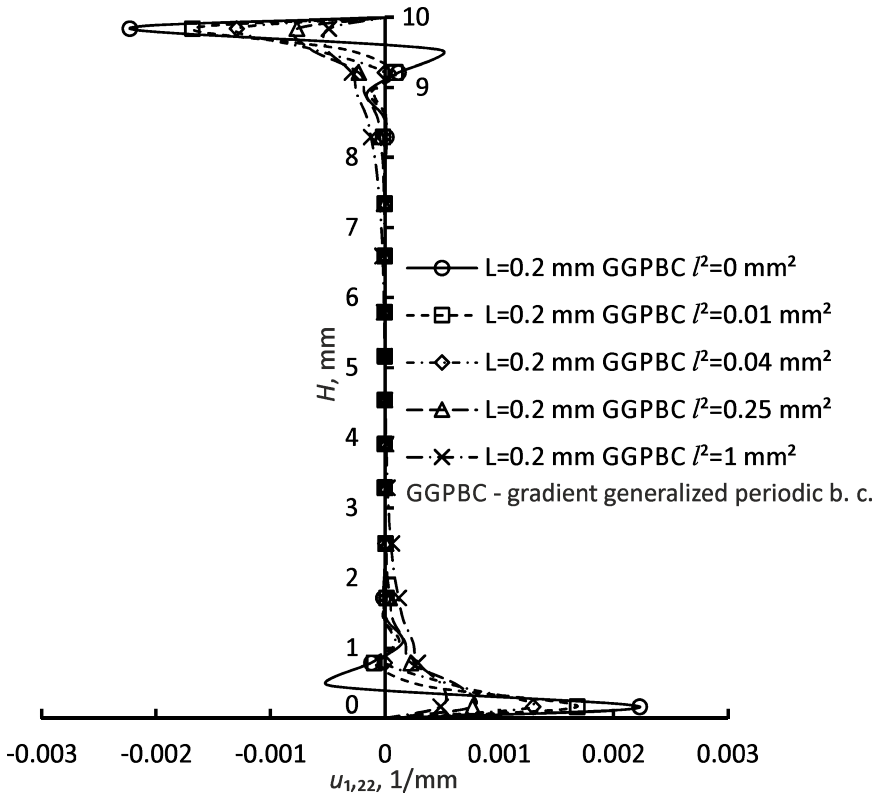

Figure 5.22 Distribution of second-order displacement gradient $u_{1,22}$ for RVE side length 0.2 mm and various microstructural parameter values

In Figs. 5.21 and 5.22 boundary layers with a vanishing shear in the vicinity of the lower and upper clamp can be clearly observed. With increase of l^2 width of the middle shear layer reduces, but there is an evident perturbation in boundary layers. For smaller values of l^2 there are high peaks appearing in the boundary layers, which suddenly drop towards the middle shear. For larger values of l^2 and stiffer material behaviour these peaks slowly reduce and exceed into a smooth change of gradients. With this peak-into-smooth transition width of a boundary layers overwhelms almost full height of the strip. Distribution of displacement gradient component $u_{1,2}$ over characteristic RVEs through height of the strip for $L = 0.2\,\text{mm}$ and $l^2 = 0$ is visualized in Figure 5.23.

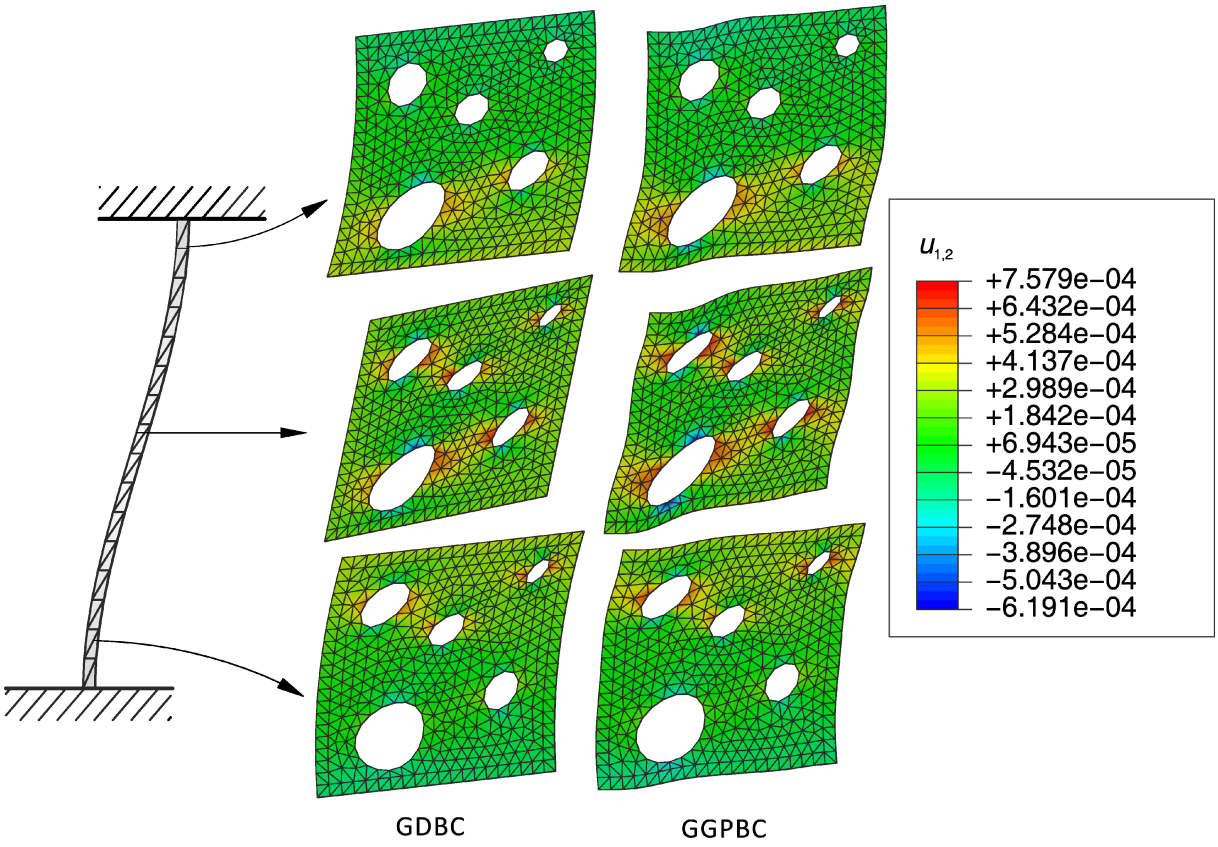

Figure 5.23 Distribution of displacement gradient component $u_{1,2}$ on RVEs through height of the strip

In Figure 5.23 response of gradient displacement and gradient generalized periodic boundary conditions are compared. Three characteristic zones are distinguishable, as before. Deformed RVE shapes correspond to ones visualized in Figure 4.13, which should be a case considering comparability of a two homogenization schemes. Gradient displacement boundary conditions provide stiffer behaviour due to suppression of microfluctuations. Further, distribution of

second-order displacement gradient $u_{1,22}$ is displayed in Figure 5.24, which was not possible in C^1-C^0 approach.

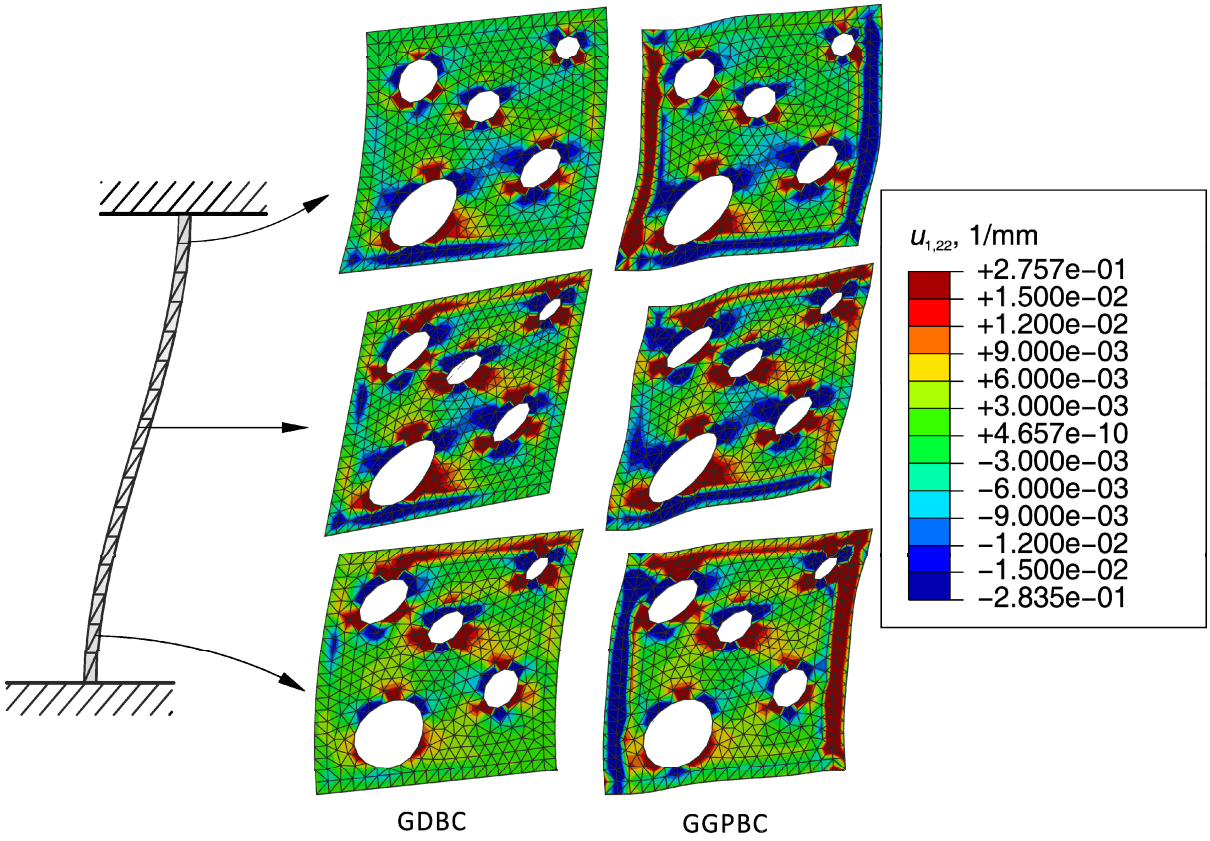

Figure 5.24 Distribution of second-order displacement gradient component $u_{1,22}$ on RVEs through height of the strip

The distinction of the gradient displacement and periodic boundary conditions in this Figure is even more prominent. There are strong gradients appearing around porosities, of a positive and negative sign which physically represent strong jumps in a curvatures around holes. Strong curvatures are also present near outside edges of the RVEs in a gradient generalized periodic boundary conditions, which is not the case for gradient displacement boundary conditions. This inequalities in a distribution of second-order derivatives clearly prove enhanced compliance of the gradient periodic boundary conditions.

5.6.2 Three point bending test

The last example considered is a three point bending test of the notched specimen. The discretized model with boundary conditions is presented in Figure 5.25. The dimensions of the test specimen are $100 \times 20 \times 10\,\text{mm}$ with a notch root radius of 0.08 mm according to the standard ASTM E1820. The support-span is 79 mm.

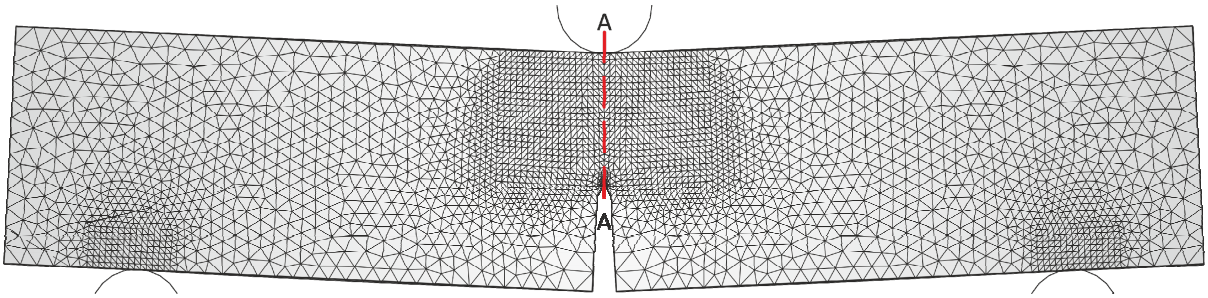

Figure 5.25 Three point bending test specimen

Boundary conditions are simulating real experimental setup. The two support and one loading rollers have a diameter of 8 mm and the force of 10 kN has been applied to the loading roller. In a numerical setup rollers are modeled as analyticaly rigid bodies. Contact properties among rollers and specimen have been assigned. A finer mesh is used in the vicinity of the notch and near the roller contact regions where high stress gradient is expected. The material considered is an academic example of a linear elastic steel with 13% randomly distributed porosities. Young's modulus is taken as 210 GPa, and Poisson's ratio is set to 0.3. Material microstructure is represented by RVE of a side length $L = 0.2\,\text{mm}$, which is discretized by 790 finite elements, as shown in Figure 5.26.

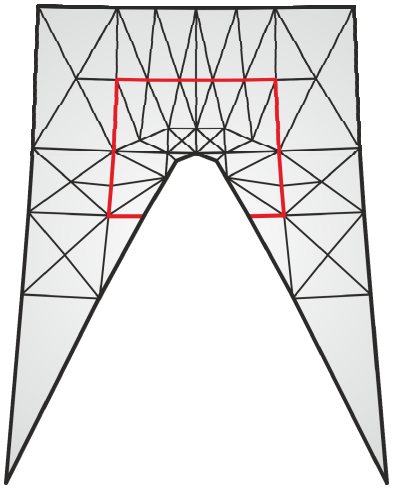

Figure 5.26 Detail of mesh arrond notch

Dense discretization has also been kept along the red line A-A displayed in Figure 5.25. Full multiscale simulation of this problem is neither recommendable nor necessary. Analysis of this problem has been conducted in an adaptive manner. Material constitutive matrices are found prior to analysis. For a linear elastic problem considered here homogenized stress tensors values can be obtained by an analytical expression from a classical FEM analysis. For

a generalized constitutive behavior due to analysis of the heterogeneous material stress tensors are then calculated as

$$\underline{\sigma}_{\mathrm{M}} = \underline{\underline{\underline{C}}}_{\sigma\varepsilon}\underline{\varepsilon}_{\mathrm{M}} + \underline{\underline{\underline{C}}}_{\sigma\varepsilon_{x_1}}\left(\underline{\varepsilon},_1\right)_{\mathrm{M}} + \underline{\underline{\underline{C}}}_{\sigma\varepsilon_{x_2}}\left(\underline{\varepsilon},_2\right)_{\mathrm{M}}, \tag{5.53}$$

$$\left(\underline{\mu}_{x_1}\right)_{\mathrm{M}} = \underline{\underline{\underline{C}}}_{\mu_{x_1}\varepsilon}\underline{\varepsilon}_{\mathrm{M}} + \underline{\underline{\underline{C}}}_{\mu_{x_1}\varepsilon_{x_1}}\left(\underline{\varepsilon},_1\right)_{\mathrm{M}} + \underline{\underline{\underline{C}}}_{\mu_{x_1}\varepsilon_{x_2}}\left(\underline{\varepsilon},_2\right)_{\mathrm{M}}, \tag{5.54}$$

$$\left(\underline{\mu}_{x_2}\right)_{\mathrm{M}} = \underline{\underline{\underline{C}}}_{\mu_{x_2}\varepsilon}\underline{\varepsilon}_{\mathrm{M}} + \underline{\underline{\underline{C}}}_{\mu_{x_2}\varepsilon_{x_1}}\left(\underline{\varepsilon},_1\right)_{\mathrm{M}} + \underline{\underline{\underline{C}}}_{\mu_{x_2}\varepsilon_{x_2}}\left(\underline{\varepsilon},_2\right)_{\mathrm{M}}. \tag{5.55}$$

Full analysis can be conducted using homogenized constitutive model and stress relations (5.53)-(5.55). Adaptivity used here means that a few elements in front of the notch inside the red line in Figure 5.26 are computed in a multiscale setting attaching an RVE to their material points, in order to track microstructural effects in front of the notch. The same analogy has been used in C^1-C^0 multiscale approach. In the following figures distribution of the relevant displacement gradient in front of the notch, along line A-A of length $H = 11\,\mathrm{mm}$ is presented. For a bending pattern exhibited here dominant gradients are $u_{1,1}$ which opens the notch, $u_{1,21}$ who gives trapezoidal deformed shape and $u_{2,11}$ representing curvature. Multiple analyses have been conducted for various values of Aifantis microstructural parameter l^2. In the case when $l^2 = 0$, C^1 approach is comparable to the conventional C^1-C^0 homogenization and comparison of the results obtained is made.

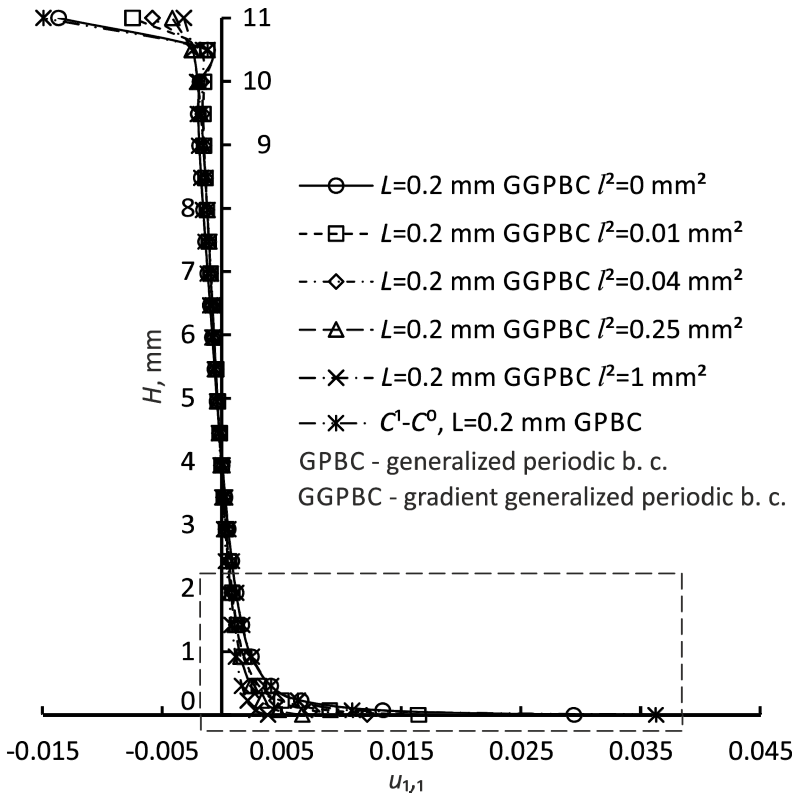

Figure 5.27 Distribution of displacement gradient component $u_{1,1}$ in front of the notch

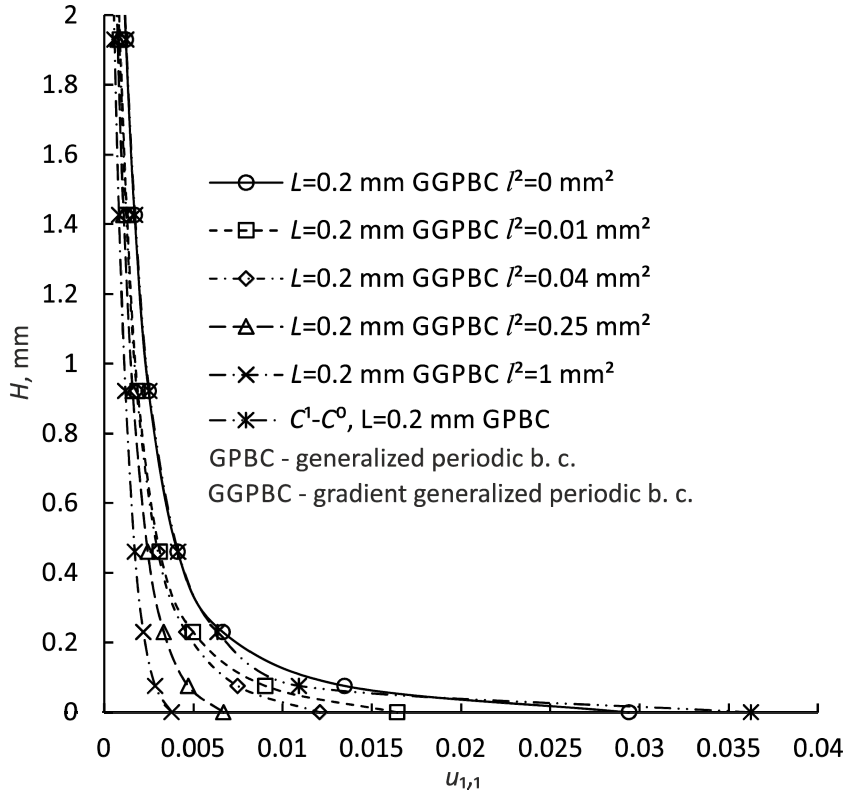

Figure 5.28 Detail of distribution of displacement gradient component $u_{1,1}$ in front of the notch

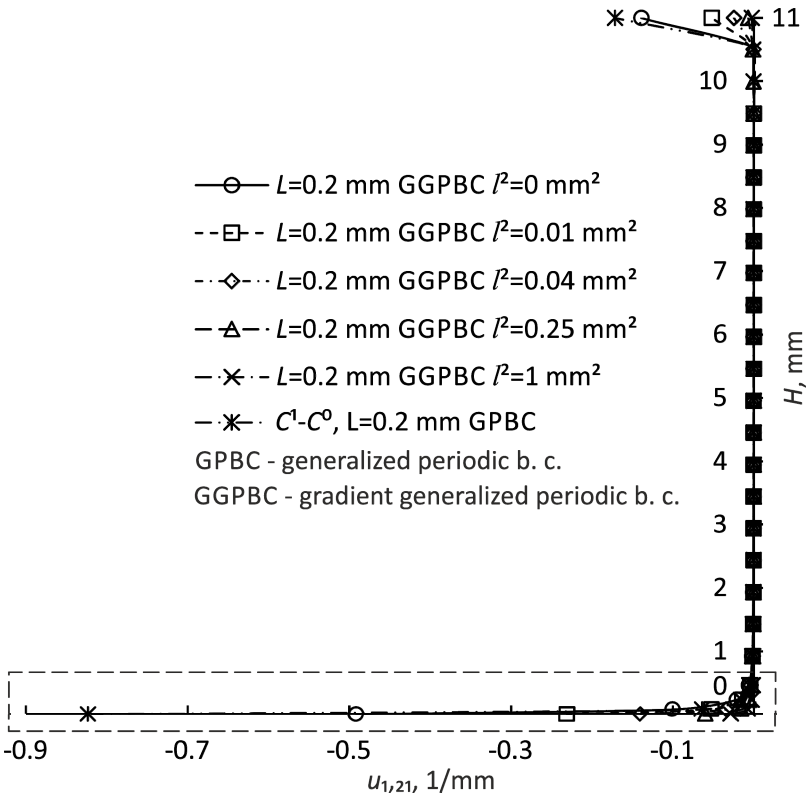

Figure 5.29 Distribution of second-order displacement gradient component $u_{1,21}$ in front of the notch

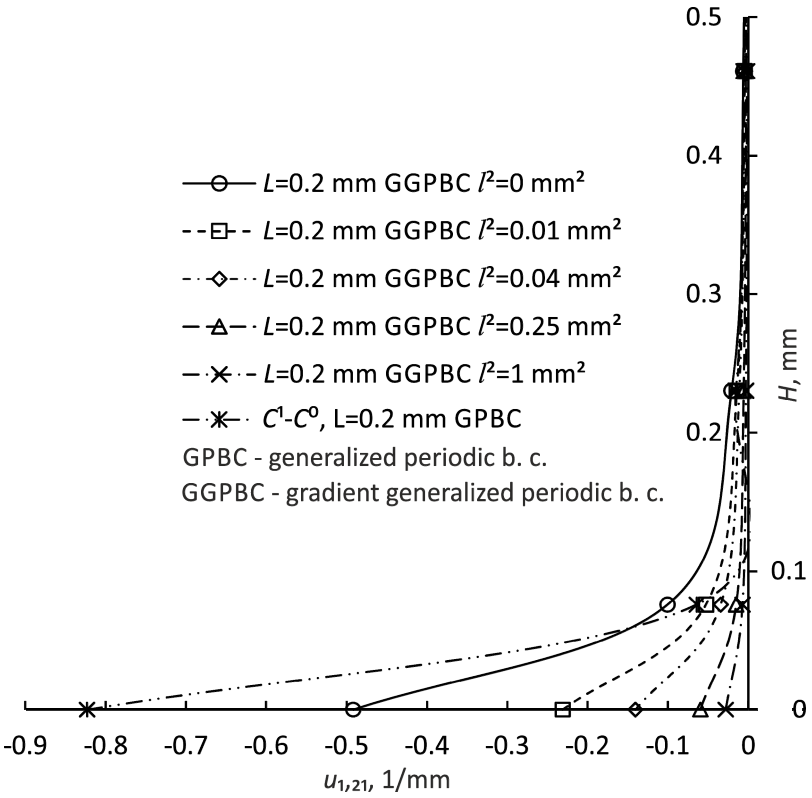

Figure 5.30 Detail of distribution of second-order displacement gradient component $u_{1,21}$ in front of the notch

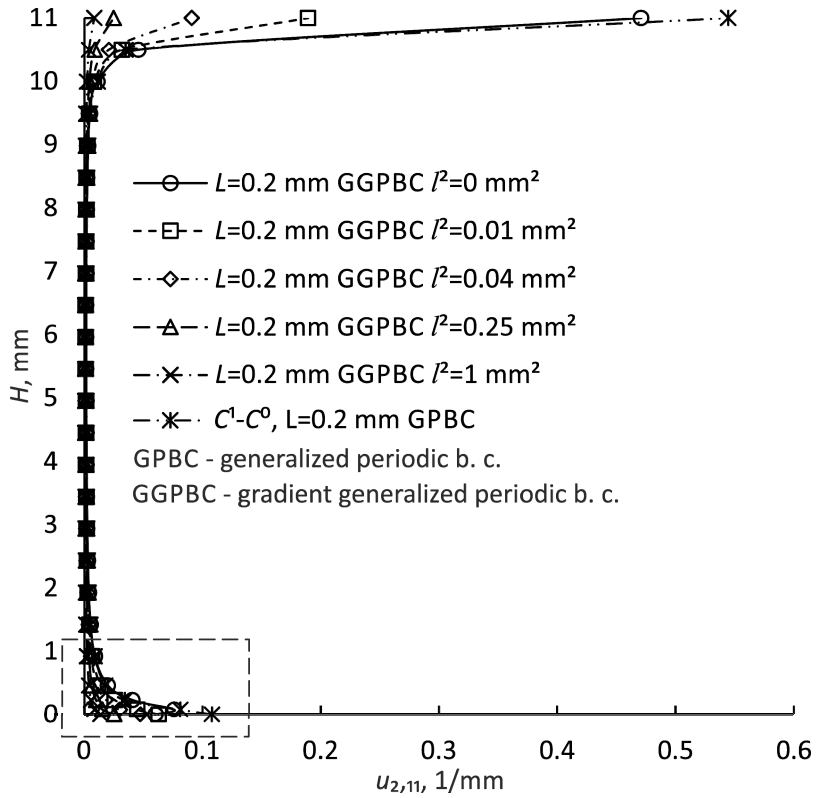

Figure 5.31 Distribution of second-order displacement gradient component $u_{2,11}$ in front of the notch

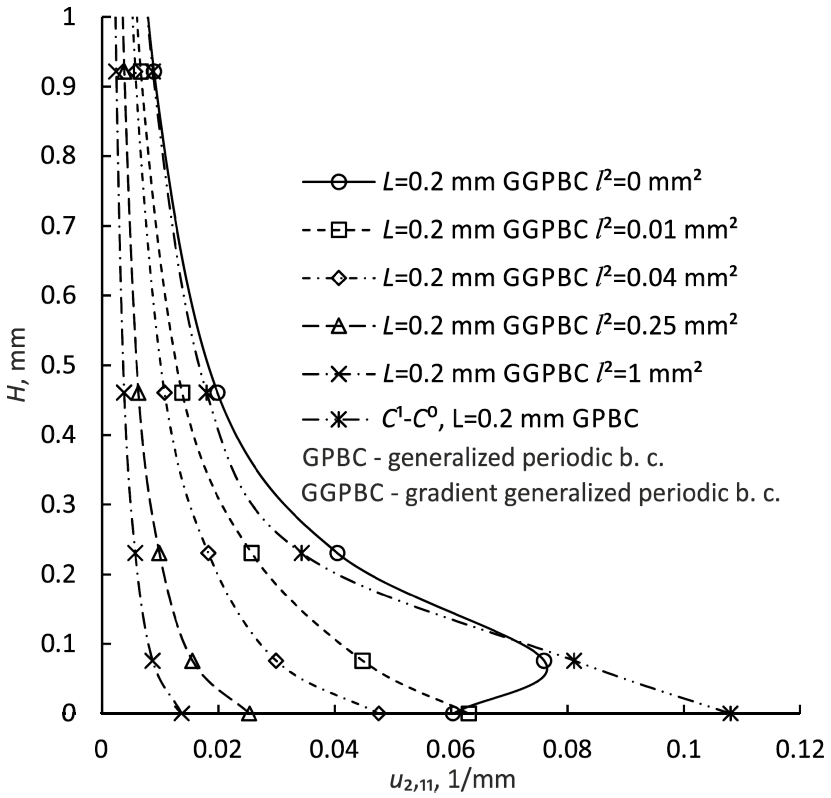

Figure 5.32 Detail of distribution of second-order displacement gradient component $u_{2,11}$ in front of the notch

Figs. 5.27, 5.29 and 5.31 display distributions of the relevant displacement gradients $u_{1,1}$, $u_{1,21}$ and $u_{2,11}$ in front of the notch. In these diagrams, the ordinate represents the distance from the notch tip in the vertical direction, denoted as H. As expected, high gradients appear in the vicinity of the notch, due to geometrical discontinuity and on the upper surface of the specimen due to roller penetration causing crimping of the material. Moving away from the notch tip peak areas gradients rapidly drop and disappear in the inner part of the specimen. With increase of l the general behaviour is preserved, but stiffness of the material is increased due to larger nonlocal influence. Detailed insight into a distributions in front of the notch are given in Figs. 5.28, 5.30 and 5.32. Stiffer response coming with increased l is common to all gradients. In comparison to the C^1-C^0 approach it can be seen that an equivalent distribution is achieved, with a slight increase of a peak value for the C^1-C^0 homogenization. Finally, Figs. 5.33, 5.34 and 5.35 show distributions of gradients at the notch tip for $l^2 = 0$. From Figures periodicity of the deformed response is clear. The dominant deformation modes can be easily observed too. As first, RVE is elongated as a consequence of $u_{1,1}$. Due to mixed second-order derivative $u_{1,21}$, trapezoidal deformation mode is prominent. Curvature as a result of $u_{2,11}$ is not expressed in such extent as a trapezoidal mode, but with further increase of the loading and for a larger RVE size, it can be easily distinguished.

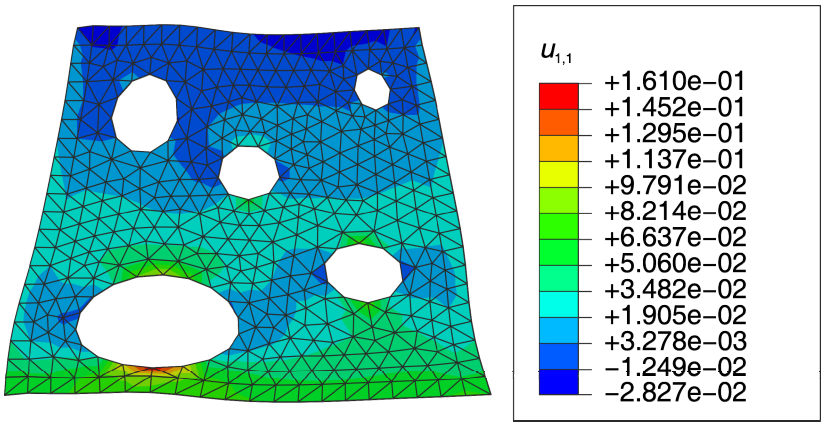

Figure 5.33 Distribution of displacement gradient component $u_{1,1}$ at the notch tip

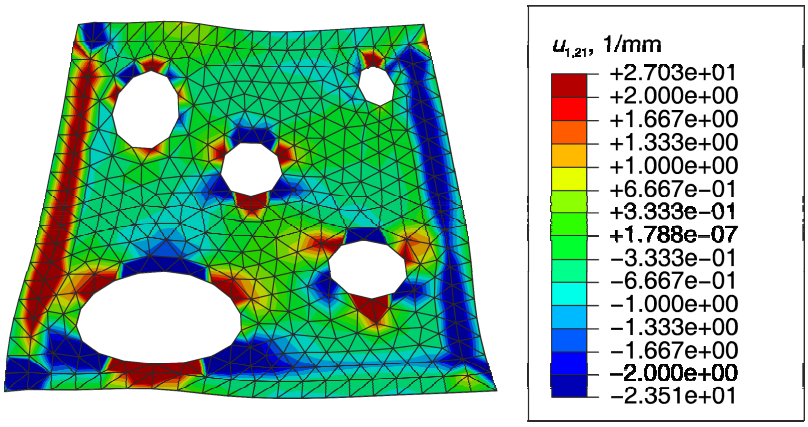

Figure 5.34 Distribution of second-order displacement gradient component $u_{1,21}$ at the notch tip

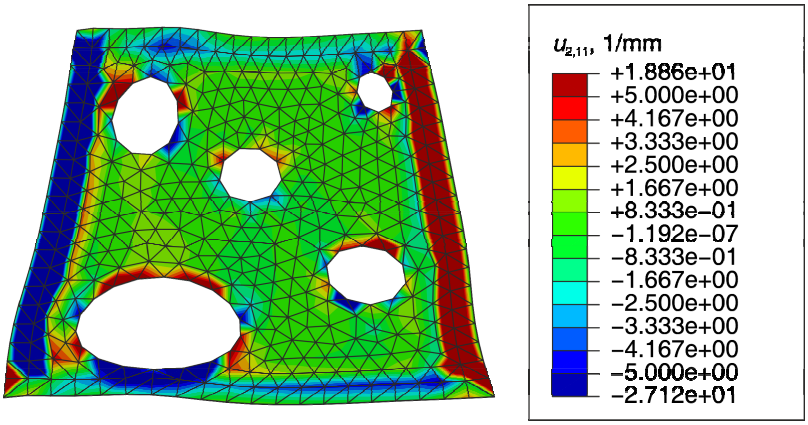

Figure 5.35 Distribution of second-order displacement gradient component $u_{2,11}$ at the notch tip

In Figure 5.33 smooth change of $u_{1,1}$ from tension to compression is visualized. On contrary, in Figs. 5.34 and 5.35 high contrasts of gradients take the place, especially around the porosities and near outer edges. Also it can been seen that the magnitude of strains is of order 10^{-1}, while second-order derivatives rise up to magnitude of 10^{1}, one hundred times larger.

6 Conclusions and recommendations

For more realistic description of mechanical behavior of heterogeneous materials advanced modeling techniques are required. This means that capturing microstructural physical phenomena includes incorporation of an analysis at the microlevel. However, classical continuum mechanics assumes material homogeneity and does not consider microstructural effects. Multiscale techniques employing microstructural effects in homogenization procedures resolve this issue, where the second-order homogenization has been mostly used. For application of a second-order homogenization second-order gradients must be defined at the macroscale level which brings necessity of a nonlocal continuum theory satisfying C^1 continuity at the macrolevel. Microstructural level represented by the representative volume element is still treated as an ordinary continuum and discretized by the C^0 finite elements. This $C^1 - C^0$ transition causes some inconsistencies in the formulations and disturbs accuracy. One of the inconsistencies arises in a volume averaging of the second-order macrolevel gradient, which cannot be related to the microlevel higher-order gradient as a true volume average. In a micro-to-macro scale transition, after resolving Hill-Mandel energy condition, homogenized double stress requires a modified definition at the microstructural level. In the case of generalized periodic boundary conditions, corner nodes fluctuations are fixed to zero, which leads to artificial stress concentrations due to strain concentrations in the corners of the RVE. Furthermore, the C^1 continuity finite elements have a complex formulation. Therefore, C^0 finite elements based on a mixed formulation have been developed. However, significant progress in modeling of a nonlocal continuum with these mixed finite elements has not been made, due to the large number of unknowns involved.

Due to the mentioned shortcomings, this thesis is concerned with a derivation and numerical implementation of a new multiscale procedures based a second-order computational homogenization schemes. Here, explanations of higher-order continuum theories are given firstly in a small and large strain setting. A special case of the small strain theory by Aifantis is derived. Next, for implementation of a nonlocal theory into FEM a three node C^1 displacement based triangular finite element has been chosen. Element formulations for a small strain, large strain and Aifantis theory are derived and verified on several patch tests and analytical examples. Since the element describes high order polynomial

displacement field, the numerical integration of the stiffness matrix requires large number of Gauss integration points. Therefore, the reduced integration scheme has been tested and confirmed as numerically efficient and justified. It has been shown that derived finite element formulations have very good performance compared to the other formulations available in the literature.

After verification, finite element has been used for discretization of the macrolevel in a two-scale methodologies derived. First case considered is usual C^1-C^0 multiscale approach. Small strain and large strain assumption are adopted. In the frame of the second-order computational homogenization, some issues related to the application of the boundary conditions on the representative volume element at the microlevel are discussed. Herein, both the linear displacement and the generalized periodic boundary conditions are considered. Finite element formulations and a multiscale framework have been implemented into commercial software ABAQUS/Standard. The numerical efficiency of the highly time demanding computational procedure is significantly improved by the derivation of the computational strategy based on the Abaqus subroutines. The derived two-scale analysis is implemented into the Abaqus architecture in an efficient way. Another advantage of such approach is the possibility of the use of different computational algorithms as well as material models available in Abaqus for the multiscale computational procedures. Comparison of a several numerical integration techniques for imposition of the microfluctuation integral, which enables complete macro-to-micro transition of the displacement gradients is performed. It is demonstrated that trapezoidal rule only gives a physically consistent deformation modes. Performance of the small strain as well as large strain multiscale scheme is tested on some benchmark examples. The obtained results demonstrate the accuracy and numerical efficiency of the proposed algorithms.

Afterwards, a new multiscale procedure for modeling of a heterogeneous materials is proposed where the macrostructure and the microstructure are described by Aifantis gradient elasticity theory. A new micro-macro transition methodology is derived, with every macrolevel variable at the macroscale expressed as a true volume average of the conjugate from a lower length scale. Despite the mathematically consistent micro-macro scheme, microfluctuation integral imposition did not vanish and it still has to be explicitly satisfied in order to get meaningful results. Discretization of the both scales is performed by the C^1 triangular finite element based on the Aifantis theory. A new gradient displacement and generalized periodic boundary conditions used at the microlevel are derived, prescribing displacements, as well as displacement gradients on RVE boundaries. Nonlocality effects in a

new scheme are directed by two nonlocal parameters, Aifantis microstructural parameter and RVE size. Their correlation is derived analytically and confirmed on a several examples. Regularity of the new developed multiscale scheme has been confirmed on a few numerical examples where both C^1-C^0 and C^1 homogenization algorithm have been compared.

Generally speaking, contributions of this thesis are done in the field of a multiscale modeling of heterogeneous materials and computational homogenization methodology. Contributions are as follows:

1) Derivation of displacement based C^1 triangular finite element

   - Formulation of the element is adjusted for the application in a multiscale scheme. In other words, integration of the element stiffness matrix is performed by numerical integration. Gauss integration technique using 13 material point is chosen as the best, which for the derived element formulation represents reduced integration scheme.
   - First form of Mindlin's continuum and Aifantis strain gradient elasticity theory have been numerically implemented into the element.

2) Development of the second-order computational homogenization based multiscale approach

   - The framework is derived for a small and large strain assumption, considering elastoplastic material behaviour. Displacement and generalized periodic boundary conditions have been derived.
   - Influence of the numerical integration technique used for imposition of a microfluctuation constraint on RVE behaviour is tested.

3) Derivation of the multiscale scheme with preservation of C^1 continuity at the microscale

   - Scale transition methodology has been derived. Consistency of the proposed approach has been demonstrated in a comparison to the actual developments. Every macrolevel variable is derived as a true volume average of microscale conjugate.
   - Gradient displacement and gradient generalized periodic boundary conditions have been derived. Thanks to the mathematically consistent

scale transition methodology, second-order strain tensor can be fully prescribed on the RVE boundaries without a microfluctuation constraint arising. However, microfluctuation needs to be explicitly satisfied to keep consistency of volume averaging.

- Nonlocality effects are described by two parameters. The first parameter is RVE size and the other is an intrinsic Aifantis microstructural parameter. Correlation between those two parameter has been derived.

All algorithms developed within thesis have shown a good performance. Advantages of C^1 scheme have been demonstrated in comparison to C^1-C^0 approach. The presented results showed that establishment of the higher-order theory at the microstructural scale for modeling of RVE behavior gave more consistent scale transition methodology, bringing more accurate homogenized results compared to actual developments in second-order homogenization. This will allow damage modeling at the microstructural level, as well as development of materials with optimal mechanical properties.

There are several possible directions of further research. On possible direction is an extension of the algorithms to the third dimension. This direction has one noticeable obstacle, and that is a C^1 three-dimensional finite element formulation. In the literature there is only a few of them and it is not necessary to note which numerical burden they carry. Besides addition of the third dimension, there is a possibility of application of the developed algorithms in modeling of micro-macro damage problems. To do this, to C^1-C^0 multiscale approach appropriate damage models for brittle or ductile materials should be invoked at the microlevel, along with dealing all the problems coming in multiscale damage homogenization discussed in the literature. In C^1-C^1 approach only brittle damage can be modeled at the moment. But it is important to say that C^1 continuous microscale problem offers an additional gradient terms as an intrinsic variables for computation of damage. For modeling of ductile damage in C^1 scheme, the first step is a development of some gradient dependent elastoplastic material model from the literature. Thanks to the C^1 continuous boundary value problem at the RVE, explicit approaches can be utilized as an advantage to C^1-C^0 approach.

Appendix A

Finite element interpolation functions

Finite element shape functions of a single node for a single direction component are written as

$$N_1 = L_1^5 + 5L_1^4L_2 + 10L_1^4L_3 + 10L_1^3L_2^2 + 10L_1^3L_3^2 + 20L_1^3L_2L_3 + 30r_{21}L_1^2L_2L_3^2 + 30r_{31}L_1^2L_3L_2^2, \tag{A.1}$$

$$N_2 = c_3L_1^4L_2 - c_2L_1^4L_3 + 4c_3L_1^3L_2^2 - 4c_2L_1^3L_3^2 + 4\left(c_3 - c_2\right)L_1^3L_2L_3 - \\ -\left(3c_1 + 15r_{21}c_2\right)L_1^2L_2L_3^2 + \left(3c_1 + 15r_{31}c_3\right)L_1^2L_3L_2^2, \tag{A.2}$$

$$N_3 = -b_3L_1^4L_2 + b_2L_1^4L_3 - 4b_3L_1^3L_2^2 + 4b_2L_1^3L_3^2 + 4\left(b_2 - b_3\right)L_1^3L_2L_3 + \\ +\left(3b_1 + 15r_{21}b_2\right)L_1^2L_2L_3^2 - \left(3c_1 + 15r_{31}b_3\right)L_1^2L_3L_2^2, \tag{A.3}$$

$$N_4 = \frac{c_3^2}{2}L_1^3L_2^2 + \frac{c_2^2}{2}L_1^3L_3^2 - c_2c_3L_1^3L_2L_3 + \left(c_1c_2 + \frac{5}{2}r_{21}c_2^2\right)L_2L_3^2L_1^2 + \left(c_1c_3 + \frac{5}{2}r_{31}c_3^2\right)L_3L_2^2L_1^2, \tag{A.4}$$

$$N_5 = -b_3c_3L_1^3L_2^2 - b_2c_2L_1^3L_3^2 + \left(b_2c_3 + b_3c_2\right)L_1^3L_2L_3 - \left(b_1c_2 + b_2c_1 + 5r_{21}b_2c_2\right)L_2L_3^2L_1^2 - \\ -\left(b_1c_3 + b_3c_1 + 5r_{31}b_3c_3\right)L_3L_2^2L_1^2, \tag{A.5}$$

$$N_6 = \frac{b_3^2}{2}L_1^3L_2^2 + \frac{b_2^2}{2}L_1^3L_3^2 - b_2b_3L_1^3L_2L_3 + \left(b_1b_2 + \frac{5}{2}r_{21}b_2^2\right)L_2L_3^2L_1^2 + \left(b_1b_3 + \frac{5}{2}r_{31}b_3^2\right)L_3L_2^2L_1^2. \tag{A.6}$$

In Eqs. (A.1)-(A.6) constants b_i and c_i appear relating nodal coordinates of the finite element in the way

$$b_i = \left(x_2\right)_j - \left(x_2\right)_k, \tag{A.7}$$

$$c_i = \left(x_1\right)_k - \left(x_1\right)_j. \tag{A.8}$$

Cartesian components x_1 and x_2 of the nodal coordinates have been put into brackets to separate them from the nodal indexes for the sake of clarity only. Indexes *i*, *j* and *k* change as a cyclic permutations of 1, 2 and 3. Parameter r_{ij} which also appears in definition of the shape functions is equal to

$$r_{ij} = \frac{b_ib_j + c_ic_j}{b_i^2 + c_i^2}. \tag{A.9}$$

The remaining interpolations for nodes 2 and 3, $N_7 \ldots N_{18}$ are easily obtained through the cyclic permutations. Since area coordinates are not convenient for the finite element formulation used in this thesis transformation of interpolations (A.1)-(A.6) into Cartesian

coordinate system is useful. Firstly, area coordinates L_i in Cartesian terms have the following form

$$L_i = \frac{a_i + b_i x_1 + c_i x_2}{\Delta}. \tag{A.10}$$

Constants b_i and c_i have already be defined in (A.7) and (A.8), respectively. Constant a_i is

$$a_i = (x_1)_j (x_2)_k - (x_1)_k (x_2)_j, \tag{A.11}$$

while Δ represents area of the finite element calculated as

$$\begin{aligned}\Delta = \frac{1}{2}\Big[&\big((x_1)_2 (x_2)_3 - (x_1)_3 (x_2)_2\big) + \big((x_1)_3 (x_2)_1 - (x_1)_1 (x_2)_3\big) + \\ &+ \big((x_1)_1 (x_2)_2 - (x_1)_2 (x_2)_1\big)\Big].\end{aligned} \tag{A.12}$$

The basic equations relating area and Cartesian coordinates can be read as

$$x_1 = L_1 (x_1)_1 + L_2 (x_1)_2 + L_3 (x_1)_3, \tag{A.13}$$

$$x_2 = L_1 (x_2)_1 + L_2 (x_2)_2 + L_3 (x_2)_3. \tag{A.14}$$

To define deformation matrices $\underline{\underline{\mathrm{B}}}$ used within the element, derivatives in the Cartesian terms are necessary. This is done using the identities

$$\frac{\partial}{\partial x_1} = \frac{1}{2\Delta}\left(b_1 \frac{\partial}{\partial L_1} + b_2 \frac{\partial}{\partial L_2} + b_3 \frac{\partial}{\partial L_3}\right), \tag{A.15}$$

$$\frac{\partial}{\partial x_2} = \frac{1}{2\Delta}\left(c_1 \frac{\partial}{\partial L_1} + c_2 \frac{\partial}{\partial L_2} + c_3 \frac{\partial}{\partial L_3}\right). \tag{A.16}$$

Shape functions described in (A.1)-(A.6) are used only for interpolation of a displacement field inside the element. Geometry of the element is interpolated using a classical shape functions of the C^0 constant strain triangle. This classifies the element as subparametric. There are also attempts of isoparametric formulation discussed in [157]. The procedures explained above can be found in almost every standard finite element handbook. For more details about this topic, see [120]. The element geometry is defined in a parent coordinate system (ξ, η), according to Figure A.1.

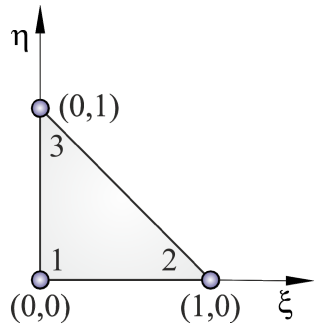

Figure A.1 Triangular finite element in parent coordinate system

Interpolations which describe geometry of the finite element are read as

$$\phi_1 = 1 - \xi - \eta\,, \tag{A.17}$$

$$\phi_2 = \xi\,, \tag{A.18}$$

$$\phi_3 = \eta\,. \tag{A.19}$$

In order to establish the stiffness matrix of the element, we must be able to differentiate the displacements with respect to the Cartesian coordinates (x_1, x_2), for a 2D case. As the shape functions ϕ_1, ϕ_2 and ϕ_3 are defined in a parent coordinates, appropriate mapping of the element geometry into Cartesian coordinates must be introduced. Taking into account chain rule of differentiation, for a 2D case we can write

$$\begin{pmatrix} \dfrac{\partial \phi_i}{\partial \xi} \\ \dfrac{\partial \phi_i}{\partial \eta} \end{pmatrix} = \begin{pmatrix} \dfrac{\partial x_1}{\partial \xi} & \dfrac{\partial x_2}{\partial \xi} \\ \dfrac{\partial x_1}{\partial \eta} & \dfrac{\partial x_1}{\partial \eta} \end{pmatrix} \begin{pmatrix} \dfrac{\partial \phi_i}{\partial x_1} \\ \dfrac{\partial \phi_i}{\partial x_2} \end{pmatrix}, \; i = 1,2,3\,. \tag{A.20}$$

Generally speaking, Eq. (A.20) can be expressed as

$$\begin{pmatrix} \dfrac{\partial}{\partial \xi} \\ \dfrac{\partial}{\partial \eta} \end{pmatrix} = \begin{pmatrix} \dfrac{\partial x_1}{\partial \xi} & \dfrac{\partial x_2}{\partial \xi} \\ \dfrac{\partial x_1}{\partial \eta} & \dfrac{\partial x_1}{\partial \eta} \end{pmatrix} \begin{pmatrix} \dfrac{\partial}{\partial x_1} \\ \dfrac{\partial}{\partial x_2} \end{pmatrix}. \tag{A.21}$$

Introducing Jacobian matrix in the form

$$\underline{\underline{\mathrm{J}}} = \begin{pmatrix} \dfrac{\partial x_1}{\partial \xi} & \dfrac{\partial x_2}{\partial \xi} \\ \dfrac{\partial x_1}{\partial \eta} & \dfrac{\partial x_1}{\partial \eta} \end{pmatrix}, \tag{A.22}$$

we can easily derive the transformation formula

$$\begin{pmatrix} \dfrac{\partial}{\partial x_1} \\ \dfrac{\partial}{\partial x_2} \end{pmatrix} = \underline{\underline{\mathbf{J}}}^{-1} \begin{pmatrix} \dfrac{\partial}{\partial \xi} \\ \dfrac{\partial}{\partial \eta} \end{pmatrix}. \tag{A.23}$$

Životopis

Tomislav Lesičar rođen je u Zagrebu, 6. ožujka 1986. godine. Osnovnu školu je pohađao u Vrbovcu, gdje je 2000. godine upisao opću gimnaziju. Nakon mature, 2004. godine je upisao Fakultet strojarstva i brodogradnje u Zagrebu, a kao smjer je odabrao Inženjersko modeliranje i računalne simulacije. Diplomirao je 2009. godine uz diplomski rad pod naslovom „Analiza cjelovitosti kućišta ventila“ pod vodstvom prof. dr. sc. Tonkovića. Nagrađen je medaljom fakulteta za najbolje studente. Od 2010. godine zaposlen je na Fakultetu strojarstva i brodogradnje na Zavodu za tehničku mehaniku kao asistent. Iste godine upisao je i postdiplomski studij, smjer Teorija konstrukcija. Kao istraživač sudjelovao je na 4 znanstvena projekta. Tokom istraživanja, 2015. godine boravio je 3 mjeseca na Sveučilištu Leibniz u Hannoveru. Autor je 18 znanstvenih radova, od kojih su dva objavljena u CC znanstvenim časopisima. Oženjen, otac jednog djeteta.

Biography

Tomislav Lesičar was born on March 06 1986 in Zagreb. He attended primary school in Vrbovec, and afterwards enrolled grammar school in 2000. After graduation in 2004, he enrolled graduate study at the Faculty of Mechanical Engineering and Naval Architecture, University of Zagreb. In 2009 he received Mag. Ing. Mech. degree with graduation thesis on the theme „Structural integrity of the valve housing“ under supervision of Professor Tonković. He has been rewarded by the Medal of the Faculty of Mechanical Engineering and Naval Architecture for the best students (student achievement award). Since 2010, he has been employed as a research assistant at the Department of Technical Mechanics at the Faculty of Mechanical Engineering and Naval Architecture, University of Zagreb. In the same year he enrolled postgraduate studies in Theory of Structures and Design. As a researcher he has been working on four scientific projects. During his research, in 2015 for three months he conducted a research in Leibniz University Hannover. He is the first author of 18 scientific publications, including two contributions published in CC scientific journals. Married, father of one child.

Bibliography

[1] J.L.L. Mishnaevsky, S. Schmauder, Continuum Mesomechanical Finite Element Modeling in Materials Development: A State-of-the-Art Review, Applied Mechanics Reviews, 54 (2001) 49-67.
[2] V.P. Nguyen, M. Stroeven, L.J. Sluys, Multiscale Continuous and Discontinuous Modeling of Heterogeneous Materials: A Review on Recent Developments, Journal of Multiscale Modelling, 03 (2011) 229-270.
[3] M.G.D. Geers, V.G. Kouznetsova, W.A.M. Brekelmans, Multi-scale computational homogenization: Trends and challenges, Journal of Computational and Applied Mathematics, 234 (2010) 2175-2182.
[4] M.H.F. Aliabadi, G. Ugo, Multiscale Modeling in Solid Mechanics, Imperial College Press, London, 2010.
[5] F. Feyel, J.L. Chaboche, FE2 multiscale approach for modelling the elastoviscoplastic behaviour of long fibre SiC/Ti composite materials, Comput. Methods in Appl. Mech. and Eng., 183 (2000) 309–330.
[6] V. Kouznetsova, W.A.M. Brekelmans, F.P.T. Baaijens, An approach to micro-macro modeling of heterogeneous materials, Comput Mech, 27 (2001) 37-48.
[7] C. Miehe, A. Koch, Computational micro-to-macro transitions of discretized microstructures undergoing small strains, Arch Appl Mech, 72 (2002) 300-317.
[8] V.G. Kouznetsova, Computational homogenization for the multi-scale analysis of multi-phase materials. Ph. D., TU Eindhoven, Eindhoven, 2002.
[9] C. Miehe, Computational micro-to-macro transitions for discretized micro-structures of heterogeneous materials at finite strains based on the minimization of averaged incremental energy, Computer Methods in Applied Mechanics and Engineering, 192 (2003) 559-591.
[10] D.J. Luscher, A hierarchical framework for the multiscale modeling of microstructure evolution in heterogeneous materials. Ph.D., Georgia Institute of Technology, Springfield, 2010.
[11] I. Ahmadi, M.M. Aghdam, A truly generalized plane strain meshless method for combined normal and shear loading of fibrous composites, Engineering Analysis with Boundary Elements, 35 (2011) 395-403.
[12] L.Y. Li, P.H. Wen, M.H. Aliabadi, Meshfree modeling and homogenization of 3D orthogonal woven composites, Composites Science and Technology, 71 (2011) 1777-1788.
[13] G.K. Sfantos, M.H. Aliabadi, Multi-scale boundary element modelling of material degradation and fracture, Computer Methods in Applied Mechanics and Engineering, 196 (2007) 1310-1329.
[14] J.C. Michel, H. Moulinec, P. Suquet, Effective properties of composite materials with periodic microstructure: a computational approach, Computer Methods in Applied Mechanics and Engineering, 172 (1999) 109-143.
[15] K. Terada, N. Kikuchi, A class of general algorithms for multi-scale analyses of heterogeneous media, Computer Methods in Applied Mechanics and Engineering, 190 (2001) 5427-5464.

[16] F. Larsson, K. Runesson, S. Saroukhani, R. Vafadari, Computational homogenization based on a weak format of micro-periodicity for RVE-problems, Computer Methods in Applied Mechanics and Engineering, 200 (2011) 11-26.
[17] A. Bacigalupo, L. Gambarotta, Second-order computational homogenization of heterogeneous materials with periodic microstructure, ZAMM - Journal of Applied Mathematics and Mechanics / Zeitschrift für Angewandte Mathematik und Mechanik, 90 (2010) 796-811.
[18] V.D. Nguyen, G. Becker, L. Noels, Multiscale computational homogenization methods with a gradient enhanced scheme based on the discontinuous Galerkin formulation, Computer Methods in Applied Mechanics and Engineering, 260 (2013) 63-77.
[19] Ä. Temizer, P. Wriggers, An adaptive multiscale resolution strategy for the finite deformation analysis of microheterogeneous structures, Computer Methods in Applied Mechanics and Engineering, 200 (2011) 2639-2661.
[20] I. Doghri, A. Ouaar, Homogenization of two-phase elasto-plastic composite materials and structures: Study of tangent operators, cyclic plasticity and numerical algorithms, International Journal of Solids and Structures, 40 (2003) 1681-1712.
[21] B. Hassani, E. Hinton, A review of homogenization and topology opimization II - analytical and numerical solution of homogenization equations, Computers & Structures, 69 (1998) 719-738.
[22] V.D. Nguyen, E. Bechet, C. Geuzaine, L. Noels, Imposing periodic boundary condition on arbitrary meshes by polynomial interpolation, Computational Materials Science, 55 (2012) 390-406.
[23] R.A. Toupin, Elastic materials with couple-stresses, Archive for Rational Mechanics and Analysis, 11 (1962) 385-414.
[24] R.D. Mindlin, Micro-structure in linear elasticity, Archive for Rational Mechanics and Analysis, 16 (1964) 51-78.
[25] R.D. Mindlin, Second gradient of strain and surface-tension in linear elasticity, International Journal of Solids and Structures, 1 (1965) 417-438.
[26] R.D. Mindlin, N.N. Eshel, On first strain-gradient theories in linear elasticity, International Journal of Solids and Structures, 4 (1968) 109-124.
[27] V. Kouznetsova, M.G.D. Geers, W.A.M. Brekelmans, Multi-scale constitutive modelling of heterogeneous materials with a gradient-enhanced computational homogenization scheme, International Journal for Numerical Methods in Engineering, 54 (2002) 1235-1260.
[28] D.J. Luscher, D.L. McDowell, C.A. Bronkhorst, A second gradient theoretical framework for hierarchical multiscale modeling of materials, International Journal of Plasticity, 26 (2010) 1248-1275.
[29] Ł. Kaczmarczyk, C.J. Pearce, N. Bićanić, Studies of microstructural size effect and higher-order deformation in second-order computational homogenization, Computers & Structures, 88 (2010) 1383-1390.
[30] T. Lesičar, Z. Tonković, J. Sorić, A second-order two-scale homogenization procedure using C1 macrolevel discretization, Comput Mech, 54 (2014) 425-441.
[31] Z.C. Xia, J.W. Hutchinson, Crack tip fields in strain gradient plasticity, Journal of the Mechanics and Physics of Solids, 44 (1996) 1621-1648.
[32] A. Zervos, S. Papanicolopulos, I. Vardoulakis, Two Finite-Element Discretizations for Gradient Elasticity, Journal of Engineering Mechanics, 135 (2009) 203-213.
[33] S. Akarapu, H. Zbib, Numerical analysis of plane cracks in strain-gradient elastic materials, Int J Fract, 141 (2006) 403-430.
[34] A. Zervos, P. Papanastasiou, I. Vardoulakis, A finite element displacement formulation for gradient elastoplasticity, International Journal for Numerical Methods in Engineering, 50 (2001) 1369-1388.

[35] S.A. Papanicolopulos, A. Zervos, A method for creating a class of triangular C1 finite elements, International Journal for Numerical Methods in Engineering, 89 (2012) 1437-1450.
[36] J.Y. Shu, N.A. Fleck, The prediction of a size effect in microindentation, International Journal of Solids and Structures, 35 (1998) 1363-1383.
[37] E. Amanatidou, N. Aravas, Mixed finite element formulations of strain-gradient elasticity problems, Computer Methods in Applied Mechanics and Engineering, 191 (2002) 1723-1751.
[38] J.Y. Shu, W.E. King, N.A. Fleck, Finite elements for materials with strain gradient effects, International Journal for Numerical Methods in Engineering, 44 (1999) 373-391.
[39] T. Matsushima, R. Chambon, D. Caillerie, Large strain finite element analysis of a local second gradient model: application to localization, International Journal for Numerical Methods in Engineering, 54 (2002) 499-521.
[40] G. Engel, K. Garikipati, T.J.R. Hughes, M.G. Larson, L. Mazzei, R.L. Taylor, Continuous/discontinuous finite element approximations of fourth-order elliptic problems in structural and continuum mechanics with applications to thin beams and plates, and strain gradient elasticity, Computer Methods in Applied Mechanics and Engineering, 191 (2002) 3669-3750.
[41] R.B. Chandran, Development of discontinuous Galerkin method for nonlocal linear elasticity. PhD, Massachusetts Institute of Technology 2007.
[42] H. Askes, E.C. Aifantis, Gradient elasticity in statics and dynamics: An overview of formulations, length scale identification procedures, finite element implementations and new results, International Journal of Solids and Structures, 48 (2011) 1962-1990.
[43] Z. Tang, S. Shen, S.N. Atluri, Analysis of materials with strain-gradient effects: A meshless local Petrov-Galerkin (MLPG) approach, with nodal displacements only, CMES - Computer Modeling in Engineering and Sciences, 4 (2003) 177-196.
[44] S. Skatulla, A. Arockiarajan, C. Sansour, A nonlinear generalized continuum approach for electro-elasticity including scale effects, Journal of the Mechanics and Physics of Solids, 57 (2009) 137-160.
[45] D. Polyzos, K.G. Tsepoura, S.V. Tsinopoulos, D.E. Beskos, A boundary element method for solving 2-D and 3-D static gradient elastic problems: Part I: Integral formulation, Computer Methods in Applied Mechanics and Engineering, 192 (2003) 2845-2873.
[46] G.F. Karlis, S.V. Tsinopoulos, D. Polyzos, D.E. Beskos, Boundary element analysis of mode I and mixed mode (I and II) crack problems of 2-D gradient elasticity, Computer Methods in Applied Mechanics and Engineering, 196 (2007) 5092-5103.
[47] G.I. Taylor, Plastic strain in metals, Journal of the Institute of Metals, 62 (1938) 307-324.
[48] S. Nemat-Nasser, M. Lori, S.K. Datta, Micromechanics: Overall Properties of Heterogeneous Materials, Journal of Applied Mechanics-transactions of The Asme, 63 (1996).
[49] P.W. Chung, K.K. Tamma, R.R. Namburu, Asymptotic expansion homogenization for heterogeneous media: computational issues and applications, Composites Part A: Applied Science and Manufacturing, 32 (2001) 1291-1301.
[50] S. Forest, F. Pradel, K. Sab, Asymptotic analysis of heterogeneous Cosserat media, International Journal of Solids and Structures, 38 (2001) 4585-4608.
[51] V.P. Smyshlyaev, N.A. Fleck, Bounds and estimates for linear composites with strain gradient effects, Journal of the Mechanics and Physics of Solids, 42 (1994) 1851-1882.
[52] R.H.J. Peerlings, N.A. Fleck, Numerical analysis of strain gradient effects in periodic media Journal de Physique IV, 11 (2001) 153-160.
[53] M.G.D. Geers, V.G. Kouznetsova, Scale transitions in solid mechanics based on computational homogenization, Eindhoven University of Technology, Eindhoven, 2010.

[54] J.D. Eshelby, The Determination of the Elastic Field of an Ellipsoidal Inclusion, and Related Problems, 1957.
[55] G. Bao, J.W. Hutchinson, R.M. McMeeking, Particle reinforcement of ductile matrices against plastic flow and creep, Acta Metallurgica et Materialia, 39 (1991) 1871-1882.
[56] J.R. Brockenbrough, S. Suresh, H.A. Wienecke, Deformation of metal-matrix composites with continuous fibers: geometrical effects of fiber distribution and shape, Acta Metallurgica et Materialia, 39 (1991) 735-752.
[57] O.v.d. Sluis, P.H.J. Vosbeek, P.J.G. Schreurs, H.E.H. Mei, Homogenization of heterogeneous polymers, International Journal of Solids and Structures, 36 (1999) 3193-3214.
[58] J.P. Gardner, Micromechanical Modeling of Composite Materials in Finite Element Analysis Using an Embedde Cell Approach. Ph. D., Massachusetts Institute of Technology, 1994.
[59] R.J.M. Smit, W.A.M. Brekelmans, H.E.H. Meijer, Prediction of the mechanical behavior of nonlinear heterogeneous systems by multi-level finite element modeling, Computer Methods in Applied Mechanics and Engineering, 155 (1998) 181-192.
[60] H. Moulinec, P. Suquet, A numerical method for computing the overall response of nonlinear composites with complex microstructure, Computer Methods in Applied Mechanics and Engineering, 157 (1998) 69-94.
[61] M. Jiang, I. Jasiuk, M. Ostoja-Starzewski, Apparent elastic and elastoplastic behavior of periodic composites, International Journal of Solids and Structures, 39 (2002) 199-212.
[62] F. Rabold, M. Kuna, Cell model simulation of void growth in nodular cast iron under cyclic loading, Computational Materials Science, 32 (2005) 489-497.
[63] A.J. Carneiro Molina, E.A. de Souza Neto, D. Perić, Homogenized tangent moduli for heterogeneous materials, in: Proc. 13th ACME conference, Sheffield, 2005.
[64] A. Romkes, J.T. Oden, K. Vemaganti, Multi-scale goal-oriented adaptive modeling of random heterogeneous materials, Mechanics of Materials, 38 (2006) 859-872.
[65] J. Fish, S. Kuznetsov, Computational continua, International Journal for Numerical Methods in Engineering, 84 (2010) 774-802.
[66] H.J. Böhm, A Short Introduction to Continuum Micromechanics, in: H. Böhm (Ed.) Mechanics of Microstructured Materials, Springer Vienna, 2004, pp. 1-40.
[67] C. Miehe, J. Schröder, J. Schotte, Computational homogenization analysis in finite plasticity Simulation of texture development in polycrystalline materials, Computer Methods in Applied Mechanics and Engineering, 171 (1999) 387-418.
[68] C. Miehe, J. Schotte, J. Schröder, Computational micro–macro transitions and overall moduli in the analysis of polycrystals at large strains, Computational Materials Science, 16 (1999) 372-382.
[69] I. Temizer, T.I. Zohdi, A numerical method for homogenization in non-linear elasticity, Comput Mech, 40 (2007) 281-298.
[70] L. Collini, Micromechanical modeling of the elasto-plastic behavior of heterogeneous nodular cast iron. Ph. D., Universita' Degli Studi di Parma, Parma, 2004.
[71] I.M. Gitman, Representative volumes and multi-scale modelling of quasi-brittle materials. Ph. D., Technische Universiteit Delft, 2006.
[72] O. van der Sluis, P.J.G. Schreurs, W.A.M. Brekelmans, H.E.H. Meijer, Overall behaviour of heterogeneous elastoviscoplastic materials: effect of microstructural modelling, Mechanics of Materials, 32 (2000) 449-462.
[73] A.M. Holger, Computational homogenization of confined granular media. PhD, Technische Universitaet Kaiserslautern, 2009.
[74] G.A. Kassem, Micromechanical material models for polymer composites through advanced numerical simulation techniques. PhD, Rheinisch-Westfälischen Technischen Hochschule Aachen, Aachen, 2009.

[75] V.G. Kouznetsova, M.G.D. Geers, W.A.M. Brekelmans, Multi-scale second-order computational homogenization of multi-phase materials: a nested finite element solution strategy, Computer Methods in Applied Mechanics and Engineering, 193 (2004) 5525-5550.
[76] A. Anthoine, Second-order homogenisation of functionally graded materials, International Journal of Solids and Structures, 47 (2010) 1477-1489.
[77] V.G. Kouznetsova, M. Geers, W.A.M. Brekelmans, Size of a Representative Volume Element in a Second-Order Computational Homogenization Framework, International Journal for Multiscale Computational Engineering, 2 (2004) 24.
[78] I.M. Gitman, H. Askes, E.C. Aifantis, The Representative Volume Size in Static and Dynamic Micro-Macro Transitions, Int J Fract, 135 (2005) L3-L9.
[79] L.K. Kaczmarczyk, C.J. Pearce, N. Bicanic, Scale transition and enforcement of RVE boundary conditions in second-order computational homogenization, International Journal for Numerical Methods in Engineering, 74 (2008) 506-522.
[80] S. Forest, D.K. Trinh, Generalized continua and non-homogeneous boundary conditions in homogenisation methods, ZAMM - Journal of Applied Mathematics and Mechanics / Zeitschrift für Angewandte Mathematik und Mechanik, 91 (2010) 90-109.
[81] N.A. Fleck, J.W. Hutchinson, A phenomenological theory for strain gradient effects in plasticity, Journal of the Mechanics and Physics of Solids, 41 (1993) 1825-1857.
[82] N.A. Fleck, J.W. Hutchinson, A reformulation of strain gradient plasticity, Journal of The Mechanics and Physics of Solids, 49 (2001) 2245-2271.
[83] J.W. Hutchinson, Generalizing J2 flow theory: Fundamental issues in strain gradient plasticity, Acta Mech Sin, 28 (2012) 1078-1086.
[84] E. Cosserat, F. Cosserat, Théorie des Corps déformables, Nature, 81 (1909) 67-67.
[85] R.D. Mindlin, H.F. Tiersten, Effects of couple-stresses in linear elasticity, Archive for Rational Mechanics and Analysis, 11 (1962) 415-448.
[86] R.D. Mindlin, Influence of couple-stresses on stress concentrations, Experimental Mechanics, 3 (1963) 1-7.
[87] W. Koiter, Couple-stresses in the theory of elasticity, 1963.
[88] R.A. Toupin, Theories of elasticity with couple-stress, Archive for Rational Mechanics and Analysis, 17 (1964) 85-112.
[89] A.C. Eringen, E.S. Suhubi, Nonlinear theory of simple micro-elastic solids—I, International Journal of Engineering Science, 2 (1964) 189-203.
[90] P. Germain, The Method of Virtual Power in Continuum Mechanics. Part 2: Microstructure, SIAM Journal on Applied Mathematics, 25 (1973) 556-575.
[91] R.A.B. Engelen, M.G.D. Geers, F.P.T. Baaijens, Nonlocal implicit gradient-enhanced elasto-plasticity for the modelling of softening behaviour, International Journal of Plasticity, 19 (2003) 403-433.
[92] R. De Borst, H.-B. Mühlhaus, Gradient-dependent plasticity: Formulation and algorithmic aspects, International Journal for Numerical Methods in Engineering, 35 (1992) 521-539.
[93] R. de Borst, J. Pamin, M.G.D. Geers, On coupled gradient-dependent plasticity and damage theories with a view to localization analysis, European Journal of Mechanics - A/Solids, 18 (1999) 939-962.
[94] N.A. Fleck, G.M. Muller, M.F. Ashby, J.W. Hutchinson, Strain gradient plasticity: Theory and experiment, Acta Metallurgica et Materialia, 42 (1994) 475-487.
[95] S.B. Altan, E.C. Aifantis, On the structure of the mode III crack-tip in gradient elasticity, Scripta Metallurgica et Materialia, 26 (1992) 319-324.
[96] E.C. Aifantis, Strain gradient interpretation of size effects, Int J Fract, 95 (1999) 299-314.

[97] H.T. Zhu, H.M. Zbib, E.C. Aifantis, Strain gradients and continuum modeling of size effect in metal matrix composites, Acta Mechanica, 121 (1997) 165-176.
[98] E.C. Aifantis, On scale invariance in anisotropic plasticity, gradient plasticity and gradient elasticity, International Journal of Engineering Science, 47 (2009) 1089-1099.
[99] G.A. Maugin, A.V. Metrikine, Mechanics of Generalized Continua, Springer, 2010.
[100] C.Q. Ru, E.C. Aifantis, A simple approach to solve boundary-value problems in gradient elasticity, Acta Mechanica, 101 (1993) 59-68.
[101] G.E. Exadaktylos, E.C. Aifantis, Two and Three Dimensional Crack Problems in Gradient Elasticity, Journal of the Mechanical Behavior of Materials, No. 2 (1996.).
[102] J.H. Argyris, I. Fried, D.W. Scharpf, The TUBA family of plate elements for the matrix displacement method, 1968.
[103] K. Bell, A refined triangular plate bending finite element, International Journal for Numerical Methods in Engineering, 1 (1969) 101-122.
[104] R. Clough, J. Tocher, Finite element stiffness matrices for analysis of plate bending, Finite element stiffness matrices for analysis of plate bending, (1965) 515-545.
[105] M.J.D. Powell, M.A. Sabin, Piecewise Quadratic Approximations on Triangles, ACM Trans. Math. Softw., 3 (1977) 316-325.
[106] H. Askes, T. Bennett, E.C. Aifantis, A new formulation and C0-implementation of dynamically consistent gradient elasticity, International Journal for Numerical Methods in Engineering, 72 (2007) 111-126.
[107] H. Askes, M.A. Gutiérrez, Implicit gradient elasticity, International Journal for Numerical Methods in Engineering, 67 (2006) 400-416.
[108] C. Britta Hirschberger, E. Kuhl, P. Steinmann, On deformational and configurational mechanics of micromorphic hyperelasticity – Theory and computation, Computer Methods in Applied Mechanics and Engineering, 196 (2007) 4027-4044.
[109] N. Kirchner, P. Steinmann, On the material setting of gradient hyperelasticity, Mathematics and Mechanics of Solids, 12 (2005) 3875-3895.
[110] N. Kirchner, P. Steinmann, A unifying treatise on variational principles for gradient and micromorphic continua, Philosophical Magazine, 85 (2005) 3875-3895.
[111] S.A. Papanicolopulos, A. Zervos, I. Vardoulakis, A three-dimensional C1 finite element for gradient elasticity, International Journal for Numerical Methods in Engineering, 77 (2009) 1396-1415.
[112] A. Zervos, I. Vardoulakis, P. Papanastasiou, Influence of Nonassociativity on Localization and Failure in Geomechanics Based on Gradient Elastoplasticity, International Journal of Geomechanics, 7 (2007) 63-74.
[113] R.d. Borst, J. Pamin, A gradient plasticity approach to finite element predictions of soil instability, Archives of Mechanics, 47 (1995) 353-377.
[114] R. De Borst, J. Pamin, Some novel developments in finite element procedures for gradient-dependent plasticity, International Journal for Numerical Methods in Engineering, 39 (1996) 2477-2505.
[115] A. Zervos, P. Papanastasiou, I. Vardoulakis, Modelling of localisation and scale effect in thick-walled cylinders with gradient elastoplasticity, International Journal of Solids and Structures, 38 (2001) 5081-5095.
[116] P. Fischer, J. Mergheim, P. Steinmann, On the C1 continuous discretization of non-linear gradient elasticity: A comparison of NEM and FEM based on Bernstein–Bézier patches, International Journal for Numerical Methods in Engineering, 82 (2010) 1282-1307.
[117] P.E. Fischer, C1 Continuous Methods in Computational Gradient Elasticity. PhD., University Erlangen-Nurnberg, Erlangen, 2011.
[118] S. Dasgupta, D. Sengupta, A higher-order triangular plate bending element revisited, International Journal for Numerical Methods in Engineering, 30 (1990) 419-430.

[119] T. Lesičar, Z. Tonković, J. Sorić, P. Čanžar, Multiscale Modelling Of Deformation Processes Of Nodular Cast Iron, in: Z. Virag, H. Kozmar, I. Smojver (Eds.) 7th Int. Congress of Croatian Society of Mech., Studio HRG, Zadar, Croatia, 2012, pp. 163-164.
[120] J. Sorić, Metoda konačnih elemenata, Golden Marketing, Zagreb, 2004.
[121] T. Lesičar, J. Sorić, Z. Tonković, Large strain, two-scale computational approach using continuity finite element employing a second gradient theory, in: Computer Methods in Applied Mechanics and Engineering, 2016, pp. 303-324.
[122] ABAQUS/Standard, in, Dassault Systemes, Providence, RI, USA, 2014.
[123] ABAQUS Documentation, in, Dassault Systèmes, Providence, RI, USA, 2014.
[124] E. Giner, N. Sukumar, F.D. Denia, F.J. Fuenmayor, Extended finite element method for fretting fatigue crack propagation, International Journal of Solids and Structures, 45 (2008) 5675-5687.
[125] E. Giner, N. Sukumar, J.E. Tarancón, F.J. Fuenmayor, An Abaqus implementation of the extended finite element method, Engineering Fracture Mechanics, 76 (2009) 347-368.
[126] A.H. Stroud, D. Secrest, Gaussian quadrature formulas, Prentice-Hall: Englewood Cliffs, N. J., 1966.
[127] O.C. Zienkiewicz, R.L. Taylor, The Finite Element Method, Butterworth-Heinemann, 2000.
[128] T.J.R. Hughes, The Finite Element Method, Linear Static and Dynamic Finite Element Analysis, Prentice Hall: Englewood Cliffs, N. J., 1987.
[129] H.T. Rathod, K.V. Nagaraja, B. Venkatesudu, N.L. Ramesh, Gauss Legendre quadrature over a triangle, Journal of Indian Institute of Science, 84 (2004) 183-188.
[130] T. Lesičar, Z. Tonković, J. Sorić, Boundary Conditions in a Multiscale Homogenization Procedure, Key Engineering Materials, 577-578 (2013) 297-300.
[131] A.-K. Soh, C. Wanji, Finite element formulations of strain gradient theory for microstructures and the C0–1 patch test, International Journal for Numerical Methods in Engineering, 61 (2004) 433-454.
[132] C. Song, Z. Ming-Jue, F. Xiang-Rong, A 4-node hybrid stress-function (HS-F) plane element with drilling degrees of freedom less sensitive to severe mesh distortions, Comput. Struct., 89 517-528.
[133] M. Rezaiee-Pajand, M. Yaghoobi, Formulating an effective generalized four-sided element, European Journal of Mechanics - A/Solids, 36 (2012) 141-155.
[134] S. Cen, X.-M. Chen, C.F. Li, X.-R. Fu, Quadrilateral membrane elements with analytical element stiffness matrices formulated by the new quadrilateral area coordinate method (QACM-II), International Journal for Numerical Methods in Engineering, 77 (2009) 1172-1200.
[135] T. Lesičar, Z. Tonković, J. Sorić, C1 Continuity Finite Element Formulation in Second-Order Computational Homogenization Scheme, Journal of Multiscale Modelling, 04 (2012) 1250013.
[136] J.-S. Chen, M. Hillman, M. Rüter, An arbitrary order variationally consistent integration for Galerkin meshfree methods, International Journal for Numerical Methods in Engineering, 95 (2013) 387-418.
[137] R. Hill, Elastic properties of reinforced solids: Some theoretical principles, Journal of the Mechanics and Physics of Solids, 11 (1963) 357-372.
[138] P. Suquet, Local and global aspects in the mathematical theory of plasticity, Plasticity today: modelling, methods and applications, (1985) 279-310.
[139] J. Guedes, N. Kikuchi, Preprocessing and postprocessing for materials based on the homogenization method with adaptive finite element methods, Computer Methods in Applied Mechanics and Engineering, 83 (1990) 143-198.

[140] I.M. Gitman, M.B. Gitman, H. Askes, Quantification of stochastically stable representative volumes for random heterogeneous materials, Arch Appl Mech, 75 (2006) 79-92.
[141] T. Kanit, S. Forest, I. Galliet, V. Mounoury, D. Jeulin, Determination of the size of the representative volume element for random composites: statistical and numerical approach, International Journal of Solids and Structures, 40 (2003) 3647-3679.
[142] H.A. Meier, E. Kuhl, P. Steinmann, A note on the generation of periodic granular microstructures based on grain size distributions, International Journal for Numerical and Analytical Methods in Geomechanics, 32 (2008) 509-522.
[143] M. Stroeven, H. Askes, L.J. Sluys, Numerical determination of representative volumes for granular materials, Computer Methods in Applied Mechanics and Engineering, 193 (2004) 3221-3238.
[144] S. Forest, K. Sab, Cosserat overall modeling of heterogeneous materials, Mechanics Research Communications, 25 (1998) 449-454.
[145] M. Ostoja-Starzewski, S.D. Boccara, I. Jasiuk, Couple-stress moduli and characteristics length of a two-phase composite, Mechanics Research Communications, 26 (1999) 387-396.
[146] H.M. Inglis, P.H. Geubelle, K. Matouš, Boundary condition effects on multiscale analysis of damage localization, Philosophical Magazine, 88 (2008) 2373-2397.
[147] Y. Cho, W. Lee, Y. Park, Effect of boundary conditions on the numerical solutions of representative volume element problems for random heterogeneous composite microstructures, Met. Mater. Int., 20 (2014) 1085-1093.
[148] M. Kamiński, Ł. Figiel, Effective elastoplastic properties of the periodic composites, Computational Materials Science, 22 (2001) 221-239.
[149] Z. Yuan, J. Fish, Toward realization of computational homogenization in practice, International Journal for Numerical Methods in Engineering, 73 (2008) 361-380.
[150] I.M. Gitman, H. Askes, L.J. Sluys, Representative volume: Existence and size determination, Engineering Fracture Mechanics, 74 (2007) 2518-2534.
[151] V.P. Nguyen, M. Stroeven, L.J. Sluys, An enhanced continuous–discontinuous multiscale method for modeling mode-I cohesive failure in random heterogeneous quasi-brittle materials, Engineering Fracture Mechanics, 79 (2012) 78-102.
[152] E.W.C. Coenen, V.G. Kouznetsova, E. Bosco, M.G.D. Geers, A multi-scale approach to bridge microscale damage and macroscale failure: a nested computational homogenization-localization framework, Int J Fract, 178 (2012) 157-178.
[153] V.P. Nguyen, O. Lloberas-Valls, M. Stroeven, L.J. Sluys, Homogenization-based multiscale crack modelling: From micro-diffusive damage to macro-cracks, Computer Methods in Applied Mechanics and Engineering, 200 (2011) 1220-1236.
[154] C. Luo, A. Chattopadhyay, Prediction of fatigue crack initial stage based on a multiscale damage criterion, International Journal of Fatigue, 33 (2011) 403-413.
[155] E. Bosco, V.G. Kouznetsova, E.W.C. Coenen, M.G.D. Geers, A. Salvadori, A multiscale framework for localizing microstructures towards the onset of macroscopic discontinuity, Comput Mech, 54 (2014) 299-319.
[156] I.M. Gitman, H. Askes, L.J. Sluys, Coupled-volume multi-scale modelling of quasi-brittle material, European Journal of Mechanics - A/Solids, 27 (2008) 302-327.
[157] J. Petera, J.F.T. Pittman, Isoparametric Hermite elements, International Journal for Numerical Methods in Engineering, 37 (1994) 3489-3519.